Tectonique et processus d'exhumation des Cordillères Blanche et Noire en contexte de subduction horizontale (Nord Pérou)

Audrey Margirier

UNIVERSITÉ GRENOBLE ALPES

THÈSE

Pour obtenir le grade de

DOCTEUR DE L'UNIVERSITÉ GRENOBLE ALPES

Spécialité : **Terre Solide**

Arrêté ministériel : 7 août 2006

Présentée par

Audrey Margirier

Thèse dirigée par **Laurence Audin** et **Xavier Robert**

préparée au sein du **Laboratoire ISTerre**
dans **l'École Doctorale Terre, Univers Environnement**

Tectonique et processus d'exhumation des Cordillères Blanche et Noire en contexte de subduction horizontale (Nord Pérou)

Thèse soutenue publiquement le **27 novembre 2015**,
devant le jury composé de :

M. Peter VAN DER BEEK
Professeur à l'Université Grenoble-Alpes, Président du jury
Mme Taylor SCHILDGEN
Professeur au GFZ Potsdam, Rapporteur
M. Fritz SCHLUNEGGER
Professeur à l'Université de Bern, Rapporteur
M. Michel DE SAINT BLANQUAT
DR CNRS à Géosciences Environnement Toulouse, Examinateur
M. Nicolas ARNAUD
DR CNRS à Géosciences Montpellier, Examinateur
Mme Cécile GAUTHERON
MdC à l'Université Paris Sud, Invitée
Mme Laurence AUDIN
CR IRD à l'Université Grenoble Alpes, Directrice de thèse
M. Xavier ROBERT
CR IRD à l'Université Grenoble Alpes, Directeur de thèse

UNIVERSITÉ GRENOBLE ALPES

THÈSE

Pour obtenir le grade de

DOCTEUR DE L'UNIVERSITÉ GRENOBLE ALPES

Spécialité : **Terre Solide**

Arrêté ministériel : 7 août 2006

Présentée par

Audrey Margirier

Thèse dirigée par **Laurence Audin** et **Xavier Robert**

préparée au sein du **Laboratoire ISTerre**
dans **l'École Doctorale Terre, Univers Environnement**

Tectonics and exhumation processes above a flat subduction: example of the Cordilleras Blanca and Negra (northern Peru)

Thèse soutenue publiquement le **27 novembre 2015**,
devant le jury composé de :

M. Peter VAN DER BEEK
Professeur à l'Université Grenoble-Alpes, Président du jury
Mme Taylor SCHILDGEN
Professeur au GFZ Potsdam, Rapporteur
M. Fritz SCHLUNEGGER
Professeur à l'Université de Bern, Rapporteur
M. Michel DE SAINT BLANQUAT
DR CNRS à Géosciences Environnement Toulouse, Examinateur
M. Nicolas ARNAUD
DR CNRS à Géosciences Montpellier, Examinateur
Mme Cécile GAUTHERON
MdC à l'Université Paris Sud, Invitée
Mme Laurence AUDIN
CR IRD à l'Université Grenoble Alpes, Directrice de thèse
M. Xavier ROBERT
CR IRD à l'Université Grenoble Alpes, Directeur de thèse

Remerciements

Cette thèse n'aurait pas abouti dans la bonne humeur sans le soutien et la compagnie de nombreuses personnes, **un grand merci à / thank you to** :

Laurence et Xavier qui m'ont offert un super encadrement : des conseils avisés, une disponibilité à toute épreuve (mention spéciale à Xavier en mission au Pérou pour la réactivité pendant la rédaction), une grande liberté scientifique (et non, je n'ai pas fais exactement ce qui était prévu à la base). Grâce à vous ces trois années ont été formidables et enrichissantes !

The jury : Taylor Schildgen, Fritz Schlunegger, Peter van der Beek, Michel de Saint Blanquat, Nicolas Arnaud and Cécile Gautheron for reading my manuscript and being here for the defense. Thank you for the interessant discussion following my presentation.

François et Francis, votre travail de préparation des échantillons a été précieux, sans vous mes échantillons seraient encore dans des bidons au fond du garage !

Matthias, Elisabeth et Mélanie pour m'avoir accueilli dans le laboratoire trace de fission et de m'avoir fait découvrir les "joies" du polissage et du comptage.

Cécile qui m'a initié au picking et l'empaquetage des apatites. Grâce à ces travaux pratiques je pourrai presque me reconvertir dans l'horlogerie ! C'étais super de discuter avec toi de l'interprétations de âges et des modélisations !

Frédéric, Georgina, Pierre and Renske pour l'accueil à Lausanne, j'ai vraiment passé des super moments avec vous... En salle noire, en chimie, devant l'ordinateur ou au bord du lac ;-)...

Jérôme Ganne qui m'a expliqué les bases de la thermobarométrie sur amphibole à la toute fin de ma thèse.

Catherine, Sarah et Sylvain pour m'avoir accueilli dans le laboratoire de chimie. Même si au final ca n'a rien donné mon passage en géochimie m'aura permis de confirmer que je ne me suis pas trompée de spécialitée !

Jean pour m'avoir initié à la modélisation numérique et aidé avec FastScape.

Sarah who organized our first field trip in the Cordillera Blanca in 2012. It was a great beginning for my PhD !

Je remercie également toutes les personnes sympathiques du laboratoire qui rendent l'environnement de travail agréable et grâce à qui j'ai passé des bons moments au laboratoire, en montagne, en ville ou en conférence...

En particulier mes sympathiques cobureaux : Charlotte, Morgane (à l'époque du bureau de filles), Jonathan et Margarita. Ca a été un plaisir de passer du temps avec vous même si parfois il fallait bosser (surtout à la fin) !

Toutes les personnes qui rendent la pause café/chocolat agréable (merci pour le chocolat).

Les autres thésards d'ISTerre avec qui j'ai partagé ces années de thèse, sans vous le labo aurait été différent : Bertrand (je t'attend pour le ski !), Vincent (j'ai gagné !), Mélanie, Margaux, Natalie (merci pour le chocolat), Anne, Cécile, Rachel. Mais aussi les thésards et docteurs d'origines plus lointaines : Arnaud, Maélianna, Chloé.

Les amis des premières années de fac : Paloma, Gwladys, Mathilde, Benjamin, Raphael (merci d'être venu pour ma soutenance et pour le beau chapeau de docteur).

Marion ma première partenaire de terrain à Digne et dans les Ecrins !

Et toutes les autres personnes que j'ai pu oublier ici !

Merci à mes parents qui m'ont soutenue et qui ont cru en moi pendant mes études (au début c'étais pas gagné), merci pour l'organisation du pot aussi ! Merci Zian pour le soutien pendant la thèse et surtout pour tous les bons moments partagés !

Processus d'exhumation des Cordillères Blanche et Noire en contexte de subduction horizontale (Nord Pérou)

Ma thèse se focalise sur l'étude des mécanismes qui ont conduit au soulèvement et à la construction du relief dans les Andes du Nord du Pérou. Dans cette région, la Cordillère Blanche forme les plus hauts sommets péruviens (> 6000 m) et constitue une anomalie à l'échelle des Andes. La morphologie de cette région des Andes est marquée par un pluton de forme atypique, allongé et à l'affleurement sur plus de 150 km. Ce pluton est bordé par une faille normale de plus de 200 km de long. La présence de cette faille normale majeure en contexte de subduction plane reste surprenante car ces zones de subduction planes semblent induire une augmentation du raccourcissement dans la plaque chevauchante. Mon travail a eu pour objectifs de caractériser les variations de l'état de contraintes régional, l'âge du soulèvement et de discuter les processus géodynamiques qui ont contribué à la formation du relief. Dans ce cadre, j'ai utilisé une approche pluridisciplinaire impliquant sur plusieurs échelles spatio-temporelles et comprenant à la fois de nouvelles données de terrain, leur analyse et leur modélisation. Mes données de microtectonique indiquent qu'il est possible de générer de l'extension au dessus d'une subduction plane à l'échelle régionale. Ces données sont en contradiction avec l'augmentation du raccourcissement classiquement attendue dans la plaque chevauchante. Mes nouvelles données de thermochronologie basse température et leur modélisation montrent une augmentation de l'exhumation induite par le soulèvement de la Cordillère Occidentale à 15 Ma. En les confrontant aux modèles précédents, je propose un soulèvement régional lié à l'aplatissement de la subduction et à la topographie dynamique associée. J'ai également étudié l'impact de l'arc Miocène sur le soulèvement à une échelle plus locale. Pour cela, j'ai compilé tous les âges de refroidissement du pluton disponibles dans la littérature. En parallèle, j'ai obtenu les premières données de profondeur de mise en place du batholite de la Cordillère Blanche. Cela m'a permis de proposer une structure du batholite en sills empilés puis basculés vers l'est. De plus, la modélisation des variations spatio-temporelle des taux d'érosion à partir des données de thermochronologie basse température indique une augmentation importante des taux d'érosion dans la Cordillère Blanche à partir de 2 Ma. L'arc Miocène ne semble donc pas contribuer significativement au soulèvement malgré sa probable contribution à l'épaississement de la lithosphère. En revanche, l'érosion glaciaire récente semble contribuer fortement à l'exhumation de la Cordillère Blanche et au basculement du batholite. Dans la dernière partie de ma thèse, pour quantifier l'importance de l'érosion dans la création du relief et le soulèvement, j'ai modélisé l'évolution du paysage de la région (FastScape). Mes modélisations numériques démontrent le rôle majeur de l'érosion et du rebond flexural associé dans la création du relief et les taux de soulèvement. Pour finir, basée sur les données de la littérature et celles apportées par mon travail de thèse, je propose un nouveau modèle pour expliquer la faille normale de la Cordillère Blanche dans son contexte régional. Ce modèle implique une faille normale d'extrado et l'érosion importante du mur de la faille.

Mots-clés *Andes, subduction plane, soulèvement, Cordillère Blanche, Cordillère Noire, faille normale, érosion glaciaire, thermochronologie basse-température, modélisation du paysage*

Exhumation processes above a flat subduction: example of the Cordillera Blanca and Negra (northern Peru

My thesis focuses on the mechanisms that controlled the uplift and construction of the relief in the northern Peruvian Andes. In this area, the Cordillera Blanca forms the highest peaks in Peru (> 6000 m), which is a topographic anomaly across the Andes. The morphology of the Cordillera Blanca is marked by an elongated pluton, which outcrops over 150 km. In addition, this pluton is bordered by the largest normal fault from South America. The presence of this major normal fault in a flat-slab context remains surprising because flat slabs usually induce an increase of the shortening in the overriding plate. The aim of my work is to characterize the variations of the regional stress field, the age of the uplift and discuss the geodynamic processes that contributed to relief building. To address these issues, I used a multidisciplinary approach involving new field data, their analysis and modeling. My microtectonic dataset reveals regional extension above the Peruvian flat-slab. This data contradicts the expected increase of shortening in the overriding plate. Modeling my new thermochronologic data shows an increase in the exhumation rates induced by the uplift of the Cordillera Occidental since 15 Ma. I propose that the regional uplift relates to the flattening of the subduction and associated dynamic topography. To address the impact of the Miocene arc on the uplift at a more local scale, I compiled the cooling ages of the pluton available in the literature. In parallel, I obtained the first amphibole thermo-barometry data that constrains emplacement depth of the Cordillera Blanca batholith. Following these data, I propose that the batholith is structured in eastward-tilted sills. In addition, modeling of the space and time variations of erosion rates based on the inversion of thermochronologic data indicates that erosion rates significantly increased in the Cordillera Blanca since 2 Ma. The Miocene arc seems to insignificantly contribute to the local uplift despite its contribution to the thickening of the lithosphere. Thus, I suggest that the recent glacial erosion contributes to the exhumation of the Cordillera Blanca and subsequent tilting of the batholith. Then, I modeled the landscape evolution for the Cordillera Blanca region to quantify the contribution of erosion in the relief building and the uplift. My numerical models (FastScape) evidence the importance of erosion and associated flexural rebound in fostering relief building and the uplift rates. Finally, based on all available data, I propose a new regional model to explain the Cordillera Blanca normal fault. This model implies an extrado normal fault and erosion of the footwall.

Keywords *Andes, flat-slab, surface uplift, Cordillera Blanca, Cordillera Negra, normal faulting, glacial erosion, low-temperature thermochronology, landscape modelling*

Table des matières

Introduction

La Cordillère des Andes est l'exemple classique d'une chaîne de montagnes formée dans un contexte de subduction, elle s'étend sur plus de 6000 km le long de la bordure pacifique de l'Amérique du Sud. Les Andes sont caractérisées par du magmatisme et de la déformation associés à la subduction de la Plaque Nazca sous le continent sud américain qui dure depuis le Jurassique. La largeur de la chaîne tout comme son altitude varient en fonction de la latitude : les Andes Centrales atteignent 500 km de large et de nombreux sommets dépassent 5000 m d'altitude ; aux extrémités sud et nord des Andes, la chaîne est plus étroite et les sommets sont moins élevés (au nord, la chaîne atteint 300 km de large et 4000 m d'altitude ; au sud, la largeur est de ∼400 km et les altitudes atteignent seulement 2000 m). La subduction est également segmentée avec trois zones de subduction planes localisées en Colombie, au Pérou et au Chili (Barazangi & Isacks 1976). Des travaux récents montrent des interactions importantes entre la géologie, la dynamique mantellique, les processus de surface et le climat (e.g., Eakin et al. 2014, Montgomery et al. 2001, Husson et al. 2010). Mais des questions de premier ordre sont encore débattues comme par exemple : Quels sont les mécanismes qui conduisent au soulèvement et à l'exhumation des Andes ? A quel moment le soulèvement des Andes s'est produit ? Quelle est la nature de l'épaississement crustal dans la Cordillère Occidentale (magmatique ou tectonique) ? Quel est l'impact des zones de subduction horizontale sur le soulèvement et l'exhumation ?

L'impact de la subduction plane du Chili et de l'entrée en subduction de la ride Juan Fernandez sur la tectonique et l'exhumation dans la plaque chevauchante ont été très étudiés (e.g., Giambiagi et al. 2001, Ramos et al. 2002, Spikings et al. 2008, Dávila et al. 2010, Manea et al. 2011, Guillaume et al. 2009) mais l'influence de la zone de subduction plane du nord Pérou est peu documentée à l'heure actuelle (Sébrier et al. 1988, Hagen & Moberly 1994, Clift et al. 2003, Clift & Ruiz 2007, Regard et al. 2009, Eakin et al. 2014). Localisée à l'aplomb de la zone de subduction plane Péruvienne, la Cordillère Blanche (6768 m) comprend le point culminant du Pérou ainsi que de nombreux sommets de plus de 6000 m. Les altitudes élevées et le relief marqué de cette région en font un objectif privilégié pour quantifier le soulèvement et l'exhumation dans la plaque chevauchante. Cette région correspond à une anomalie à l'échelle andine. En effet, les sommets de la Cordillère Blanche sont formés par un pluton Miocène (Mukasa 1984, Giovanni 2007) de forme allongée et orienté parallèlement à la chaîne andine. L'activité magmatique qui a permit la mise en place du pluton est également anormale car localisée au dessus d'une zone de subduction horizontale. Les sommets de la Cordillère Blanche forment le mur d'une faille normale (CBNF) parallèle à la chaîne et de ∼200 km de long. Depuis ∼5 Ma, la CBNF a accommodé au moins 4500 m de déplacement vertical (Bonnot 1984, Giovanni 2007). Différents modèles ont été proposés pour expliquer la présence de cette faille normale au coeur des Andes (Dalmayrac & Molnar 1981, McNulty & Farber 2002) mais son origine est encore mal comprise.

La thermochronologie basse température (traces de fission, (U-Th)/He) permet d'obtenir des informations sur l'histoire thermique des roches dans la croute entre 120 et 40°C (Gallagher et al. 1998, Gautheron et al. 2009). Les histoires thermiques peuvent ensuite, en accord avec la géologie, être interprétées en terme d'exhumation qu'il est, sous certaines conditions, possible de traduire en terme de soulèvement. La thermochronologie permettra de contraindre l'histoire de l'exhumation andine au nord du Pérou. La mise en relation de l'exhumation avec le contexte géologique permettra de faire des interprétations en terme de soulèvement de la Cordillère Occidentale. En comparant nos données avec des données de géodynamique régionale (subduction de la ride de Nazca et aplatissement de la subduction, Rosenbaum et al. 2005, Gutscher et al. 1999), je propose d'explorer l'impact de l'aplatissement du slab sur l'exhumation et le soulèvement. De façon plus locale, j'ai mené une étude structurale et microstructurale pour contraindre le contexte tectonique lors de la mise en place et l'exhumation de la Cordillère Blanche, contexte qui est encore débattu à l'heure actuelle (Petford & Atherton 1992, McNulty & Farber 2002). Pour contraindre la dynamique de la mise en place du batholite de la Cordillère Blanche et son exhumation j'ai utilisé la thermobarométrie sur amphibole et j'ai étudié la répartition des âges géochronologiques. Enfin, pour reconstruire les variations spatio-temporelles des taux d'érosion dans la Cordillère Blanche, tous les âges thermochronologiques disponibles dans la région ont été inversés suivant la méthode de Fox et al. (2014).

Après une introduction sur le contexte géodynamique des Andes et le contexte régional (Chapitre 1), je détaille les méthodes que j'ai mises en oeuvre au cours de ma thèse (Chapitre 2). Les chapitres suivants (Chapitres 3, 4, 5, 6) sont consacrés aux résultats que j'ai obtenus. Pour finir, le Chapitre 7 résume mes conclusions et apporte des perspectives à mon travail.

Contexte 1

Sommaire

Ce chapitre introduit la géologie des Andes, la région de la Cordillère Blanche et la problématique de mon travail.

This chapter introduces Andean geology, the Cordillera Blanca area and the issue of my thesis.

1.1 Les Andes, une chaîne segmentée

La Cordillère des Andes est la plus haute (6000 m) et la plus longue chaîne de montagnes associée à une convergence océan-continent. Les Andes s'étendent sur plus de 7000 km du Sud vers le Nord pour une largeur maximale de ~500 km dans les Andes Centrales. Les sommets de la Cordillère des Andes forment une barrière orographique majeure dans l'hémisphère Sud, cette barrière induit de fortes variations spatiales de climat dans toute l'Amérique du Sud.

1.1.1 Topographie

Dans les Andes Centrales (Pérou, Bolivie), la chaîne se compose de deux cordillères qui atteignent 6000 m d'altitude : la Cordillère Orientale et la Cordillère Occidentale. Elles sont séparées par un bassin endorhéique, l'Altiplano, qui forme un plateau à ~4000 m d'altitude (Fig. 1.1). Dans leur partie sud (Chili, Argentine), les Andes forment une seule Cordillère assez étroite, d'altitude modérée (~2000 m ; Fig. 1.1). Les Andes du nord (Colombie) s'organisent en plusieurs Cordillères qui correspondent à des arcs volcaniques d'ages différents, et atteignent des altitudes élevées (~4000 m ; Fig. 1.1).

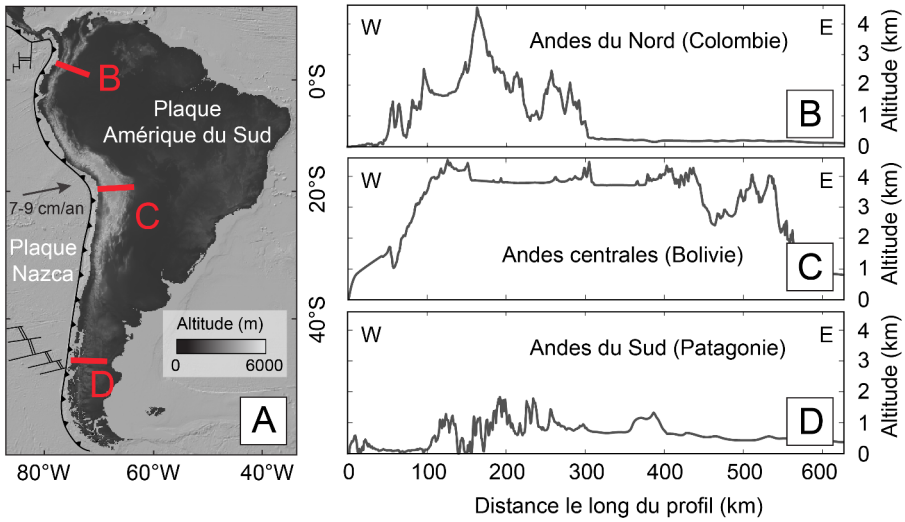

FIGURE 1.1 – *Carte et coupes montrant les différences de relief de la chaîne andine. A) Carte topographique de l'Amérique du sud et localisation des coupes. B) Coupe E-W dans les Andes du nord. C) Coupe au niveau des Andes Centrales. D) Coupe dans les Andes du sud.*

1.1.2 Climat

Dans les Andes Centrales, le versant ouest des Andes est hyperaride tandis que sur le versant Amazonien à l'est, l'humidité augmente très nettement. Le climat aride de la côte Pacifique du Pérou est lié à sa position dans le flux descendant dans la cellule de circulation atmosphérique de

Hadley ; à la circulation des masses océaniques et en particulier au déplacement en direction du nord du courant froid de Humboldt qui provient de l'Antarctique et à la barrière orographique des Andes. L'âge de la mise en place du climat actuel sur le versant ouest des Andes est discuté (Mortimer 1980, Alpers & Brimhall 1988, Dunai et al. 2005) mais il est probablement Néogène (∼15 Ma).

1.1.3 Segmentation de la subduction

Trois zones de subduction horizontales le long des Andes

Aux variations géographiques et climatiques dans la Cordillère des Andes s'ajoutent des variations de la géométrie de la subduction le long de la marge. En moyenne, le pendage de la plaque plongeante est de ∼30° vers l'est mais il existe des segments où la plaque plongeante est subhorizontale. Le long de la marge andine trois zones de subduction horizontales ont été identifiées (Fig. 1.2) : au Chili (28°S - 33°S), au nord du Pérou (4°S-14°S) et en Colombie (2°N-12°N) (Barazangi & Isacks 1976, Ramos & Folguera 2009). D'autres segments de subduction horizontale ont existé par le passé et ont marqué la morphologie de la chaîne (Ramos & Folguera 2009, Martinod et al. 2010, O'Driscoll et al. 2012). En effet, les zones de subduction horizontale affectent l'activité magmatique le long de la chaîne, l'arc s'éloigne de la fosse puis cesse de fonctionner lors de l'aplatissement de la subduction (Ramos & Folguera 2009). L'applatissement de la subduction augmente également le couplage à l'interface entre les deux plaques et induit une augmentation et une migration du raccourcissement vers l'est (e.g., Ramos & Folguera 2009). De nombreux travaux montrent un soulèvement dans les régions d'avant arc et d'arrière arc en lien avec la géométrie de la subduction (e.g., Spikings et al. 2008, Clift et al. 2003, Clift & Ruiz 2007, Regard et al. 2009, Eakin et al. 2014).

Origines des variations de pendages de la plaque plongeante

Dans les zones de subduction la majorité des séismes est localisée à l'interface entre la plaque plongeante et le manteau, la répartition des séismes permet donc d'obtenir une image du plan de subduction et de définir le pendage de la plaque plongeante. Les valeurs de pendages sont très différentes suivant la zone de subduction étudiée (∼30° au niveau de l'Amérique du Sud, ∼80° dans la région des Mariannes).

De nombreuses études ont été réalisées pour déterminer quels paramètres contrôlent le pendage de la plaque plongeante, différents paramètres ont été proposés : (I) l'âge de la plaque plongeante (Vlaar & Wortel 1976, Molnar & Atwater 1978), (II) le régime thermique de la plaque plongeante (e.g., Furlong & Chapman 1982), (III) le taux de convergence (Luyendyk 1970, Furlong & Chapman 1982), (IV) la traction associée à la plaque plongeante et la poussée au niveau de la ride (Uyeda & Kanamori 1979), (V) la direction de la plaque plongeante (E vs. W ; Doglioni et al. 1999), (VI) la vitesse absolue et la nature de la plaque chevauchante (Schellart 2005, Lallemand et al. 2005). Les travaux récents de Lallemand et al. (2005) mettent en évidence qu'il n'y a pas de corrélation entre

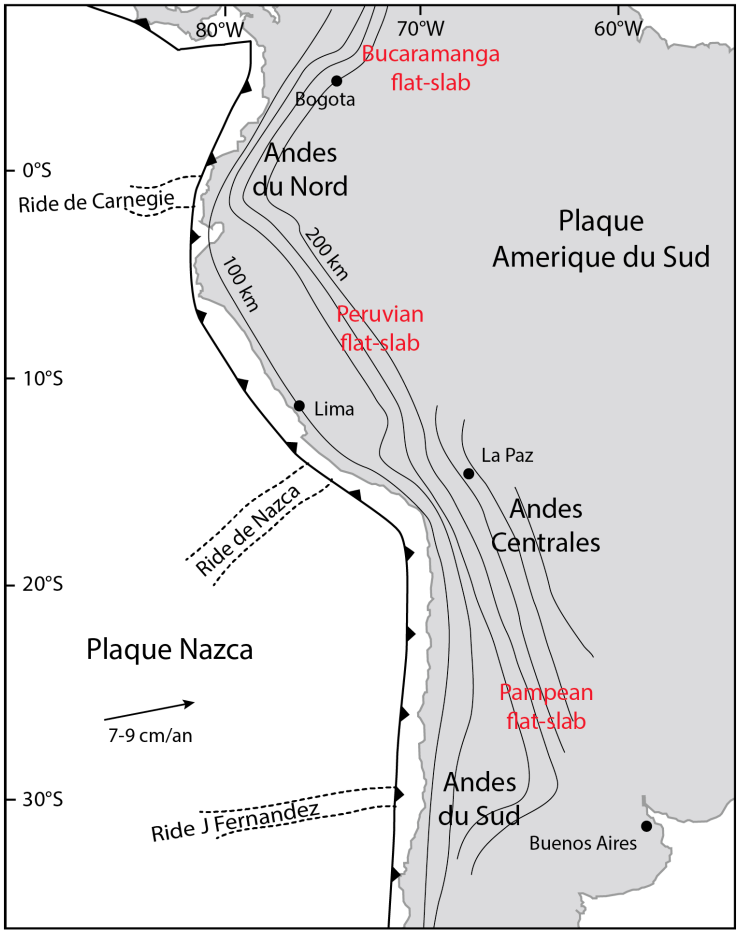

FIGURE 1.2 – *Les segments de subduction plane de la Plaque Nazca et positions actuelles des rides qui entrent en subduction, modifiée d'après Ramos & Folguera (2009). La limite entre les plaques Amérique du Sud et Nazca est représentée par un trait épais, les iso-profondeurs de la Plaque Nazca au niveau de la subduction sont représentées par des traits fins, les contours des rides qui entrent en subduction sont matérialisés par des pointillés.*

le taux de convergence, le régime thermique, l'age de la lithosphère, la traction ou la poussée de la plaque plongeante et la direction de la subduction ; seule la vitesse absolue de la plaque chevauchante contrôlerait le pendage de la plaque plongeante. Dans le cas de la subduction andine, le mouvement vers l'ouest de l'Amérique du Sud, lié à l'ouverture de l'océan Atlantique depuis ~130-125 Ma (Larson & Ladd 1973), entraine une migration de la fosse vers l'océan et une subduction faiblement pentée (~30° en moyenne). Les variations latitudinales du pendage de la plaque Nazca et les segments de subduction planes semblent s'expliquer par l'entrée en subduction de zones de fractures (Ride de Nazca et Ride de Juan Fernandez) présentes sur la Plaque Nazca. La flottabilité importante de ces zones empêcherait la plaque océanique de plonger et entrainerait ainsi un aplatissement de la plaque plongeante (van Hunen et al. 2002).

1.1.4 Modèles de soulèvement des Andes

Le soulèvement des Andes a été majoritairement étudié dans les Andes Centrales, au niveau de L'Altiplano. Sur le versant est des Andes les structures tectoniques sont bien documentées, des structures en compression contribuent à l'épaississement crustal et au soulèvement (e.g., Espurt et al. 2011, Gautheron et al. 2012, Barke & Lamb 2006, Isacks 1988, McQuarrie 2002, Kley & Monaldi 1998). En revanche, sur le flanc ouest des Andes les structures géologiques sont moins bien connues et les mécanismes qui ont contribué à l'épaississement crustal et au soulèvement de la Cordillère Occidentale sont encore débattus (e.g., Barnes & Ehlers 2009). Deux dynamiques de soulèvement s'opposent, le premier correspond à un soulèvement constant depuis 40 Ma (McQuarrie et al. 2005) tandis que le second serait un soulèvement rapide entre 10 et 6 Ma (Garzione et al. 2006, Schildgen et al. 2007). La part du contrôle tectonique vis à vis des processus d'altération et de dégradation du relief est discutée à l'heure actuelle et a peu été étudiée au Pérou. Différents modèles ont été proposés pour expliquer le soulèvement de l'Altiplano (Fig. 1.3) : (I) un raccourcissement tectonique réparti (e.g., Isacks 1988, Kley & Monaldi 1998, McQuarrie 2002), (II) un épaississement magmatique (Thorpe et al. 1981, James & Sacks 1999, Mamani et al. 2010), (III) des changements de propriété de la plaque continentale, des changements de géométrie de la subduction ou des changements des propriétés de l'interface entre les plaques (e.g., Isacks 1988, Gephart 1994, Allmendinger & Gubbels 1996, Lamb & Davis 2003), (IV) le sous placage du craton brésilien (Lamb & Hoke 1997), (V) une délamination et un fluage latéral de la croute inférieure (e.g., Garzione et al. 2006, Schildgen et al. 2007, Garzione et al. 2008, Husson 2003), (VI) un changement climatique ou un gradient d'érosion (e.g., Masek et al. 1994, Horton 1999, Montgomery et al. 2001, Lamb & Davis 2003, Barnes & Pelletier 2006, McQuarrie et al. 2008, Strecker et al. 2009).

Pour comprendre les processus qui ont conduits au soulèvement des Andes et les liens éventuels avec la géométrie de la subduction mon travail de thèse se focalise sur la Cordillère Blanche qui, située juste au dessus du segment de subduction horizontale du nord Pérou, présente des contrastes de relief importants et les plus hauts sommets du Pérou.

1.2 Région de la Cordillère Blanche

1.2.1 Contexte tectonique régional et faille normale de la Cordillère Blanche

Le nord du Pérou et la région de la Cordillère Blanche ont été affectées par différentes phases tectoniques depuis l'Eocène (Mégard et al. 1984). L'épisode de déformation Incaïque (Eocène) correspond à la plus importante phase de raccourcissement dans les Andes Péruviennes et Boliviennes. Au nord du Pérou, cet épisode de raccourcissement s'est traduit par la formation de la zone de plis et de chevauchements du Marañón qui a ensuite été réactivée en compression au début du Mio-

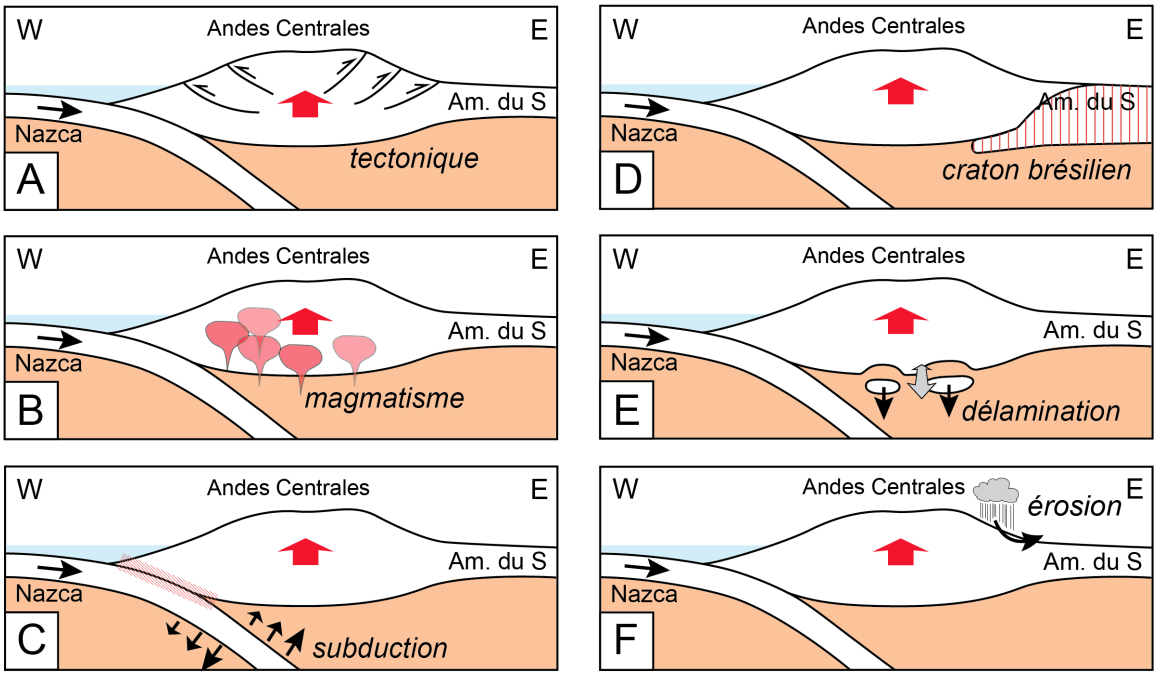

FIGURE 1.3 – *Les différents modèles proposés pour expliquer le soulèvement des Andes Centrales. A) Raccourcissement tectonique. B) Ajouts de magma. C) Changement des propriétés de l'interface de subduction ou changement de la géométrie de la subduction. D) Sous-placage du craton brésilien. E) Délamination de la croute inférieure et fluage de celle ci. F) Gradient d'érosion.*

cène (épisode Quechua 1). L'épisode Quechua 2 s'est traduit principalement par du décrochement le long de structures NW-SE. Par la suite, la déformation migre dans les subandes au cours de l'épisode Quechua 3 (Mégard et al. 1984). Actuellement le front de déformation actif se situe à l'est des Andes.

La région de la Cordillère Blanche est structurée par une grande faille normale. Orientée NNW-SSE avec un pendage moyen de 40°W, la faille normale de la Cordillère Blanche borde le flanc ouest de la Cordillère Blanche sur ∼200 km (Fig. 1.6). Cette faille est visible dans la morphologie de la région, elle forme des facettes triangulaires qui peuvent atteindre 1000 m de haut dans la partie nord de la Cordillère Blanche (Fig. 1.4). La faille recoupe et décale aussi des moraines et des dépôts fluvio-glaciaires sur le flanc ouest de la Cordillère blanche (Fig. 1.4). Depuis ∼5.4 Ma, la faille normale de la Cordillère Blanche a accommodé au moins 4500 m de déplacement vertical (Bonnot 1984, Giovanni 2007). Au sud et au nord de la Cordillère blanche la trace de la faille disparait : au sud la faille se termine en échelons, au nord la faille l'absence de marqueurs géomorphologiques (surfaces, terrasses, moraines) et l'incision forte des vallées ne permet pas de voir la terminaison de la faille. Une foliation ductile associée au jeu normale sur la faille est facilement identifiable sur le flanc ouest du granite de la Cordillère Blanche. Cette foliation est visible sur plusieurs kilomètres en direction du coeur du granite. Des marqueurs de la déformation ductile (filons déformés et boudinés) sont également visibles à proximité du plan de faille.

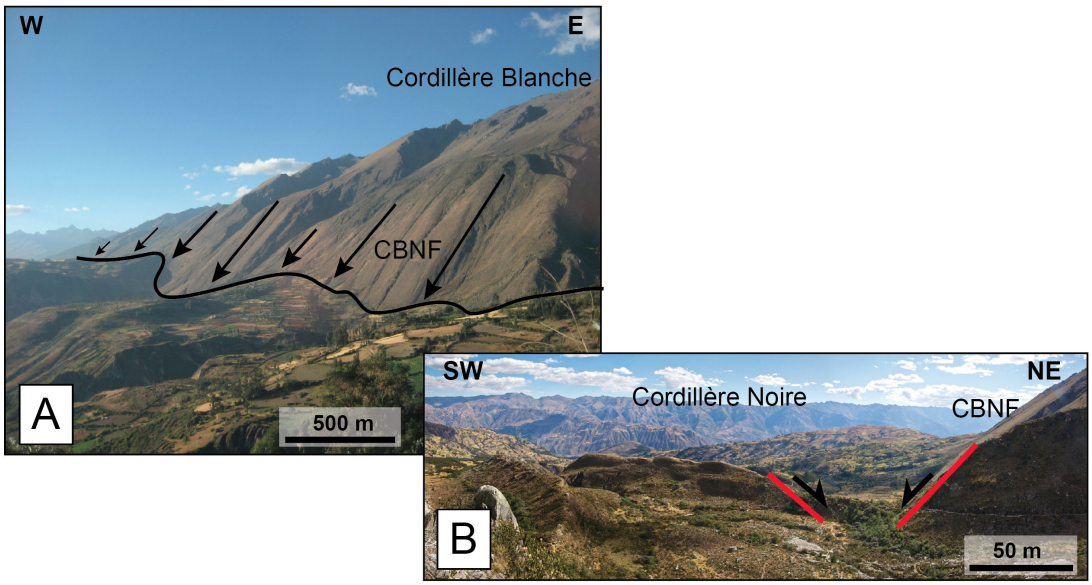

FIGURE 1.4 – *Photos de la faille normale de la Cordillère Blanche. A) Facettes triangulaires du plan de faille (partie nord de la Cordillère Blanche, vue vers le nord). B) Moraine découpée et décalée par la faille.*

Différents modèles ont été proposés pour expliquer la présence de cette faille normale au coeur des Andes. Dalmayrac & Molnar (1981), Deverchère et al. (1989), Petford & Atherton (1992) proposent que l'extension sur la faille est le résultat d'un effondrement gravitaire de la croûte surépaissie ; plus récemment, McNulty & Farber (2002) suggèrent que l'arrivée de la ride de Nazca sous la Cordillère Blanche augmenterait le couplage à l'interface entre les deux plaques et contrôlerait l'extension sur la faille de la Cordillère Blanche (Fig. 1.5). Ces modèles n'intègrent pas le contexte géologique régional, encore mal connu.

1.2.2 La Cordillère Blanche

Les sommets de la Cordillère Blanche forment le footwall de la faille normale de la Cordillère Blanche. La Cordillère Blanche (6768 m) regroupe les plus hauts sommets du Pérou, elle s'étend parallèlement à la chaîne andine sur plus de 200 km de long pour, en moyenne, une vingtaine de kilomètres de large (Fig. 1.6). La Cordillère Blanche correspond à un pluton granitique d'âge Miocène (12-5 Ma ; Mukasa 1984, McNulty et al. 1998, Giovanni 2007) qui s'est mis en place dans des sédiments Jurassique et Crétacé de la formation Chicama. Sa mise en place au dessus de la zone de subduction horizontale du nord Pérou, où le faible pendage de la plaque plongeante ne permet, en théorie, pas la fusion et aucune activité magmatique y est attendue (e.g., Ramos & Folguera 2009, Barazangi & Isacks 1976, Jordan et al. 1983, Ramos et al. 2002). Sa composition adakitique (e.g., Atherton & Petford 1993) indique une source basaltique et une fusion à haute température, c'est à dire située en base de croûte ou dans la plaque plongeante et non dans le coin mantellique (Ather-

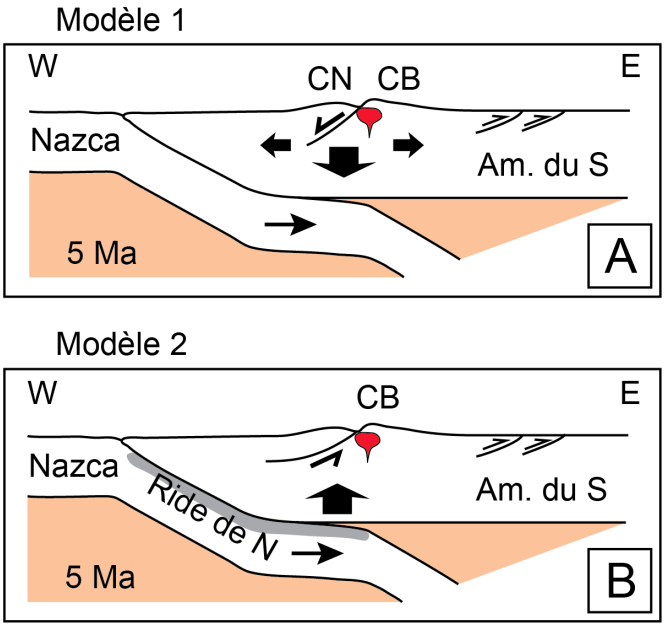

FIGURE 1.5 – *Modèles proposés pour expliquer la faille normale de la Cordillère Blanche. A) Modèle d'effondrement gravitaire de la croute surépaissie (e.g., Dalmayrac & Molnar 1981). B) Modèle de soulèvement de la Cordillère Blanche après la subduction de la ride de Nazca (McNulty & Farber 2002).*

ton & Petford 1993, Petford & Atherton 1996, Coldwell et al. 2011). Le contexte tectonique de la mise en place du batholite de la Cordillère blanche est débattu ; Petford & Atherton (1992) suggèrent un contexte décrochant dextre sur la base d'observations de la déformation ductile dans le batholite, alors que McNulty et al. (1998), basés sur des données de susceptibilité magnétique d'échantillons du batholite, proposent une mise en place dans un régime décrochant sénestre. Le timing de la mise en place comme la composition chimique du batholite sont anormales. Actuellement, la morphologie de la Cordillère Blanche est marquée par les glaciations passées avec par exemple des vallées glaciaires de plus de 1000 m de profondeur qui recoupent le granite et de nombreuses moraines (Fig. 1.4 Farber et al. 2005, Clapperton 1983, Rodbell 1993).

1.2.3 Le Callejón de Huaylas

Le Callejón de Huaylas est le bassin sédimentaire situé juste à l'ouest de la Cordillère Blanche (Fig. 1.6). La présence de la formation volcanique Yungay (8-3 Ma) exclusivement dans le Callejón de Huaylas indique que ce bassin correspond à une dépression topographique depuis 8 Ma (Farrar & Noble 1976, Cobbing et al. 1981, Wise & Noble 2003, Giovanni et al. 2010). Les ignimbrites de la Formation Yungay peuvent atteindre jusqu'à 950 m d'épaisseur et ont une chimie similaire au granite de la Cordillère Blanche (Coldwell et al. 2011), elles correspondent au volcanisme contemporain de la mise en place de la Cordillère Blanche (Atherton & Petford 1993, Coldwell et al. 2011).

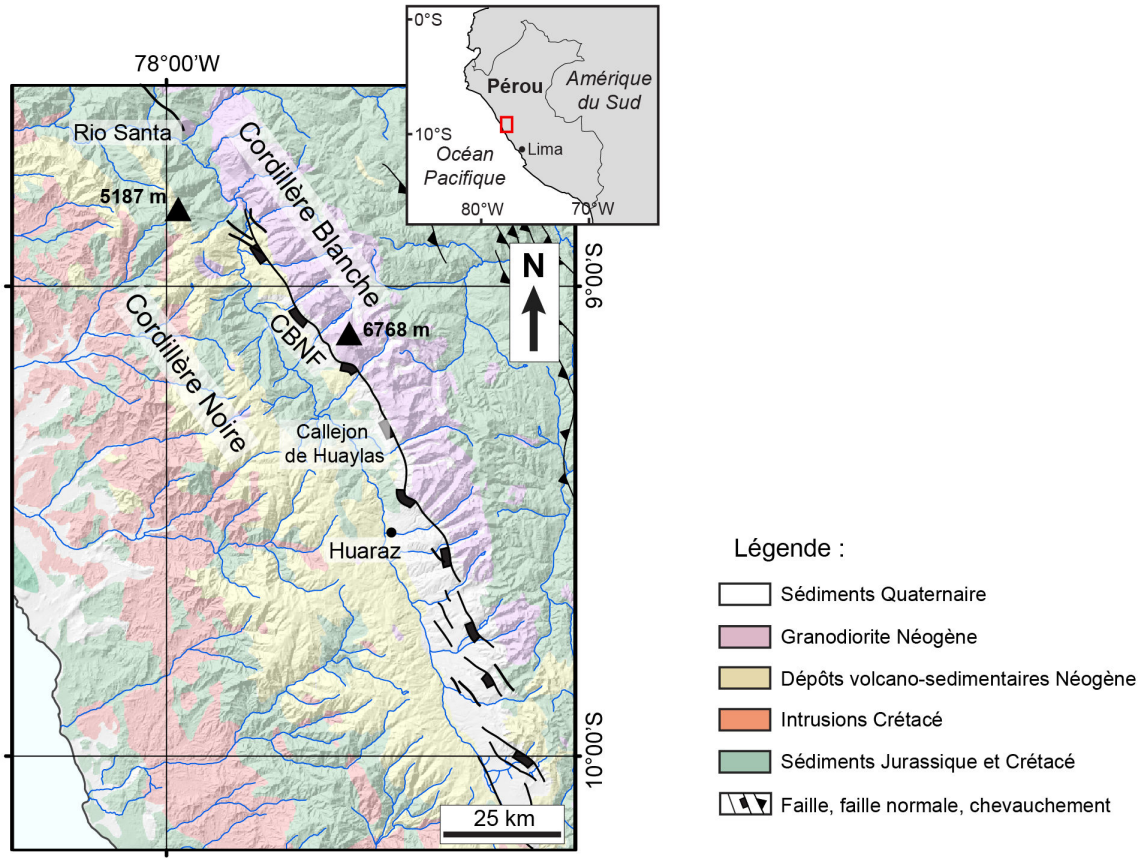

FIGURE 1.6 – *Carte géologique de la région de la Cordillère Blanche, modifiée d'après INGEMMET.*

Sur la base de leur composition chimique Coldwell et al. (2011) suggèrent que la source du magma se situe en base de croute. Par la suite, le Callejón de Huaylas enregistre aussi la subsidence liée à l'activité de la faille normale de la Cordillère Blanche et la datation d'une couche volcanique à la base de la série sédimentaire a permis d'estimer l'initiation de cette subsidence à ∼5.4 Ma (Giovanni 2007, Giovanni et al. 2010). Le bassin en subsidence est rempli par des dépôts fluvio-glaciaires de la Formation Llocla (Pliocène-Quaternaire ; Fig. 1.7) qui indiquent l'érosion glaciaire de la Cordillère Blanche (< 5 Ma ; Bonnot 1984, Giovanni 2007, Giovanni et al. 2010) puis l'érosion du granite de la Cordillère Blanche (Formation Llocla Sup. ; Fig. 1.7 ; Giovanni 2007, Giovanni et al. 2010). De nombreux dépôts Quaternaires sont également présents dans le Callejón de Huaylas, dans la partie supérieure du bassin (sud-est) comme sur la bordure de la Cordillère Blanche où les moraines et dépôt fluvio-glaciaires sont omniprésents (Farber et al. 2005, Rodbell et al. 2009). Le long du Rio Santa on peut également noter la présence des différents niveaux de terrasses alluviales et, dans la partie nord du bassin, de nombreux cônes alluviaux et des dépôts issus de glissements de terrain qui sont recoupés par le Rio Santa.

1.2.4 La Cordillère Noire

La Cordillère Noire (5187 m) forme un plateau incisé par des vallées profondes à l'ouest, elle correspond à l'hangingwall de la faille normale de la Cordillère Blanche (Fig. 1.6). Elle est constituée de sédiments d'âges Jurassique et Crétacé de la Formation Chicama dans lesquels des roches magmatiques se sont mises en place du Crétacé au Paléogène (73-48 Ma ; Mukasa & Tilton 1984, Wilson 1975, Beckinsale et al. 1985). La partie sud de la Cordillère Noire est recouverte par des roches volcano-sédimentaires Néogène de la Formation Calipuy (54-15 Ma ; Cobbing et al. 1981). Contrairement à la Cordillère Blanche, les glaciations ont peu affecté la Cordillère Noire, seules quelques moraines sont visibles à des altitudes >4200 m. L'évolution récente de la Cordillère Noire est très mal contrainte, notamment en terme de soulèvement et d'exhumation.

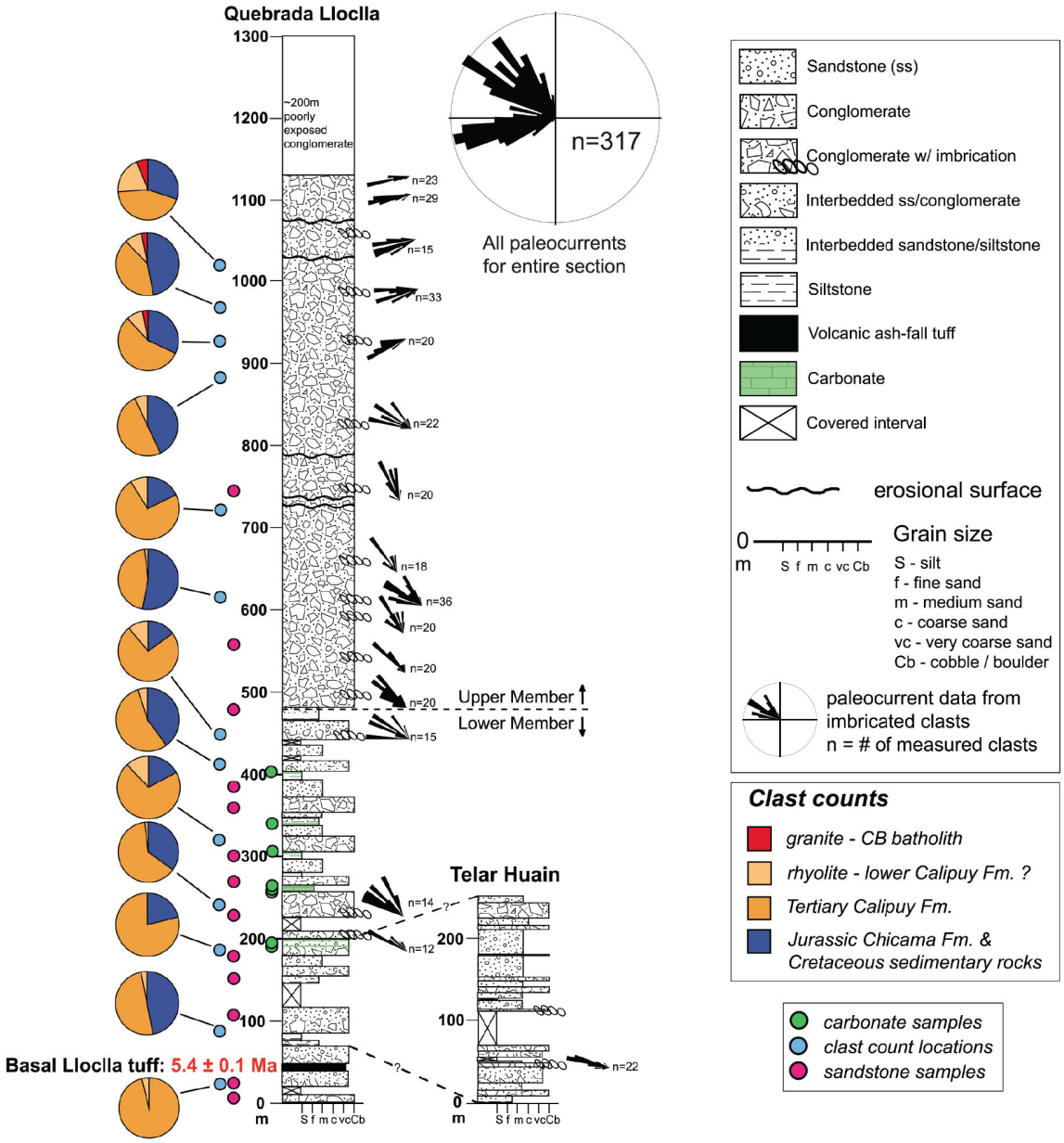

FIGURE 1.7 – *Log stratigraphique de la Formation Llocllа au niveau de la Quebrada Llocllа et de la Quebrada Telar Huain (d'après Giovanni et al. 2010). La composition des conglomérats, les paléocourants mesurés et l'âge $^{40}Ar/^{39}Ar$ obtenu pour le tuff situé à la base de la Formation Llocllа sont également indiqués.*

Méthodes

2

Sommaire

Dans ce chapitre, je présente les différentes méthodes que j'ai utilisées au cours de mon travail de thèse. J'ai quantifié l'exhumation grâce à différents thermochronomètres basse température (traces de fission et (U-Th)/He sur apatites). La géologie structurale et l'inversion des données microtectoniques de la région de la Cordillère Blanche m'ont permit de contraindre et de discuter le contexte tectonique lors de la mise en place et de l'exhumation de la Cordillère Blanche. J'ai fait de la thermobarométrie sur amphibole pour quantifier la profondeur de mise en place du batholite de la Cordillère Blanche et mieux contraindre la dynamique de mise en place du batholite. Pour finir, j'ai choisi de modéliser numériquement l'évolution du paysage pour quantifier l'importance respective de la faille normale et de l'érosion de la Cordillère Blanche sur le soulèvement du batholite.

In this chapter, I present the different methods used in my thesis. Quantifying the exhumation was carried out through different low-temperature thermochronometers (fission-tracks and (U-Th)/He in apatite).

2.1 Thermochronologie basse température

La thermochronologie basse température regroupe un ensemble de méthodes qui utilisent des mesures géochimiques (traces de fission sur apatites, (U-Th)/He sur apatites) ou physiques (thermochronologie OSL) pour contraindre l'histoire thermique d'une roche. Lors de leur exhumation (ou leur enfouissement), les roches traversent les isothermes de la croûte (Fig. 2.1). Les différent thermochronomètres, ayant des températures de fermeture différentes, donnent accès à l'ensemble de l'histoire de l'exhumation (l'enfouissement) des roches et donnent des contraintes sur l'évolution du relief (Fig. 2.1).

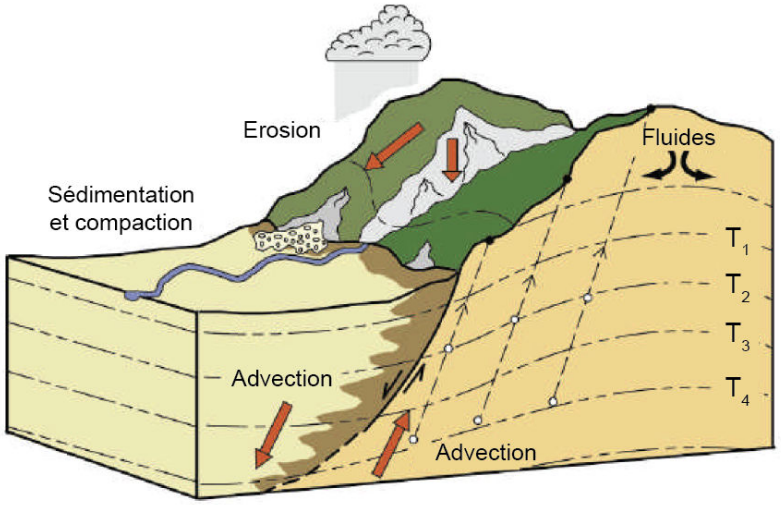

FIGURE 2.1 – *Structure thermique d'une chaîne de montagnes bordée par une faille normale (modifiée d'après Ehlers & Farley 2003). Les isothermes (traits noirs) sont défléchis par l'advection de masse et de chaleur dans le toit et le mur de la faille ainsi que par le relief (flèches rouges). Les roches en profondeur sont exhumées (ronds blancs) puis échantillonnées à la surface (ronds noirs).*

2.1.1 Traces de fission sur apatites (AFT)

Principe

La méthode traces de fission dépend de l'équation générale de la décroissance radioactive. Elle se base sur la production d'isotopes radiogéniques (fils) à la suite de la désintégration d'éléments radioactifs (pères). Lors de la décroissance radioactive de l'Uranium des particules α et β sont émises mais parfois une fission spontanée de l'atome d'^{238}U se produit ; dans ce cas, les deux noyaux positivement chargé se repoussent et créent des dommages dans le réseau cristallin. Dans les minéraux riches en Uranium, comme par exemple les apatites et les zircons, la fission spontanée de l'^{238}U créé des dommages dans le cristal, les traces de fission. La température de fermeture du système AFT est de 110°C mais jusqu'à 60°C les traces peuvent raccourcir ou disparaitre selon la vitesse

de refroidissement et la composition chimique de l'apatite. Ce gap de température (110-60°C) est appelé zone de retention/recuit partielle. Lorsque le cristal passe en dessous de la température de fermeture du système les traces de fission restent et s'accumulent suivant la décroissance radioactive de l'^{238}U. L'âge du système thermochronologique trace de fission sur apatite peut être écrit suivant l'équation :

$$t = \frac{1}{\lambda_d} ln \left(\frac{\lambda_d N_s}{\lambda_f \, {}^{238}U} + 1 \right) \tag{2.1}$$

avec λ_d la constante de désintégration radioactive de l'^{238}U, N_s le nombre de traces de fission spontanées dans l'échantillon, λ_f la constante de désintégration radioactive associée à la fission spontanée de l'^{238}U, ^{238}U le nombre d'atomes d'^{238}U présents dans l'échantillon.

Le système thermochronologique traces de fission est basé sur la reconnaissance et le comptage des traces de fissions spontanées. J'ai utilisé la méthode du détecteur externe pour déterminer la quantité d'^{238}U dans chaque grain (Hurford & Green 1982). J'ai obtenus les âges AFT en utilisant une calibration du ζ, avec un ζ de 268 ± 7 (A. Margirier) pour le verre de dosimètre IRMM-540M. Cette calibration est nécessaire pour réduire les incertitudes liées à la technique de comptage. Au laboratoire ISTerre (Grenoble) le paramètre de calibration ζ est déterminé grâce aux standards Durango et Fish Canyon Tuff datés à 31.02 ± 0.22 Ma (McDowell et al. 2004) et 27.5 ± 0.1 Ma (Lanphere & Baadsgaard 2001). Pour déterminer un âge, les traces de fission spontanées sont comptées sur une surface donnée d'un grain d'apatite. La quantité d'^{238}U est déterminé de la même façon, par le comptage de traces induites au niveau de cette surface. L'échantillon est irradié par des neutrons thermique de basse énergie qui induisent une réaction de fission de l'^{235}U. Etant donné que le flux de neutrons est contrôlé, à partir du nombre de traces induites on obtient la quantités d'^{235}U grâce auquel on obtient la quantité d'^{238}U (le rapport $^{235}U/^{238}U$ étant constant dans la nature).

$$\frac{^{235}U}{^{238}U} = \frac{1}{137,88} \tag{2.2}$$

Protocole et détermination des âges

Pour mon travail de thèse, j'ai échantillonné des granites et des quartzites dans les Cordilleras Blanca et Negra au nord du Pérou. J'ai préparé les échantillons à l'ISTerre (Grenoble, France) avec l'aide de F. Coeur et F. Senebier. Après avoir été broyés, les échantillons ont été tamisés et passés dans un séparateur magnétique (F. Coeur). Les apatites sont ensuite séparées grâce à un protocole de séparation par des liqueurs denses (polytungstate de sodium et iodométhane, densités de 2.8 et 3.3) (F. Senebier). j'ai sélectionné les apatites pour la thermochronologie AFT sous une loupe binoculaire jusqu'à obtenir une centaine de grains. Les grains d'apatite triés sont montés dans une résine epoxy et polis pour révéler leur surface interne. Pour pouvoir observer les traces de fission il faut procéder à une attaque chimique. Les apatites ont été attaquées avec de l'acide nitrique (HNO^3, 5.5 M) pendant 20 secondes à 21 ± 1°C. Avant l'irradiation une lame de mica est collée à la surface

polie du grain, elle permet d'enregistrer les traces de fission induites. Les échantillons ont été irradiés au réacteur FRM II à Garching (Munich, Allemagne) avec une fluence nominale de 8×10^{15} neutrons/cm^2. Après l'irradiation, les micas sont attaqués pendant 18 minutes dans de l'acidité fluorhydrique (HF) à 48% à $21 \pm 1°C$ pour révéler les traces induites. La densité de traces est comptée à la même position sur le grain et sur le mica. j'ai compté et mesuré les traces de fission à l'aide d'un microscope optique Olympus à un grossissement de $\times$1250, selon les recommandations de Laslett et al. (1994). J'ai effectué le calcul de l'âge et des statistiques avec le logiciel Trackkey (Dunkl 2002). Je rapporte les âges AFT sous la forme de l'âge central à $\pm1\sigma$. En raison de la faible teneur en uranium et des âges jeunes de la plupart des échantillons, ils ne présentent pas suffisamment de traces confinées pour étudier la distribution des longueurs de trace. Pour accroître le nombre de traces confinées attaquées J'ai fait irradier 3 échantillons avec une source au Californium (Cf) à l'Université de Melbourne (Australie). J'ai utilisé la mesure du Dpar (diamètre moyen des traces de fission parallèles à l'axe C du cristal après l'attaque chimique) pour caractériser la composition chimique des cristaux d'apatite et estimer la cinétique dans chaque grain (Donelick 1993).

2.1.2 (U-Th)/He sur apatites

Principe

Les apatites contiennent naturellement des éléments radioactifs. La méthode de thermochronologie (U-Th)/He sur apatite se base sur la production d'^{4}He par les réactions de désintégration radioactive de ^{238}U, ^{235}U, ^{232}Th, ^{147}Sm et sur la diffusion de l'^{4}He au sein du crystal. La température de fermeture du système est de 75$\pm$15°C (Wolf et al. 1996, Farley 2000). Différents facteurs peuvent faire varier les âges (U-Th)/He sur apatite et doivent être corrigés ou pris en compte lors de l'interprétation. La présence de micro-inclusions, avec des concentrations d'U, Th et Sm différentes du grain, invisibles lors de la sélection des grains et qui ne dégazent pas une quantité importante d'hélium lors de la seconde extraction peuvent vieillir un échantillon. Pour essayer de minimiser cette erreur, plusieurs grains sont dégazés pour chaque échantillon. Les particules α produites lors de la désintégration radioactive de l'U, du Th et du Sm ont une énergie cinétique importante, elles sont éjectées de leur position de production jusqu'à une distance d'arrêt moyenne de 20 μm (Farley et al. 1996). Les particules α produites peuvent donc transiter d'un grain à un autre entrainant une perte d'^4He pour un grain d'apatite donné et un éventuellement un gain pour un grain d'apatite voisin. Le cristal d'apatite doit donc être suffisamment gros (> 60 μm) pour que la perte d'^4He par éjection α puisse être corrigée par le facteur de correction F_T (Farley et al. 1999). Ce facteur fait l'hypothèse d'une répartition uniforme des éléments pères dans l'apatite (Farley 2000) et prend en compte la géométrie du grain. L'assimilation d'^{4}He depuis un minéral voisin comme un zircon, une monazite ou une apatite est plus difficilement quantifiable (Spiegel et al. 2009). La quantité d'He est donnée par l'équation :

$$^4He = 8\ ^{238}U(e^{\lambda_{238}t} - 1) + 7\ \frac{^{238}U}{137.88}(e^{\lambda_{235}t} - 1) + 6\ ^{232}Th(e^{\lambda_{232}t} - 1) +^{147} Sm(e^{\lambda_{147}t} - 1) \quad (2.3)$$

avec ^4He, ^{238}U, ^{232}Th, ^{147}Sm les abondance mesurées dans le grain, t l'âge thermochronologique de l'échantillon et λ la constante de désintégration radioactive des éléments pères ^{238}U, ^{232}Th et ^{147}Sm.

Cette méthode se base sur trois hypothèses, l'absence d'^{4}He dans le cristal à l'état initial, l'absence d'^{4}He issus d'une implémentation α et l'^{4}He peut diffuser hors du cristal, la pression partielle d'^{4}He à l'extérieur n'influence pas la diffusion dans le cristal.

Détermination d'un âge AHe

Les âges (U-Th)/He sont le résultat de la production, de l'éjection et de la diffusion de l'hélium au sein d'un cristal d'apatite pour une histoire thermique donnée. Pour déterminer un âge (U-Th)/He sur apatite il faut mesurer les quantités d'^{4}He et d'U-Th contenues dans le grain. Au dessus de la température de fermeture du système (75°C) les atomes d'hélium produits diffusent rapidement hors du grain d'apatite. En dessous de 75°C la diffusion est moins importante, l'hélium produit reste dans le grain. La température de fermeture du système (U-Th)/He dépend de la vitesse de refroidissement, et de la taille du grain. La température de fermeture très basse pour le système (U-Th)/He sur apatite implique qu'il est particulièrement sensible à l'histoire thermique lors de l'exhumation récente des roches (Fig. 2.1) mais aussi à tout les réchauffements potentiels (réenfouissement, incendies ; e.g., Mitchell & Reiners 2003).

Protocole

Le protocole de préparation des échantillons est similaire au protocole suivi pour les traces de fission jusqu'à l'obtention des cristaux d'apatite. Une fois les cristaux obtenus, j'ai sélectionné les apatites pour la thermochronologie (U-Th)/He sous une loupe binoculaire suivant leur morphologie, leur taille (>60 μm) et leur pureté. L'absence d'inclusion est essentielle, en effet une inclusion peut contenir de l'hélium et majorer la quantité d'^{4}He mesurée. J'ai aussi écarté les grains présentant des fractures, les fractures pouvant faciliter l'éjection de l'hélium. J'ai mesuré les cristaux d'apatites sélectionnés pour calculer leur facteur d'éjection suivant la technique de simulation Monte Carlo développée par Gautheron & Tassan-Got (2010). Pour finir, j'ai mis chaque cristal dans une capsule millimétrique en platine. J'ai réalisé l'extraction de l'hélium à Orsay, en collaboration avec Cécile Gautheron, la chimie pour connaitre la quantité d'U-Th a été réalisée par la suite (R. Pinna-James). L'hélium contenu dans l'échantillon est dégazé sous vide par chauffage laser de la capsule platine qui contient le grain d'apatite ($T = 1050 \pm 50°C$, 2 minutes). Une solution entraineur de concentration connue en ^{3}He est ajoutée à l'^{4}He. Le rapport ^{4}He/^{3}He est mesuré par un spectromètre de masse quadrupole. L'étape d'extraction est répétée sur le même échantillon pour s'assurer qu'il n'y a plus d'He dans l'échantillon. Dans le cas où la quantité d'^{4}He est supérieure à 10% de la quantité

extraite lors de la première chauffe, l'^{4}He peut provenir d'inclusions, il faut donc être prudent vis à vis de l'âge obtenu. Après l'extraction de l'hélium les tubes de platines sont placés dans des flacons en polypropylène et les cristaux d'apatites sont dissous pendant 1 h dans 50 μl de solution de HNO_3 à 90°C et de concentration connue en ^{235}U, ^{230}Th et ^{149}Sm que nous avons ensuite rempli avec 1 ml d'eau pure. Les mesures de l'U du Th et du Sm ont été réalisées suivant le protocole de Evans et al. (2005) grâce à un spectromètre de masse quadrupole (ICP-QMS ; série CCT Thermo-Electron au LSCE, Gif-sur-Yvette, France). Les analyses ont été calibrées avec des standards comprenant le tuff de Limberg et les apatites de Durango qui donnent respectivement des âges de 16.5 $\pm$ 1.6 Ma et 31.4 $\pm$ 2.3 Ma. Ces valeurs sont en accord avec les valeurs données dans la littérature, 16.8 $\pm$ 1.1 Ma pour le tuff de Limberg (Kraml et al. 2006) et 31.02 $\pm$ 0.22 pour Durango (McDowell et al. 2004). J'ai corrigé les âges en utilisant le facteur d'éjection F_T que j'ai déterminé par une simulation Monte Carlo (Ketcham et al. 2011), j'ai calculé le rayon de la sphère équivalente du cristal en suivant la procédure décrite par (Gautheron & Tassan-Got 2010). J'ai quantifié l'incertitude analytique par l'analyse de standards, elle est en moyenne de 10%. Elle reflète la somme des erreurs de correction du facteur d'éjection et la dispersion des âges des standards. A cette incertitude s'ajoute la reproductibilité de l'âge obtenu pour les différents grains d'un même échantillon.

2.1.3 Thermochronologie OSL

Dans le cadre de ma thèse j'ai également appliqué la thermochronologie par Optically Stimulated Luminescence (OSL) sur des échantillons localisés sur le plan de faille de la Cordillera Blanca. La thermochronologie par Optically stimulated luminescence (OSL) est une méthode novatrice développée par F. Herman (IDYST, Lausanne), de température de fermeture de 30-35°C, qui permet l'accès aux processus d'exhumation des roches les plus récents jusqu'alors non décrits par les méthodes traditionnelles (herman et al. 2010). L'application de cette technique permettrait de faire le lien entre l'histoire de l'exhumation obtenue grâce aux méthodes de thermochronologie classiques (traces de fission sur apatite et (U-Th)/He sur apatite) (échelle 10^6-10^7 ans) et la néotectonique (échelle 10^3-10^5 ans).

Principe

La thermochronologie OSL permet de déterminer le temps à partir duquel les grains de quartz commencent à piéger la charge dans les pièges à électrons appropriés en réponse à une exposition aux radiations ionisantes de l'environnement (radioactivité, émission de radiations ...), lorsqu'ils refroidissent en dessous de la température de fermeture du système (herman et al. 2010). En effet, le signal OSL dépend du nombre d'électrons piégés, il augmente avec la dose d'irradiation reçue. Lorsque les roches ont reçu une trop forte dose le signal sature.

Le signal et le niveau de saturation diffèrent selon le matériel traité, ils sont caractéristiques des défauts des cristaux. En dessous du niveau de saturation, le signal augmente proportionnellement à

la dose reçue. En théorie, pour un signal OSL donné, une fois la dose environnementale mesurée, il est possible de calculer un âge. Toutefois certains cristaux perdent une partie des charges piégées au cours du temps, ce phénomène appelé "fading" induit une sous estimation de la dose d'irradiation reçue.

Cette technique est adaptée pour des âges jeunes soit à des régions à taux de soulèvement élevés (1-10 mm/an). En effet, à partir du moment où tous les pièges à électrons sont pleins, l'échantillon est saturé, la charge piégée n'augmente plus même si il est toujours exposé aux radiations environnementales et donc l'échantillon ne peut plus être daté par cette méthode. La limite supérieure des âges mesurables est en moyenne de 500 ka, elle est essentiellement contrôlée par la quantité de radiations ionisantes environnementales. Dans certains cas le niveau de saturation est atteint très rapidement ce qui rend cette méthode inapplicable mais parfois il est possible d'obtenir des âges supérieurs à 1000 ka, en particulier si la concentration d'isotopes radioactifs est faible dans l'environnement du cristal (Rhodes et al. 2006).

Protocole

J'ai scié les roches dans une chambre noire de façon à conserver le coeur, non exposé à la lumière, des blocs. J'ai ensuite broyé les roches manuellement et je les ai tamisées dans une chambre noire (IDYST, lausanne ; Fig. 2.2A). J'ai traité les fractions de taille de grains 180-212 μm avec de l'HCl et de l'H_2O_2 pour dissoudre les carbonates et la matière organique. Les minéraux magnétiques ont été retirés grâce à l'utilisation d'agitateurs magnétiques. J'ai isolé les fractions de quartz et de feldspath grâce à des liqueurs denses (polytungstate de sodium, densité 2.7 et 2.58 g.cm^{-3}) et attaquées avec de l'HF à 40% durant 1 h.

J'ai réalisé toutes les mesures de luminescence grâce au détecteur TL/OSL Ris 1 (IDYST, Lausanne ; Fig. 2.2B) Pour déterminer la paléodose, j'ai mesuré le signal de luminescence naturel puis je l'ai comparé au signal régénéré au moyen d'une dose artificielle délivrée par une source au laboratoire.

Applicabilité de cette méthode à la région étudiée et à la chaîne Andine

J'ai testé l'application de cette méthode sur quatre échantillons situés sur le plan de faille de la Cordillère Blanche, au nord du massif. Dans cette région les taux d'exhumation récents (1-0 Ma) prédits par Farber & Hancock (submit) sur la faille normale de la Cordillère Blanche sont de 5 mm/an. Mes résultats indiquent pourtant que le thermochronomètre OSL est saturé et donc inutilisable pour quantifier l'exhumation récente de la Cordillère Blanche.

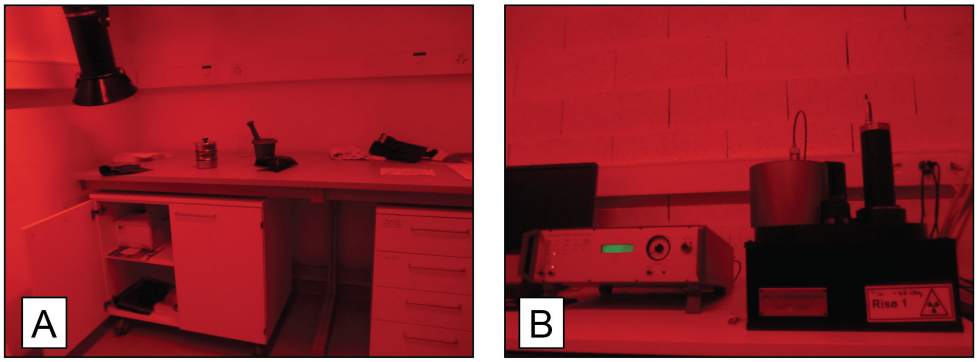

FIGURE 2.2 – *Photographies illustarnt les conditions de travail pour les analyse OSL. A) Salle de broyage des échantillons pour les datations OSL (IDYST, Lausanne). B) Détecteur TL/OSL Ris 1 où le signal OSL des échantillons de la Cordillère Blanche a été mesuré (IDYST, Lausanne).*

2.1.4 Méthodes d'inversion numériques des données de thermochronologie

QTQt : inversion Température-temps

J'ai déterminé l'histoire thermique des échantillons grâce au logiciel QTQt (Gallagher et al. 2009, Gallagher 2012). Ce logiciel permet d'inverser le recuit des traces de fission ainsi que les paramètres de diffusion de l'hélium dans les apatites avec une méthode de Monte-Carlo par chaîne de Markov pour des profils verticaux complets. Ce code d'inversion intègre des modèles cinétiques de diffusion de l'hélium dans l'apatite (Flowers 2009, Gautheron et al. 2009) et de recuit des traces de fission (Ketcham et al. 2007). Pour tous les modèles, la gamme de composition chimique du grain peut être prise en considération suivant Gautheron et al. (2013). La procédure de modélisation est détaillée par Gallagher (2012).

Les paramètres d'entrée utilisés pour modéliser chaque profil sont : les âges centraux AFT, la répartition des longueurs de traces, les valeurs de Dpar et les âges AHe (monograin) avec la taille des grains et leurs caractéristiques chimiques. Il est également possible d'apporter des contraintes données par la géologie, comme les âges et température de mise en place des roches (qu'elles soient intrusives ou sédimentaires) ou une période de mise à la surface, si elles sont connues.

Glide : inversion spatio-temporelle des taux d'exhumation

Pour obtenir les variations spatio-temporelles des taux d'érosion dans la région de la Cordillère Blanche nous avons utilisé la méthode proposée par Fox et al. (2014) et modifiée par Herman & Brandon (2015). Toutes les données de thermochronologie basse température disponibles dans cette région (Montario 2001, Wipf 2006, Montario 2006, Giovanni 2007, Hodson 2012, Michalak 2013) ont été inversées et permettent d'estimer quantitativement l'histoire de l'érosion. Cette procédure

implique une inversion des moindres carrés faiblement non-linéaire et permet un traitement efficace d'un grand nombre de données réparties dans l'espace. Cette méthode exploite les informations contenues dans les profils âge-altitude et dans les différents systèmes thermochronologiques. Dans cette approche, plusieurs paramètres doivent être testés pour s'assurer que les taux d'exhumation présumés sont robustes. Pour une discussion détaillée de chacun de ces paramètres se référer à Fox et al. (2014). I) La profondeur de la température de fermeture est exprimée par l'intégrale du taux d'érosion à partir de l'âge de thermochronologique actuel. L'intégrale est discrétisée en une série de pas de temps fixes (Δt), qui doivent être choisis. II) La profondeur des isothermes de fermeture est calculée en utilisant un modèle thermique 1-D qui comprend une correction pour les effets de la topographie et de son domaine thermique sous-jacent. L'impact du modèle thermique est testé en modifiant les conditions aux limites inférieures (T). III) La méthode suppose que les échantillons sont corrélés dans l'espace par une fonction de corrélation qui comprend un écart (σ). IV) Les taux d'exhumation calculés représentent un écart par rapport à une exhumation a priori ($\dot{e}_{pr}$) qui est mise à jour à des taux d'exhumation postérieurs. Dans la figure 2.3, je montre l'effet des variations de Δt, T, σ et $\dot{e}_{pr}$ pour évaluer leur impact sur les histoires d'exhumation. La solution est représentée en deux points situés de chaque côté de la faille normale de la Cordillère Blanche.

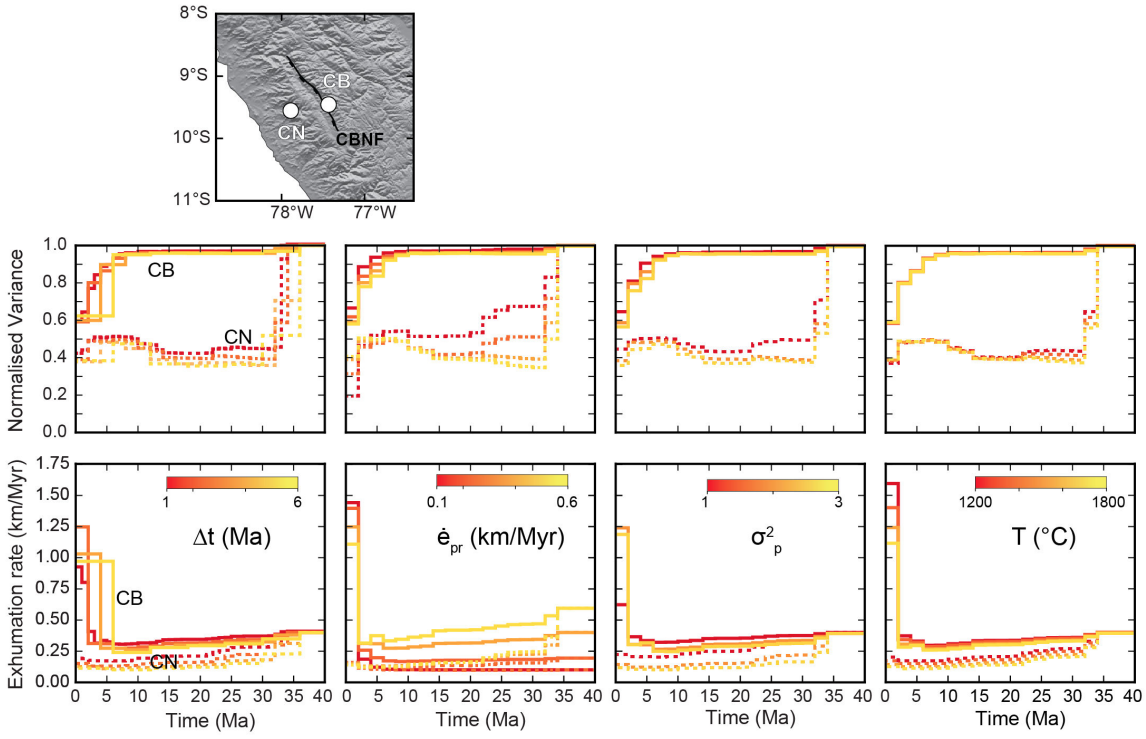

FIGURE 2.3 – *Sensibilité des taux d'exhumation prédits en fonction de différents paramètres. A) Localisation des points de chaque côté de la faille normale. B-E) Variance normalisée pour chaque histoire d'exhumation, plus la variance est faible, plus l'exhumation est bien contrainte. F-I) Variation des taux d'exhumation pour différentes valeurs de Δt, T, σ, $\dot{e}_{pr}$ et σ_p^2.*

2.2 Analyse de la fracturation : inversion de populations de plans striés

2.2.1 Principe

Les méthodes utilisées pour déterminer l'orientation des paléocontraintes à partir d'une population de plan striés peuvent être divisées en deux groupes : les méthodes graphiques et les méthodes d'inversion numériques. Les méthodes graphiques permettent d'obtenir une première estimation du régime de contrainte, elles ont l'avantage de ne pas être perturbées par les failles étrangères à la population analysée (e.g., méthode des dièdres droits ; Angelier & Mechler 1977). Les méthodes d'inversion numériques considèrent que la direction de contrainte est parallèle à la direction du glissement matérialisée par la strie pour un plan de faille donné (Wallace 1951, Bott 1959). Pour cette méthode le calcul de la paléocontrainte consiste à minimiser l'angle entre la strie mesurée et la strie théorique associée à la solution. La paléocontrainte est définie par l'orientation des trois contraintes principales ($\sigma 1 > \sigma 2 > \sigma 3$) et par le rapport ϕ ($\phi = (\sigma 2 - \sigma 3) / (\sigma 1 - \sigma 3)$) qui permet de mieux caractériser le régime de contrainte (e.g., Ritz & Taboada 1993). Ces méthodes d'inversions sont applicables sous réserve que I) le milieu soit homogène et non déformé de façon ductile, II) le champ de contraintes soit uniforme dans l'affleurement, III) la contrainte ne change pas au cours d'une même phase tectonique et IV) les mouvements des blocs soient faibles.

2.2.2 Protocole

Travail de terrain

Pour chaque site j'ai mesuré entre 2 et 34 plans striés sur des affleurements n'excédant pas 50 m de long. La nature des mouvements affectant les plans de failles a été contrainte par les indices cinématiques classiques (stries, fibres, écailles). J'ai pris note de la qualité de chacune de mes mesures, et notamment du degré de confiance pour le sens de déplacement déterminé sur le terrain. En cas de forte incertitude, la faille a été rejetée ou notée comme incertaine. La majorité de mes sites de mesures sont situés en bordure de route, ce type d'affleurement présente l'avantage d'exposer des roches "fraiches" et d'exposer un panel complet des failles. Pour les sites de mesures "naturels", il est plus difficile de trouver un nombre important de plans striés : les plans sont altérés et les stries ne sont pas bien préservées.

Inversion des différentes populations de plans striés

L'inversion nécessite au moins 4 couples faille/strie. Un nombre de données plus important permet d'obtenir une solution mieux contrainte. Ici je prend en compte uniquement les inversions qui ont été réalisées avec plus de 6 plans striés aux orientations différentes. J'ai réalisé l'inversion des données grâce au logiciel WinTensor (Delvaux 2012) qui permet d'inverser un ensemble de

données à partir de la méthode des dièdres droits (Angelier & Mechler 1977) et de la méthode PBT (Angelier 1984).

2.3 Thermobarométrie sur amphibole

2.3.1 Principe

La texture et la composition des amphiboles sont utilisées pour déduire les processus magmatiques et les paramètres de cristallisation (Bachmann & Dungan 2002, Rutherford & Devine 2008, Ridolfi et al. 2010, Ridolfi & Renzulli 2012, De Angelis et al. 2013, Shane & Smith 2013, Turner et al. 2013). L'amphibole est souvent utilisée pour calculer la température et la pression de cristallisation d'un magma. Son utilisation comme géothermomètre est généralement admise, mais son utilisation en tant que géobaromètre continue d'être débattue (e.g., Shane & Smith 2013, Holland & Blundy 1994, Bachmann & Dungan 2002, Rutherford & Devine 2003). Les premiers baromètres amphiboles ont été calibrés pour la teneur totale en Al de l'amphibole, aux pressions de la croûte et du manteau supérieur, et des intervalles de température limités (e.g., pour ∼750 °C : Johnson & Rutherford 1989, Schmidt 1992). Récemment, Ridolfi et al. (2010) et Ridolfi & Renzulli (2012) ont publié des équations thermobarométriques pour estimer la température, la pression, fO2, l'hydratation du magma, et la composition en oxydes, qui entrent dans la composition des amphiboles. Leurs calibrations sont recommandés pour des amphiboles cristallisées dans des magmas calco-alcalins à alcalins (c'est le cas de la Cordillère Blanche), pour des pressions mantelliques jusqu'à la partie supérieure de la croûte, pour différentes conditions d'oxydation et d'hydratation. Les formulations de Ridolfi et al. (2010) et Ridolfi & Renzulli (2012) utilisent les concentrations de Si, Ti, Al, Fe, Mg, Ca, Na, K dans les amphiboles pour le calcul de pression et de température. Grâce à leur large gamme d'applications possibles et leur facilité d'utilisation, ces thermobaromètres sont souvent utilisés.

2.3.2 Protocole

J'ai réalisé des sucres à l'ISTerre à partir d'échantillons du pluton de la Cordillère Blanche puis je les ai envoyés en Italie pour la confection de lames minces (Pierluigi Canepa, Laboratorio Petrografico, Quart). Les lames minces contenant des amphiboles ont été couvertes par un film de carbone de façon à rendre la surface de l'échantillon électriquement conductrice et à éviter le chargement par le faisceau d'électrons de la microsonde. J'ai réalisé les analyses à l'ISTerre (Grenoble) sur la Microsonde électronique JEOL JXA-8230. Pour chaque échantillon, j'ai analysé entre trois et cinq amphiboles en éléments majeurs. Les analyses ont été faites en suivant des profils passant par le coeur des cristaux pour détecter d'éventuelles variations de composition au sein des amphiboles. Classiquement, les compositions les plus appauvries en Si (pôles ferropargasite ou ferrotschermakite selon la valeur (Na+K)A) sont caractérisées par une concentration en Fe élevée et les amphiboles

enrichies en Si (magnesiohornblende ou edenite) sont caractérisées par une concentration élevée en Mg.

2.3.3 Calcul de pression et de température de mise en place du granite

Les estimations de pressions et de températures sont basées sur le thermobaromètre de l'amphibole de Ridolfi & Renzulli (2012), calibré pour les roches magmatiques alcalines et calco-alcalines. Ce thermobaromètre prend en compte la composition en plusieurs éléments des clinoamphiboles et calcule les conditions de pressions et de température lors de la mise en place du granite. J'ai filtré les données de composition des amphiboles sur la base d'un pourcentage d'erreur apparente (APE) liée à la pression et calculé grâce à la méthode thermo-barométrique de Ridolfi & Renzulli (2012). L'APE maximum pour garder les données a été fixé à 50, comme préconisé par les auteurs (filtre 1, indice de confiance modéré). J'ai appliqué un second filtre (indice de confiance élevé) qui permet d'exclure les amphiboles dont la chimie ne correspond pas à la gamme de compositions et de formules structurales pour lesquelles le thermo-baromètre a été calibré. Après l'application de ces 2 filtres, ∼15% des amphiboles ont été écartées.

2.3.4 Validitée de la méthode de Ridolfi & Renzulli (2012)

En dépits des nombreux contrôles et des mesures sélectives de Ridolfi & Renzulli (2012), quelques études ont souligné des problèmes systématiques (pas de prise en compte de la composition du magma) et des différences entre les conditions de cristallisation estimées à partir de la composition des amphiboles et d'autres méthodes (e.g., De Angelis et al. 2013, Shane & Smith 2013, Kiss et al. 2014). Plusieurs auteurs ont proposé que les pressions calculées en utilisant le baromètre de Ridolfi & Renzulli (2012) sont sensibles aux variations de la composition du magma (De Angelis et al. 2013, Shane & Smith 2013, Erdmann et al. 2014). Cependant, la plupart des études considèrent que les conditions de cristallisation calculées avec les équations de Ridolfi & Renzulli (2012) sont fiables (Turner et al. 2013, Costa et al. 2013, Zanon et al. 2013, Yücel et al. 2013, Brenna et al. 2014, Putirka 2014), et démontrent que le baromètre de Ridolfi & Renzulli (2012) donne des résultats satisfaisants de pressions sur les amphiboles expérimentales dans une large gamme de compositions de magma (basalte - rhyolite) et de pressions (200-800 MPa).

2.4 Modélisation numérique de l'évolution du paysage : FastScape

2.4.1 Principe

Le code FastScape (Braun & Willett 2013) résout la stream-power law, loi qui contrôle l'incision des vallées et l'évolution du paysage dans la plupart des contextes.

$$\frac{\partial h}{\partial t} = K_f \, \Phi^m \, S^n \tag{2.4}$$

Avec $\frac{\partial h}{\partial t}$ le taux d'érosion, Φ la surface drainée, S la pente de la rivière ; K_f, m et n sont des constantes.

Ce nouvel algorithme est très efficace : le temps de calcul augmente linéairement avec le nombre de points qui caractérisent le paysage, ce qui permet de travailler avec une haute résolution spatiale.

2.4.2 Intérêt de cette méthode

Ce code présente différents avantages. Le temps de calcul est très rapide, le code permet d'ajouter une faille, de définir des intrusions (densité et érodabilité), de prendre en compte le rebond flexural (et de fixer l'épaisseur élastique) et de définir la topographie initiale du modèle. L'utilisation de ce code pour modéliser l'évolution du paysage me permettra de quantifier I) l'impact de la faille, II) de l'érosion et III) de la présence du granite de la Cordillère Blanche (densité 2.8) sur le soulèvement et la création du relief dans cette région. IV) Il sera également possible de contraindre la paléogéographie de la région grâce à l'étude de la morphologie du réseau de drainage (localisation de la ligne de partage des eaux).

3 Subduction horizontale, magmatisme et soulèvement de la Cordillère Occidentale (Nord Pérou)

Sommaire

L'impact des processus de subduction sur le soulèvement et la construction du relief dans les Andes n'est pas encore bien compris. La Cordillère Blanche (6768 m) et la Cordillère Noire (5187 m), localisées au dessus de la zone de subduction plane du nord Pérou, regroupent les plus hauts sommets des Andes. Dans ce chapitre je présente de nouvelles données (U-Th)/He et traces de fission sur apatites provenant de trois profils verticaux localisés dans la Cordillère Blanche et la Cordillère Noire. Ces nouvelles données me permettent de discuter l'impact de l'aplatissement de la subduction et du magmatisme associé sur la topographie andine et le soulèvement régional.

The impact of subduction processes on surface uplift and relief building in the Andes is not well understood. Some of the highest Andean peaks, the Cordillera Blanca (6768 m) and the Cordillera Negra (5187 m), are located in northern Peru, just above the Peruvian flat-slab. In this chapter, I present new apatite (U-Th)/He and fission-track data from three vertical profiles in the Cordillera Blanca and the Cordillera Negra. These data provide new constraints on surface uplift and permit to explore the impact of subduction processes and magmatism on paleogeography and surface uplift in the Andes.

Résumé étendu en français

Le corps de ce chapitre est un article que j'ai publié dans la revue Geology. Les coauteurs de cet article (X. Robert, L. Audin, C. Gautheron, M. Bernet, S. Hall, and T. Simon-Labric) m'ont apporté un support technique pour l'échantillonnage, pour l'obtention des données ainsi que des discussions constructives qui m'ont permis d'élaborer l'idée directrice, puis d'écrire la démonstration.

L'impact des processus de subduction sur le soulèvement et la construction du relief n'est pas bien compris dans les Andes. Dans le nord du Pérou, l'étude de la répartition des séismes sur le plan de subduction a permis d'identifier un segment de subduction plane (3-15°S ; Barazangi & Isacks 1976). La géométrie, l'âge et l'évolution de l'aplatissement de ce segment de subduction sont bien contraints (Gutscher et al. 1999, Rosenbaum et al. 2005). Certains des plus hauts sommets des Andes, la Cordillère Blanche (6768 m) et la Cordillère Noire (5187 m), sont situés juste au-dessus du segment de subduction horizontal Péruvien. Cette région est donc une cible idéale pour explorer l'impact de l'aplatissement de la subduction et des processus associés sur la topographie des Andes et leur soulèvement.

Dans ce chapitre, je présente des nouvelles données (U-Th)/He et traces de fission sur apatites provenant de trois profils verticaux dans la Cordillère Blanche et la Cordillère Noire. Les trajets temps-température que j'ai obtenus à partir de la modélisation inverse des données thermochronologiques suggèrent que l'exhumation dans la Cordillère Noire commence à ∼15 Ma. Ces modélisations me permettent de montrer que l'exhumation de la Cordillère Noire est très probablement liée à l'érosion provoquée par un soulèvement régional à cette date. Ce scénario renforce les études précédentes qui contraignent le soulèvement de la Cordillère Occidentale du nord du Pérou entre le début et la fin du Miocène (e.g., Farrar & Noble 1976, Myers 1976, Giovanni et al. 2010, Hoorn et al. 2010, Feng & Poulsen 2014). Le soulèvement de la Cordillère Noire daté à 15 Ma est synchrone avec le début de la subduction de la ride de Nazca (Rosenbaum et al. 2005) et avec la migration du magmatisme vers l'est (Cobbing et al. 1981, Mukasa 1984, Giovanni 2007). Je propose que la subduction de la ride de Nazca à partir de 15 Ma ainsi que l'aplatissement de la subduction qui en découle ont conduit à un soulèvement régional. Celui-ci serait causé par la topographie dynamique induite par le changement de la géométrie de la subduction (Eakin et al. 2014). Le magmatisme semble également contribuer localement à la création de relief dans la Cordillère Occidentale. Les données que je présente dans ce chapitre mettent en évidence le contrôle des processus de subduction (géométrie de la plaque plongeante et magmatisme) sur la paléogéographie et le soulèvement des Andes dans le nord du Pérou.

Dans le sud du Pérou, d'autres processus ont été proposés pour expliquer le soulèvement de la Cordillère Occidentale comme par exemple un raccourcissement tectonique, un changement de propriété de la plaque continentale ou de l'interface de subduction, le sous placage du craton brési-

lien, une délamination et un fluage latéral de la croute inférieure, un changement climatique ou un gradient d'érosion (e.g., Isacks 1988, Kley & Monaldi 1998, McQuarrie 2002, Gephart 1994, Allmendinger & Gubbels 1996, Lamb & Davis 2003, Lamb & Hoke 1997, Garzione et al. 2006, Schildgen et al. 2007, Husson 2003, Masek et al. 1994, Horton 1999, Montgomery et al. 2001, Lamb & Davis 2003) mais il n'est pas exclu que la topographie dynamique associée à l'aplatissement de la subduction dans le nord du Pérou participe également au soulèvement observé dans le Sud du Pérou depuis $\sim$10 Ma (Schildgen et al. 2007). En effet, les modélisations de Eakin et al. (2014) suggèrent que l'influence du segment plat sur la topographie dynamique s'étend jusqu'au sud du Pérou, au sud de la transition entre la subduction plane et la subduction normale. Ainsi le soulèvement mis en évidence par (Schildgen et al. 2007) dans le sud du Pérou à $\sim$9 Ma pourrait être en partie causé par le changement de géométrie de la subduction dans le nord du Pérou et la propagation de la topographie dynamique vers le Sud.

Slab flattening, magmatism and surface uplift in the Cordillera Occidental (northern Peru)

A. Margirier, X. Robert, L. Audin, C. Gautheron, M. Bernet, S. Hall, and T. Simon-Labric

publié dans

Geology (2015)

Slab flattening, magmatism, and surface uplift in the Cordillera Occidental (northern Peru)

Audrey Margirier[1], Xavier Robert[1,2], Laurence Audin[1,2], Cécile Gautheron[3], Matthias Bernet[1], Sarah Hall[4], and Thibaud Simon-Labric[5]

[1]Université Grenoble Alpes, ISTerre, F-38041 Grenoble, France
[2]Institut de Recherche pour le Développement (IRD), ISTerre, F-38041 Grenoble, France
[3]Université Paris Sud, UMR GEOPS-CNRS 8148, 91405 Orsay, France
[4]College of the Atlantic, 105 Eden Street, Bar Harbor, Maine 04609, USA
[5]Institut des Dynamiques de la Surface Terrestre (IDYST), Université de Lausanne, CH-1015 Lausanne, Switzerland

ABSTRACT

The impact of subduction processes on surface uplift and relief building in the Andes is not well understood. In northern Peru, we have access to a modern flat subduction zone (3°–15°S) where both the geometry and timing of the flattening of the slab are well constrained. Some of the highest Andean peaks, the Cordillera Blanca (6768 m) and the Cordillera Negra (5187 m), are located just above the Peruvian flat slab. This is a perfect target to explore the impact of slab flattening and associated magmatism on Andean topography and uplift. We present new apatite (U-Th)/He and fission-track data from three vertical profiles in the Cordillera Blanca and the Cordillera Negra. Time-temperature inverse modeling of the thermochronological data suggests that regional exhumation in the Cordillera Occidental started at ca. 15 Ma, synchronous with the onset of subduction of the Nazca Ridge and eastward movement of regional magmatism. We propose that ridge subduction at 15 Ma and onset of slab flattening drove regional surface uplift, with an important contribution of magmatism to relief building in the Cordillera Occidental.

INTRODUCTION

The Andes are often presented as the classic example of relief building along a non-collisional convergent plate boundary, but many subduction zone processes, specifically related to surface uplift, are still not fully understood. Along the western Andean margin, topography and slab dip vary significantly, resulting in a clear segmentation along strike, with two modern flat-slab segments in northern Peru (3°–15°S; Fig. 1) and central Chile (28°–32°S) (Barazangi and Isacks, 1976). These flat-slab subduction zones influence the occurrence and location of magmatic activity along the Andean range, with the magmatic arc migrating away from the trench and even ceasing to exist during slab flattening. Slab flattening also increases coupling at the plate interface, resulting in an increase and eastward displacement of shortening in the overriding plate and consequent surface uplift in both the Andean forearc and backarc (e.g., Ramos and Folguera, 2009). However, the impact of slab flattening on surface uplift in the western part of the Andes (Cordillera Occidental) remains unclear.

The geometry and timing of slab flattening in northern Peru are constrained by the subduction of two buoyant features, the Nazca Ridge and the Inca Plateau (e.g., Gutscher et al., 1999; Rosenbaum et al., 2005). In this region, the Cordillera Blanca (CB), a Miocene batholith exhumed along an ~150-km-long crustal-scale normal fault trending parallel to the range, forms the highest Peruvian peaks (Fig. 1; e.g., McNulty and Farber, 2002). In the context of flat subduction, which is expected to produce shortening, the presence of this major normal fault is surprising. Two models have been proposed to explain the Cordillera Blanca normal fault (CBNF). Dalmayrac and Molnar (1981) suggested that extension was induced by gravitational collapse of a thickened crust, whereas McNulty and Farber (2002) suggested extension due to the arrival of the Nazca Ridge beneath this region, which temporarily increased the coupling with the overriding plate. Understanding the exhumation of the CB and extension along the CBNF in this compressive regime is important for understanding the impact of ridges and flat subduction on Andean relief development.

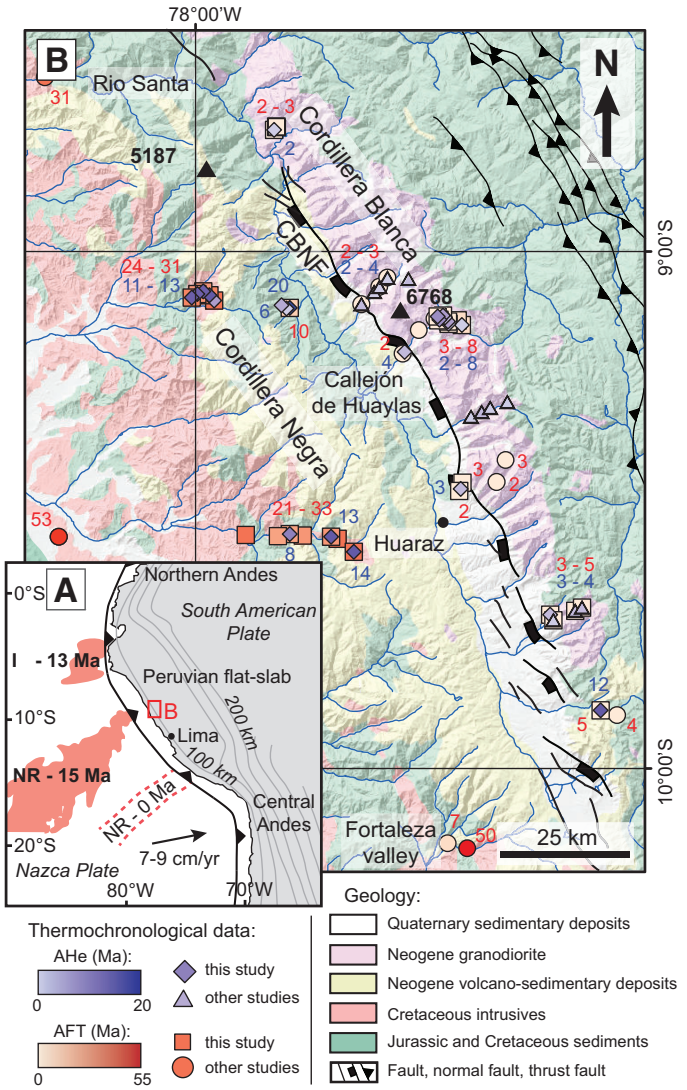

Figure 1. A: Study area location within Peruvian flat slab and South American Pacific margin (modified after Ramos and Folguera, 2009). Respective positions of Nazca Ridge (NR) at ca. 15 Ma and 0 Ma and of Inca Plateau (IP) at ca. 13 Ma (Rosenbaum et al., 2005) are represented in red. B: Geological map of Cordillera Occidental (northern Peru) showing apatite fission-track (AFT) ages (red) and apatite (U-Th)/He (AHe) ages (blue) (modified from geologic map of Ancash; INGEMMET, 1999). CBNF—Cordillera Blanca normal fault.

The aim of this paper is to evaluate the relationship between changes in geodynamics and relief evolution in the Cordillera Occidental in northern

Peru. We infer relief evolution from apatite (U-Th)/He (AHe) and fission-track (AFT) data of the CB and the Cordillera Negra (CN). We compare time-temperature inverse modeling (QTQt software; Gallagher, 2012) with the timing of the arrival of the Nazca Ridge at the subduction zone, periods of magmatic activity, and periods of uplift.

GEOLOGIC AND GEODYNAMIC CONTEXT

Reconstructions of the timing and location of the initial Nazca Ridge subduction and its subsequent southeastward migration constrain the timing of slab flattening (e.g., McNulty and Farber, 2002; Rosenbaum et al., 2005). These reconstructions are based on symmetric seafloor spreading in a hotspot reference frame, and rely on the calculation of the Nazca plate motion with respect to South America, which may contain considerable errors. Rosenbaum et al. (2005) presented a regionally refined plate circuit that suggests ridge subduction beginning at 15 Ma at 10°S and the arrival of the Inca Plateau at the trench at 5°S at 13 Ma (Fig. 1).

The CB is a 14–5 Ma granitic pluton (zircon U-Pb; Mukasa, 1984; Giovanni, 2007) intruded into Jurassic sediments. The high summits of the CB build the footwall of the CBNF, which has produced >4500 m of vertical offset since 5 Ma (Bonnot, 1984; Giovanni, 2007). The Callejón de Huaylas, a 150-km-long range-parallel intra-mountain basin, separates the CB and the CN. The 8–3 Ma Yungay ignimbrites in the northern part of the basin (Farrar and Noble, 1976; Cobbing et al., 1981; Wise and Noble, 2003) and 5.4 ± 0.1 Ma ignimbrites at the base of the stratigraphy of this basin constrain the timing of basin formation in relation to CBNF activity (Giovanni et al., 2010). The CB batholith and synchronous volcanic deposits indicate the last activity before the cessation of magmatism (Petford and Atherton, 1992) associated with slab flattening.

The Cretaceous and Paleogene plutons (73–48 Ma; Beckinsale et al., 1985) intruded into Jurassic sediments of the CN form a plateau with summits >5000 m and 1–2-km-deep valleys incised into its western flank. Some Neogene volcano-sedimentary deposits cap the CN (54–15 Ma Calipuy Formation; Cobbing et al., 1981). Few studies have addressed volcanism in the CN (Farrar and Noble, 1976; Myers, 1976; Noble et al., 1990), and no thermochronological data are currently available. In the CB, few AFT and AHe data are available, mostly from glacial valleys along longitudinal profiles (Montario, 2001; Giovanni, 2007; Hodson, 2012). Thermochronological data outside of our CB and CN study areas are limited (Wipf, 2006; Michalak, 2013; Eude et al., 2015), preventing any regional thermal modeling. Due to the absence of thermochronological data in the CN, earlier exhumation models focused on the CBNF.

METHODS

AFT and AHe thermochronology record the temperature evolution of the crust from 120 to 40 °C (e.g., Gallagher et al., 1998; Gautheron et al., 2009), which can be related to local exhumation or thermal events. Although thermochronological data do not allow direct quantification of surface uplift, with complementary information, exhumation can be interpreted to be the result of surface uplift and enhanced erosion. We determine the thermal history for a vertical profile using the QTQt software, which inverts AFT annealing and AHe diffusion parameters with the Markov chain Monte Carlo method (Gallagher, 2012; details on sample processing, analysis, and modeling are provided in the GSA Data Repository[1]). We use the multi-kinetic annealing model of Ketcham et al. (2007) to model the AFT ages and track-length dispersion, and the recoil damage model of Gautheron et al. (2009) to model AHe ages.

[1]GSA Data Repository item 2015347, details on sample processing, analysis, and modeling; Figure DR1 (predicted *T-t* paths using the Flowers et al. (2009) He diffusion model); Table DR1 (AHe ages); and Table DR2 (AFT data), is available online at www.geosociety.org/pubs/ft2015.htm, or on request from editing@geosociety.org or Documents Secretary, GSA, P.O. Box 9140, Boulder, CO 80301, USA.

NEW THERMOCHRONOLOGICAL DATA

We sampled three profiles with elevations spanning 0.9–1.9 km, one in the CB batholith (>10 km from the CBNF to avoid a tectonic exhumation signal) and two in the CN, providing 33 AFT ages, track-length measurements, and single-grain AHe ages for 23 samples (Fig. 1). The AFT ages in the CB range from 1.5 ± 0.3 Ma to 7.7 ± 1.1 Ma, and AHe ages range from 1.9 ± 0.2 Ma to 13.7 ± 1.4 Ma (Fig. 1). The AHe ages are scattered and older than AFT ages, raising the question of their reliability. Indeed, ^{4}He implantation from an external U-Th source can generate 50% of excess He and cause age dispersion (Gautheron et al., 2012). In the CN, AFT ages range from 21.1 ± 1.3 Ma to 33.2 ± 1.9 Ma and AHe ages range from 1.9 ± 0.2 Ma to 32.6 ± 3.3 Ma.

TIME-TEMPERATURE INVERSION

Thermal inversion of the CB age-elevation profile indicates rapid cooling at ~200 °C/m.y. between 4.5 and 4 Ma following batholith emplacement at high temperatures (Fig. 2). This rapid cooling is bracketed by the batholith emplacement ages (14–5 Ma; Mukasa, 1984; Giovanni, 2007) and AFT ages. At ca. 4 Ma, the cooling rate decreased to 25 °C/m.y.

Inverse modeling of the northern CN suggests an initial cooling stage between 30 and 23 Ma, followed by a progressive reheating between 23 and 15 Ma (Fig. 2). Between 15 Ma and today, the rocks have cooled at 7 °C/m.y. The southern CN model indicates an initial cooling episode between 30 and 18 Ma, and then a 18–15 Ma heating event. From 15 Ma to today, the rocks have recorded a cooling phase with a rate of ~7 °C/m.y. (Fig. 2). For both CN profiles, the obtained temperature-time paths indicate slow cooling during the Oligocene followed by reheating during the early Miocene and finally monotonic cooling since ca. 15 Ma (Fig. 2).

DISCUSSION

Middle Miocene Exhumation of the Northern Peruvian Andes

Both CN profiles indicate reheating of the crust over several million years before 15 Ma and subsequent cooling. This progressive reheating likely corresponds to regional heating during emplacement of the volcanic Calipuy Formation (54–15 Ma; Cobbing et al., 1981). The presence of the Calipuy magmatic arc possibly increased the geothermal gradient in the Cordillera Occidental.

The cause of the onset of exhumation recorded by the cooling phase in the CN between 15 and 0 Ma is not straightforward. Pollen analyses constrained a maximum possible elevation of 2 km in the Peruvian Andes before the middle Miocene (Hoorn et al., 2010). At that time, the CN formed the drainage divide (Fig. 3A; Wise and Noble, 2003). McLaughlin (1924) suggested that the CN Jurassic sediments, deposited near sea level, were uplifted and eroded to a low-relief surface (Puna surface) until ca. 15 Ma, during the Quechua 1 deformation event. This surface is presently located at ~4400 m above sea level. Late Miocene volcanic rocks (7.4 Ma; Wipf, 2006) fill a paleovalley (now reincised) along the Rio Fortaleza, which has its headwaters in the CN. This morphology records a change in base level indicating that some uplift and incision occurred between 15 and 7 Ma (Farrar and Noble, 1976; Myers, 1976). Giovanni et al. (2010) showed from $\delta^{18}O$ analyses of paleolake deposits that high elevations in the Callejón de Huaylas basin (Fig. 1) were attained by latest Miocene times. Therefore, the cooling recorded at 15 Ma in the CN is likely related to erosion triggered by regional surface uplift. This scenario is consistent with previous studies bracketing the uplift of the western Andes of northern Peru between the early and late Miocene (e.g., Farrar and Noble, 1976; Myers, 1976; Giovanni et al., 2010; Hoorn et al., 2010).

Ridge Subduction, Slab Flattening, and Surface Uplift

The initiation of exhumation at ca. 15 Ma in the CN correlates with subduction of the Nazca Ridge (Fig. 3B; Rosenbaum et al., 2005). Exhumation in the CN has continued after initial ridge subduction and its southward

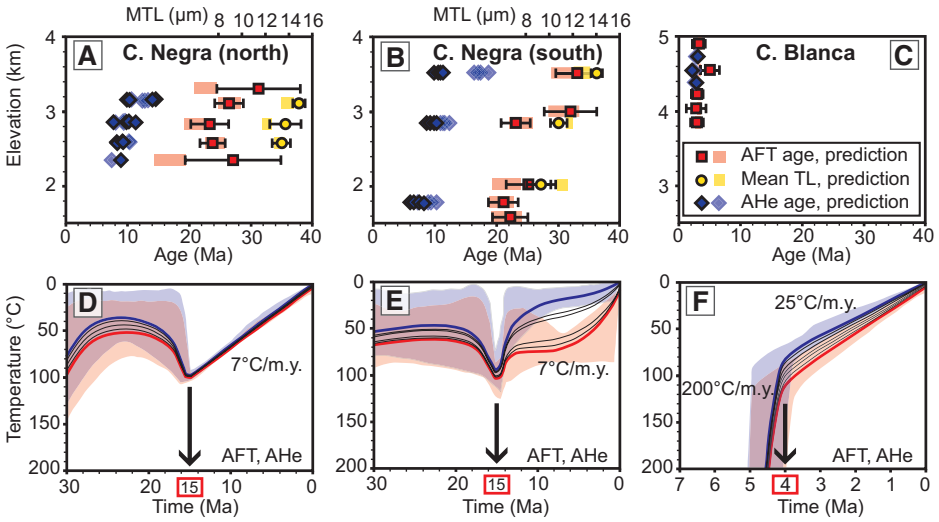

Figure 2. Age-elevation plots and temperature-time (*T-t*) paths predicted for thermochronological ages using Gautheron et al. (2009) He diffusion model. A–C: Age-elevation plots showing apatite fission-track (AFT) ages (red), mean track length (MTL; yellow) and apatite (U-Th)/He (AHe) ages (blue); ages predicted by thermal history are plotted in pastel colors. A: Northern Cordillera Negra (CN) profile.B: Southern CN profile. C: Cordillera Blanca (CB) profile. D–F: *T-t* paths for northern and southern CN and CB profiles. Each line represents *T-t* path of a sample; red line represents path of lowest-elevation sample and blue line highest, pastel shading represent uncertainties.

migration until today (Figs. 3C and 3D). The timing (15 Ma) and location (10°S) of the initial Nazca Ridge subduction proposed by Rosenbaum et al. (2005) is consistent with the middle Miocene continental shelf uplift at this latitude (von Huene and Suess, 1988), with the propagation of the orogenic front toward the east at ca. 8 Ma (Mégard, 1987) and with the shift of magmatic sources toward the east from the Calipuy Formation (54–15 Ma; Cobbing et al., 1981) to the CB magmas (CB batholith, Fortaleza and Yungay ignimbrites, 14–3 Ma; Mukasa, 1984; Wise and Noble, 2003; Wipf, 2006; Giovanni, 2007; Giovanni et al., 2010). Eakin et al. (2014) suggested that slab flattening has an influence on the evolution of the overriding plate and proposed ~1000 m of positive dynamic topography in the Cordillera Occidental after slab flattening. As no important compressive phase has been documented during the middle Miocene in the Cordillera Occidental in northern Peru (Mégard, 1987), we suggest that regional uplift resulted from positive dynamic topography above the flat slab.

Magmatism and Exhumation in the Cordillera Blanca

The CB thermal history indicates rapid cooling (200 °C/m.y.) of the batholith followed by slower cooling (25 °C/m.y.) beginning at ca. 4 Ma. The rapid cooling likely corresponds to the post-magmatic cooling of the CB batholith; coeval exhumation is not excluded. The slower cooling likely corresponds to exhumation. This cooling rate suggests higher exhumation rates in the CB than in the CN. Following McNulty et al. (1998) and Petford and Atherton (1992), we propose that strike-slip faulting facilitated the earlier stage of CB exhumation (Fig. 3C). Our data combined with previously published thermochronological data (U-Pb and Ar-Ar; Giovanni, 2007) indicate that the CB emplacement and onset of exhumation are coeval, suggesting that the crustal emplacement of low-density magma participated in the exhumation of the CB (Petford and Atherton, 1992). The presence of polished granitic clasts in Pliocene sediments indicates glacial erosion of the CB (Bonnot, 1984), placing the CB at elevations at least in excess of ~3500 m at this time. Finally, we suggest that magmatism and glacial erosion (Fig. 3D) continued to drive the local CB uplift and exhumation in a context of regional surface uplift following slab flattening.

The CB exhumation cannot be explained with models involving increased coupling at the plate interface and shortening in the upper plate. Such models are not compatible with extension related to the CBNF. The initiation of the CBNF (ca. 5.4 Ma; Giovanni et al., 2010) is ~10 m.y. after the subduction of the Nazca Ridge (15 Ma; Rosenbaum et al., 2005), demonstrating that the subduction of the ridge does not control extension on the CBNF and CB exhumation, as suggested by McNulty and Farber (2002). Collapse models (e.g., Dalmayrac and Molnar, 1981) are in contradiction with the 15–0 Ma exhumation of the CN. We suggest that the fault is accommodating the differential exhumation of the two cordilleras.

SUMMARY

Thermochronological data and temperature-time history modeling suggest exhumation since 15 Ma in the Cordillera Negra. We interpret this exhumation phase as the result of elevated erosion rates in response to regional surface uplift. This scenario is in agreement with other studies bracketing the timing of uplift of the Cordillera Occidental between the early and late Miocene (e.g., Hoorn et al., 2010), but contradicts models of extensional or gravitational collapse of thickened crust (e.g., Dalmayrac and Molnar, 1981). We propose that surface uplift in the Cordillera Occidental was driven by the Nazca Ridge subduction, slab flattening, and

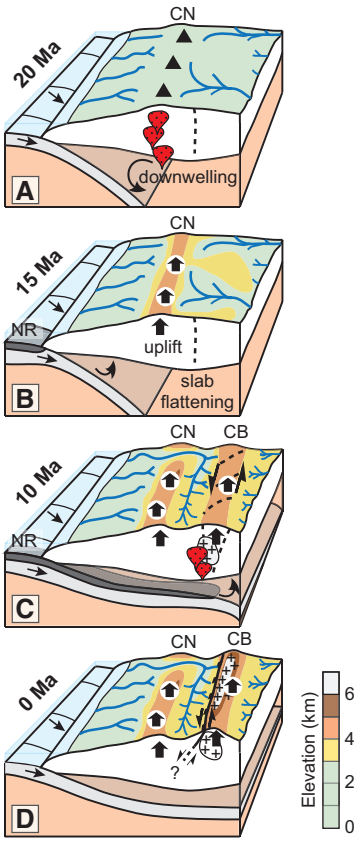

Figure 3. Block diagrams showing uplift history and paleogeography of Cordillera Occidental in northern Peru. Diagrams represent surface uplift (bold arrow), volcanism (black triangle), partial melting (red droplet), faults (dotted and continuous black lines), drainage network, and Cordillera Blanca (CB) batholith. A: Calipuy Formation emplaces in Cordillera Negra (CN) above "normal" subduction (54–15 Ma). B: Subduction of Nazca Ridge (NR), slab flattening, and corresponding surface uplift in CN at 15 Ma. C: During slab flattening, magmatism shuts down in CN and moves eastward. CB batholith emplaces at depth and is exhumed in strike-slip context. D: Cordillera Blanca normal fault accommodates recent exhumation of CB resulting in modern elevations >6 km.

associated magmatism (i.e., CB magmas). By constraining the timing of heating and cooling of upper crustal rocks from the late Oligocene to the present, this study provides new evidence linking flat subduction to the topographic evolution of the northern Peruvian Andes.

ACKNOWLEDGMENTS

This work was supported by a grant from LabEx OSUG@2020 (Observatoire des Sciences de l'Univers de Grenoble, Investissements d'Avenir, ANR10 LABX56), ECOS-NORD/COLCIENCIAS/ICETEX, and SMINGUE. We thank the SERNAMP for allowing sampling in the Cordillera Blanca, and F. Coeur, F. Senebier, E. Hardwick, M. Balvay, R. Pinna-Jamme, K. Hodson, and M. Michalak for sample preparation. We thank C. Lithgow and two anonymous reviewers for their constructive reviews.

REFERENCES CITED

Barazangi, M., and Isacks, B.L., 1976, Spatial distribution of earthquakes and subduction of the Nazca plate beneath South America: Geology, v. 4, p. 686–692, doi:10.1130/0091-7613(1976)4<686:SDOEAS>2.0.CO;2.

Beckinsale, R.D., Sanchez-Fernandez, A.W., Brook, M., Cobbing, E.J., Taylor, W.P., and Moore, N.D., 1985, Rb-Sr whole-rock isochron and K-Ar age determinations for the Coastal Batholith of Peru, *in* Pitcher, W.S., and Atherton, M.P., eds., Magmatism at a Plate Edge: The Peruvian Andes: Glasgow, Blackie, p. 177–202.

Bonnot, D., 1984, Néotectonique et tectonique active de la Cordillère Blanche et du Callejon de Huaylas (Andes nord-péruviennes) [unpublished Ph.D. thesis]: Centre d'Orsay, Université de Paris-Sud, 202 p.

Cobbing, J., Pitcher, W., Baldock, J., Taylor, W., McCourt, W., and Snelling, N.J., 1981, Estudio geológico de la Cordillera Occidental del norte del Perú: Instituto Geológico Minero y Metalúrgico [Peru] Boletín 10, Serie D: Estudios Especiales, 252 p.

Dalmayrac, B., and Molnar, P., 1981, Parallel thrust and normal faulting in Peru and constraints on the state of stress: Earth and Planetary Science Letters, v. 55, p. 473–481, doi:10.1016/0012-821X(81)90174-6.

Eakin, C.M., Lithgow-Bertelloni, C., and Dávila, F.M., 2014, Influence of Peruvian flat-subduction dynamics on the evolution of western Amazonia: Earth and Planetary Science Letters, v. 404, p. 250–260, doi:10.1016/j.epsl.2014.07.027.

Eude, A., Roddaz, M., Brichau, S., Brusset, S., Calderon, Y., Baby, P., and Soula, J.C., 2015, Controls on timing of exhumation and deformation in the northern Peruvian eastern Andean wedge as inferred from low-temperature thermochronology and balanced cross section: Tectonics, v. 34, p. 715–730, doi:10.1002/2014TC003641.

Farrar, E., and Noble, D.C., 1976, Timing of late Tertiary deformation in the Andes of Peru: Geological Society of America Bulletin, v. 87, p. 1247–1250, doi:10.1130/0016-7606(1976)87<1247:TOLTDI>2.0.CO;2.

Gallagher, K., 2012, Transdimensional inverse thermal history modeling for quantitative thermochronology: Journal of Geophysical Research, v. 117, B02408, doi:10.1029/2011JB008825.

Gallagher, K., Brown, R., and Johnson, C., 1998, Fission track analysis and its applications to geological problems: Annual Review of Earth and Planetary Sciences, v. 26, p. 519–572, doi:10.1146/annurev.earth.26.1.519.

Gautheron, C., Tassan-Got, L., Barbarand, J., and Pagel, M., 2009, Effect of alpha-damage annealing on apatite (U–Th)/He thermochronology: Chemical Geology, v. 266, p. 157–170, doi:10.1016/j.chemgeo.2009.06.001.

Gautheron, C., Tassan-Got, L., Ketcham, R.A., and Dobson, K.J., 2012, Accounting for long alpha-particle stopping distances in (U-Th-Sm)/He geochronology: 3D modeling of diffusion, zoning, implantation, and abrasion: Geochimica et Cosmochimica Acta, v. 96, p. 44–56, doi:10.1016/j.gca.2012.08.016.

Giovanni, M.K., 2007, Tectonic and thermal evolution of the Cordillera Blanca detachment system, Peruvian Andes: Implication for normal faulting in a contractionnal orogen [unpublished Ph.D. thesis]: Los Angeles, University of California–Los Angeles, 255 p.

Giovanni, M.K., Horton, B.K., Garzione, C.N., McNulty, B., and Grove, M., 2010, Extensional basin evolution in the Cordillera Blanca, Peru: Stratigraphic and isotopic records of detachment faulting and orogenic collapse in the Andean hinterland: Tectonics, v. 29, TC6007, doi:10.1029/2010TC002666.

Gutscher, M.-A., Olivet, J.-L., Aslanian, D., Eissen, J.-P., and Maury, R., 1999, The "lost Inca Plateau": Cause of flat subduction beneath Peru?: Earth and Planetary Science Letters, v. 171, p. 335–341, doi:10.1016/S0012-821X(99)00153-3.

Hodson, K.R., 2012, Morphology, exhumation, and Holocene erosion rates from a tropical glaciated mountain range: The Cordillera Blanca, Peru [unpublished M.S. thesis]: Montréal, McGill University, 94 p.

Hoorn, C., et al., 2010, Amazonia through time: Andean uplift, climate change, landscape evolution, and biodiversity: Science, v. 330, p. 927–931, doi:10.1126/science.1194585.

INGEMMET (Instituto Geológico, Minero y Metalúrgico), 1999, Mapa geológico del Perú: Lima, Peru, Instituto Geológico, Minero y Metalúrgico, Sector Energía y Minas, scale 1:1,000,000.

Ketcham, R.A., Carter, A., Donelick, R.A., Barbarand, J., and Hurford, A.J., 2007, Improved measurement of fission-track annealing in apatite using c-axis projection: The American Mineralogist, v. 92, p. 789–798, doi:10.2138/am.2007.2280.

McLaughlin, D.H., 1924, Geology and physiography of the Peruvian Cordillera, Departments of Junin and Lima: Geological Society of America Bulletin, v. 35, p. 591–632, doi:10.1130/GSAB-35-591.

McNulty, B.A., and Farber, D.L., 2002, Active detachment faulting above the Peruvian flat slab: Geology, v. 30, p. 567–570, doi:10.1130/0091-7613(2002)030<0567:ADFATP>2.0.CO;2.

McNulty, B.A., Farber, D.L., Wallace, G.S., Lopez, R., and Palacios, O., 1998, Role of plate kinematics and plate-slip-vector partitioning in continental magmatic arcs: Evidence from the Cordillera Blanca, Peru: Geology, v. 26, p. 827–830, doi:10.1130/0091-7613(1998)026<0827:ROPKAP>2.3.CO;2.

Mégard, F., 1987, Structure and evolution of the Peruvian Andes: The anatomy of mountain ranges, *in* Schaer, J.P., and Rodgers J., eds., The Anatomy of Mountain Ranges: Princeton, New Jersey, Princeton University Press, p. 179–210.

Michalak, M.J., 2013, Exhumation of the Peruvian Andes: Insights from mineral chronometers [Ph.D. thesis]: Santa Cruz, University of California, 166 p.

Montario, M.J., 2001, Exhumation of the Cordillera Blanca, Northern Peru, based on apatite fission track analysis [unpublished Ph.D. thesis]: Schenectady, New York, Union College, Department of Geology, 55 p.

Mukasa, S.B., 1984, Comparative Pb isotope systematics and zircon U-Pb geochronology for the Coastal, San Nicolas and Cordillera Blanca batholiths, Peru [unpublished Ph.D. thesis]: Santa Barbara, University of California–Santa Barbara, 362 p.

Myers, J.S., 1976, Erosion surfaces and ignimbrite eruption, measures of Andean uplift in northern Peru: Geological Journal, v. 11, p. 29–44, doi:10.1002/gj.3350110104.

Noble, D.C., McKee, E.H., Mourier, T., and Mégard, F., 1990, Cenozoic stratigraphy, magmatic activity, compressive deformation, and uplift in northern Peru: Geological Society of America Bulletin, v. 102, p. 1105–1113, doi:10.1130/0016-7606(1990)102<1105:CSMACD>2.3.CO;2.

Petford, N., and Atherton, M.P., 1992, Granitoid emplacement and deformation along a major crustal lineament: The Cordillera Blanca, Peru: Tectonophysics, v. 205, p. 171–185, doi:10.1016/0040-1951(92)90425-6.

Ramos, V.A., and Folguera, A., 2009, Andean flat-slab subduction through time, *in* Murphy, J.B., et al., eds., Ancient Orogens and Modern Analogues: Geological Society of London Special Publication 327, p. 31–54, doi:10.1144/SP327.3.

Rosenbaum, G., Giles, D., Saxon, M., Betts, P.G., Weinberg, R.F., and Duboz, C., 2005, Subduction of the Nazca Ridge and the Inca Plateau: Insights into the formation of ore deposits in Peru: Earth and Planetary Science Letters, v. 239, p. 18–32, doi:10.1016/j.epsl.2005.08.003.

von Huene, R., and Suess, E., 1988, Ocean Drilling Program Leg 112, Peru continental margin: Part 1, Tectonic history: Geology, v. 16, p. 934–938, doi:10.1130/0091-7613(1988)016<0934:ODPLPC>2.3.CO;2.

Wipf, M.A., 2006, Evolution of the Western Cordillera and coastal margin of Peru: Evidence from low-temperature thermochronology and geomorphology [Ph.D. thesis]: Zürich, Swiss Federal Institute of Technology, 163 p.

Wise, J.M., and Noble, D.C., 2003, Geomorphic evolution of the Cordillera Blanca, Northern Peru: Boletín de la Sociedad Geológica del Perú, v. 96, p. 1–21.

Manuscript received 12 June 2015
Revised manuscript received 14 September 2015
Manuscript accepted 16 September 2015

Printed in USA

Les données thermochronologiques présentées dans ce chapitre m'ont permis de discuter le timing du soulèvement des Andes au nord du Pérou. Basée sur ces données, j'ai proposé dans ce chapitre que l'aplatissement de la subduction induit un soulèvement régional dans la Cordillère Occidentale et que les processus de subduction ont un impact important sur l'évolution paléographique des Andes. En revanche, les données que j'ai présentées ici ne donnent aucune contrainte sur le contexte tectonique régional au dessus du segment de subduction horizontale péruvien et le contexte de mise en place du batholite de la Cordillère Blanche. Ces points seront abordés dans les chapitres suivants.

Thermochronological data presented in this chapter permit to discuss the timing of uplift of the Andes in northern Peru. Based on AFT and AHe data, I proposed in this chapter that the flattening of the subduction induced regional uplift in the Cordillera Occidental and that subduction processes have a significant impact on the paleogeography of the Andes. However, the data that I have presented here do not provide any constraints on the tectonic context above the peruvian flat-slab nor the context of emplacement of the Cordillera Blanca batholith. I will address these issues in the next chapters.

---

4 Evolution temporelle du régime tectonique en contexte de subduction plane (Cordillère Blanche, Nord Pérou)

Sommaire

Dans ce chapitre, je présente mes données de déformation ductile et mes données de microtectonique sur la déformation fragile. Ces données me permettront de discuter le contexte tectonique qui a accompagné la mise en place du batholite de la Cordillère Blanche et de documenter l'état de contrainte au dessus du segment de subduction horizontale Péruvien.

I present in this chapter ductile and brittle deformation data from the Cordillera Blanca region. Based on these data, I discuss the tectonic context of the Cordillera Blanca emplacement and I address the stress field evolution above the Peruvian flat-slab.

Résumé étendu en français

Le corps de ce chapitre est un article en préparation pour Journal of South American Earth Sciences. J'ai réalisé la plus grande partie des mesures de terrain (> 50% des mesures de plans striés) et j'ai traité les données obtenues avec un logiciel approprié. Les coauteurs de cet article (X. Robert, L. Audin, A. Pêcher, S. Schwartz) m'ont apporté un support technique pour les mesures sur le terrain, pour le traitement des données ainsi que des discussions constructives qui m'ont permis d'élaborer l'idée directrice de ce chapitre.

En contexte de subduction, le régime tectonique de la plaque chevauchante est étroitement liée au pendage et à la géométrie de la plaque plongeante (Ramos & Folguera 2009). Il est classiquement admis que les segments de subduction horizontale augmentent le couplage au niveau de l'interface de subduction. Il en résulte une augmentation et une migration du raccourcissement dans la plaque chevauchante vers la région d'arrière arc (Jordan et al. 1983, Ramos & Folguera 2009, Martinod et al. 2010). A l'aplomb du segment de subduction plane du Pérou, une faille normale crustale de 200 km de long, parallèle à la chaîne andine, délimite le flanc ouest des hauts sommets de la Cordillère Blanche (Bonnot 1984, McNulty & Farber 2002, Giovanni 2007). Ces sommets (> 6000 m) dominent le plateau dont l'altitude moyenne ne dépasse pas 4400 m. La présence conjointe de la faille normale de la Cordillère Blanche et des hauts reliefs est inattendue dans ce contexte de subduction plane. L'objectif de ce chapitre est de préciser et de contraindre l'évolution du champ de contraintes au cours du temps dans cette région avec de nouvelles données de microstructurale. En effet, l'analyse de la déformation cassante (inversions avec la méthode des dièdres droits et PBT, logiciel WinTensors ; Angelier & Mechler 1977, Angelier 1984, Delvaux 2012) dans la croûte permettra d'évaluer l'impact de la subduction plane sur le régime de contraintes dans la plaque supérieure. De plus, la connaissance de l'évolution régionale du régime de contraintes pourrait fournir des informations sur les processus de mise en place du batholite de la Cordillère Blanche et son exhumation. J'ai déterminé l'évolution du régime de contraintes dans cette région grâce à l'analyse de la déformation ductile à partir d'observations de terrain et d'analyses d'images satellites et à l'inversion de plans de failles striés, que j'ai mesurés en différents sites.

L'analyse de la déformation ductile dans la partie est du batholite de la Cordillère Blanche (∼8 Ma) trace la déformation lors de la mise en place du granite et suggère que le batholite s'est mis en place dans un contexte décrochant dextre. Ces données sont en accord avec les conclusions de Petford & Atherton (1992). La déformation cassante reflète le régime de contraintes plus récent qui se superpose à la déformation ductile acquise au cours de la mise en place de la Cordillère Blanche et de son exhumation. La gamme de tenseurs obtenue suggère une histoire complexe avec une succession de différents épisodes tectoniques. Le tenseur de contraintes le plus représenté correspond à une extension de direction NE-SW (80% des sites). L'extension n'est pas limitée à la Cordillère Blanche. En effet, les deux sites localisés dans la Cordillère Noire enregistrent respectivement une

extension E-W, ainsi que de la transtension (direction d'extension E-W). En outre, les tenseurs de contraintes calculés indiquent du décrochements (50% des sites), de l'extension N-S (Quebradas Ulta, Queroccocha et Pastoruri, 30% des sites) et de la compression E-W (Quebradas Llaca et Ulta, 15% des sites). Les tenseurs de compression E-W indiquent qu'une phase de compression affecte la région de la Cordillère Blanche après la mise en place du pluton. Ainsi, depuis ∼8 Ma plusieurs régimes tectoniques se sont succédés dans la région de la Cordillère Blanche.

La présence d'une faille normale d'échelle crustale et les tenseurs de contraintes indiquant une extension NE-SW suggèrent que les segments de subduction plane peuvent générer de l'extension dans la Cordillère Occidentale tandis que le raccourcissement migre vers l'est (Mégard 1984). Dans le cas du segment de subduction plane péruvien, l'extension peut être facilitée par la présence d'une croûte épaissie (Froidevaux & Isacks 1984) ou par une diminution de la vitesse de convergence et un faible couplage à l'interface de la plaque (Somoza 1998, Nocquet et al. 2014). Je propose que les segments de subduction plane n'augmentent pas forcément le couplage à l'interface de subduction au niveau de la fosse, mais augmentent seulement le couplage à l'arrière de la chaîne où ils favorisent le raccourcissement.

Stress field evolution above the Peruvian flat-slab (Cordillera Blanca, northern Peru)

A. Margirier, L. Audin, X. Robert, A. Pêcher, S. Schwartz

en préparation pour

Journal of South American Earth Sciences

Stress field evolution above the Peruvian flat-slab (Cordillera Blanca, northern Peru)

A. Margirier[1,2], L. Audin[1,2,3], X. Robert[1,2,3], A. Pêcher[1,2], S. Schwartz[1,2]

[1]*Université de Grenoble, Alpes, ISTerre, F-38041 Grenoble, France*

[2]*Centre national de la recherche scientifique, ISTerre, F-38041 Grenoble, France*

[3]*Institut de recherche pour le développement (IRD), ISTerre, F-38041 Grenoble, France*

Abstract

In subduction settings, the tectonic regime of the overriding plate is closely related to the dip and geometry of the subducting plate. Flat-slab segments appear to increase coupling at the plate interface, resulting in an increase and eastward migration of the shortening in the overriding plate. Above the Peruvian flat-slab, a 200 km-long normal fault trend parallel to the range and delimits the western flank of the Cordillera Blanca. In a context of flat subduction, expected to produce shortening, the presence of the Cordillera Blanca normal fault (CBNF) is surprising. We performed a systematic inversion of striated fault planes in the Cordillera Blanca region to better characterize the spatio-temporal variation of the stress field above the Peruvian flat-slab. It evidences the succession of different tectonic regimes. NE-SW extension is predominant in most of the sites indicating a regional extension. We suggest that the Peruvian flat-slab trigger extension in the Cordillera Occidental while the shortening migrate eastward. Finally, we propose that flat-slab segments do not increase the coupling at the trench neither the shortening in the overriding plate and only favor shortening migration backward. The stress field of the overriding plate arises from convergence rate, plate interface properties or oceanic plate geometry.

1. Introduction

The western South American margin is segmented, with changing Andean topography and along-strike slab dip variations (*Barazangi and Isacks*, 1976). Two flat-slab segments have been identified by seismological data in northern Peru (3-15°S) and central Chile (28-32°S) (*Barazangi and Isacks*, 1976). In subduction settings, the tectonic regime of the overriding plate is closely related to the dip and geometry of the subducting plate (*Ramos and Folguera*, 2009). Flat-slab segments appear to increase coupling at the plate interface, resulting in both an increase and eastward migration of the shortening in the overriding plate (*Jordan et al.*, 1983; *Ramos and Folguera*, 2009; *Martinod et al.*, 2010).

Above the Peruvian flat-slab, a single 200 km-long normal fault trending parallel to the range delimits the western flank of the Cordillera Blanca high peaks (*Bonnot*, 1984; *McNulty and Farber*, 2002; *Giovanni*, 2007). Those peaks (> 6000 m) are abnormally higher than the average plateau altitude at this place (~4400 m). In a context of flat subduction, expected to produce shortening, the joint presence of the Cordillera Blanca normal fault (CBNF) with high reliefs is surprising. Two models have been proposed to explain the occurrence of extension in this part of the high Andes: *Dalmayrac and Molnar* (1981) suggested an extensional collapse of a thickened crust, whereas *McNulty and Farber* (2002) involved oceanic ridge buoyancy under the Cordillera Blanca. Despite these models, the tectonic setting of the Cordillera Blanca emplacement is still debated: while *Petford and Atherton* (1992) suggested that the Cordillera Blanca batholith has emplaced in a dextral regime based on ductile deformation structures, *McNulty et al.* (1998) interpreted some magnetic susceptibility data from the batholith as the result of a sinistral tectonic regime.

As this opposition is a key issue for Andean geodynamics, the aim of this paper is to precise and constrain the stress field evolution through time in this region with new microstructural data. Indeed, analyzing the ductile and brittle tectonic deformation in the crust permits to describe the impact of flat subduction on the stress field in the overriding plate in northern Peru. Moreover, the knowledge of the regional stress field evolution could provide

54 information on processes driving the Cordillera Blanca batholith emplacement and
55 exhumation. Its evolution above the flat-slab is inferred from both ductile deformation pattern
56 and inversions of striated fault planes measured on different outcrops in the Cordillera Blanca
57 region.
58
59 **2. Geodynamic and tectonic context of northern Peru**
60 **2.1. Geodynamic setting**
61 The Andes are the result of the long-lasting subduction of the Nazca plate beneath the South
62 America plate. The subduction zone has been active since at least Cretaceous time, with
63 convergence rates, obliquity and subduction dip changing through time (e.g., *Somoza*, 1998;
64 *Ramos and Folguera*, 2009; *Martinod et al.*, 2010). These changes have been associated to
65 different tectonic phases affecting the Andean range (e.g., *Jordan et al.*, 1983; *Pardo-Casas*
66 *and Molnar*, 1987; *Somoza*, 1998) and influenced the magmatic activity along strike (*Kay and*
67 *Kay*, 2002; *Ramos and Folguera*, 2009).
68 The northern Peruvian margin displays a present-day flat subduction zone where both, the
69 geometry and timing of slab flattening are well constrained for the last 15 Ma (e.g., *Gutscher*
70 *et al.*, 1999; *Hampel*, 2002; *Rosenbaum et al.*, 2005; *Antonijevic et al.*, 2015). *Gutscher et al.*,
71 (2000) suggested that the flat-slab has a ~20 km deep sag between the Nazca Ridge and the
72 Inca Plateau thickened parts (Fig. 1). The subduction of these two buoyant features have been
73 proposed to induce the slab flattening in northern Peru (*Gutscher et al.*, 1999). Based on this
74 hypothesis, several reconstructions of the timing and location of the initial Nazca ridge
75 subduction based on symmetric seafloor-spreading in a hotspot reference frame constrained
76 the timing of the slab flattening (e.g., *Hampel*, 2002; *McNulty and Farber*, 2002; *Rosenbaum*
77 *et al.*, 2005; *Antonijevic et al.*, 2015). However, all of these models rely on calculations of the
78 motion of the Nazca plate with respect to South America, which may contain considerable
79 errors. *Rosenbaum et al.* (2005) presented a regionally refined plate circuit that suggests the

initiation of the Nazca Ridge subduction at 15 Ma at 10°S and the arrival of the Inca plateau at 13 Ma at 5°S. This reconstruction, in agreement with the timing of magmatism migration eastward, indicates that the slab flattening occur at the latitude of the Cordillera Blanca region from ~15 Ma.

2.2. Geologic and Quaternary tectonic settings of the Cordillera Blanca region

The Cordillera Blanca is a Miocene granitic pluton (14-5 Ma; *Mukasa*, 1984; *McNulty et al.*, 1998; *Giovanni*, 2007) emplaced in deformed Jurassic sediments of the Chicama formation at pressures ranging from 1 to 2 kbar (*Petford and Atherton*, 1992; *Margirier et al.,* in prep). The Cordillera Blanca batholith and associated magmas, the Fortaleza and Yungay ignimbrites emplaced respectively around 7.4 Ma (*Wipf*, 2006) and between 8 and 3 Ma (*Wise and Noble*, 2003; *Giovanni*, 2007; *Giovanni et al.*, 2010) correspond to the last magmatic activity before the cessation of magmatism associated to the slab flattening in northern Peru (*Petford and Atherton*, 1992).

The elongated shape (trending parallel to the Andean range) and the internal fabric of the batholith indicate its emplacement along a pre-existing structure, in a strike slip context. However, there is no consensus about the kinematics (dextral versus senestral; *Petford and Atherton*, 1992; *McNulty et al.*, 1998).

The high summits of the Cordillera Blanca built the footwall of the Cordillera Blanca normal fault (CBNF). The CBNF is a 200 km-long crustal-scale extensional structure. No historical earthquake has been recorded on the CBNF itself but some microseismicity occurs in the Cordillera Blanca region. The related focal mechanisms indicate present-day NE-SW extension compatible with Quaternary offsets along the CBNF (*Deverchère et al.*, 1989).

Preliminary studies addressed the Cordillera Blanca Quaternary tectonic history with microtectonic data and stress reconstructions (*Bonnot*, 1984; *Sébrier et al.*, 1988). Their fault slip dataset contains several populations and suggests different tectonic phases. *Bonnot* (1984)

106 proposed the succession of the following tectonic phases: (I) Pliocene E-W extension (σ_3 sub-
107 horizontal N285, σ_1 sub-vertical), (II) Quaternary E-W compression (σ_1 sub-horizontal N080,
108 σ_3 sub-vertical) and N-S compression (σ_1 sub-horizontal N150, σ_3 sub-vertical), (III) N-S
109 extension from the Pleistocene to present day. *Sébrier et al.* (1988) only focused on the last
110 fault slip and suggested N-S extension in the Cordillera Blanca. Nor the Quaternary
111 compression nor the N-S extension they evidenced in the Cordillera Blanca is in agreement
112 with present day extensional microseismicity.

113 General trends of the main fault zone, its segmentation and variations of the scarp heights
114 suggest that the CBNF is segmented (Fig. 2; *Giovanni*, 2007). Field studies evidence
115 discontinuous NW-SE striking scarps that displace Quaternary glacial moraines as well as
116 plutonic rocks (Fig. 3; e.g., *Bonnot*, 1984). Along the fault zone, repeated displacements
117 imprinted the landscape, with ~2 to 100 m-high scarps, corresponding to vertical
118 displacements cumulated during the Quaternary and 1 km-high triangular facets (Fig. 3A). In
119 total, the CBNF shows at least 4500 m of vertical displacement since ~5 Ma (*Bonnot*, 1984;
120 *Giovanni*, 2007; *Margirier et al.*, in prep).
121 For the last 3 Ma, *Giovanni* (2007) and *Hodson* (2012), based on thermochronologic data,
122 gave estimation of exhumation rate at ~2 mm/yr and >1 mm/yr respectively on the central
123 part of the CBNF and decreasing exhumation rates toward the South. For the last 4 Ma,
124 *Margirier et al.* (2015) suggest lower exhumation rate (1 mm/yr) for the Central part of the
125 Cordillera Blanca. Based on the CBNF morphology and the Cordillera Blanca geology
126 *Bonnot* (1984) estimated slip rates of ~0.7 mm/yr on the CBNF between 7 and 5 Ma. On a
127 more recent time scale (30-0 ka), the CBNF displacement rates have been constrained by ^{10}Be
128 dating of scarps (*Siame et al.*, 2006) and geomorphic features (moraines) displaced by the
129 fault (Fig. 3B, C; *Farber and Hancock*, in prep; *Schwartz*, 1988). The vertical slip rates
130 decrease from north to south (Fig. 2B). *Siame et al.* (2006) and *Farber and Hancock* (in prep)
131 estimated slip rate in the Quebrada Huaytapallana at 3.0 ± 1.0 mm/yr and 5.1 ± 0.8 mm/yr

132 respectively. The estimated slip rate in the Quebrada Cojup reach 2.9 ± 0.3 mm/yr (*Farber*
133 *and Hancock*, in prep). Farther south the slip rate decrease significantly to 0.86-1.36 mm/yr or
134 0.77 ± 0.1 mm/yr in the Quebrada Querococha (*Schwartz*, 1988; *Farber and Hancock*, in
135 prep) and in the Quebrada Tuco or 0.59 ± 0.2 mm/yr (*Farber and Hancock*, in prep).

136 In terms of active seismicity, no historical earthquake has been reported for the CBNF
137 (*Silgado*, 1992). However, some microseismicity occurs in the Cordillera Blanca region. The
138 focal mechanisms indicated present-day NE-SW extension in adequacy with Quaternary
139 offsets along the CBNF (*Deverchère et al.*, 1989). The most significant coseismic surface
140 faulting has been reported in 1946 along the Quiches normal fault (Mw = 6.8; *Doser*, 1987;
141 *Bellier et al.*, 1991), north of the CBNF. No significant seismic event (Mw>4) has been
142 reported South of the CBNF segments neither along the Cordillera Huayhuash neither farther
143 South (Neotectonic Open Database[1]).

144 West of the Cordillera Blanca, the Callejón de Huaylas, an elongated range-parallel intra-
145 mountain basin (150 km long), separates the Cordillera Blanca and the Cordillera Negra. The
146 Callejón de Huaylas extends along the granitic massif outcrop and fade north or south of its
147 superficial expression. The sedimentary series filling this intra-mountain basin recorded its
148 subsidence associated to the CBNF initiation and activity (*Bonnot*, 1984). Indeed, at the base
149 of the series some ignimbrites dated at 5.4 ± 0.1 Ma suggest that normal faulting initiated at
150 ~5.4 Ma (*Giovanni*, 2007, *Giovanni et al.*, 2010). Westward, the Cordillera Negra builds the
151 hanging-wall of the CBNF. This range consists of Cretaceous and Paleogene plutons (73-48
152 Ma; *Mukasa*, 1984; *Beckinsale et al.*, 1985) intruded in the Chicama formation. Neogene
153 volcano-sedimentary deposits capped the older formations in the southern part of the
154 Cordillera Negra.

155

156 **3. Methods**

[1] neotec-opendata.com

3.1. Satellite image analysis

In mountain ranges, the landscapes are largely controlled by the lithology and tectonic structures. Fracturing favors chemical weathering and weaken the rocks. Satellite imageries can be used to constrain these processes at up to kilometers scale in rocky landscapes/areas. Here, we analyzed satellite images (Landsat images, 2001-2002, visible band with a resolution of 15 m) to extract the main trending faults at regional/km scale. Mapping displacements along active faults is based on displacement of surfaces or geomorphic markers such as moraines or Quaternary pediment surfaces. For each lineament we checked if it corresponds to a fault and not to a fold axis or more competent rocks. To discuss the contradictory conclusions of previous works on the ductile deformation in the Cordillera Blanca (*Petford and Atherton*, 1992; *McNulty et al.*, 1998), we also collected ductile deformation data on the field and from satellite image (Google Earth).

3.2. Tectonic stress inversion

3.2.1. Principe

Several methods permit to obtain paleostress tensors based on sets of fault planes and slickenlines with kinematic indicators (e.g., *Angelier and Mechler*, 1977; *Angelier*, 1984). The reduced stress tensor, obtained from faults-striations pairs inversion, provides the orientation of the principal stress axes σ_1, σ_2, σ_3 (with $\sigma_1 > \sigma_2 > \sigma_3$ and compression being positive) and a shape parameter that we defined here as $\phi = (\sigma_2 - \sigma_3)/(\sigma_1 - \sigma_3)$ (e.g., *Angelier*, 1984; *Delvaux and Sperner*, 2003). These inversion methods rely on three assumptions: (a) the stress is uniform in the volume of rock considered, (b) the stress tensor is equivalent to the deformation tensor obtained from natural data, and (c) the slip vector on fault planes (given by the slickenlines) is parallel to the maximum shear stress along the plane as deduced from the stress tensor (*Bott*, 1959). These assumptions imply careful choice of the measurement stations, and brittle deformation measurements.

184 ***3.2.2. Fieldwork***

185 For each site we measured between 2 and 34 striated fault planes (supplementary tables A1
186 and A2) on outcrops no larger than 50 m with homogenous macroscopic fabric. We measured
187 all types of fault plane with objectivity. We constrained the displacement on each fault plane
188 with classical kinematic indicators (fibers, striations, scales…). We reported each
189 measurement quality and confidence level for the sense of the displacement found on the field
190 (Table A2). The fault plane is rejected in the case of strong uncertainties. Most of our sites are
191 located along roads for quality of outcroppings: it is constituted of fresh rocks and all the
192 faults populations can be measured. For "natural" outcrops fault planes are weathered and the
193 striations are not well preserved, leading to too few measurements to be able to use them for
194 analysis. Measurement sites are mostly located in the Cordillera Blanca but some
195 measurements stations are in the Cordillera Negra and the Callejón de Huaylas (Fig. 2). This
196 heterogeneous sampling is related to difficulties to find sites with competent, fractured and
197 low weathering rocks in the Cordillera Negra.

198

199 ***3.2.3. Inversion methods***

200 Different computer softwares have been developed to determine the reduced stress tensor that
201 best explains the slip distribution on a set of fault planes (e.g., TectonicsFP, FaultKinWin,
202 TENSOR, WinTensor, Mim; *Marrett and Allmendinger*, 1990; *Sperner et al.*, 1993; *Yamaji*,
203 2000; *Ortner et al.*, 2002; *Delvaux and Sperner*, 2003; *Delvaux*, 2012). As they are based on
204 the same physical concepts, all these methods are expected to give similar results (*Delvaux*
205 *and Barth*, 2010; *Lacombe*, 2012). The inversion of the data was here performed using the
206 software WinTensor (*Delvaux*, 2012) which inverts a dataset with the rights dihedral method
207 (*Angelier and Mechler*, 1977) and the PBT method (*Angelier*, 1984). The inversion requires at
208 least 4 fault-striation pairs. A higher number of data better constrains the solution. Here, we
209 used at least 6 pairs of fault-striation for an inversion. The angular misfits between the

210 measured striation and the theoretical striation predicted from the calculated tensor indicate
211 the quality of the inversion. Here, the mean misfit is lower than 30° for all the inversions.
212 The data were processed following a multistep approach (*Zeilinger et al.*, 2000). For each
213 valley when our sites are close to each other (< 10 km), we group the sites located in
214 tectonically homogeneous units to process them as single sites and average the regional stress
215 field (*Zeilinger et al.*, 2000; *Pêcher et al.*, 2008). The larger number of fault-striation pairs for
216 grouped sites permits a more robust determination of tensors.
217

218 **4. Results**

219 ***4.1. Ductile deformation and local cooling ages of the Cordillera Blanca batholith***

220 We analyzed punctual ductile deformation evidences from fieldwork and from satellite image
221 to discuss the tectonic context during the Cordillera Blanca batholith emplacement. The veins
222 developed in the sediments close to the batholith contact are excellent deformation markers
223 ranging from field to satellite scale. Their ductile deformation provides a reliable constraint of
224 the upper plate regional stress field contemporary of their emplacement.
225 Along the eastern limit of the Cordillera Blanca batholith, some deformed dykes intruded the
226 Jurassic sediments and indicates a dextral sense of shearing along the batholith (Fig. 2 and
227 4A). The surrounding granite is dated at ~8 Ma (zircon U-Pb and muscovite Ar-Ar; *Giovanni*,
228 2007). In the Canyon del Pato close to the contact between the batholith and sediments, a
229 deformed dyke complex intrudes sedimentary rocks of the Chicama Formation. Its ductile
230 deformation indicates normal sense of shearing and NE-SW extension (shearing plane =
231 N145 30SW, extension lineation = N50 20SW; Fig. 4B). Close to this outcrop, the Cordillera
232 Blanca batholith cooling is younger, ages range from 3.6 to 5 Ma (muscovite Ar-Ar and K-
233 Ar; *Stewart et al.*, 1974; *Giovanni*, 2007).
234

235 ***4.2. Brittle deformation***

236 ***4.2.1. Example of a multistep deformation history in the Canyon del Pato***

In the Canyon del Pato, we collected data from 5 sites spread along a 5 km-distance. All the sites are located in the Cordillera Blanca batholith close to the CBNF (Fig. 2). We measured in this area 128 couples fault-striation (Fig. 5). A single stress tensor cannot explain our data; the angular deviation is > 50° for ~50% of the data. The important dispersion of fault orientations (Fig. 5) suggests a multistep brittle deformation history. We obtained 3 stress tensors from faults-striations inversion. The predominant tensor (T1, 66 faults) corresponds to NE-SW pure extension (Fig. 5). The second stress tensor (T2, 12 faults) is related to E-W transpression. The third stress tensor (T3, 11 faults) corresponds to about E-W pure extension. None of the T3 axis is vertical indicating that this tensor has been tilted.

4.2.1. Regional stress fields

Most of our measurements were taken in the Cordillera Blanca batholith. In addition, five sites are located in the southern part of the Cordillera Blanca (Quebrada Pastoruri), in sedimentary and volcanic rocks, one is in the Callejón de Huaylas (Caraz) and two sites are located in the Cordillera Negra (Fortaleza Valley and Pueblo Libre). We measured more than 400 couples fault-striation on 38 sites in the Cordillera Blanca region (Table 1). The results of stress tensors for grouped sites are presented in the Table 1. The average misfit, less than 30° for each stress tensor and corresponding fault-striation dataset, demonstrates the quality of our inversions.

The Cordillera Blanca brittle deformation reflects the recent stress field that is superimposed on ductile deformation acquired during the Cordillera Blanca emplacement and early exhumation. The wide range of tensors suggests a multistep brittle deformation history in the Cordillera Blanca region. The most represented stress tensor corresponds to NE-SW extension (80% of the sites; Figs. 6, 7A). The extension is not restricted to the Cordillera Blanca. Indeed, the Pueblo Libre and the Fortaleza sites recorded respectively E-W extension and transtension with horizontal E-W sigma 3 axis. In addition, the calculated stress tensors indicate strike slip (50% of the sites), N-S extension (in Quebradas Ulta, Queroccocha and

Pastoruri, 30% of the sites) and E-W compression (in Quebradas Llaca and Ulta, 15% of the sites) (Fig. 7). The E-W compression tensors indicate that a compressional phase affect the Cordillera Blanca region after the Cordillera Blanca emplacement. Therefore, since ~8 Ma several tectonic regimes followed one another in the Cordillera Blanca region.

5. Discussion

5.1. Tectonic context for the Cordillera Blanca emplacement

Our ductile deformation data indicates two different strain regimes: a dextral strike-slip and an E-W extension. As for both sites the Cordillera Blanca batholith display different ages, we suggest that the ductile deformation results form different tectonic phases.

First, the granite emplaced in a dextral strike-slip regime (~8 Ma). Our data are here in agreement with the ductile deformation evidenced by *Petford and Atherton* (1992). This dextral strike-slip likely corresponds to the Quechua 2 tectonic phase (9.5-8.5 Ma) which is characterized by strike-slip movements on NW-SE faults resulting from N-S compression (*Mégard*, 1984; *Mégard et al.*, 1984).

Close to the CBNF the ductile deformation recorded NE-SW extension. In this area the batholith is young ~4.5 Ma (*Stewart et al.*, 1974; *Giovanni*, 2007); this NE-SW extension is thus consistent with the 5.4-0 Ma extension on the CBNF (*Bonnot*, 1984; *Giovanni*, 2007).

5.2. Chronology of the different stress field imprinted in the Cordillera Blanca batholith

The Cordillera Blanca region recorded two steps of ductile deformation and a multistep brittle deformation history. The identified stress fields are: NE-SW extension, N-S extension, E-W compression and ~E-W transtension (Table 1, Fig. 7). Despite numerous markers of superposed movements on fault planes their relative chronology was unclear. It is not possible to reconstruct the chronology of stress field based on field criteria. Therefore, we compare calculated stress tensor with tectonic phases documented by *Mégard* (1984) in northern Peru and with the present day stress field inferred from microseismicity (*Deverchère et al.*, 1989).

291 The ductile deformation indicates a dextral strike-slip at ~8 Ma in the eastern part of the
292 Cordillera Blanca. This deformation can be related to the Quechua 2 period, which has
293 produced dextral strike slip on NW-Se trending faults in Ayacucho basin between 9.5 and 8.5
294 Ma (*Mégard et al.*, 1984). Then, the ductile NE-SW extension observed in the Canyon del
295 Pato (~5 Ma) likely corresponds to the brittle deformation NE-SW extensional tensors. This
296 extension at ~4.5 Ma is in agreement with the initiation of the CBNF at ~5.4 Ma (*Bonnot*,
297 1984) and is similar to the regional stress tensor deduced from a microseimicity survey
298 (*Deverchère et al.*, 1989). Thus, we suggest that these ductile and brittle deformation phases
299 are related to the present day state of stress in the Cordillera Blanca region, which last at least
300 for ~5 Ma. The extensional stress tensors are not restricted to the Cordillera Blanca. It likely
301 corresponds to a large-scale process driving extension in the overriding plate. In addition, the
302 brittle deformation indicates that E-W compression episode occurs in the Cordillera Blanca
303 batholith. This compressional episode is also recorded in the Callejón de Huaylas basin
304 (*Bonnot*, 1984). It can be related to the Pliocene Quechua 3 compressional phase (*Mégard*,
305 1984) which could have trigger punctual compressional phase during the CBNF activity
306 (since ~5.4 Ma). Finally, we suggest that the N-S extension in the Cordillera Blanca is related
307 to the recent (2-0 Ma) rapid exhumation of the central part of the Cordillera Blanca
308 (*Margirier et al.*, in prep).
309
310 **5.3. Different tectonic phases above the Peruvian flat-slab**
311 This study evidence the occurrence of several tectonic phase during the past 8 Myr in
312 agreement with *Bonnot* (1984). These successive tectonic phases and the occurrence of
313 perpendicular to the trench extension suggest that flat-slab segments do not always induce
314 compression in the upper plate as previously suggested (*Jordan et al.*, 1983; *Ramos and*
315 *Folguera*, 2009; *Martinod et al.*, 2010a). The tectonic regime changes may be associated to
316 other parameters as plates velocities, plates directions, the absolute movement of the trench,
317 the age of the oceanic plate, the presence of sediments or the geometry of the oceanic plate.

As the tectonic regime change occurs in a short period of time it could be link to a local process (versus a large scale geodynamic process). The Peruvian flat slab geometry includes two thickened parts, the Nazca Ridge and the Inca Plateau, and a "sag" between these two features (*Gutscher et al.*, 1999). Plate reconstructions indicated that the Nazca ridge subduction initiate at ~10°S at ~15 Ma and then the ridge migrate southward (*Hampel*, 2002; *Rosenbaum et al.*, 2005; *Antonijevic et al.*, 2015). The subduction of the Nazca ridge below the Cordillera Blanca could have induced an increase of the coupling (e.g., *Gutscher et al.*, 2000; *McNulty and Farber*, 2002; *Martinod et al.*, 2010) and triggered compressional stress field in this area. After the migration of the ridge toward the South when the "sag" arrived below the Cordillera Blanca, the coupling could have decreased and permitted extension in the overriding plate. In addition, the decrease of convergence rate evidenced by *Somoza* (1998) could also favor extension (Fig. 8). *Gérault et al.* (2015) already suggested the role of the mantle dynamic and of a weak subduction interface in the neutral state of stress above the Mexican flat-subduction.

However, all flat slab segments do not trigger extension. For example, no extension have been reported above the Pampean flat-slab in Chile (e.g., *Ramos et al.*, 2002), whereas the Nazca Plate have the same age and dip in these two segments (*Barazangi and Isacks*, 1976; *Müller et al.*, 2008). The presence of a thick plateau (~50 km, *James*, 1971) in Peru could favor extension independently than subduction properties (*Froidevaux and Isacks*, 1984). In addition, the amount of sediments on the oceanic plate is different in Peru and Chile: The sediment thickness reaches ~500 m in Peru, in Chile there is no sediments (*Divins*, 2006). The presence of sediment can change the plate interface properties (*Ruff*, 1989). Indeed, in Peru GPS survey suggest the subduction interface is not coupled contrary to in Chile (*Nocquet et al.*, 2014).

6. Conclusions

344 The analysis of ductile deformation in the eastern part of the Cordillera Blanca batholith (8
345 Ma) suggests that the batholith emplaced in a dextral strike-slip context according to *Petford*
346 *and Atherton* (1992).
347 Then, the multistep deformation recorded in the Cordillera Blanca indicated the succession of
348 different tectonic regimes (dextral strike-slip, NE-SW extension, E-W compression and NE-
349 SW extension) above the Peruvian flat-slab. The presence of the crustal-scale CBNF and the
350 NE-SW extensional stress tensor suggest that flat subduction can trigger extension in the
351 Cordillera Occidental while the shortening migrate eastward (Mégard, 1984). The extension
352 may be facilitated by the presence of a thickened crust in Peru (*Froidevaux and Isacks*, 1984)
353 or by a decrease of the convergence rate and a low coupling at the plate interface (Somoza,
354 1998; *Nocquet et al.*, 2014). We suggest that flat-slabs do not increase the coupling at the
355 trench but only increase the coupling backward and favor shortening migration backward.
356
357 **References**

358 Angelier, J. (1984), Tectonic analysis of fault slip data sets, *Journal of Geophysical Research:*
359 *Solid Earth*, *89*(B7), 5835–5848.

360 Angelier, J., and P. Mechler (1977), Sur une methode graphique de recherche des contraintes
361 principales également utilisables en tectonique et en séismologie: la méthode des dièdres
362 droits, *Bulletin de la Société Géologique de France*, *19*(6), 1309–1318.

363 Antonijevic, S. K., L. S. Wagner, A. Kumar, S. L. Beck, M. D. Long, G. Zandt, H. Tavera,
364 and C. Condori (2015), The role of ridges in the formation and longevity of flat slabs,
365 *Nature*, *524*(7564), 212–215, doi:10.1038/nature14648.

366 Barazangi, M., and B. L. Isacks (1976), Spatial distribution of earthquakes and subduction of
367 the Nazca plate beneath South America, *Geology*, *4*(11), 686–692.

368 Beckinsale, R. D., A. W. Sanchez-Fernandez, M. Brook, E. J. Cobbing, W. P. Taylor, and N.
369 B. Moore (1985), Rb-Sr whole rock isochron and K-Ar determination for the Coastal
370 Batholith of Peru, in *Magmatism at a Plate Edge: The Peruvian Andes*, edited by W. S.
371 Pitcher, M. P. Atherton, E. J. Cobbing, and R. D. Beckinsale, pp. 177–202, Blackie
372 Halstead press, Glasgow.

373 Bellier, O., J. F. Dumont, M. Sébrier, and J. L. Mercier (1991), Geological constraints on the
374 kinematics and fault-plane solution of the quiches fault zone reactivated during the 10
375 November 1946 Ancash earthquake, northern Peru, *Bulletin of the Seismological Society*
376 *of America*, *81*(2), 468–490.

377 Bonnot, D. (1984), Néotectonique et tectonique active de la Cordillère Blanche et du Callejon

de Huaylas (Andes nord-péruviennes), *Thèse présentée pour obtenir le grade de docteur, Université de Paris-Sud, Centre d'Orsay*, 1–202.

Bott, M. (1959), The mechanics of oblique slip faulting, *Geol. Mag.*

Cobbing, J., W. Pitcher, J. Baldock, W. Taylor, W. McCourt, and N. J. Snelling (1981), Estudio geológico de la Cordillera Occidental del norte del Perú, *Instituto Geologico Minero y Metalurgico, Serie D. Estudios Especiales*, *10*(D), 1–252.

Dalmayrac, B., and P. Molnar (1981), Parallel thrust and normal faulting in peru and constraints on the state of stress, *Earth and Planetary Sciences Letters*, *55*, 473–481.

Delvaux, D. (2012), Release of program Win-Tensor 4.0 for tectonic stress inversion: statistical expression of stress parameters, *EGU General Assembly Conference Abstracts*.

Delvaux, D., and A. Barth (2010), African stress pattern from formal inversion of focal mechanism data, *Tectonophysics*, *482*, 105–128, doi:10.1016/j.tecto.2009.05.009.

Delvaux, D., and B. Sperner (2003), New aspects of tectonic stress inversion with reference to the TENSOR program, *Geological Society, London, Special Publications*, *212*(1), 75–100, doi:10.1144/GSL.SP.2003.212.01.06.

Deverchère, J., C. Dorbath, and L. Dorbath (1989), Extension related to a high topography: results from a microearthquake survey in the Andes of Peru and tectonic implications, *Geophysical Journal International*, *98*(2), 281–292.

Divins, D. L. (2006), Total sediment thickness of the world's oceans and marginal seas,

Doser, D. I. (1987), The Ancash, Peru, earthquake of 1946 November 10: evidence for low-angle normal faulting in the high Andes of northern Peru, *Geophysical Journal of the Royal Astronomical Society*, *91*, 57–71.

Farber, D. L., G. S. Hancock (in prep), Tectonic and glacial forcing of motion along an active detachment fault.

Froidevaux, C., and B. L. Isacks (1984), The mechanical state of the lithosphere in the Altiplano-Puna segment of the Andes, *Earth and Planetary Science letters*, *71*(2), 305–314.

Gérault, M., L. Husson, M. S. Miller, and E. D. Humphreys (2015), Flat-slab subduction, topography, and mantle dynamics in southwestern Mexico, *Tectonics*, doi:10.1002/(ISSN)1944-9194.

Giovanni, M. K. (2007), Tectonic and Thermal Evolution of the Cordillera Blanca Detachment System, Peruvian Andes: Implication for Normal Faulting in a Contractionnal Orogen, 1–255 pp. University of California, Los Angeles.

Giovanni, M. K., B. K. Horton, C. N. Garzione, B. McNulty, and M. Grove (2010), Extensional basin evolution in the Cordillera Blanca, Peru: Stratigraphic and isotopic records of detachment faulting and orogenic collapse in the Andean hinterland, *Tectonics*, *29*(6), TC6007, doi:10.1029/2010TC002666.

Gutscher, M. A., J. Malavieille, S. Lallemand, and J.-Y. Collot (1999), Tectonic segmentation of the North Andean margin: impact of the Carnegie Ridge collision, *Earth and Planetary Science letters*, *168*(3), 255–270.

418 Gutscher, M.-A., W. Spakman, H. Bijwaard, and E. R. Engdahl (2000), Geodynamics of flat
419 subduction: Seismicity and tomographic constraints from the Andean margin, *Tectonics*,
420 *19*(5), 814–833.

421 Hampel, A. (2002), The migration history of the Nazca Ridge along the Peruvian active
422 margin: a re-evaluation, *Earth and Planetary Science letters*, *203*(2), 665–679.

423 Hodson, K. R. (2012), Morphology, exhumation, and Holocene erosion rates from a tropical
424 glaciated mountain range: the Cordillera Blanca, Peru, 1–94 pp. McGill University
425 Masters of science.

426 James, D. E. (1971), Plate tectonic model for the evolution of the Central Andes, *Geological*
427 *Society of America Bulletin*, *82*, 3325–3346.

428 Jordan, T. E., B. L. Isacks, R. W. Allmendinger, J. A. Brewer, V. A. Ramos, and C. J. Ando
429 (1983), Andean tectonics related to geometry of subducted Nazca plate, *Geological Study*
430 *of America Bulletin*, *94*, 341–361.

431 Kay, R. W., and S. M. Kay (2002), Andean adakites: three ways to make them, *Acta*
432 *Petrologica Sinica*.

433 Lacombe, O. (2012), Comptes Rendus Geoscience, *Comptes Rendus Geoscience*, *344*(3-4),
434 159–173, doi:10.1016/j.crte.2012.01.006.

435 Margirier, A., X. Robert, L. Audin, C. Gautheron, M. Bernet, S. Hall, and T. Simon-Labric
436 (2015), Slab flattening, magmatism and surface uplift in the Cordillera Occidental
437 (northern Peru), *Geology*, 1–4, doi:10.1130/G37061.1.

438 Margirier, A., L. Audin, X. Robert, F. Herman, J. Ganne and S. Schwartz (in prep),
439 Emplacement dynamics, exhumation and erosion of the Cordillera Blanca batholith along
440 a major Normal Fault in a subduction context (Peruvian Andes), *Journal of Geophysical*
441 *Research: Solid Earth*.

442 Marrett, R., and R. W. Allmendinger (1990), Kinematic analysis of fault-slip data, *Journal of*
443 *Structural Geology*, *12*(8), 973–986.

444 Martinod, J., L. Husson, P. Roperch, B. Guillaume, and N. Espurt (2010a), Horizontal
445 subduction zones, convergence velocity and the building of the Andes, *Earth and*
446 *Planetary Science letters*, *299*(3-4), 299–309, doi:10.1016/j.epsl.2010.09.010.

447 Martinod, J., L. Husson, P. Roperch, B. Guillaume, and N. Espurt (2010b), Horizontal
448 subduction zones, convergence velocity and the building of the Andes, *Earth and*
449 *Planetary Science letters*, *299*(3), 299–309, doi:10.1016/j.epsl.2010.09.010.

450 McNulty, B. A., and D. L. Farber (2002), Active detachment faulting above the Peruvian flat
451 slab, *Geology*, *30*(6), 567–570.

452 McNulty, B. A., D. L. Farber, G. S. Wallace, R. Lopez, and O. Palacios (1998), Role of plate
453 kinematics and plate-slip-vector partitioning in continental magmatic arcs: Evidence from
454 the Cordillera Blanca, Peru, *Geology*, *26*(9), 827–830.

455 Mégard, F. (1984), The Andean orogenic period and its major structures in central and
456 northern Peru, *Journal of the Geological Society*, *141*(5), 893–900.

457 Mégard, F., D. C. Noble, E. H. McKEE, and H. Bellon (1984), Multiple pulses of Neogene

458 compressive deformation in the Ayacucho intermontane basin, Andes of central Peru,
459 *Geological Society of America Bulletin*, *95*(9), 1108–1117.

460 Mukasa, S. B. (1984), Comparative Pb isotope systematics and zircon U-Pb geochronology
461 for the Coastal, San Nicolás and Cordillera Blanca Batholiths, Peru, University of
462 California, Santa Barbara, September.

463 Müller, R. D., M. Sdrolias, C. Gaina, and W. R. Roest (2008), Age, spreading rates, and
464 spreading asymmetry of the world's ocean crust, *Geochem. Geophys. Geosyst.*, *9*(4), 1–
465 19, doi:10.1029/2007GC001743.

466 Nocquet, J.-M. et al. (2014), Motion of continental slivers and creeping subduction in the
467 northern Andes, *Nature Geoscience*, *7*(4), 287–291, doi:10.1038/ngeo2099.

468 Ortner, H., F. Reiter, and P. Acs (2002), Easy handling of tectonic data: the programs
469 TectonicVB for Mac and TectonicsFP for Windows™, *Computers & Geosciences*,
470 *28*(10), 1193–1200.

471 Pardo-Casas, F., and P. Molnar (1987), Relative motion of the Nazca (Farallon) and South
472 American plates since Late Cretaceous time, *Tectonics*, *6*(3), 233–248.

473 Petford, N., and M. P. Atherton (1992), Granitoid emplacement and deformation along a
474 major crustal lineament: the Cordillera Blanca, Peru, *Tectonophysics*, *205*(1), 171–185.

475 Pêcher, A. et al. (2008), Stress field evolution in the northwest Himalayan syntaxis, northern
476 Pakistan, *Tectonics*, *27*(6), n/a–n/a, doi:10.1029/2007TC002252.

477 Ramos, V. A., and A. Folguera (2009), Andean flat-slab subduction through time, *Geological*
478 *Society, London, Special Publications*, *327*(1), 31–54, doi:10.1144/SP327.3.

479 Ramos, V. A., E. O. Cristallini, and D. J. Pérez (2002), The Pampean flat-slab of the Central
480 Andes, *Journal of South American Earth Sciences*, *15*(1), 59–78.

481 Rosenbaum, G., D. Giles, M. Saxon, P. G. Betts, R. F. Weinberg, and C. Duboz (2005),
482 Subduction of the Nazca Ridge and the Inca Plateau: Insights into the formation of ore
483 deposits in Peru, *Earth and Planetary Science letters*, *239*(1-2), 18–32,
484 doi:10.1016/j.epsl.2005.08.003.

485 Ruff, L. J. (1989), Do trench sediments affect great earthquake occurrence in subduction
486 zones? *Subduction Zones Part II*, *129*(1-2), 264–282.

487 Schwartz, D. P. (1988), Paleoseismicity and neotectonics of the Cordillera Blanca fault zone,
488 northern Peruvian Andes, *Journal of Geophysical Research*, *93*(B5), 4712–4730.

489 Sébrier, M., J. L. Mercier, J. Macharé, D. Bonnot, J. Cabrera, and J. L. Blanc (1988), The
490 state of stress in an overriding plate situated above a flat slab: The Andes of Central Peru,
491 *Tectonics*, *7*(4), 895–928.

492 Siame, L. L., M. Sébrier, O. Bellier, and D. Bourles (2006), Can cosmic ray exposure dating
493 reveal the normal faulting activity of the Cordillera Blanca Fault, Peru? *Revista de la*
494 *Asociación Geológica Argentina*, *61*(4), 536–544.

495 Silgado, E. F. (1992), *Investigaciones de sismicidad histórica en la América del Sur en los*
496 *siglos XVI, XVII, XVIII y XIX*, Consejo Nacional de Ciencia y Tecnología, Lima.

497 Somoza, R. (1998), Updated Nazca (Farallon)—South America relative motions during the
498 last 40 My: implications for mountain building in the central Andean region, *Journal of*
499 *South American Earth Sciences*, *11*(3), 211–215.

500 Sperner, B., L. Ratschbacher, and R. Ott (1993), Fault-striae analysis: a Turbo Pascal program
501 package for graphical presentation and reduced stress tensor calculation, *Computers &*
502 *Geosciences*, *19*(9), 1361–1388.

503 Stewart, J. W., J. F. Evernden, and N. J. Snelling (1974), Age determinations from Andean
504 Peru: a reconnaissance survey, *Geological Society of America Bulletin*, *85*(7), 1107–1116.

505 Wipf, M. (2006), Evolution of the Western Cordillera and Coastal Margin of Peru: Evidence
506 from low-temperature Thermochronology and Geomorphology, 1–163 pp. Swiss Federal
507 Institute of Technology Zürich, 7 March.

508 Wise, J. M., and D. C. Noble (2003), Geomorphic evolution of the Cordillera Blanca,
509 Northern Peru, *Boletin de la sociedad Geologica del Peru*, *96*, 1–21.

510 Yamaji, A. (2000), The multiple inverse method: a new technique to separate stresses from
511 heterogeneous fault-slip data, *Journal of Structural Geology*, *22*(4), 441–452,
512 doi:10.1016/S0191-8141(99)00163-7.

513 Zeilinger, G., J. P. Burg, N. Chaudhry, H. Dawood and S. Hussain (2000), Fault systems and
514 Paleo-stress tensors in the Indus Suture Zone (NW Pakistan), *Journal of Asian Earth*
515 *Sciences, 18*, 547-559.

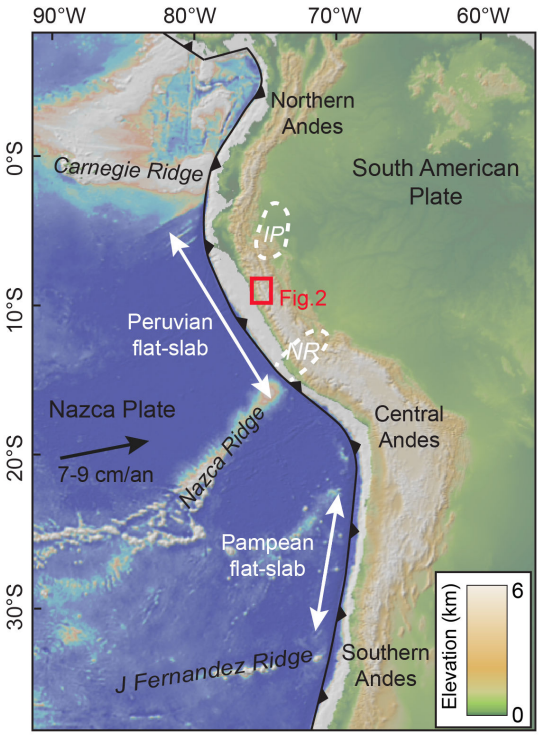

516

517 Figure 1: Topographic map of the Andes (SRTM data) including flat slab segments and
518 bathymetric features as the Nazca Ridge (NR) and the Inca plateau (IP; Inca Plateau location
519 after *Gutscher et al.* (1999). The study area is indicated by the red rectangle.

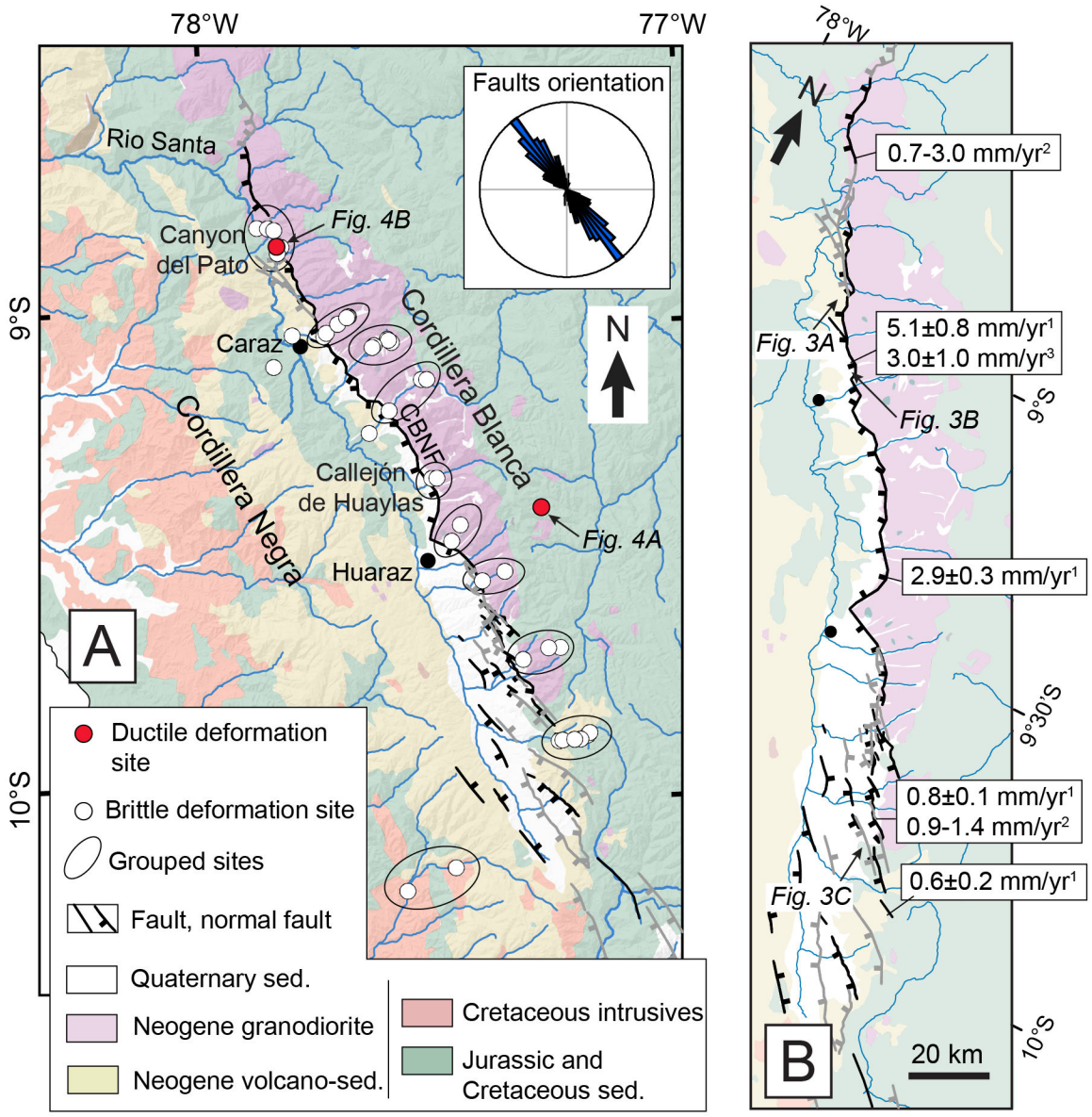

Figure 2: Geological maps of the study area. A) Map showing the active faults mapped in this study (black lines) and from Neotectonic Open Database (grey lines), the measurement stations (white dot), the grouped stations and the sites where ductile deformation was analyzed (red dot). Inset shows a rose diagram of the fault segments azimuth B) Zoom on the CBNF with Quaternary slip-rates from [1]*Farber and Hancock* (in prep), [2]*Schwartz* (1988) and [3]*Siame et al.* (2006).

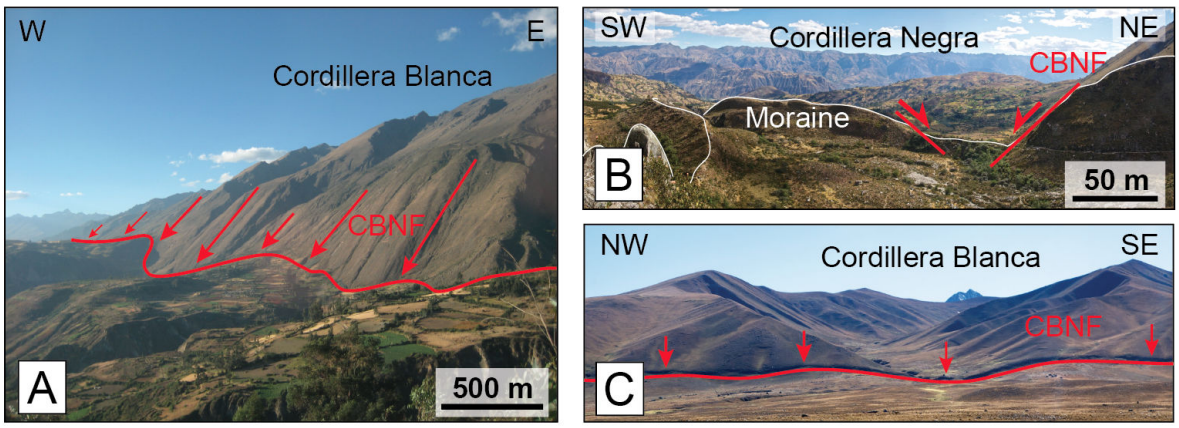

Figure 3: Photographs of the CBNF. See the Figure 2 for locations. A) Triangular facets in the northern part of the Cordillera Blanca (1000 m high). B) Moraine offset at the outlet of the Quebrada Huaytapallana (offset ~100 m). C) Quaternary scarp in the Lloclla Formation (southern Cordillera Blanca) (offset ~4 m).

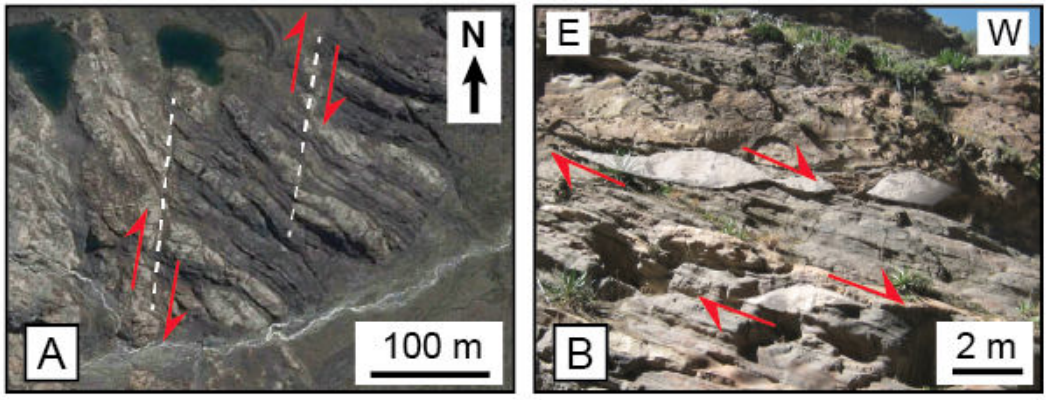

Figure 4: Ductile deformation in the Cordillera Blanca. See Figure 2 for location. A) Satellite image with dextral strike slip in the eastern Cordillera Blanca. B) Photograph of the ductile deformation of dykes in the Canyon del Pato.

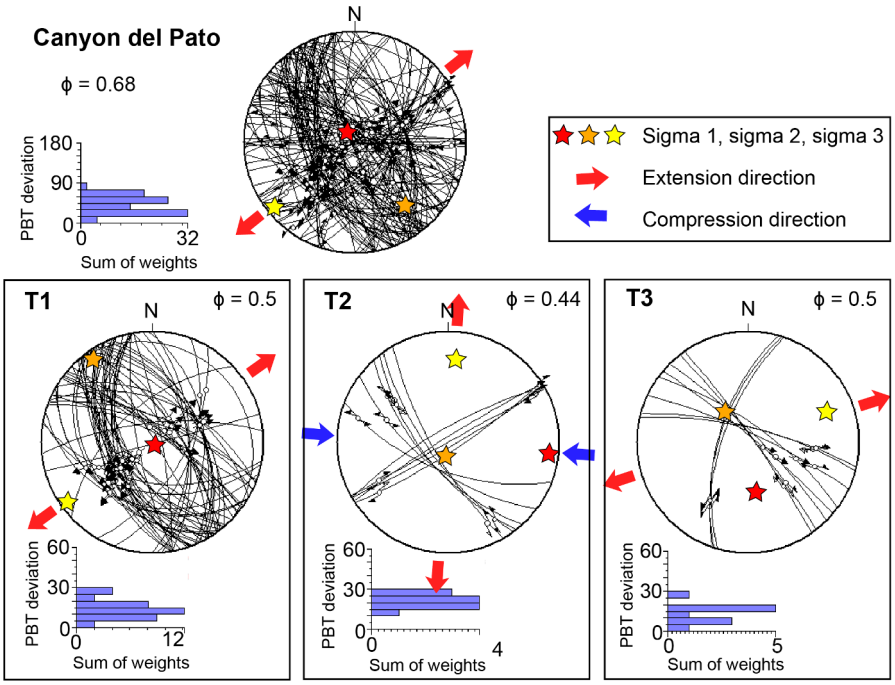

536

537 Figure 5: Faults in the Canyon del Pato (Cordillera Blanca), Wulff lower hemisphere
538 stereographic projection. A) All faults measurements and associated tensor calculation (PBT
539 method) the angular deviation is shown by the histogram. B-D) Tensors T1, T2, T3 and
540 related fault-striation pairs.

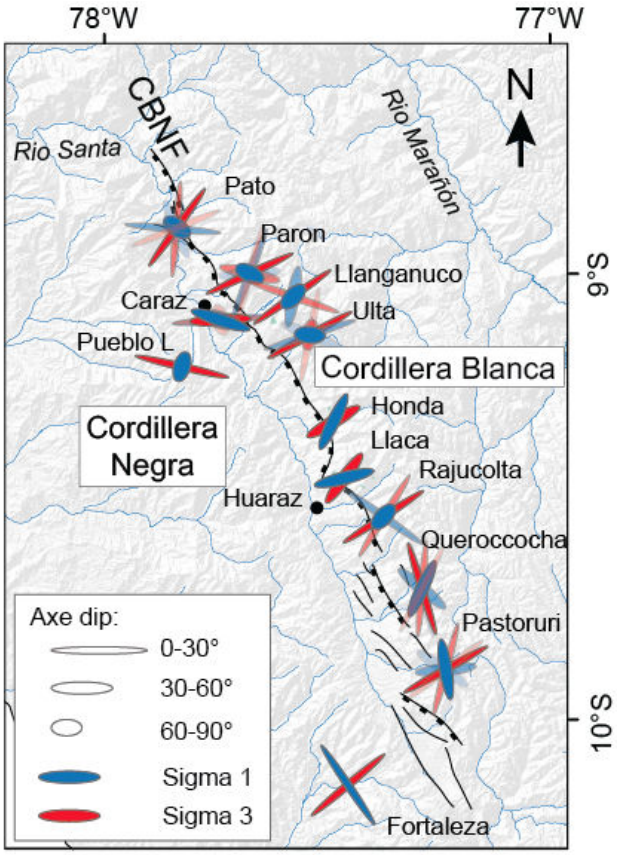

Figure 6: Stress orientation for grouped sites in the Cordillera Blanca region. Stress tensors were calculated using all the couple fault-striation available in one region. Ellipses represents the stress (sigma 1 in blue, sigma 3 in red), the direction of the ellipse great axis corresponds to the azimuth of the stress axis; the shape of the ellipse gives the plunge. The three best stress tensors are shown T1 (bright color), T2 (lighter color) and T3 (very light color).

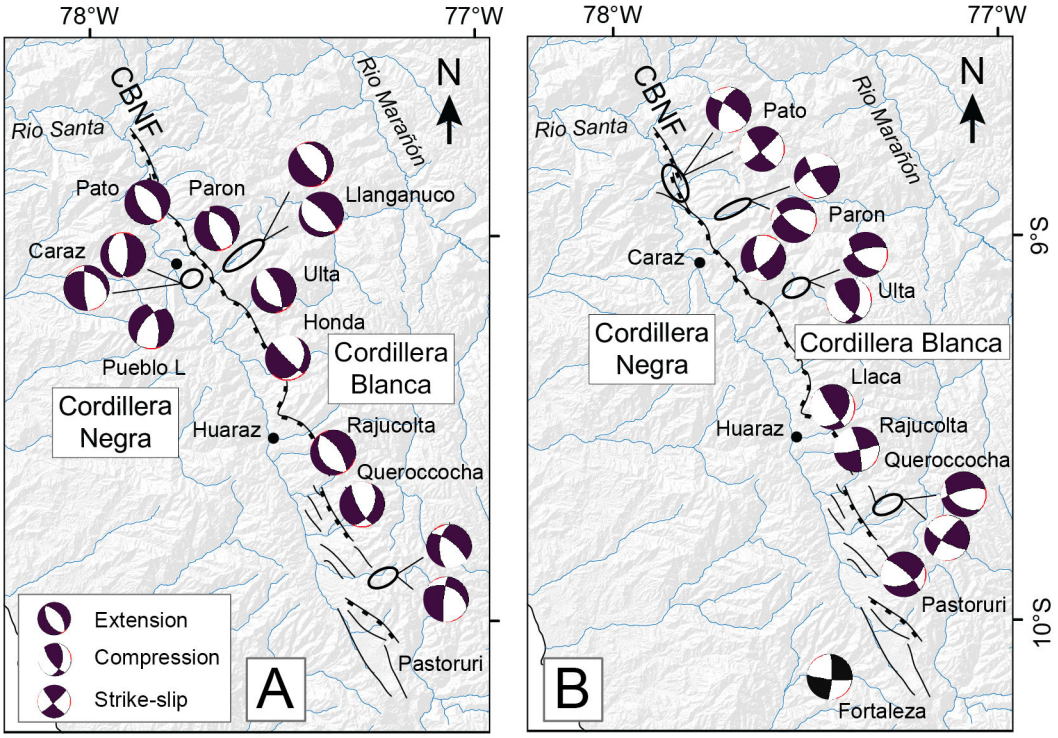

Figure 7: Stress tensors for grouped stations. A) Stress tensors corresponding to the present day regional stress tensor (NE-SW extension) inferred from microearthquakes survey (*Deverchère et al.*, 1989). B) Other stress tensors recorded by the brittle deformation.

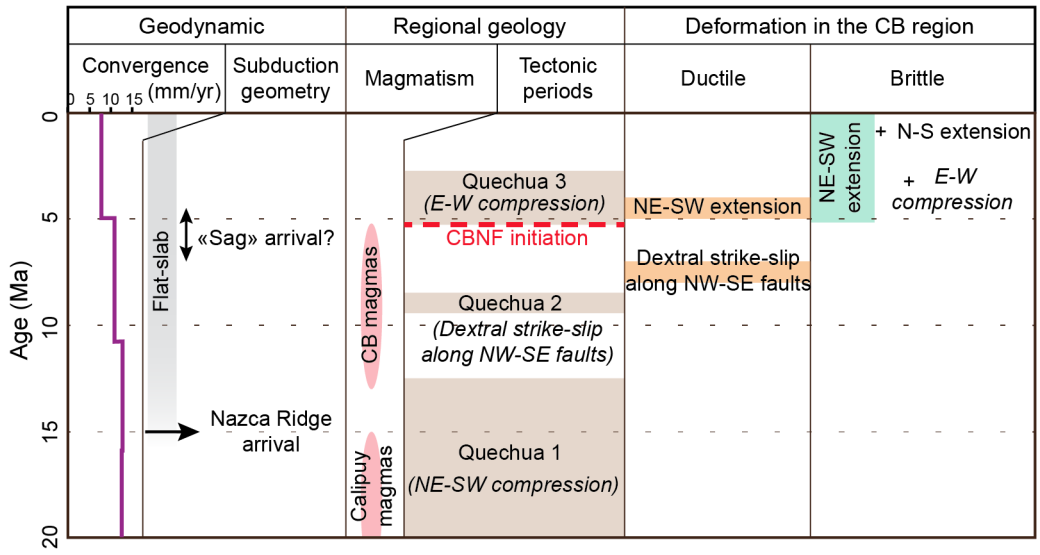

Figure 8: Schematic table that summarizes the northern Peru geodynamic events, regional geology and our stress field results for the past 20 Ma. The table incudes the mean convergence rate *(Somoza*, 1998), subduction geometry (*Barazangi and Isacks*, 1976; *Gutscher et al.*, 1999; *Margirier et al.*, 2015), geodynamic events (*Rosenbaum et al.*, 2005), magmatism age (e.g., *Cobbing et al.*, 1981; *Mukasa*, 1984; *Beckinsale et al.*, 1985), tectonic phases (*Mégard,* 1984) and our ductile and brittle deformation results.

Grâce à mes nouvelles données de déformation ductile et les inversions de population de plans striés j'ai pu mettre en évidence dans ce chapitre a) la mise en place du batholite de la Cordillère blanche dans un contexte décrochant dextre en accord avec les données de Petford & Atherton (1992) et b) des changements du régime de contrainte au dessus de la zone de subduction horizontale du nord Pérou depuis ∼8 Ma. Je n'ai pas pu dissocier les rôles respectifs de la tectonique et du magmatisme dans le soulèvement du batholite de la Cordillère Blanche grâce à mon travail sur la déformation de la région. Cela pose la question de la contribution du magmatisme dans l'exhumation de la Cordillère Blanche. Cette possible contribution sera traitée dans le Chapitre 5.

Ductile deformation data and striated planes inversions indicate a) the establishment of the Cordillera Blanca batholith in a dextral strike-slip context in accordance with Petford & Atherton (1992) and b) changes of the stress field above the flat subduction zone of northern Peru for ∼8 Ma. My work on the ductile and brittle deformation in the Cordillera Blanca area do not permit to dissociate the roles of tectonics and magmatism in the uplift of the Cordillera Blanca batholith through. This raises the question of the magmatism contribution in the exhumation of the Cordillera Blanca. I will be addressed this eventual contribution in Chapter 5.

---

5 Mise en place et érosion glaciaire du batholite de la Cordillère Blanche (Nord Pérou)

Sommaire

Dans ce chapitre, je présente les premières données de profondeur de mise en place du batholite de la Cordillère blanche, une première compilation des données géochronologiques issues de la littérature ainsi qu'une inversion des âges thermochronologiques basse température disponibles dans la région. Ces nouvelles données et modèles me permettent d'aller plus loin que la description du timing de l'exhumation et de proposer un scénario de mise en place et d'exhumation de la Cordillère Blanche intégré au contexte géodynamique régional qui est décrit dans le premier chapitre.

In this chapter, I present the first emplacement depth data for the Cordillera Blanca batholith, geochronological ages from the literature and an inversion of low-temperature thermochronological ages available in the area. I discuss these data and I propose a new scenario for the emplacement and exhumation of the Cordillera Blanca.

Résumé étendu en français

Le corps de ce chapitre est un article en préparation pour JGR, Solid Earth. Les compositions des amphiboles ont été obtenues grâce à des analyses microsonde que j'ai mises en oeuvre. J'ai également modélisé les taux d'érosion. Mes coauteurs (L. Audin, X. Robert, F. Herman, J. Ganne, S. Schwartz) m'ont apporté un support technique lors de l'échantillonnage, du traitement des données de chimie des amphiboles et pour la modélisation des données thermochronologiques. Nos discussions constructives m'ont permis d'élaborer l'idée directrice et d'écrire mon raisonnement et de proposer une interprétation régionale des données tout en intégrant le contexte géodynamique.

La Cordillère des Andes est le résultat de la subduction de la plaque océanique de Nazca sous la plaque Amérique du Sud depuis plus de 100 Ma. L'activité magmatique liée à la subduction est importante mais la contribution de ce magmatisme à l'épaississement de la croûte reste activement débattue (e.g., James & Sacks 1999, Kono et al. 1989, Barnes & Ehlers 2009). En revanche, l'arc actuel représente une contribution non négligeable à l'évolution géomorphologique de la Cordillère Occidentale dans le sud du Pérou (e.g., James & Sacks 1999, Mamani et al. 2010, Boekhout et al. 2012). Dans le nord du Pérou, l'arc Miocène forme les plus hauts sommets péruviens mais aucune étude de ce type n'a été menée jusqu'à présent (Cordillère Blanche, Nord Pérou ; Mukasa 1984, McNulty & Farber 2002, Giovanni 2007).

Le batholite de la Cordillère Blanche (12-5 Ma) forme les plus hauts sommets Péruviens. La Cordillère Blanche correspond au mur d'une faille normale crustale majeure. Plusieurs modèles ont été proposés pour expliquer la présence de cette faille normale en contexte de subduction horizontale mais les processus qui contrôlent l'exhumation de la Cordillère Blanche et l'extension le long de la faille sont encore débattus (e.g., McNulty & Farber 2002, Dalmayrac & Molnar 1981). Jusqu'à présent, les modèles étaient focalisés sur la faille normale de la Cordillère blanche et ne prenaient pas en compte l'histoire de la mise en place de la Cordillère Blanche ni son évolution géomorphologique récente (5-0 Ma).

Le but de ce chapitre est d'apporter de nouvelles contraintes sur les causes du soulèvement et de l'exhumation de l'arc Miocène du nord du Pérou. La quantification des profondeurs de mise en place du batholite de la Cordillère Blanche permettra de contraindre l'exhumation liée à la faille. La modélisation des variations spatiotemporelles de l'érosion (Fox et al. 2014, Herman & Brandon 2015) contraindra l'âge et les vitesses d'exhumation de l'arc.

Basée sur mes nouvelles données de thermobarométrie sur amphibole (Ridolfi & Renzulli 2012) et sur une compilation des données de refroidissement du batholite (zircon U-Pb ; hornblende Ar-Ar and K-Ar ; muscovite Ar-Ar, K-Ar and Rb-Sr ; biotite Ar-Ar, K-Ar et Rb-Sr ; Mukasa 1984, Giovanni 2007, Stewart et al. 1974, Wilson 1975, Beckinsale et al. 1985, Cobbing et al. 1981, Giletti & Day 1968), je propose que le batholite de la Cordillère blanche se mette en place à faible profondeur

(∼3 km), entre 14 et 5 Ma, sous la forme d'une succession de sills. A l'heure actuelle, les roches à l'affleurement les plus jeunes sont également celles qui se sont mises en place le plus profond (∼6 km), elles sont situées sur le flanc ouest du batholite, à proximité de la faille normale de la Cordillère Blanche, ce qui suggère un basculement vers l'est du batholite après 5 Ma.

Au cours du Quaternaire, la Cordillère Blanche a été fortement marquée par les glaciations (Farber et al. 2005, Clapperton 1993, Rodbell 1993, Smith et al. 2005). Les vallées glaciaires en forme de U, les roches moutonnées, des gorges de raccordement et de nombreuses moraines localisées dans la Cordillère Blanche et aux débouchés des vallées principales témoignent de l'étendue de ces glaciations et de leur impact sur l'érosion de la chaîne (Farber et al. 2005, Smith et al. 2005). Pour quantifier les variations spatio-temporelles de l'érosion j'ai inversé les données thermochronologiques disponibles dans la région (zircon (U-Th)/He, apatite fission-track et (U-Th)/He ; Montario 2001, Wipf 2006, Giovanni 2007, Hodson 2012, Michalak 2013, Margirier et al. 2015). J'ai utilisé la méthode de Fox et al. (2014), modifiée par Herman & Brandon (2015) qui exploite les informations contenues dans les profils verticaux et les différents systèmes thermochronologiques. Mes résultats indiquent une augmentation des taux d'érosion dans la Cordillère Blanche au cours du Quaternaire (à partir de ∼2 Ma). Les taux d'érosion les plus élevés correspondent aux parties nord et centrale de la Cordillère Blanche qui sont les régions de plus fort relief, où les vallées sont les plus profondes (∼3 km au nord et au centre, ∼1 km au sud). Pour conclure, je propose que l'érosion glaciaire (incision des vallées) a eu un fort impact sur l'exhumation récente de la Cordillère Blanche (2-0 Ma). La présence de la faille normale de la Cordillère Blanche et les taux d'érosion récents élevés permettent l'exhumation de roches jeunes mise en place en profondeur à proximité de la faille. Pour finir, mes résultats suggèrent que l'arc Miocène ne contribue ni à un épaississement crustal important ni au soulèvement régional et à l'exhumation du nord du Pérou.

Emplacement dynamics, exhumation and erosion of the Cordillera Blanca batholith along a major Normal Fault in a subduction context (Peruvian Andes)

A. Margirier, L. Audin, X. Robert, F. Herman, J. Ganne, S. Schwartz

en préparation pour

Journal of Geophysical Research, Solid Earth

Emplacement dynamics, exhumation and erosion of the Cordillera Blanca batholith along a major Normal Fault in a subduction context (Peruvian Andes)

Audrey Margirier[1,2], Laurence Audin[1,2,3], Xavier Robert[1,2,3], Frédéric Herman[4], Jérôme Ganne[5], Stéphane Schwartz[1,2]

[1]*Université de Grenoble, Alpes, ISTerre, F-38041 Grenoble, France*

[2]*Centre national de la recherche scientifique, ISTerre, F-38041 Grenoble, France*

[3]*Institut de recherche pour le développement (IRD), ISTerre, F-38041 Grenoble, France*

[4]*Institut des dynamiques de la surface terrestre (IDYST), University of Lausanne, CH-1015 Lausanne, Switzerland*

[5]*Géosciences Environnement Toulouse, UMR CNRS-IRD-Université de Toulouse, F-31400, Toulouse, France*

Abstract

The Cordillera Blanca batholith (12-5 Ma) formed the highest Peruvian summits and built the footwall of the Cordillera Blanca normal fault (CBNF). Even if several models have been proposed, the processes driving both the exhumation of the Cordillera Blanca and extensional deformation along the CBNF are still debated. Here we quantify the emplacement depth and exhumation of the batholith of the northern Peru arc from the late Miocene to present. Based on a compilation of crystallization ages and new thermobarometry data in the Cordillera Blanca batholith we propose that the batholith was emplaced at ~3 km in successive sills from 14 to 5 Ma. At the present day, the younger rocks exposed at the surface were emplaced deeper (i.e., ~6 km) and are located close to the CBNF, suggesting post 5 Ma tilting. Furthermore, a formal inversion of the thermochronologic data indicates an increase of the

erosion rates in the Cordillera Blanca during the Quaternary. The higher predicted erosion rates correlate with areas of high relief, both in the northern and central part of the Cordillera Blanca, suggesting that Quaternary valley carving and glaciations had a significant impact on the latest stage of the Cordillera Blanca exhumation (2-0 Ma).

Introduction

Subduction of the oceanic Nazca Plate beneath the continental South American plate is building the Andean range for more than 100 Myrs. The uplift history and the present day high elevations of the Central Andes are the result of an important crustal thickening (60-80 km; *James*, 1971; *Kono et al.*, 1989 *James and Snoke*, 1994; *Zandt et al.*, 1994). For the past 30 years, several processes have been proposed to explain this crustal thickening, including: tectonic shortening (e.g., *Isacks*, 1988; *Kley and Monaldi*, 1998; *McQuarrie*, 2002), magmatic addition (e.g., *James and Sacks*, 1999), changes of the upper plate properties (e.g., *Isacks*, 1988), in the subduction interface (e.g., *Lamb and Davis,* 2003), in the subduction geometry (e.g., *Jordan et al.*, 1983; *Isacks*, 1988; *Gephart*, 1994; *Kley et al.*, 1999), delamination and crustal flow (*Husson and Sempéré*, 2003; *Garzione et al.*, 2006; *Schildgen et al.*, 2007), cratonic under-thrusting (*Lamb and Hoke*, 1997) and erosion (e.g., *Masek et al.*, 1994; *Pope and Willett*, 1998; *Horton*, 1999; *Lamb and Davis,* 2003; *Barnes and Pelletier*, 2006). The magmatic contribution to the crustal thickening is still debated, but the present day active arc in southern Peru represents at least a non negligible contribution to the western Andes Miocene geomorphologic evolution (e.g., *James and Sacks*, 1999; *Mamani et al.*, 2010; *Boekhout et al.*, 2012). Whereas, the Late Miocene arc builds the highest Peruvian summits in the Cordillera Blanca (Cordillera Occidental, northern Peru; *Mukasa*, 1984; *McNulty and Farber*, 2002; *Giovanni*, 2007), no such study has been performed in this region.

The aim of this paper is to time and identify the causes of uplift and exhumation of the northern Peru late Miocene arc. In this area, the Cordillera Blanca batholith (14-5 Ma; *Mukasa*, 1984; *McNulty and Farber*, 2002; *Giovanni*, 2007) builds the footwall of the 200 km

54 long Cordillera Blanca normal fault (CBNF, Fig. 1A; *Bonnot et al.*, 1988) and its exhumation
55 is closely link to the CBNF activity (*Bonnot et al.*, 1988; *Schwartz*, 1988). However, the
56 processes driving the exhumation of the Cordillera Blanca and extension along the CBNF are
57 still debated. The extent to which both magmatism and normal faulting influenced Andean
58 relief development is particularly unclear (e.g. *Margirier et al.*, 2015). *Dalmayrac and*
59 *Molnar* (1981), *Deverchère et al.* (1989) and *Petford and Atherton* (1992) suggested that
60 extension resulted from gravitational collapse of a thickened crust, while *McNulty and Farber*
61 (2002) suggested extension due to the arrival of the Nazca ridge beneath the Cordillera Blanca,
62 increasing temporarily the coupling with the overriding plate. These models focused on the
63 CBNF, and did not explore the emplacement history of the Cordillera Blanca, its recent
64 geomorphological evolution (5-0 Ma) or its present shape. Emplacement depths of the
65 Cordillera Blanca batholith are not well constrained and have never been studied as a whole
66 (*Wise and Noble,* 2003). Its magmatic structure is also uncertain (*Egeler and De Booy*, 1956;
67 *Cobbing et al*., 1981; *Atherton and Sanderson*, 1987; *Petford and Atherton*, 1996). On the
68 basis of metamorphic mineral assemblages in the surrounding basement, the emplacement
69 depth of the batholith is roughly estimated ~9 km (*Petford and Atherton*, 1992; *McNulty et al.*,
70 1998). In this paper, we report new amphibole thermobarometry data to quantify
71 emplacement depths across the batholith. We then estimate the total exhumation of the
72 Cordillera Blanca batholith and the total displacement on the CBNF. Additionally, we
73 constrain the recent evolution of the batholith by modeling erosion rates through time to
74 discuss the passive or active role of the CBNF and/or climate in the Cordillera Blanca
75 exhumation.
76
77 **Geological context**
78 The Cordillera Blanca consists of a young granitic pluton (14-5 Ma; *Mukasa*, 1984; *McNulty*
79 *and Farber*, 2002; *Giovanni*, 2007) emplaced in deformed Jurassic sediments of the Chicama
80 formation (*Atherton and Sanderson*, 1987). The Cordillera Blanca batholith and its associated

81 magmas, the Fortaleza and Yungay ignimbrites, emplaced during the Miocene (*Farrar and*
82 *Noble*, 1976; *Cobbing et al.*, 1981; *Mukasa*, 1984; *Giovanni*, 2007) and correspond to the last
83 magmatic activity in northern Peru (*Petford and Atherton*, 1992). The calc-alkaline
84 composition (high-Na, low HREE, high-Al with garnet residues) of the Cordillera Blanca
85 batholith and associated volcanic rocks differs from typical calc-alkaline magmas (*Atherton*
86 *and Sanderson,* 1987; *Petford and Atherton*, 1996; *Coldwell et al.,* 2011). These magmatic
87 rocks display an adakitic signature indicating a high temperature basaltic melt, i.e., either a
88 source issued from thick underplated crust or from the subducting oceanic slab (*Petford and*
89 *Atherton*, 1996; *Coldwell et al.*, 2011). The present-day data do not enable to decipher
90 between these two sources.
91 The Cordillera Blanca batholith is ~150 km-long and trend parallel to the Andean range (Fig.
92 1A). In the northern and central part, the total width of the batholith is more than 15 km (Fig.
93 1B). In the southern part, the batholith is exposed sporadically within the Chicama
94 sedimentary Formation (*Atherton and Sanderson*, 1987). These sediments, metamorphosed at
95 the contact with the batholith, are still preserved on some summits of the central and northern
96 Cordillera Blanca (Fig. 1B; *Atherton and Sanderson*, 1987; *Wise and Noble*, 2003), indicating
97 that the roof of the batholith is culminating today at ~6000 m (Fig. 1; W*ise and Noble*, 2003).
98 Since emplacement, the Cordillera Blanca batholith has been exhumed to reach 6000 m and to
99 build the highest Peruvian summit. Recent low-temperature thermochronologic data suggest
100 rapid (250°C/Ma) magmatic cooling of the batholith until 4 Ma and its subsequent
101 exhumation (~1 mm/yr) between 4 and 0 Ma (*Margirier et al.*, 2015). This last stage is
102 closely linked to the CBNF. The CBNF is a crustal scale extensional structure characterized
103 by ~1000 m-high triangular facets and is responsible for a vertical relief over 4000 m: this
104 fault shows at least 4500 m of vertical displacement since ~5.4 Ma (*Bonnot*, 1984; *Giovanni*,
105 2007). Based on TCN dating of the main scarp, *Siame et al.* (2006) estimate a vertical slip-
106 rate of 3±1 mm/yr, on the Central part of the CBNF, for the last 3000 years. *Giovanni* (2007),
107 *Hodson* (2012) and *Margirier et al.* (2015) estimated exhumation rate at ~2 mm/yr, >1

mm/yr and ~1 mm/yr respectively on the central part of the CBNF for the last 3 Myrs based on low-temperature thermochronologic data. Triangular facets located in the northern and central part of the Cordillera Blanca and the height of recent scarps decreasing southward suggest lower exhumation rates in the southern part of the Cordillera Blanca.

West of the Cordillera Blanca, The Callejon de Huaylas, an elongated range-parallel intra-mountain basin (150 km long), separates the Cordillera Blanca and the Cordillera Negra. The first stratified series filling in this intra-mountain basin recorded its first episodes of tectonic subsidence associated to the CBNF initiation with some ignimbrites dated at 5.4 ± 0.1 Ma (*Giovanni*, 2007; *Giovanni et al.*, 2010).

The Cordillera Negra builds the hanging-wall of the CBNF. This range consists of Cretaceous and Paleogene plutons (73-48 Ma; (*Mukasa and Tilton*, 1984; *Beckinsale et al.*, 1985) intruded in the Chicama Formation. Neogene volcano-sedimentary deposits capped the older formations in its southern part. *Margirier et al.* (2015) suggested that the Cordillera Negra has been uplifted and eroded (~0.3 mm/yr) during the last 15 Ma.

Glacial valleys morphology in the Cordillera Blanca

Past Quaternary glaciations had a strong imprint on the Cordillera Blanca landscape (*Clapperton*, 1983; *Rodbell*, 1993). *Farber et al.* (2005) and *Smith et al.* (2005) suggested extensive pre Late Glacial Maximum (pre-LGM) glaciation in the Cordillera Blanca and Junin basins. Conspicuous geomorphic glacial features such as U-shaped valleys are observed on the western flank of the Cordillera Blanca batholith (Fig. 1C). Several relicts of moraines and some striated roches moutonnées can also be found on the flanks and outlet of these valleys (Fig. 1B and 1C).

The Cordillera Blanca relief is directly linked to the depth of the valleys carving of the batholith. The relief (relief = max alt - min alt in a given specific area) is approximated with swath profiles of ~10 km and ~30 km width (Fig. 2). On Figure 2, the distance between the blue and the green lines represents an approximation of the local relief. The maximum relief

is located in the central and northern part of the Cordillera Blanca (~3 km; Fig. 2). Most of the 6000 m high summits are located in the northern and central part of the Cordillera Blanca, reaching a maximum in central part (Fig. 2B). Even if the mean elevation of the southern part of the Cordillera Blanca is higher than in the northern part, relief is lower (~1 km; Fig. 2). In the central and northern part of the Cordillera Blanca the large relief (~3 km) suggests substantial valley carving due to glacial erosion. In the southern part, lower relief suggests less glacial erosion. Relief and maximum elevation are also larger on the western flank (~3 km, 6500 m) than in the eastern flank (~2 km, 6000 m) in the central part of the Cordillera Blanca indicating more incision in the western flank (Fig. 2C, D, E).

Methods

Amphibole thermobarometry

Amphibole thermobarometry has been widely used to estimate both the emplacement pressure and temperature of calc-alkaline igneous rocks (e.g., *Costa et al.*, 2013; *Turner et al.*, 2013; *Brenna et al.*, 2014; *Leuthold et al.*, 2014). In this study, we applied the thermobarometer (RR2012) introduced by *Ridolfi and Renzulli* (2012), which is calibrated for calc-alkaline and alkaline igneous rocks. This thermobarometer takes in account clinoamphibole composition in Si, Ti, Al, Fe, Mn, Mg, Ca, Na and K to calculate pressure and temperature conditions during pluton emplacement. A chemical trend is classically observed for the clinoamphibole with the most Si-depleted composition (ferropargasite or ferrotschermakite endmembers according to the $(Na+K)_A$ value), which are characterized by high-Fe contents, whereas Si-enriched amphiboles (magnesiohornblende or edenite) are characterized by elevated Mg contents (Fig. 3).

Chemical data collected on magmatic amphiboles were filtered on the base of pressure-related "apparent percentage error" (APE) values calculated with the RR2012 thermo-barometric method. Following recommendations by the authors, we fixed a maximum of 50 for the APE to retain or exclude the data for pressure and temperature calculations (first filter: moderate

confidence level). We also applied a second filter (high-confidence level) to exclude amphiboles whose chemistry did not match the dedicated range of chemical composition and structural formulae.

It is also worth pointing that the amphibole barometer of *Ridolfi and Renzulli* (2012) has been under scrutiny recently (e.g., *Walker et al.*, 2012; *Shane and Smith*, 2013; *Erdmann et al.*, 2014; *Kiss et al.*, 2014). Some authors have proposed that the estimated pressures are very sensitive to variations in melt composition (*De Angelis et al.*, 2013; *Shane and Smith*, 2013; *Erdmann et al.*, 2014). However, *Putirka* (2014) showed that it gives a satisfactory results when compared to experimental results from a broad range of starting compositions (basalt to rhyolite) and pressures (200-800 MPa). In situ major element abundances were measured on thin section with an electron microprobe JEOL JXA-8230 at ISTerre (Grenoble), operating condition were 15 kV and 12 nA.

Crystallization ages and high temperature thermochronology ages

We compile data from the Cordillera Blanca batholith for geochronometers and high temperature (>300°C) thermochronometers: zircon U-Pb, hornblende K-Ar, hornblende Ar-Ar, muscovite and biotite Rb-Sr, muscovite and biotite K-Ar / Ar-Ar, matrice K-Ar which have closures temperature ranging from 800°C to 300°C (*Giletti and Day*, 1968; *Stewart et al.*, 1974; *Wilson*, 1975; *Cobbing et al.*, 1981; *Mukasa*, 1984; *Beckinsale et al.*, 1985; *Giovanni*, 2007). These geochronometers provide crystallization and cooling ages. They enable us to quantify both the chronology and the dynamics of the batholith emplacement in the crust.

Inversion of the thermochronologic data

We formally invert the extensive set of thermochronometric (zircon (U-Th)/He, apatite fission-track and (U-Th)/He; *Montario*, 2001; *Wipf*, 2006; *Giovanni*, 2007; *Hodson*, 2012; *Michalak*, 2013; *Margirier et al.*, 2015) to quantitatively estimate the erosion history, using

188 data shown in Figure 1A. We used the method proposed by *Fox et al.* (2014) and modified by
189 *Herman and Brandon* (2015). This procedure involves a weakly non-linear least-squares
190 inversion and allows efficient treatment of a large number of spatially distributed data. This
191 method exploits the information contained in both age-elevation profiles and multi-
192 thermochronometric systems strategies.
193 In this approach, several parameters must be tested to ensure that the inferred exhumation
194 rates are robust. We refer the reader to *Fox et al.* (2014) for an in-depth discussion on each of
195 these parameters. First, the depth to the closure temperature is expressed as the integral of
196 erosion rate from the thermochronometric age to present-day. The integral is discretized in a
197 series of fixed time-steps (Δt), which must be selected. Second, the depth of the closure
198 isotherms is calculated using a 1-dimensional thermal model that includes a correction for the
199 effects of topography its underlying thermal field. We tested the impact of the thermal model
200 by changing the bottom boundary conditions (T). Third, the method assumes that the samples
201 are spatially correlated through a correlation function that includes a variance (σ). Finally, the
202 calculated exhumation rates represent a deviation from an a priori exhumation ($\dot{e}_{pr}$) rate that is
203 updated to posterior exhumation rates.
204 We show in Figure 4 that changing Δt, T and $\dot{e}_{pr}$ assess its impact on the estimated
205 exhumation patterns. The solution is shown at two selected locations on either side of the
206 fault.
207
208 **Results**
209 *Thermobarometry in the Cordillera Blanca batholith*
210 The amphiboles chemistry from the Cordillera Blanca batholith is very similar to the
211 calibration of *Ridolfi and Renzulli* (2012) paper. Amphibole crystals are not abundant in the
212 Cordillera Blanca batholith; only 5 of our 20 samples contain amphiboles. We performed
213 microprobe analysis on at least 3 amphiboles by sample (Fig. 5 and Table 1 in the

supplemental files). After the application of the two filters of the RR2012 method, we discarded ~15 % of the calcic-amphiboles.

Estimated emplacement pressure range from 1.2 ± 0.1 to 2.3 ± 0.3 kbar, at a temperature range from 725°C to 777°C (Table 1 and Fig. 5). Calculated depths (using an average rock density of 2.7 g/cm^3) indicate that the Cordillera Blanca batholith emplaced at shallow crustal level, i.e. between 3.1 and 6.3 km. Pressure estimations vary spatially along and across the batholith. Pressures are greater close to the CBNF (South-West; 2.3 ± 0.3 kbar) and decrease toward the North-East (1.2 ± 0.1 kbar) (Fig. 6B). Moreover, along the CBNF, the estimated emplacement pressures of the batholith decrease toward the South (Fig. 6B).

Crystallization and cooling ages

Crystallization and cooling ages (Tc > 300°C) range from 30 ± 0.0 to 3.3 ± 1.2 Ma in the Cordillera Blanca batholith (Fig. 6A). Some muscovite Rb-Sr and zircon U-Pb ages are significantly older than other published ages in the same area, which makes it difficult to quantify the crystallization and cooling of the Cordillera Blanca batholith. *Giovanni* (2010) proposed that ages >25 Ma may correspond to zircon recycling. Thus, we exclude these ages for our interpretation.

Along strike, ages are younger in the central and northern part of the Cordillera Blanca batholith (4-7 Ma), and older (~14 Ma) in the southern tip of the granite. Across strike crystallization ages increase away from the CBNF, in the central part of the batholith (Fig. 6A and 6C). The spatial distribution of young emplacement ages corresponds to high-pressure crystallization conditions of the batholith (Fig. 6) and both criteria are found where the granitic outcrop is the thickest (i.e. western flank of the central and northern parts of the batholith).

Inversion of thermochronologic data

Modeling of thermochronologic ages from northern Peru reveals space-time variations in erosion rates over the past 20 Ma. Modeled erosion rates are much higher in the Cordillera Blanca (x5) than in the Cordillera Negra for the last 6 Ma. Erosion rates are higher in the Central part of the Cordillera Blanca than in the southern and the northern tip of the batholith, where the granite is still caped by the sedimentary country rocks (Fig. 1).

Our most striking result is that exhumation rates increase over the past 5 Myrs with a small acceleration at ~5 Ma in the southern part of the Cordillera Blanca followed by a strong acceleration of exhumation rates over the past 2 Myrs. In the Cordillera Blanca erosion rates increase from ~0.25 mm/yr, between 6 and 4 Ma, to ~1 mm/yr, between 2 and 0 Ma, where young ages are observed. In the Cordillera Negra and in the Marañon region, results indicate a mean erosion rate of 0.2 mm/yr for the last 30 Ma.

Discussion

Emplacement depth and magmatic structure of the Cordillera Blanca batholith

Thermobarometry data suggest emplacement of the Cordillera Blanca batholith between 1.2 ± 0.1 and 2.3 ± 0.3 kbar. These pressures indicate that the roof of the Cordillera Blanca batholith was emplaced at ~1 kbar (close to the sediments in the eastern and southern part of the Cordillera Blanca). In contrast, in the central part of the Cordillera Blanca, in the vicinity of the fault, pressure is greater and reaches 2.3 ± 0.3 kbar (Fig. 6). The observed pressures are lower than pressure estimates by previous studies (> 2 kbar) based on metamorphic mineral assemblages in the contact metamorphic aureole (*Petford and Atherton*, 1992; *McNulty and Farber*, 2002). They indicate an emplacement at shallow crustal level consistent with the low assimilation of country rocks and the sharp contact (*Petford and Atherton*, 1992). Our amphibole barometry results indicate emplacement depths ranging from 3.1 to 6.3 km. Our results also indicate that the granite was emplaced at greater depth close to the CBNF, suggesting more exhumation in the vicinity of the fault and a tilting of ~15° of the Cordillera Blanca batholith since its emplacement (eq. 1, Fig. 8):

$$\alpha = \tan^{-1}\left(\frac{6.3-3.1}{15}\right) \approx 15° \quad (1)$$

The emplacement depth obtained close to the CBNF (6.3 km) indicates that there is at least ~6 km of vertical displacement on the CBNF assuming a regional mean elevation of ~4000 m during the batholith emplacement. *Giovanni et al.* (2010) proposed a stratigraphic column of the Lloclla formation, its thickness indicates at least 1300 m of basin subsidence since 5.4 Ma (*Giovanni et al.*, 2010). Using a 40° dipping fault plane, these vertical offsets correspond to a displacement of ~11.4 km on the CBNF coherent with previous estimations from *Wise and Noble* (2003). The shallow emplacement of the batholith (3.1 km) questions the use of high temperature thermochronometers to quantify exhumation rates in the Cordillera Blanca.

Our compilation of crystallization ages and high temperature thermochronologic data indicates that cooling ages are younger close to the CBNF, and where the exhumation of the granite is stronger (central part of the Cordillera Blanca). *Petford and Atherton* (1992) already showed this trend and suggested three hypotheses: (a) they are due to magmatism migration toward the east, or (b) there is a heating/slow cooling close to the fault or (c) there is argon loss is the deformed zone. Instead, our data suggest that this trend arises from the variations in the chronology and depth emplacement of the batholith, recorded by series of sills. First, the magma crystallized at shallow crustal depth and then the following magmas emplaced as sills below the first one (Fig. 8). Large intrusions usually emplaced as a succession of sills as the Torres del Paine, the Cho Oyu, the Everest and the Sierra Nevada batholith in the American Cordilleras or Himalaya (e.g., *Sisson et al.*, 1996; *Searle*, 1999; *Leuthold et al.*, 2012). Afterward the Cordillera Blanca have been tilted toward the east exhuming younger rocks that have crystallized deeper close to the CBNF (Fig. 8).

Exhumation of the Cordillera Blanca along the CBNF

The exhumation rates obtained for the Cordillera Blanca are in the same order of magnitude than those obtained by *Giovanni* (2007), *Hodson* (2012) and *Margirier et al.* (2015) for the

293 last 3 Myrs and *Schwartz* (1988) on a more recent time scale (3000 yrs). Our results also
294 suggest an increase of erosion rate during the last 2 Ma in agreement with *Giovanni* (2007).
295 The emplacement of the Cordillera Blanca at shallow crustal levels and the erosion rate
296 modeling through time indicate that the Cordillera Blanca exhumation is delayed compared to
297 the batholith emplacement (emplacement at 9-4 Ma, exhumation at 5-0 Ma; Figs. 6 and 7).
298 Based on the late erosion rate increase and in agreement with *Giovanni et al.* (2010) we
299 suggest that the Cordillera Blanca exhumation is not driven by the batholith emplacement as
300 previously proposed by *Petford and Atherton* (1992).
301 Provenance analysis and WNW paleocurrent directions recorded the first erosion of the
302 Cordillera Blanca granite marking its surface outcrop in the southern part of the Cordillera
303 Blanca batholith at 6.4 Ma (*Bonnot*, 1984; *Giovanni*, 2007). It suggests, in agreement with our
304 data, that the exhumation initiated in the southern part of the Cordillera Blanca and then
305 propagated northwards (Fig. 7). We propose that the erosion increase from 5 Ma in the
306 southern part of the Cordillera Blanca is related to the initiation of the CBNF at ~5.4 Ma and
307 consequent relief building (*Bonnot*, 1984; *Giovanni et al.*, 2010). The presence of granitic
308 polished clasts in the fluvio-glacial LLoclla formation signs Pliocene glacial erosion of the
309 Cordillera Blanca (*Bonnot*, 1984). Moreover, the central part of the Cordillera Blanca exhibits
310 the most conspicuous glacial features (cf: depth of glacial valleys), corresponding to the
311 higher erosion rate from 2 Ma (Fig. 7). The rapid increase of the erosion rates over the past 2
312 Ma could correspond to the glacial valley carving since 1.4 Myrs (Fig. 7; *Smith et al.*, 2005).
313 In addition, there is a possibility that the late increase in erosion rate was related to a change
314 in the regional base level related to the Cañon del Pato incision in the northern part of the
315 Callejon de Huaylas. Considering that the higher erosion rates are located in the central part
316 of the Cordillera Blanca that is not yet reach by headwards erosion of the Rio Santa (Fig. 7),
317 we favor the glacial erosion to explain the late increase of erosion rates in the Cordillera
318 Blanca in agreement with global analysis (*Peizhen et al.*, 2001; *Herman et al.*, 2013).
319

Conclusions

Emplacement age compilation indicates that the Cordillera Blanca batholith emplaced from 14 to 5 Ma. This first compilation evidence a trend in crystallization ages with the younger ages (~5 Ma) located in the Central part of the Cordillera Blanca, close to the CBNF. Additionally, we present the first thermobarometry data from the Cordillera Blanca batholith. These new data show a shallow emplacement of the magma in the crust (~3 km) and indicates that the batholith crystalized at greater pressure close to the CBNF (~6 km). Based on these data we propose that the batholith emplaced in successive sills from 9 to 4 Ma and have been tilted after ~5 Ma. The inversion of the thermochronological data points out an increase of the erosion rate in the Cordillera Blanca during the Quaternary (~0.2 km/Ma at 6 Ma to ~1 km/Ma at 2 Ma). The higher predicted erosion rate correlates with area of higher relief (northern and central part of the Cordillera Blanca). This suggests that valley carving and glaciations had a strong impact on the late stage of the Cordillera Blanca exhumation (2-0 Ma). The presence of a crustal-scale normal fault and high recent erosion rates permit to exhume younger rocks emplaced deeper close to the CBNF. Finally, our data suggest that the Miocene magmatic arc does not directly contribute to major crustal thickening nor to regional surface uplift and exhumation in northern Peru.

Recent tectonic and geomorphology contributions to the understanding of orogen-scale processes demonstrate the coupling of deformation and erosion in mountain ranges building (e.g., *Horton*, 1999; *Montgomery et al.,* 2001; *Whipple and Meade*, 2004). However, displacements on crustal-scale normal faults have been considerably larger in the Himalayas for example (e.g., *Pêcher*, 1991; *Brunel et al.*, 1994, *Searle et al.*, 2006, *Kali et al.*, 2010, *Thiede et al.*, 2013), whereas there is no evidence of large-scale extension in the Central Andes except in the Cordillera Blanca region (e.g., *Dalmayrac and Molnar*, 1981; *Bonnot*, 1984; *McNulty et al.*, 2002), which also includes the highest Peruvian peaks. The Cordillera Blanca batholith emplacement depth revealed a displacement of ~11 km on the CBNF for the last 5 Ma. The presence of the batholith localized the deformation and focused the > 5000 m

347 relief building. Moreover, consecutive glacial erosion of the Miocene arc contributes to its
348 recent exhumation and also possibly accelerated the relief building.
349
350 **References**

351 Atherton, M. P., and L. M. Sanderson (1987), The Cordillera Blanca Batholith: a study of
352 granite intrusion and the relation of crustal thickening to peraluminosity, *Geologische*
353 *Rundschau*, *76*(1), 213–232.

354 Barnes, J. B., and J. D. Pelletier (2006), Latitudinal variation of denudation in the evolution of
355 the Bolivian Andes, *American Journal of Science*, *306*, 1–31.

356 Beckinsale, R. D., A. W. Sanchez-Fernandez, M. Brook, E. J. Cobbing, W. P. Taylor, and N.
357 B. Moore (1985), Rb-Sr whole rock isochron and K-Ar determination for the Coastal
358 Batholith of Peru, in *Magmatism at a Plate Edge: The Peruvian Andes*, edited by W. S.
359 Pitcher, M. P. Atherton, E. J. Cobbing, and R. D. Beckinsale, pp. 177–202, Blackie
360 Halstead press, Glasgow.

361 Boekhout, F., R. Spikings, T. Sempere, M. Chiaradia, A. Ulianov, and U. Schaltegger (2012),
362 Mesozoic arc magmatism along the southern Peruvian margin during Gondwana breakup
363 and dispersal, *Lithos*, *146-147*(C), 48–64, doi:10.1016/j.lithos.2012.04.015.

364 Bonnot, D. (1984), Néotectonique et tectonique active de la Cordillère Blanche et du Callejon
365 de Huaylas (Andes nord-péruviennes), *Thèse présentée pour obtenir le grade de docteur,*
366 *Université de Paris-Sud, Centre d'Orsay*, 1–202.

367 Bonnot, D., M. Sébrier, and J. Mercier (1988), Évolution géodynamique plio-quaternaire du
368 bassin intra-cordillérain du Callejon de Huaylas et de la Cordillère Blanche, Pérou,
369 *Géodynamique*, *3*(1-2), 57–83.

370 Brenna, M., R. Price, S. J. Cronin, I. E. M. Smith, Y. K. Sohn, G. B. Kim, and R. Maas

(2014), Final Magma Storage Depth Modulation of Explosivity and Trachyte-Phonolite Genesis at an Intraplate Volcano: a Case Study from Ulleung Island, South Korea, *Journal of Petrology*, *55*(4), 709–747, doi:10.1093/petrology/egu004.

Brunel, M., N. Arnaud, P. Tapponnier, Y. Pan, and Y. Wang (1994), Kongur Shan normal fault: Type example of mountain building assisted by extension (Karakoram fault, eastern Pamir), *Geology*, 22(8), 707–710.

Clapperton, C. M. (1983), The glaciation of the Andes, *Quaternary Science Reviews*, *2*, 83–155.

Cobbing, E. J. (1981), *The Coastal Batholith and other aspects of Andean magmatism in Peru*, British geological survey, Keyworth, Nottinglham NG12 5GG, UK.

Cobbing, J., W. Pitcher, J. Baldock, W. Taylor, W. McCourt, and N. J. Snelling (1981), Estudio geológico de la Cordillera Occidental del norte del Perú, *Instituto Geologico Minero y Metalurgico, Serie D. Estudios Especiales*, *10*(D), 1–252.

Coldwell, B., J. Clemens, and N. Petford (2011), Deep crustal melting in the Peruvian Andes: Felsic magma generation during delamination and uplift, *Lithos*, *125*(1-2), 272–286, doi:10.1016/j.lithos.2011.02.011.

Costa, F., S. Andreastuti, C. B. de Maisonneuve, and J. S. Pallister (2013), Journal of Volcanology and Geothermal Research, *Journal of Volcanology and Geothermal Research*, *261*(C), 209–235, doi:10.1016/j.jvolgeores.2012.12.025.

Dalmayrac, B., and P. Molnar (1981), Parallel thrust and normal faulting in peru and constraints on the state of stress, *Earth and Planetary Sciences Letters*, *55*, 473–481.

De Angelis, S. H., J. Larsen, and M. Coombs (2013), Pre-eruptive Magmatic Conditions at Augustine Volcano, Alaska, 2006: Evidence from Amphibole Geochemistry and Textures,

394 *Journal of Petrology*, *54*(9), 1939–1961, doi:10.1093/petrology/egt037.

395 Deverchère, J., C. Dorbath, and L. Dorbath (1989), Extension related to a high topography:
396 results from a microearthquake survey in the Andes of Peru and tectonic implications,
397 *Geophysical Journal International*, *98*(2), 281–292.

398 Egeler, C. G., and T. De Booy (1956), Geology and petrology of part of the southern
399 Cordillera Blanca, Peru, *Koninklijk Nederlands Geologisch Mijnbouwkundig*
400 *Genootschap*, 1–1.

401 Erdmann, S., C. Martel, M. Pichavant and A. Kushnir (2014), Amphibole as an archivist of
402 magmatic crystallization conditions: problems, potential, and implications for inferring
403 magma storage prior to the paroxysmal 2010 eruption of Mount Merapi, Indonesia,
404 *Contributions to Mineral Petrol*, doi:10.1007/s00410-014-1016-4.

405 Farber, D. L., G. S. Hancock, R. C. Finkel, and D. T. Rodbell (2005), The age and extent of
406 tropical alpine glaciation in the Cordillera Blanca, Peru, *J. Quaternary Sci.*, *20*(7-8), 759–
407 776, doi:10.1002/jqs.994.

408 Farrar, E., and D. C. Noble (1976), Timing of late Tertiary deformation in the Andes of Peru,
409 *Geological Society of America Bulletin*, *87*(9), 1247–1250.

410 Fox, M., F. Herman, S. D. Willett, and D. A. May (2014), A linear inversion method to infer
411 exhumation rates in space and time from thermochronometric data, *Earth Surf. Dynam.*,
412 *2*(1), 47–65, doi:10.5194/esurf-2-47-2014.

413 Garver, J. I., P. W. Reiners, L. J. Walker, J. M. Ramage, and S. E. Perry (2005), Implications
414 for Timing of Andean Uplift from Thermal Resetting of Radiation-Damaged Zircon in the
415 Cordillera Huayhuash, Northern Peru, *The Journal of Geology*, *113*(2), 117–138,
416 doi:10.1086/427664.

417 Garzione, C. N., P. Molnar, J. C. Libarkin, and B. J. MacFadden (2006), Rapid late Miocene
418 rise of the Bolivian Altiplano: Evidence for removal of mantle lithosphere, *Earth and*
419 *Planetary Science letters*, *241*(3-4), 543–556, doi:10.1016/j.epsl.2005.11.026.

420 Gephart, J. W. (1994), Topography and subduction geometry in the central Andes: Clues to
421 the mechanics of a noncollisional orogen, *Journal of Geophysical Research: Solid Earth*,
422 *99*(B6), 12279–12288.

423 Giletti, B. J., and H. W. Day (1968), Potassium–Argon Ages of Igneous Intrusive Rocks in
424 Peru, *Nature*, *220*(5167), 570–572, doi:10.1038/220570a0.

425 Giovanni, M. K. (2007), Tectonic and Thermal Evolution of the Cordillera Blanca
426 Detachment System, Peruvian Andes: Implication for Normal Faulting in a
427 Contractionnal Orogen, 1–255 pp. University of California, Los Angeles.

428 Giovanni, M. K., B. K. Horton, C. N. Garzione, B. McNulty, and M. Grove (2010),
429 Extensional basin evolution in the Cordillera Blanca, Peru: Stratigraphic and isotopic
430 records of detachment faulting and orogenic collapse in the Andean hinterland, *Tectonics*,
431 *29*(6), TC6007, doi:10.1029/2010TC002666.

432 Herman, F., and M. T. Brandon (2015), Mid-latitude glacial erosion hotspot related to
433 equatorial shifts in southern Westerlies, *Geology*, 1–4. doi:10.1130/G37008.1

434 Herman, F., D. Seward, P. G. Valla, A. Carter, and B. Kohn (2013), Worldwide acceleration
435 of mountain erosion under a cooling climate, Nature, doi:10.1038/nature12877.

436 Hodson, K. R. (2012), Morphology, exhumation, and Holocene erosion rates from a tropical
437 glaciated mountain range: the Cordillera Blanca, Peru, *McGill University Masters of*
438 *science*, 1–94.

439 Horton, B. K. (1999), Erosional control on the geometry and kinematics of thrust belt

development in the central Andes, *Tectonics*, *18*(6), 1292–1304, doi:10.1029/1999TC900051.

Husson, L., and T. Sempéré (2003), Thickening the Altiplano crust by gravity-driven crustal channel flow, *Geophys. Res. Lett.*, *30*(5), 1243, doi:10.1029/2002GL016877.

Isacks, B. L. (1988), Uplift of the central Andean plateau and bending of the Bolivian orocline, *Journal of Geophysical Research: Solid Earth (1978–2012)*, *93*(B4), 3211–3231.

James, D. E. (1971), Plate tectonic model for the evolution of the Central Andes, *Geological Society of America Bulletin, 82*, 3325-3346.

James, D. E., and I. S. Sacks (1999), Cenozoic formation of the Central Andes: a geophysical perspective, in *Geology and ore deposits of the Central Andes*, vol. 7, edited by B. J. skinner, Society of Economic Geologists.

James, D. E., and J. A. Snoke (1994), Structure and tectonics in the region of flat subduction beneath central Peru: Crust and uppermost mantle, *Journal of Geophysical Research, 99*(B4), 6899-6912.

Jordan, T. E., B. L. Isacks, R. W. Allmendinger, J. A. Brewer, V. A. Ramos, and C. J. Ando (1983), Andean tectonics related to geometry of subducted Nazca plate, *Geological Study of America Bulletin*, *94*, 341–361.

Kali, E., P. H. Leloup, N. Arnaud, G. Mahéo, D. Liu, E. Boutonnet, J. Van Der Woerd, X. Liu, J. Liu-Zeng, and H. Li (2010), Exhumation history of the deepest central Himalayan rocks, Ama Drime range: Key pressure-temperature-deformation-time constraints on orogenic models, *Tectonics*, 29(2), 1-31, doi:10.1029/2009TC002551.

Kiss, B., S. Harangi, T. Ntaflos, P. R. D. Mason, and E. Pál-Molnár (2014), Amphibole perspective to unravel pre-eruptive processes and conditions in volcanic plumbing

463 systems beneath intermediate arc volcanoes: a case study from Ciomadul volcano (SE
464 Carpathians), *Contrib Mineral Petrol*, *167*(3), 1–27, doi:10.1007/s00410-014-0986-6.

465 Kley, J., and C. R. Monaldi (1998), Tectonic shortening and crustal thickness in the Central
466 Andes: How good is the correlation? *Geology*, *26*(8), 723–726.

467 Kley, J., C. R. Monaldi, and J. A. Salfity (1999), Along-strike segmentation of the Andean
468 foreland: causes and consequences, *Tectonophysics*, *301*(1), 75–94.

469 Kono, M., Y. Fukao, and A. Yamamoto (1989), Mountain building in the Central Andes,
470 *Journal of Geophysical Research,* 94(B4), 3891-3905.

471 Lamb, S., and L. Hoke (1997), Origin of the high plateau in the Central Andes, Bolivia, South
472 America, *Tectonics, 16*(4), 623-649.

473 Lamb, S., and P. Davis (2003), Cenozoic climate change as a possible cause for the rise of the
474 Andes, *Nature*, *425*(6960), 792–797.

475 Leuthold, J., O. Muntener, L. P. Baumgartner, and B. Putlitz (2014), Petrological Constraints
476 on the Recycling of Mafic Crystal Mushes and Intrusion of Braided Sills in the Torres del
477 Paine Mafic Complex (Patagonia), *Journal of Petrology*, *55*(5), 917–949,
478 doi:10.1093/petrology/egu011.

479 Leuthold, J., O. Müntener, L. P. Baumgartner, B. Putlitz, M. Ovtcharova, and U. Schaltegger
480 (2012), Time resolved construction of a bimodal laccolith (Torres del Paine, Patagonia),
481 *Earth and Planetary Science letters*, *325-326*(C), 85–92, doi:10.1016/j.epsl.2012.01.032.

482 Mamani, M., G. Wörner, and T. Sempere (2010), Geochemical variations in igneous rocks of
483 the Central Andean orocline (13 S to 18 S): Tracing crustal thickening and magma
484 generation through time and space, *Geological Society of America Bulletin*, *122*(1-2),
485 162–182, doi:10.1130/B26538.1.

Margirier, A., X. Robert, L. Audin, C. Gautheron, M. Bernet, S. Hall, and T. Simon-Labric (2015), Slab flattening, magmatism and surface uplift in the Cordillera Occidental (northern Peru), *Geology*, 1–4, doi:10.1130/G37061.1.

Masek, J. G., B. L. Isacks, and T. L. Gubbels (1994), Erosion and tectonics at the margins of continental plateaus, *Journal of Geophysical Research, 99*(B7), 13,941-13,956.

McNulty, B. A., and D. L. Farber (2002), Active detachment faulting above the Peruvian flat slab, *Geology*, *30*(6), 567–570.

McNulty, B. A., D. L. Farber, G. S. Wallace, R. Lopez, and O. Palacios (1998), Role of plate kinematics and plate-slip-vector partitioning in continental magmatic arcs: Evidence from the Cordillera Blanca, Peru, *Geology*, *26*(9), 827–830.

McQuarrie, N. (2002), The kinematic history of the central Andean fold-thrust belt, Bolivia: Implications for building a high plateau, *Geological Society of America Bulletin*, *114*(8), 950–963.

Michalak, M. (2013), Exhumation of the Peruvian Andes; insight from mineral chronometers,, 1–177 pp. University of California, Santa Cruz.

Montario, M. J. (2001), Exhumation of the Cordillera Blanca, NorthernPeru, based on apatite fission track analysis, *Departement of Geology, Unpublished Thesis, Union Colllege, Schenectady, New York*, 1–12.

Montario, M. J. (2006), Thermochronological evidence for Neogene incision of the Rio Pativilca Canyon, Northern Peru, 1–214 pp. University at Albany, State University of New York.

Montgomery, D. R., G. Balco, and S. D. Willett (2001), Climate, tectonics, and the morphology of the Andes, *Geology*, 29(7), 579–582.

509 Mukasa, S. B. (1984), Comparative Pb isotope systematics and zircon U-Pb geochronology
510 for the Coastal, San Nicolás and Cordillera Blanca Batholiths, Peru, University of
511 California, Santa Barbara, September.

512 Mukasa, S. B., and G. R. Tilton (1984), Lead isotope systematics in batholithic rocks of the
513 western and coastal cordilleras, Peru, in *Andean Magmatism*, Birkhäuser Boston, 180–
514 189.

515 Pêcher, A. (1991), The contact between the Higher Himalaya Crystallines and the Tibetan
516 Sedimentary Series: Miocene large-scale dextral shearing, *Tectonics*, 10(3), 587–598.

517 Peizhen, Z., P. Molnar, and W. R. Downs (2001), Increased sedimentation rates and grain
518 sizes 2–4 Myr ago due to the influence of climate change on erosion rates, *Nature*, *410*,
519 891–897.

520 Petford, N., and M. Atherton (1996), Na-rich partial melts from newly underplated basaltic
521 crust: the Cordillera Blanca Batholith, Peru, *Journal of Petrology*, *37*(6), 1491–1521.

522 Petford, N., and M. P. Atherton (1992), Granitoid emplacement and deformation along a
523 major crustal lineament: the Cordillera Blanca, Peru, *Tectonophysics*, *205*(1), 171–185.

524 Pope, D. C., and S. D. Willett (1998), Thermal-mechanical model for crustal thickening in the
525 central Andes driven by ablative subduction, *Geology*, *26*(6), 511, doi:10.1130/0091-
526 7613(1998)026<0511:TMMFCT>2.3.CO;2.

527 Putirka, K. (2014), Amphibole-liquid equilibria: Barometers and thermometers for volcanic
528 systems, *2014 GSA Annual Meeting in Vancouver*.

529 Ridolfi, F., and A. Renzulli (2012), Calcic amphiboles in calc-alkaline and alkaline magmas:
530 thermobarometric and chemometric empirical equations valid up to 1,130°C and 2.2 GPa,
531 *Contrib Mineral Petrol*, *163*(5), 877–895, doi:10.1007/s00410-011-0704-6.

532 Rodbell, D. T. (1993), Subdivision of late Pleistocene moraines in the Cordillera Blanca, Peru,
533 based on rock-weathering features, soils, and radiocarbon dates, *Quaternary Research*.

534 Schildgen, T. F., K. V. Hodges, K. X. Whipple, P. W. Reiners, and M. S. Pringle (2007),
535 Uplift of the western margin of the Andean plateau revealed from canyon incision history,
536 southern Peru, *Geology*, *35*(6), 523, doi:10.1130/G23532A.1.

537 Schmidt, M. W. (1992), Amphibole composition in tonalite as a function of pressure: an
538 experimental calibration of the Al-in-hornblende barometer, *Contrib Mineral Petrol*.

539 Schwartz, D. P. (1988), Paleoseismicity and neotectonics of the Cordillera Blanca fault zone,
540 northern Peruvian Andes, *J. Geophys. Res.*, *93*(B5), 4712–4730.

541 Searle, M. P. (1999), Emplacement of Himalayan leucogranites by magma injection along
542 giant sill complexes: examples from the Cho Oyu, Gyachung Kang and Everest
543 leucogranites (Nepal Himalaya), *Journal of Asian Earth Sciences*, *17*, 773–783.

544 Searle, M. P., R. D. Law, and M. J. Jessup (2006), Crustal structure, restoration and evolution
545 of the Greater Himalaya in Nepal-South Tibet: implications for channel flow and ductile
546 extrusion of the middle crust, *Geological Society of London*, Special Publications, 268,
547 355–378.

548 Shane, P., and V. C. Smith (2013), Using amphibole crystals to reconstruct magma storage
549 temperatures and pressures for the post-caldera collapse volcanism at Okataina volcano,
550 *Lithos*, *156-159*(C), 159–170, doi:10.1016/j.lithos.2012.11.008.

551 Sisson, T. W., T. L. Grove, and D. S. Coleman (1996), Hornblende gabbro sill complex at
552 Onion Valley, California, and a mixing origin for the Sierra Nevada batholith, *Contrib*
553 *Mineral Petrol*, *126*(1-2), 81–108, doi:10.1007/s004100050237.

554 Smith, J. A., R. C. Finkel, D. L. Farber, D. T. Rodbell, and G. O. Seltzer (2005), Moraine

preservation and boulder erosion in the tropical Andes: interpreting old surface exposure ages in glaciated valleys, *J. Quaternary Sci.*, *20*(7-8), 735–758, doi:10.1002/jqs.981.

Stewart, J. W., J. F. Evernden, and N. J. Snelling (1974), Age determinations from Andean Peru: a reconnaissance survey, *Geological Society of America Bulletin*, *85*(7), 1107–1116.

Thiede, R. C., E. R. Sobel, J. Chen, L. M. Schoenbohm, D. F. Stockli, M. Sudo, and M. R. Strecker (2013), Late Cenozoic extension and crustal doming in the India-Eurasia collision zone: New thermochronologic constraints from the NE Chinese Pamir, *Tectonics*, 32(3), 763–779, doi:10.1002/tect.20050.

Turner, S. J., P. Izbekov, and C. Langmuir (2013), Journal of Volcanology and Geothermal Research, *Journal of Volcanology and Geothermal Research*, 1–14, doi:10.1016/j.jvolgeores.2012.12.014.

Walker, B. A., E. W. Klemetti, A. L. Grunder, J. H. Dilles, F. J. Tepley, and D. Giles (2012), Crystal reaming during the assembly, maturation, and waning of an eleven-million-year crustal magma cycle: thermobarometry of the Aucanquilcha Volcanic Cluster, *Contrib Mineral Petrol*, *165*(4), 663–682, doi:10.1007/s00410-012-0829-2.

Whipple, K. X., and B. J. Meade (2004), Controls on the strength of coupling among climate, erosion, and deformation in two-sided, frictional orogenic wedges at steady state, *J. Geophys. Res.*, 109(F1), 1-24, doi:10.1029/2003JF000019.

Wilson, P. A. (1975), K-Ar age studies in Peru with special reference to the emplacement of the Coastal Batholith, 1–1 pp. University of Liverpool, Liverpool.

Wipf, M. (2006), Evolution of the Western Cordillera and Coastal Margin of Peru: Evidence from low-temperature Thermochronology and Geomorphology, 1–163 pp. Swiss Federal Institute of Technology Zürich, 7 March.

578 Wise, J. M., and D. C. Noble (2003), Geomorphic evolution of the Cordillera Blanca,
579 Northern Peru, *Boletin de la sociedad Geologica del Peru*, *96*, 1–21.

580 Zandt, G., A. A. Velasco, and S. L. Beck (1994), Composition and thickness of the southern
581 Altiplano crust, Bolivia, *Geology*.

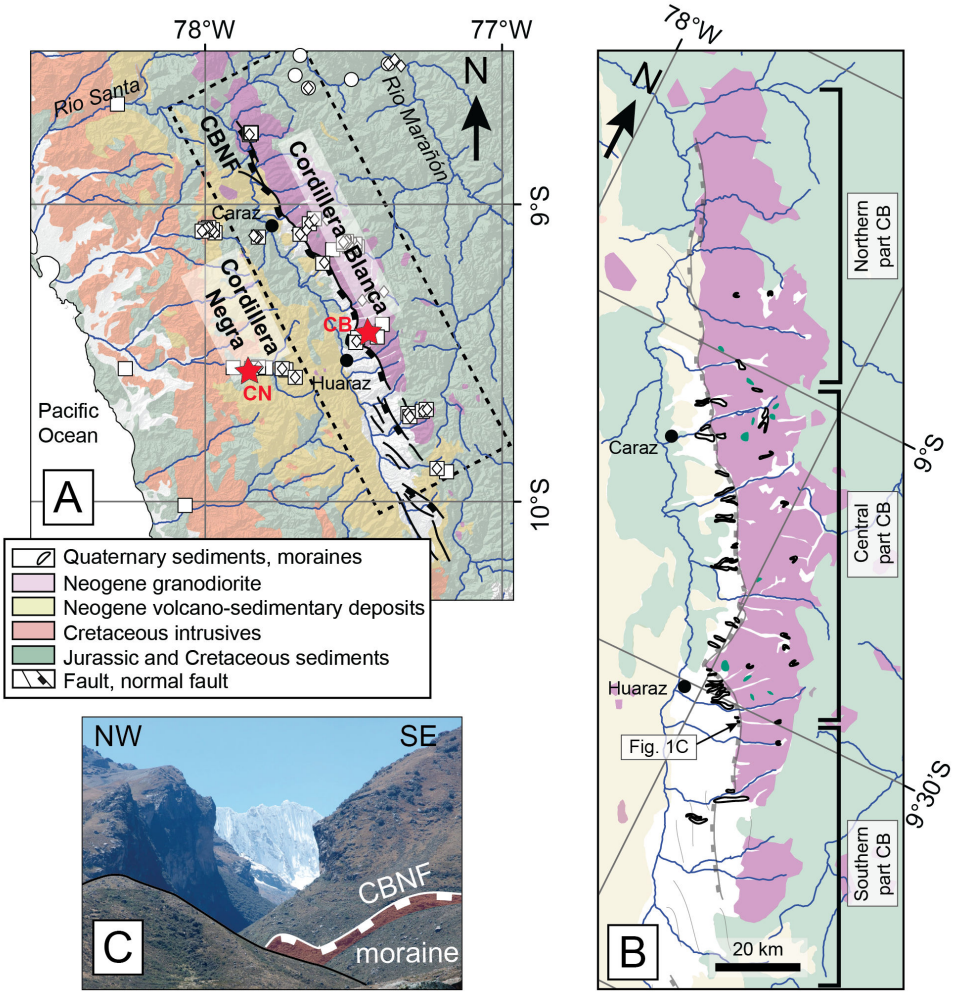

Figure 1: Geology of the Cordillera Blanca region. A) Geological map of the Cordillera Occidental (northern Peru; modified from INGEMMET geologic map of Ancash; INGEMMET, 1999) showing location of low-temperature thermochronological data (white circles: zircon (U-Th)/He data; squares: apatite fission-track; diamonds: (U-Th)/He data; *Montario*, 2001; *Wipf*, 2006; *Giovanni*, 2007; *Hodson*, 2012; *Michalak*, 2013; *Margirier et al.*, 2015). Red stars point out the locations (CB and CN) of the tests of parameters for the inversion of thermochronologic data. B) Simplified geological map of the Cordillera Blanca showing the batholith (pink), the contact between the batholith and Jurassic sediments (green), the CBNF (grey) and the main moraines (black). C) Photograph of the outlet of a U-shaped glacial valley (Quebrada Shallap).

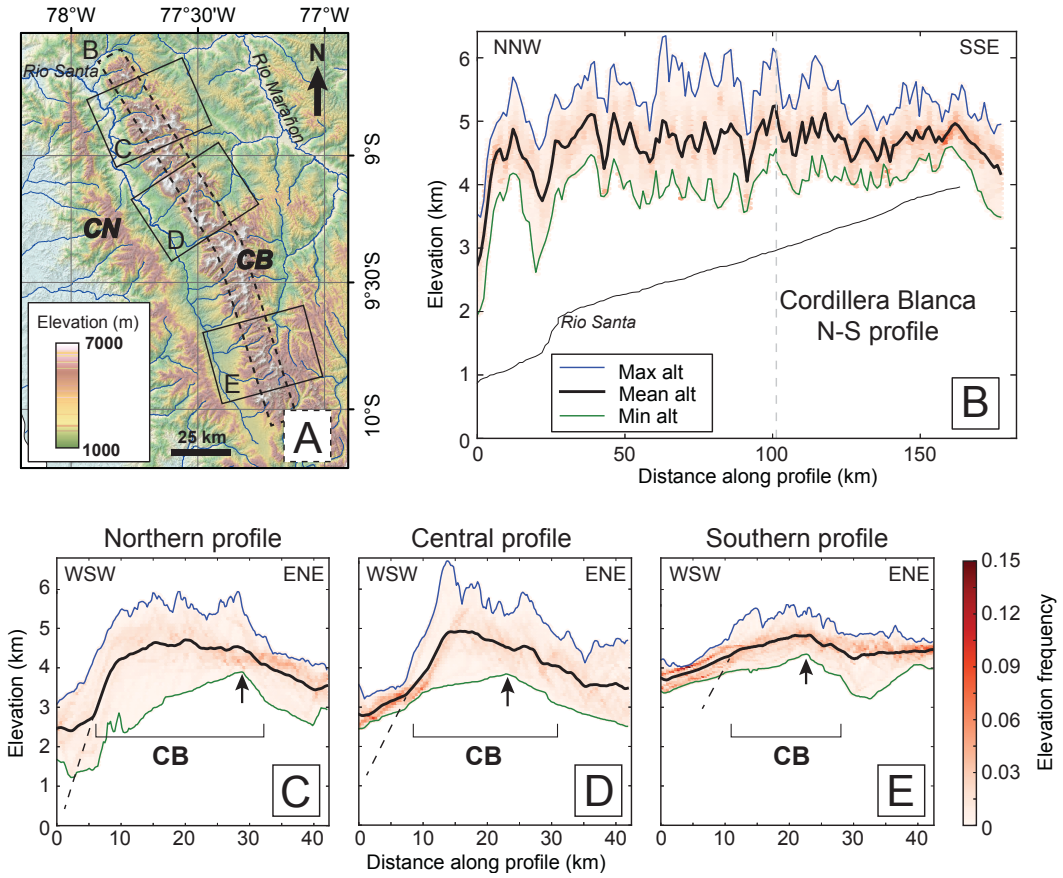

593

594 Figure 2: Elevation and relief of the Cordillera Blanca. A) Topographic map showing the
595 Cordillera Blanca (CB), the Cordillera Negra (CN) and the location of the profiles. B)
596 Cordillera Blanca N-S profile (profile width ~10 km) and C-E) E-W profiles in the northern,
597 central and southern part of the Cordillera Blanc showing the maximum, mean and minimum
598 elevation (profiles width ~30 km).

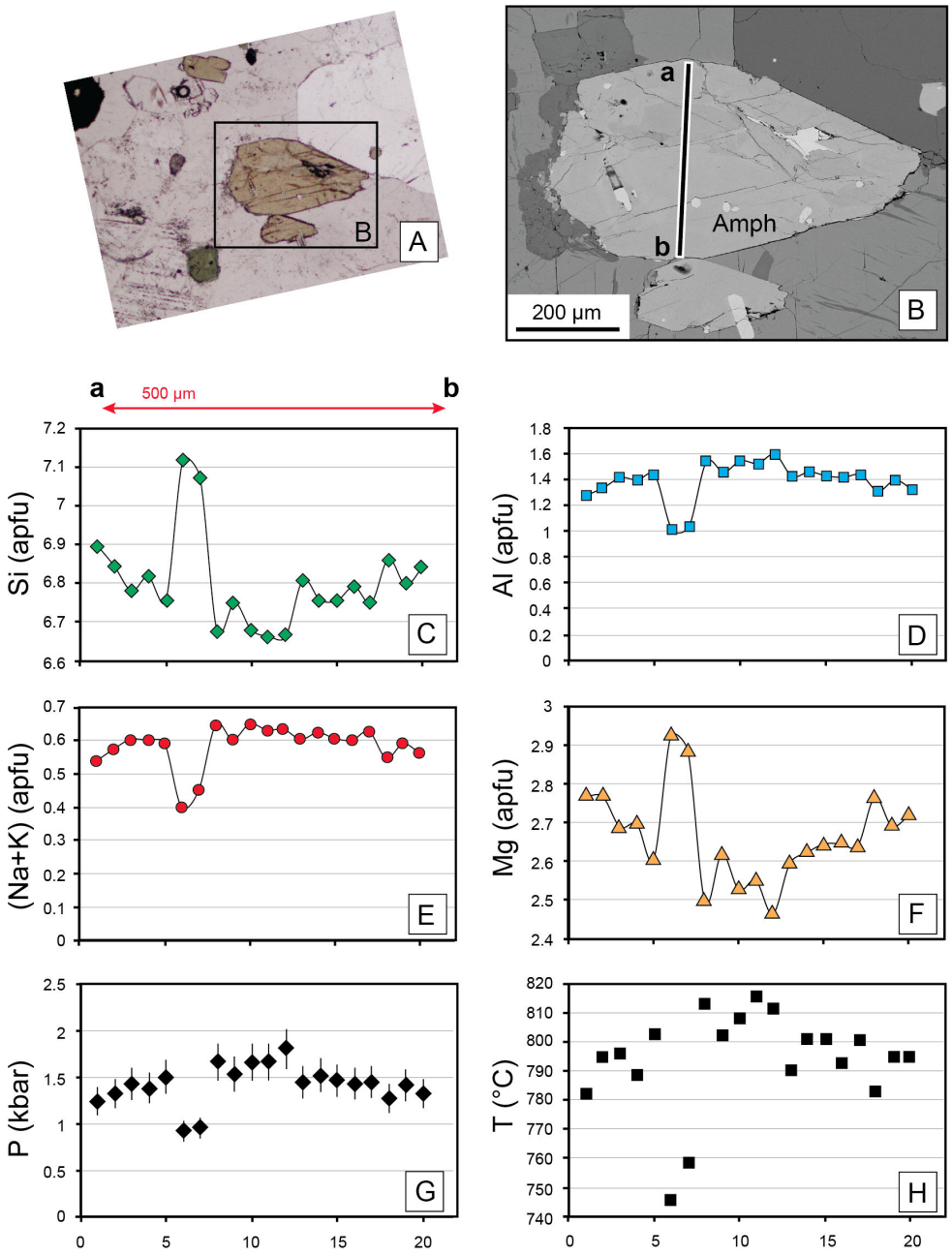

Figure 3: Example for sample CB-08 (amphibole 4). A) Photograph of the thin section (optic microscope, x50). B) Microprobe image of the analyzed amphibole showing the transect A-B. C-F) Chemical composition of the amphibole along the transect a-b. G,H) Pressure and temperature obtained along this transect using RR2012 thermo-barometric method.

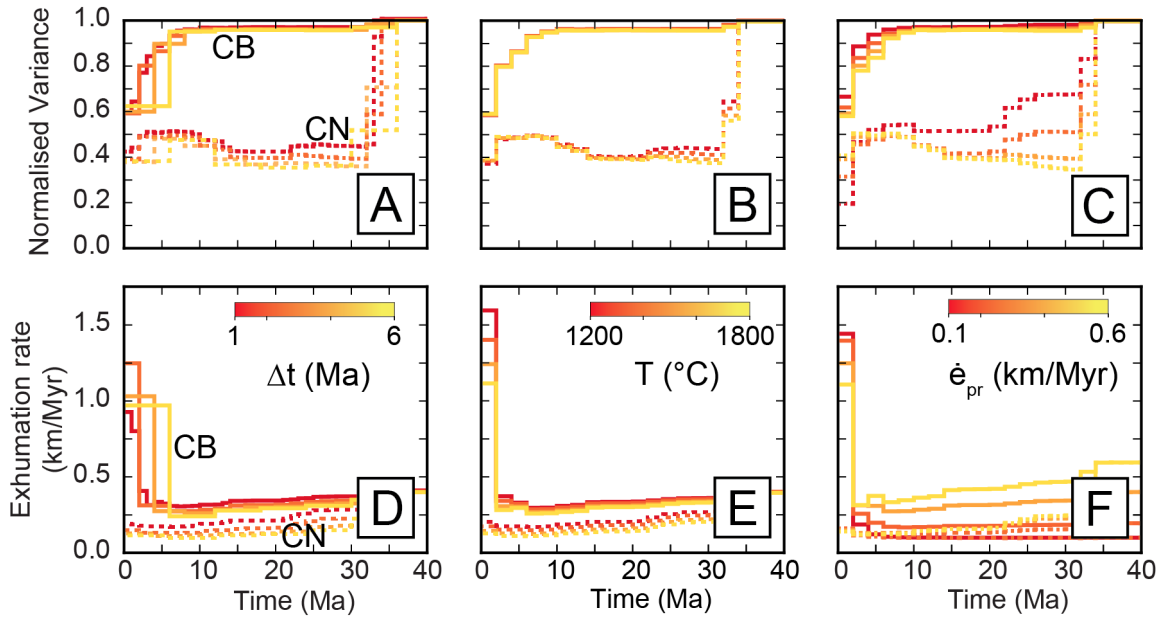

Figure 4: Sensitivity of exhumation rate to different parameters. The location of the two points (CB and CN) is shown Figure 1 by red stars. A-C) Normalized variance for each exhumation history, the lower the normalized variance is, better the inversion is constrain. D-F) Exhumation rate history for a range of Δt, T and $\dot{e}_{pr}$,.

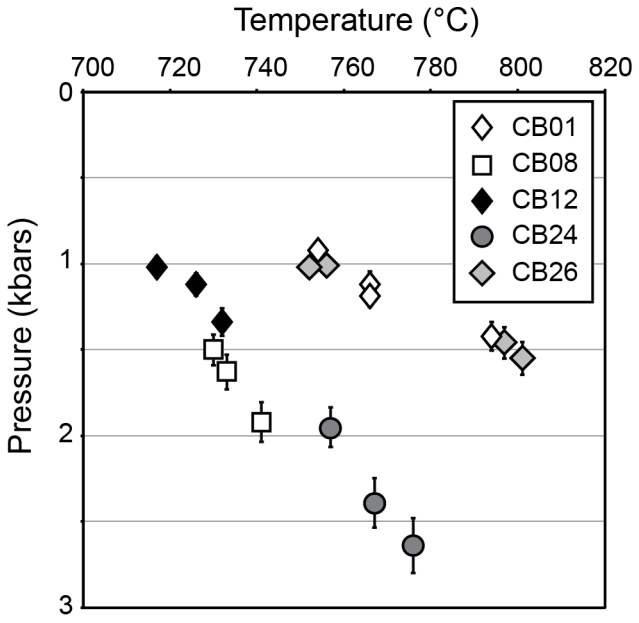

609

610 Figure 5: Magmatic pressures and temperatures calculated for the Cordillera Blanca batholith
611 using the thermobarometer of *Ridolfi and Renzulli* (2012). Each point represents estimates
612 based on averages of multiple analyses within an individual amphibole crystal (12 analyses
613 per amphibole in average).

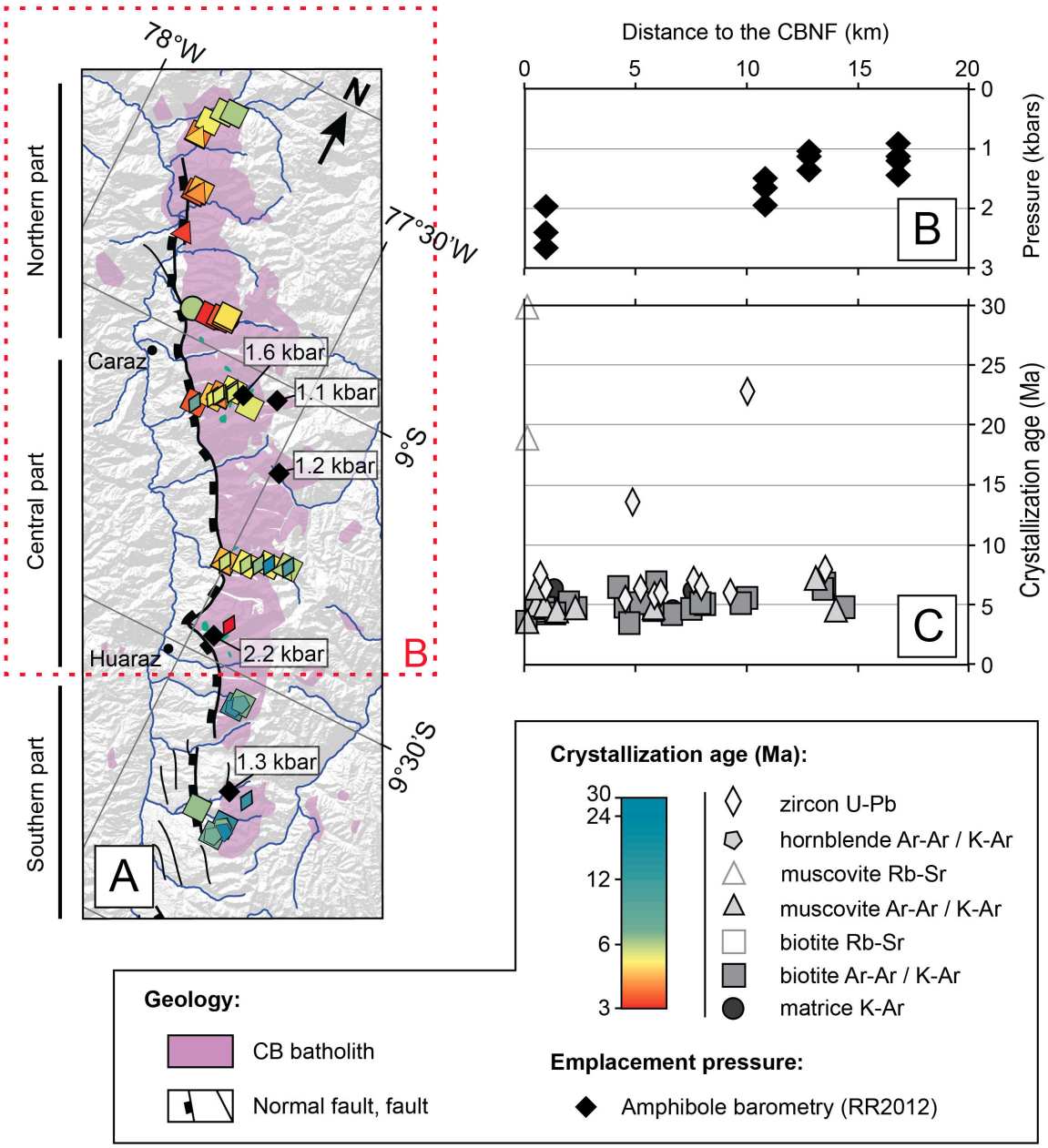

614

615 Figure 6: Spatial repartition of magmatic pressure and cooling ages. A) Map showing the
616 cooling ages (colored symbols) and the emplacement pressure (black diamonds) of the
617 Cordillera Blanca batholith. B) Magmatic pressure (black diamonds) versus distance to the
618 CBNF. Magmatic pressures were calculated for the Cordillera Blanca batholith using the
619 thermobarometer of *Ridolfi and Renzulli* (2012). C) Crystallization and cooling ages versus
620 distance to the CBNF (*Stewart et al.*, 1974; *Wilson*, 1975; *Cobbing et al.*, 1981; *Mukasa*,
621 1984; *Beckinsale et al.*, 1985; *McNulty et al.*, 1998; *Giovanni*, 2007).

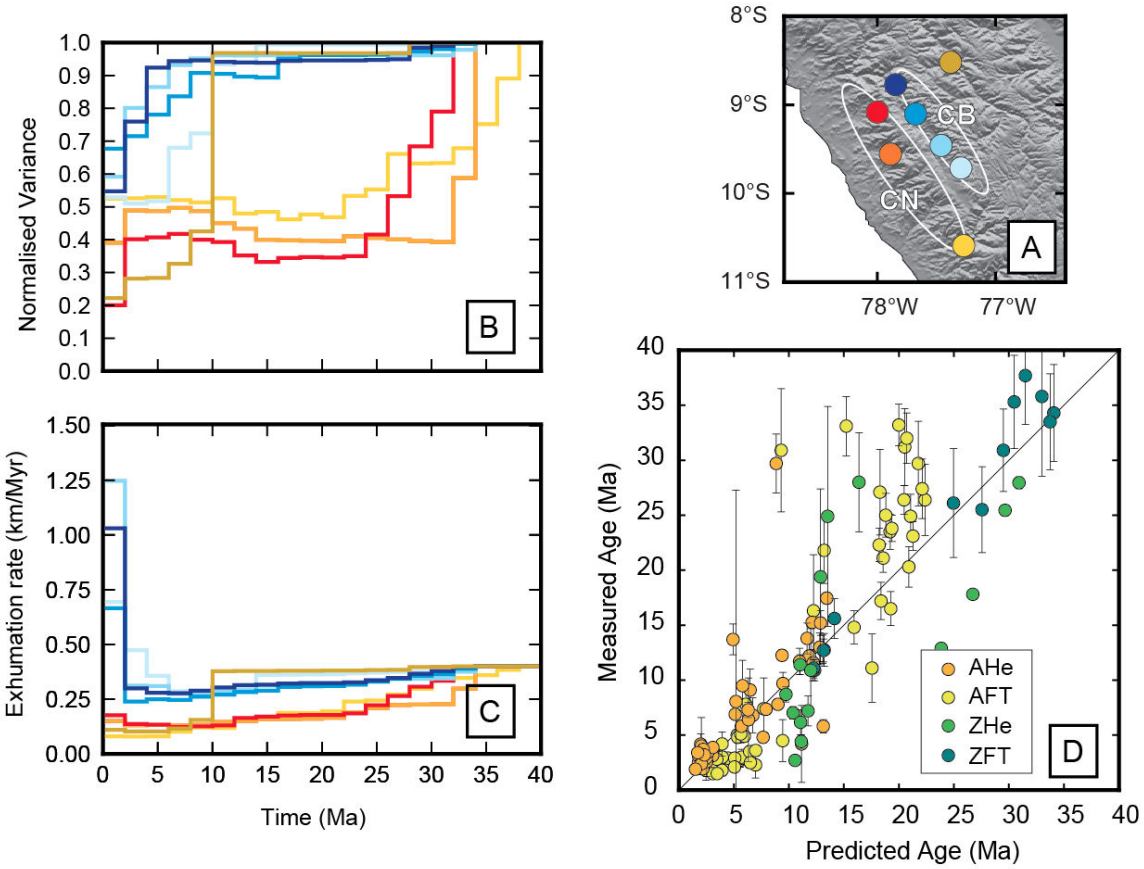

622

623 Figure 7: A) DEM with location of the exhumation rate. Colors of the points are used in the
624 graphs B and C to track each sample. B) Variance of the erosion rate inversion for the
625 different locations. C) Exhumation rate versus time for the different points. Model parameters
626 include an a priori exhumation rate of 0.4 ± 0.2 km/Myr, an exponential correlation function
627 with length scale of 20 km and an initial geothermal gradient of 32°C/km. The calculation
628 was done for 2 Myrs time steps. D) Misfit of the inversion.

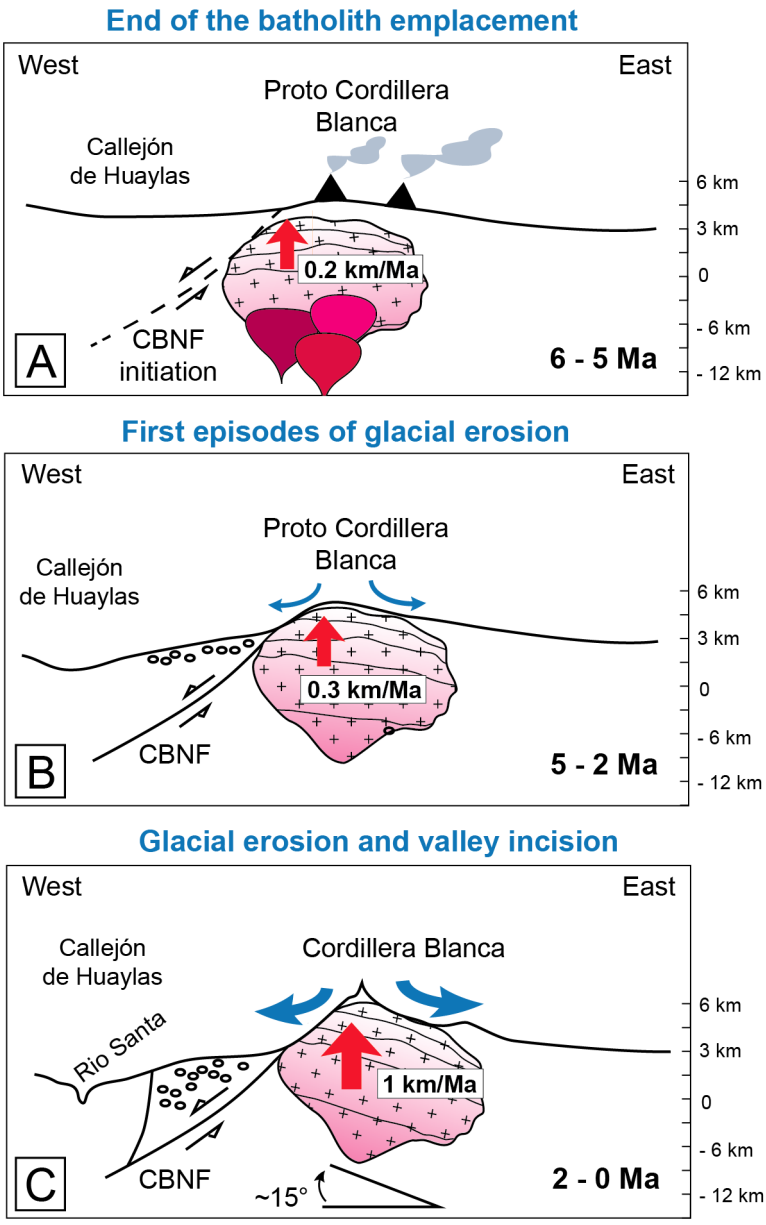

629

630 Figure 8: Schematic W-E cross-section of the Cordillera Blanca and the CBNF. A) 6-5 Ma:
631 Final stage of the Cordillera Blanca emplacement; CBNF initiation. B) 5-2 Ma: Cordillera
632 Blanca exhumation along the CBNF, deposit of the first residuals eroded from the CB in the
633 Callejón de Huaylas C) Glacial valley incision, increase of erosion rates and tilting of the
634 Cordillera Blanca batholith.

Dans ce chapitre j'ai quantifié la profondeur de mise en place du batholite de la Cordillère blanche grâce à la thermobarométrie sur amphibole, et j'ai proposé que le batholite montre une structure magmatique en forme de sills basculés. J'ai inversé les données thermochronologiques disponibles dans la bibliographie pour obtenir les variations spatio-temporelles des taux d'érosion dans la région de la Cordillère Blanche. Ces données ne permettent pas de quantifier les processus qui contribuent au soulèvement de la Cordillère Blanche. Pour me rapprocher de cette problématique, je vais tester dans le prochain chapitre l'impact de l'érosion et de la réponse flexurale associée en utilisant un modèle d'évolution du paysage incorporant les lois d'érosion et la flexure.

In this chapter we quantify the emplacement depth of the Cordillera Blanca batholith, we propose a magmatic structure in sills and a later tilt toward the east. The time-exhumation inversion of the low-temperature thermochronologic data available in this area provides spatial and temporal changes in erosion rates in the Cordillera Blanca region. However, these data do not quantify processes that contribute to the uplift of the Cordillera Blanca. I will use in the next chapter a landscape evolution model incorporating erosion laws and flexure to test the impact of erosion and associated flexural response and thus bring better constrains to this question.

---

6 Faille normale d'extrado, érosion et rebond flexural dans la Cordillère Blanche (Nord Pérou)

Sommaire

Dans ce chapitre, je présente mes modélisations de l'évolution du paysage appliquées à la Cordillère Blanche (FastScape). Mes résultats indiquent que l'érosion et le rebond flexural associé augmentent significativement les taux de soulèvement dans la Cordillère Blanche. Basée sur des études précédentes et les résultats de mes modélisations, je propose un nouveau modèle impliquant une faille normale d'extrado pour la faille normale de la Cordillère Blanche et l'exhumation de la Cordillère Blanche.

This chapter presents landscape evolution modeling (FastScape) for the Cordillera Blanca region. My results suggest that erosion and associated flexural rebound contribute significantly to the Cordillera Blanca uplift. Based on my data and on recents studies, I proposed a new model involving extrado normal faulting and erosion for the CBNF and for the Cordillera Blanca exhumation.

Résumé étendu en français

Le corps de ce chapitre est un article en préparation pour Geophysical Research Letter. Mes coauteurs (J. Braun, L. Audin, X. Robert) m'ont apporté un support technique pour la modélisation ainsi que des discussions constructives qui m'ont permis de construire l'idée directrice, construire les modèles et de développer mon raisonnement.

Les plus hauts sommets péruviens sont situés dans le batholite de la Cordillère Blanche (14-5 Ma). Le soulèvement et l'exhumation de ce batholite sont étroitement liés à la faille normale de la Cordillère Blanche qui borde son flanc ouest. Plusieurs modèles ont été proposés (1) pour expliquer la présence de cette faille normale majeure en contexte de convergence. Cependant, l'existence de cette faille majeure comme le soulèvement rapide de la Cordillère Blanche sont encore incompris.

Alors que la morphologie de la Cordillère Blanche indique une érosion importante, l'impact de l'érosion sur le soulèvement de cette région des Andes n'a jamais été exploré. La morphologie de la Cordillère Blanche pose la question de rétroactions possibles entre l'érosion et l'exhumation le long de la faille normale de la Cordillère Blanche. Le but de ce chapitre est de quantifier l'importance du rebond isostatique induit par l'incision des vallées et l'érosion du batholite dans le soulèvement de la Cordillère Blanche. Pour quantifier l'importance respective de la faille et de l'érosion (i.e. du rebond flexural lié à l'érosion du granite) dans le soulèvement, j'ai modélisé l'évolution du paysage (avec des paramètres adaptés à la région de la Cordillère Blanche) avec l'algorithme FastScape (Braun & Willett 2013).

Mes résultats mettent en évidence l'importante contribution de l'érosion et du rebond flexural associé au soulèvement de la Cordillère Blanche. Même si la tectonique extensive Quaternaire contribue à la construction du relief, l'érosion tardive de ce relief joue un rôle important. En effet, les hauts sommets de la Cordillère Blanche agissent comme une barrière orographique en localisant les précipitations et donc l'érosion. Finalement, le rebond flexural induit par l'érosion augmente les taux de soulèvement. Je suggère que les plus hauts sommets péruviens sont le résultat de la construction tectonique du relief et du rebond flexural associé à l'érosion locale importante dans la Cordillère Blanche. Sur la base de mes résultats et des résultats d'études précédentes qui portaient sur le soulèvement au dessus du segment de subduction horizontal du nord Pérou (Eakin et al. 2014, Margirier et al. 2015), je propose un nouveau modèle pour la faille normale de la Cordillère Blanche, qui implique un soulèvement régional, une faille normale d'extrado et l'érosion glaciaire de la Cordillère Blanche.

Les conclusions de ce chapitre sont en accord avec d'autres travaux récents qui ont mis en évidence le contrôle de l'érosion et du rebond flexural sur l'évolution topographique des chaînes de montagnes (e.g., Avouac & Burov 1996, Montgomery & Brandon 2002, Montgomery 1994, Stern et al. 2005, Cederbom et al. 2004, Willett 1999, Beaumont et al. 1992). Plusieurs études ont déjà

suggéré le rôle du climat et de l'érosion sur l'évolution du relief dans la Cordillère des Andes, principalement dans la Cordillère Orientale (Montgomery et al. 2001, Masek et al. 1994, Horton 1999). Nos résultats montrent que la variabilité climatique et l'érosion sont également des processus à prendre en compte dans l'évolution du relief et le soulèvement de la Cordillère Occidentale, même pour des régions où les précipitations sont relativement faibles (< 2 m/an).

Extrado normal faulting, erosion and flexural rebound drive the Cordillera Blanca uplift (northern Peru)

A. Margirier, J. Braun, L. Audin, X. Robert

en préparation pour

Geophysical Research Letter

Extrado normal faulting, erosion and flexural rebound drive the Cordillera Blanca uplift (northern Peru)

Audrey Margirier[1,2], Jean Braun[1,2], Xavier Robert[1,2,3], Laurence Audin[1,2,3]

[1]*Université de Grenoble, Alpes, ISTerre, F-38041 Grenoble, France*

[2]*Centre national de la recherche scientifique, ISTerre, F-38041 Grenoble, France*

[3]*Institut de recherche pour le développement (IRD), ISTerre, F-38041 Grenoble, France*

Abstract

The highest Peruvian peaks are located in the Cordillera Blanca batholith (14-5 Ma). Its uplift and exhumation are closely linked to the Cordillera Blanca normal fault (CBNF) that delimits the western flank of the batholith. Several models have been proposed to explain the presence of this normal fault in a compressional setting but the CBNF and the Cordillera Blanca recent rapid uplift remain enigmatic. Whereas the Cordillera Blanca morphology indicates its important erosion and thus a significant mass of rocks removal, the impact of erosion on the Cordillera Blanca uplift have never been explored. In this paper we address the role of erosion and associated flexural rebound in the uplift and exhumation of the Cordillera Blanca with numerical modeling of landscape evolution (FastScape). Our results evidence the important contribution of erosion and associated flexural rebound to uplift of the Cordillera Blanca. Based on our results and previous studies of uplift above flat subduction we propose a new model for the CBNF involving regional surface uplift, extrado normal faulting and glacial erosion of the Cordillera Blanca.

1. Introduction

In compressional settings the occurrence of major normal faulting can be surprising. The study of processes leading to relief building is essential to understand processes driving normal faulting in the Andes. The Cordillera Blanca normal fault (CBNF), in northern Peru, is the most spectacular normal fault of the Andean range (~200 km long, > 4 km of displacement; Fig. 1). The Cordillera Blanca, a Miocene batholith, builds the footwall of this crustal scale normal fault. It includes the highest Peruvian peaks at present day. Its fast exhumation (~1mm/yr) has been linked to motion on the CBNF [e.g., *Bonnot*, 1984; *McNulty and Farber*, 2002; *Giovanni*, 2007; *Margirier et al.*, 2015]. The CBNF trend parallel to the Andean range and display at least 4 km of vertical offset since ~5 Ma [*Bonnot*, 1984]. This normal fault is located above the Peruvian flat-slab [*Barazangi and Isacks*, 1976], which is expected to trigger compression in the upper plate [*Ramos and Folguera*, 2009].

Two models have been proposed to explained extension on the CBNF: *Dalmayrac and Molnar* [1981] proposed that this fault is the result of a gravitational collapse of the thickened crust whereas *McNulty and Farber* [2002] suggested that the subduction of the buoyant Nazca Ridge below the Cordillera Blanca drove the footwall uplift. In the light of some recent studies, these two models are inconsistent with the geodynamic and geologic context [*Hampel*, 2002; *Rosenbaum et al.*, 2005; *Antonijevic et al.*, 2015; *Margirier et al.*, 2015]. Indeed, *Margirier et al.* (2015) demonstrated the occurrence of a regional uplift above the Peruvian flat-slab. The surface uplift they evidenced in the Cordillera Negra is not coherent with the collapse model. In addition, new reconstructions of the timing and location of the initial Nazca Ridge subduction [*Hampel*, 2002; *Rosenbaum et al.*, 2005; *Antonijevic et al.*, 2015] disagree with the initiation of normal faulting in the Cordillera Blanca. New thermobarometry data and erosion rates reconstruction based on thermochronologic data indicate a recent increase of erosion rates in the Cordillera Blanca (~2-0 Ma; [*Margirier et al.*, in prep]).

Margirier et al. [in prep] also proposed an important contribution of glacial erosion in the recent exhumation of the Cordillera Blanca batholith. Indeed, the removal of such a mass of material represents a significant upward load on the lithosphere, which would drive flexural uplift. This unloading and flexural uplift would have also generated large stresses in the lithosphere, which could have interacted with tectonic inheritance (fault re-activation, tectonic displacement rate increase). Previous studies demonstrated that the flexural uplift driven by valley erosion could reach rates similar to those attain during a tectonic uplift [*Montgomery*, 1994; *Small and Anderson*, 1995; *Cederbom et al.*, 2004; *Stern et al.*, 2005]. Moreover *Braun et al.* [2014] evidenced a density-dependent isostatic rebound: the densest rocks (intrusions) are exhumed faster than less dense rocks (surrounding sediments).

The general settings in the Cordillera Blanca ask the question of the feedbacks interplays between erosion and exhumation along the CBNF. The aim of this paper is thus to quantify the importance of isostatic rebound associated to valley incision and densest rocks erosion in the Cordillera Blanca uplift and to test the validity of this flexure driven model. To address this issue, we model landscape evolution for the Cordillera Blanc settings with FastScape algorithm [*Braun and Willett*, 2013] to quantify the respective importance of faulting, erosion, and density driven flexural rebound in Cordillera Blanca uplift.

2. Context

Geodynamic context

The northern Peruvian margin displays a present-day flat subduction zone (3-15°S) where both the geometry and timing of slab flattening are well constrained [e.g., *Barazangi and Isacks*, 1976; *Gutscher et al.*, 1999; *Hampel*, 2002; *Rosenbaum et al.*, 2005; *Antonijevic et al.*, 2015]. *Gutscher et al.* [1999] proposed that the subduction of two buoyant features, the Nazca Ridge and the (Lost) Inca Plateau, control the slab flattening. The Peruvian flat-slab influence the occurrence and location of magmatic activity: the magmatic arc migrates away from the

77 trench and even ceases to exist during slab flattening. In addition, the shortening in the
78 overriding plate move eastward to sub-Andes during the slab flattening [e.g., *Ramos and*
79 *Folguera*, 2009]. Finally the Peruvian flat-slab induce dynamic topography [*Eakin et al.*,
80 2014] that can be recorded by low temperature thermochronology: Margirier et al. (2015)
81 evidenced a regional surface uplift from 15 Ma in northern Peru associated to these dynamic
82 topography process. In terms of mechanics, *Froidevaux and Isacks* [1984] described a neutral
83 to extensional stress regime within the high plateau. They suggested that as elevation of the
84 plateau increases the tectonic regime change from compression to extension. It contrasts with
85 the compressional regime on the eastern sub-Andes and along the subduction zone.
86
87 *Geologic and climatic context*
88 The Cordillera Blanca built the highest Peruvian summits with a cluster of 6000 m peaks (Fig.
89 1). The Cordillera Blanca corresponds to a 14–5 Ma granitic pluton (zircon U-Pb; [*Mukasa*,
90 1984; *Giovanni*, 2007]) emplaced at ~3 km depth into deformed Jurassic sediments
91 [*Margirier et al.*, in prep]. The Cordillera batholith is elongated (150 × 15 km) and trend
92 parallel to the Andean range. Whereas the higher peaks in the Cordillera Blanca are located
93 close to the CBNF, where the maximum tectonic uplift is expected, the drainage divide is
94 located farther east (Fig. 2A). The batholith is deeply incised by deep U-shaped valleys
95 resulting from major glacial erosion. Several other glacial geomorphic features (moraines,
96 roches moutonnées) records the large extension of the glaciations that imprinted the
97 Cordillera Blanca morphology [*Farber et al.*, 2005]. At present day, the high elevations of the
98 Cordillera Blanca build the Andean drainage divide [*Wise and Noble*, 2003] and act as an
99 orographic barrier to moisture coming from the Amazon basin (Fig. 1B; [*Bookhagen and*
100 *Strecker*, 2008]). Even if the most important orographic effect of the Andes is located in the
101 first relief of the sub-Andes, the Cordillera Blanca high elevations prevent moisture from
102 reaching the western flank of the Andes, resulting in wetter climatic conditions in the

103 Cordillera Blanca (~1.5 m/yr) than in the Cordillera Negra (~0.5 m/yr), farther west
104 [*Bookhagen and Strecker*, 2008]).

105 The Cordillera Negra forms a plateau at ~4500 m with 1–2 km-deep valleys incised into its
106 western flank. The range comprises Cretaceous and Paleogene plutons (73–48 Ma;
107 [*Beckinsale et al.*, 1985]) intruded into Jurassic sediments. Neogene volcano-sedimentary
108 deposits cap the Cordillera Negra (54–15 Ma Calipuy Formation; [*Cobbing et al.*, 1981]).
109 Rare and discrete moraines (above ~4200 m) indicate the occurrence of glaciations with small
110 spatial extension in the Cordillera Negra [*Bonnot*, 1984].

111 The CBNF is located on the western flank of the Cordillera Blanca (Fig. 1). The Cordillera
112 Blanca and the Cordillera Negra form respectively the hanging wall and the footwall of the
113 CBNF. The CBNF is active since ~5.4 Ma [*Bonnot*, 1984; *Giovanni*, 2007] and shows ~8 km
114 of vertical offset in total [*Margirier et al.*, in prep].

115

116 *Paleogeography*

117 Different studies addressed the Late Miocene paleogeography of the Cordillera Blanca region
118 [*Wise and Noble*, 2003; *Giovanni*, 2007; *Hoorn et al.*, 2010]. Based on pollen analyses, Hoorn
119 et al. (2010) constrained elevation of ~4 km in the Middle Miocene. At that time, the
120 Cordillera Negra topography formed the drainage divide (Wise and Noble, 2003). Based on
121 the repartition of some volcanic deposits in the Callejón de Huaylas, *Wise and Noble* [2003]
122 and *Giovanni* [2007] suggested that a depression already existed at the end of the Late
123 Miocene. Based on $\delta^{18}O$ analyses of paleolake deposits, Giovanni et al. (2010) showed that
124 high elevations in the Callejón de Huaylas basin were attained by latest Miocene times.
125 Whereas the paleogeography of the Cordillera Negra and the Callejón de Huaylas have been
126 addressed the topography of the Cordillera Blanca before the batholith emplacement is not yet
127 documented.

128

3. Methods

The FastScape algorithm [*Braun and Willett*, 2013] solves the stream power law to predict landscape evolution in a given tectonic and geomorphic setting. This algorithm is implicit in time and computational time increase linearly with the number of point used to discretize the topography. FastScape can be used with a very high spatial discretization without extended calculation time. This code permits to define the initial topography, the precipitation rates and pattern, the presence of intrusions (density and erodability), a fault (defined by vertical displacement rate) and the occurrence of flexural isostatic rebound in response to erosion. This model uses the elastic deformation equations to solve the deflection of a thin plate when a varying load is applied to it [*Turcotte and Schubert*, 2002].

The runs were performed on a 200 × 200 km square domain, the resolution of the models is defined by the 250 × 250 grid points (Table A1). The runs last 6 Ma, we fixed the time step length at 1 ka (model parameters are detailed in the Table A1). We used the stream power law assuming linear slope dependence (m = 0.4; kf = 1×10^{-5}). We imposed precipitation rates of 0.5 and 1.0 m/yr in the Cordillera Negra and Cordillera Blanca respectively according to *Bookhagen and Strecker* [2008]. Based on *Perez-Gussinye et al.* [2009] regional crustal elastic thickness results, we fixed the elastic thickness (T_e) of the model at 2 km. We defined the initial topography with a "proto Cordillera Negra" (3500 m; [*Wise and Noble*, 2003; *Hoorn et al.*, 2010]) and we fixed the surface uplift at 0.1 mm/yr for all models [*Margirier et al.*, 2015]. Some models involve a vertical N-S fault defined by footwall vertical uplift rates of 0.5 to 0.3 mm/yr from the center to the extremities and a 150 × 20 km granite defined by higher density and lower erodability (density anomaly = 0.4; hardness = 0.6, with $0 < E < 1$, smaller E corresponds to lower erodability).

4. Results

Role of initial topography

155 We performed modeling a) without relief at the present location of the Cordillera Blanca (Fig.
156 2B) and b) with the presence of a "proto Cordillera Blanca" (3000 m; Fig. 2C). To the first
157 order, the predicted flexural topography is for both model well correlated with the observed
158 topographic bulge in the Cordillera Blanca. However, for the model without initial relief in
159 the Cordillera Blanca the drainage divide is located close to the CBNF, which is not the case
160 on the field. If we add a proto Cordillera Blanca, this relief controls the early drainage
161 network and localizes the drainage divide farther east in the Cordillera Blanca. Our results
162 suggest that the presence of an initial relief is needed to localize the drainage divide at its
163 present position (eastern part of the Cordillera Blanca). In addition, it is important to notice
164 that the presence of a "proto Cordillera Blanca" does not change drastically the expected
165 elevations at the end of the model (~6000 m after 6 Ma; Figs. 2B and 2C).
166
167 *Role of tectonics and erosion*
168 All following results are obtained from models with an initial relief in both the Cordillera
169 Blanca (3000 m) and the Cordillera Negra (3500 m). The main parameters in the model are
170 the presence/absence of a fault, the occurrence of flexural isostatic rebound in response to
171 erosion and the presence/absence of an intrusion.
172 If we add a fault and choose to ignore the flexural rebound due to erosion, the uplift rates
173 correspond to the vertical displacement on the fault (0.5 km/m.y.), the maximum elevation is
174 moderated (~3000 m; Fig. 3). Considering the low elastic thickness (T_e) of the crust in the
175 Cordillera Blanca region (0-10 km; [*Perez-Gussinye et al.*, 2009]) the flexural rebound should
176 not be ignored. Indeed, when we consider flexural rebound, the uplift rates and the
177 topography (~5800 m; Fig. 3) are higher. Then, if we take in account the presence of the
178 Cordillera Blanca batholith (denser rocks) in the footwall, the uplift rates and the topography
179 are higher (maximum elevation ~6700 m). If we remove the fault the uplift rates are lower

and the elevation attains 3800 m (Fig. 3). It evidences that without vertical displacement on the fault the uplift rates and the topography remain low in the footwall.

Finally, after 6 Ma, models involving faulting and flexural rebound are the only ones that permit the footwall to reach ~6000 m (Fig. 3).

5. Discussion

Paleogeography

The important surface uplift and induced erosion in the Cordillera Blanca prevent to study the paleogeography in this area. However, the drainage network geometry and the drainage divide location provide robust constraints on the past Cordillera Blanca topography and its evolution. Our results evidence that the location of the drainage divide in the eastern part of the Cordillera Blanca is controlled by an initial topography in the Cordillera Blanca area and an inherited drainage network. Based on these results we propose that a proto-Cordillera Blanca existed before the CBNF initiation. The presence of such a relief is in agreement with *Giovanni et al.* [2010] and *Wise and Noble* [2003] studies, which already proposed that the Callejón de Huaylas was a topographic depression during the Late Miocene. *Wise and Noble* [2003] suggested that at that time, before the Cordillera Blanca exhumation, the Cordillera Negra correspond to the drainage divide. However, the presence of a proto-Cordillera Blanca questions the location of the Andean drainage divide during the Miocene.

The Cordillera Blanca high topography: the result of erosion and flexural rebound?

Our results show the contribution of the flexural rebound associated to the Cordillera Blanca erosion to the uplift rates and high elevation building. We evidence that > 50% of the uplift rates are the consequence of the erosion of the Cordillera Blanca and associated flexural response. This flexural rebound might be facilitated by the existence of inherited faults and warm crust after the Cordillera Blanca batholith emplacement during the Miocene [*Mukasa*,

206 1984; *Giovanni*, 2007], which result in low elastic thickness [*Perez-Gussinye et al.*, 2009].
207 However, our results suggest that the effect of eroding a densest material is minor on a < 10
208 Ma time scale. Whereas the presence of the batholith does not influence significantly the
209 uplift rates and elevation ranges, the Cordillera Blanca batholith appears to localize
210 deformation on its western flank with the CBNF. The presence of the CBNF is thus essential;
211 this normal fault does contribute to relief building in the Cordillera Blanca and thus permits to
212 reach early high elevation. Moreover, the occurrence of the CBNF localizes relief building
213 and thus enhanced erosion in the uplifted area [*Montgomery and Brandon*, 2002]. Since the
214 Cordillera Blanca summits reached high elevation, the Cordillera Blanca acts as an orographic
215 barrier for moisture carried from the Amazon basin [*Montgomery et al.*, 2001; *Bookhagen and*
216 *Strecker*, 2008]. The induced rain shadow created prevents erosion of the Cordillera Negra,
217 and results in higher erosion rates in the Cordillera Blanca and differential exhumation of the
218 two ranges. Then, Quaternary glaciations in the Cordillera Blanca (~1.5-0 Ma; [*Farber et al.*,
219 2005; *Smith et al.*, 2005]) also increased erosion rates, with deep U-shaped valley incision, as
220 suggested by *Margirier et al.* [in prep] and by *Montgomery* [2002] for the Olympic
221 Mountains. Finally, the recent glacial retreat (since ~21 ka; [*Seltzer et al.*, 2002; *Farber et al.*,
222 2005; *Smith et al.*, 2005]) could have induced a flexural rebound that both increased uplift
223 rates in the Cordillera Blanca and slip-rates on the CBNF [e.g., *Hetzel and Hampel*, 2005;
224 *Hampel et al.*, 2007].
225
226 *New model for the CBNF*
227 Processes driving extension on the CBNF and uplift of the footwall remain not understood
228 [e.g., *Dalmayrac and Molnar*, 1981; *McNulty and Farber*, 2002]. Our results suggest that >
229 50% of the uplift in the footwall of the CBNF is directly due to the erosion and isostatic
230 rebound of the Cordillera Blanca. As a consequence, the important displacement on the
231 CBNF is only partly due to extensional tectonics. Previous studies suggest the occurrence of a

232 long wavelength antiform above the Peruvian flat-slab and large scale uplift in the Cordillera
233 Occidental [*Martinod et al.*, 2013; *Eakin et al.*, 2014; *Margirier et al.*, 2015]. Moreover,
234 inherited faults and sutures appear to localize deformation in this region [*Jaillard*, 1994; *Eude*
235 *et al.*, 2015]. Thus, we propose that the CBNF is an extrado normal fault that reactivates an
236 inherited tectonic feature (Fig. 4A). This scenario is in agreement a) with the middle Miocene
237 erosion of the Callejón de Huaylas which could be associated to the regional uplift evidenced
238 by previous studies [*Eakin et al.*, 2014; *Margirier et al.*, 2015] and b) with the low subsidence
239 in the Callejón de Huaylas since ~5.4 Ma [*Bonnot*, 1984; *Giovanni et al.*, 2010]. Then, the
240 higher moisture and extensive glaciations in the Cordillera Blanca favor its uplift and
241 exhumation along the CBNF.
242

243 ## 6. Conclusions

244 Our results evidence the important contribution of erosion and associated flexural rebound to
245 local Andes uplift in the Cordillera Blanca. Even if Quaternary extensional tectonics
246 contributes to high relief building, the late relief erosion plays an important role. Indeed, high
247 reliefs act as an orographic barrier and localize precipitation and erosion, which enhance
248 surface uplift. We suggest that the highest Peruvian peaks are the result of tectonic-driven
249 high-relief construction and flexural rebound associated to local important erosion. Based on
250 our results and previous studies that addressed uplift above the flat subduction [*Eakin et al.*,
251 2014; *Margirier et al.*, 2015]; we propose a new model for the CBNF, which involves
252 regional surface uplift, extrado normal faulting and erosion of the Cordillera Blanca.
253 This study is consistent with previous studies that evidence the control of erosion and
254 flexural rebound on mountain belt topographic evolution [e.g., *Montgomery*, 1994; *Avouac*
255 *and Burov*, 1996; *Willett*, 1999; *Montgomery and Brandon*, 2002; *Cederbom et al.*, 2004;
256 *Stern et al.*, 2005]. Several studies provide evidence of climate and erosion control on the
257 relief evolution at the scale of the Andean range and in the Cordillera Oriental [*Masek et al.*,

1994; *Horton*, 1999; *Montgomery et al.*, 2001]. Our results evidence that climate variability and erosion are also important processes in the relief evolution and surface uplift in the Cordillera Occidental, even when the rainfall is < 2 m/yr. Erosion and flexural rebound in the Andes should not be underestimated because of the low elastic thickness in the Andean range [*Perez-Gussinye et al.*, 2009]. These processes can explain local uplift in some highly eroded areas like the Cordillera Blanca.

References

Antonijevic, S. K., L. S. Wagner, A. Kumar, S. L. Beck, M. D. Long, G. Zandt, H. Tavera, and C. Condori (2015), The role of ridges in the formation and longevity of flat slabs, *Nature*, *524*(7564), 212–215, doi:10.1038/nature14648.

Avouac, J. P., and E. B. Burov (1996), Erosion as a driving mechanism of intracontinental mountain growth, *Journal of Geophysical Research*, *101*(B8), 747–769.

Barazangi, M., and B. L. Isacks (1976), Spatial distribution of earthquakes and subduction of the Nazca plate beneath South America, *Geology*, *4*(11), 686–692.

Beckinsale, R. D., A. W. Sanchez-Fernandez, M. Brook, E. J. Cobbing, W. P. Taylor, and N. B. Moore (1985), Rb-Sr whole rock isochron and K-Ar determination for the Coastal Batholith of Peru, in *Magmatism at a Plate Edge: The Peruvian Andes*, edited by W. S. Pitcher, M. P. Atherton, E. J. Cobbing, and R. D. Beckinsale, pp. 177–202, Blackie Halstead press, Glasgow.

Bonnot, D. (1984), Néotectonique et tectonique active de la Cordillère Blanche et du Callejon de Huaylas (Andes nord-péruviennes), *Thèse présentée pour obtenir le grade de docteur, Université de Paris-Sud, Centre d'Orsay*, 1–202.

Bookhagen, B., and M. R. Strecker (2008), Orographic barriers, high-resolution TRMM rainfall, and relief variations along the eastern Andes, *Geophys. Res. Lett.*, *35*(6), L06403, doi:10.1029/2007GL032011.

Braun, J., and S. D. Willett (2013), A very efficient O(n), implicit and parallel method to solve the stream power equation governing fluvial incision and landscape evolution, *Geomorphology*, *180-181*, 170–179, doi:10.1016/j.geomorph.2012.10.008.

Braun, J., T. Simon-Labric, K. E. Murray, and P. W. Reiners (2014), Topographic relief driven by variations in surface rock density, *Nature Geoscience*, *7*, 534–540, doi:10.1038/ngeo2171.

Cederbom, C. E., H. D. Sinclair, and F. Schlunegger (2004), Climate-induced rebound and exhumation of the European Alps, *Geology*, *32*(8), 709–712, doi:10.1130/G20491.1.

Cobbing, J., W. Pitcher, J. Baldock, W. Taylor, W. McCourt, and N. J. Snelling (1981), Estudio geológico de la Cordillera Occidental del norte del Perú, *Instituto Geologico*

294 *Minero y Metalurgico, Serie D. Estudios Especiales*, *10*(D), 1–252.

295 Dalmayrac, B., and P. Molnar (1981), Parallel thrust and normal faulting in peru and
296 constraints on the state of stress, *Earth and Planetary Sciences Letters*, *55*, 473–481.

297 Eakin, C. M., C. Lithgow-Bertelloni, and F. M. Dávila (2014), Influence of Peruvian flat-
298 subduction dynamics on the evolution of western Amazonia, *Earth and Planetary Science*
299 *letters*, *404*(C), 250–260, doi:10.1016/j.epsl.2014.07.027.

300 Eude, A., M. Roddaz, S. Brichau, S. Brusset, Y. Calderon, P. Baby and J. C. Soula (2015),
301 Controls on timing of exhumation and deformation in the northern Peruvian eastern
302 Andean wedge as inferred from low-temperature thermochronology and balanced cross-
303 section, *Tectonics*, *34*(4), 715-730*,* doi:10.1002/2014TC003641.

304 Farber, D. L., G. S. Hancock, R. C. Finkel, and D. T. Rodbell (2005), The age and extent of
305 tropical alpine glaciation in the Cordillera Blanca, Peru, *J. Quaternary Sci.*, *20*(7-8), 759–
306 776, doi:10.1002/jqs.994.

307 Froidevaux, C., and B. L. Isacks (1984), The mechanical state of the lithosphere in the
308 Altiplano-Puna segment of the Andes, *Earth and Planetary Science letters*, *71*(2), 305–
309 314.

310 Giovanni, M. K. (2007), Tectonic and Thermal Evolution of the Cordillera Blanca
311 Detachment System, Peruvian Andes: Implication for Normal Faulting in a
312 Contractionnal Orogen, Ph.D. Thesis, 1–255 pp. University of California, Los Angeles.

313 Giovanni, M. K., B. K. Horton, C. N. Garzione, B. McNulty, and M. Grove (2010),
314 Extensional basin evolution in the Cordillera Blanca, Peru: Stratigraphic and isotopic
315 records of detachment faulting and orogenic collapse in the Andean hinterland, *Tectonics*,
316 *29*(6), TC6007, doi:10.1029/2010TC002666.

317 Gutscher, M. A., J. Malavieille, S. Lallemand, and J.-Y. Collot (1999), Tectonic segmentation
318 of the North Andean margin: impact of the Carnegie Ridge collision, *Earth and Planetary*
319 *Science letters*, *168*(3), 255–270.

320 Hampel, A. (2002), The migration history of the Nazca Ridge along the Peruvian active
321 margin: a re-evaluation, *Earth and Planetary Science letters*, *203*(2), 665–679.

322 Hampel, A., R. Hetzel, and A. L. Densmore (2007), Postglacial slip-rate increase on the Teton
323 normal fault, northern Basin and Range Province, caused by melting of the Yellowstone
324 ice cap and deglaciation of the Teton Range?, *Geology*, *35*(12), 1107-1110,
325 doi:10.1130/G24093A.1.

326 Hetzel, R., and A. Hampel (2005), Slip rate variations on normal faults during glacial–
327 interglacial changes in surface loads, *Nature, 435*, 81-84.

328 Hoorn, C. et al. (2010), Amazonia Through Time: Andean Uplift, Climate Change, Landscape
329 Evolution, and Biodiversity, *Science*, *330*(6006), 927–931, doi:10.1126/science.1194585.

330 Horton, B. K. (1999), Erosional control on the geometry and kinematics of thrust belt
331 development in the central Andes, *Tectonics*, *18*(6), 1292–1304,
332 doi:10.1029/1999TC900051.

333 Jaillard, E. (1994), Kimmeridgian to Paleocene tectonic and geodynamic evolution of the

334 Peruvian (and Ecuadorian) margin, *in Cretaceous tectonics in the Andes*, edited by J. A.
335 Salfity, pp. 101–167, Vieweg, Braunschweig/Wiesbaden.

336 Margirier, A., X. Robert, L. Audin, C. Gautheron, M. Bernet, S. Hall, and T. Simon-Labric
337 (2015), Slab flattening, magmatism and surface uplift in the Cordillera Occidental
338 (northern Peru), *Geology*, 1–16, doi:10.1130/G37061.1.

339 Margirier, A., L. Audin, X. Robert, F. Herman, J. Ganne and S. Schwartz (in prep),
340 Emplacement dynamics, exhumation and erosion of the Cordillera Blanca batholith along
341 a major Normal Fault in a subduction context (Peruvian Andes), Journal of Geophysical
342 Research: Solid Earth.

343 Martinod, J., B. Guillaume, N. Espurt, and C. Faccenna (2013), Effect of aseismic ridge
344 subduction on slab geometry and overriding plate deformation: Insights from analogue
345 modeling, *Tectonophysics*, doi:10.1016/j.tecto.2012.12.010>.

346 Masek, J. G., B. L. Isacks, and T. L. Gubbels (1994), Erosion and tectonics at the margins of
347 continental plateaus, *Journal of Geophysical Research, 99*(B7), 13941-13956.

348 McNulty, B. A., and D. L. Farber (2002), Active detachment faulting above the Peruvian flat
349 slab, *Geology*, *30*(6), 567–570.

350 Montgomery, D. R. (1994), Valley incision and the uplift of mountain peaks, *Journal of*
351 *Geophysical Research: Solid Earth, 99*(B7), 13913-13921.

352 Montgomery, D. R. (2002), Valley formation by fluvial and glacial erosion, *Geology*, *30*(11),
353 1047–1050.

354 Montgomery, D. R., and M. T. Brandon (2002), Topographic controls on erosion rates in
355 tectonically active mountain ranges, *Earth and Planetary Science letters, 201*, 481-489.

356 Montgomery, D. R., G. Balco, and S. D. Willett (2001), Climate, tectonics, and the
357 morphology of the Andes, *Geology*, *29*(7), 579–582.

358 Mukasa, S. B. (1984), Comparative Pb isotope systematics and zircon U-Pb geochronology
359 for the Coastal, San Nicolás and Cordillera Blanca Batholiths, Peru, Ph.D. Thesis, 1-362
360 pp., University of California, Santa Barbara.

361 Perez-Gussinye, M., C. J. Swain, J. F. Kirby, and A. R. Lowry (2009), Spatial variations of
362 the effective elastic thickness, Te, using multitaper spectral estimation and wavelet
363 methods: Examples from synthetic data and application to South America, *Geochem.*
364 *Geophys. Geosyst.*, *10*(4), 1-10, doi:10.1029/2008GC002229.

365 Ramos, V. A., and A. Folguera (2009), Andean flat-slab subduction through time, *Geological*
366 *Society, London, Special Publications*, *327*(1), 31–54, doi:10.1144/SP327.3.

367 Rosenbaum, G., D. Giles, M. Saxon, P. G. Betts, R. F. Weinberg, and C. Duboz (2005),
368 Subduction of the Nazca Ridge and the Inca Plateau: Insights into the formation of ore
369 deposits in Peru, *Earth and Planetary Science letters*, *239*(1-2), 18–32,
370 doi:10.1016/j.epsl.2005.08.003.

371 Seltzer, G. O., D. T. Rodbell, P. A. Baker, S. C. Fritz, P. M. Tapia, H. D. Rowe, and R. B.
372 Dunbar (2002), Early warming of tropical South America at the last glacial-interglacial
373 transition, *Science*, *296*, 1685–1686.

374 Small, E. E., and R. S. Anderson (1995), Geomorphically driven late Cenozoic rock uplift in
375 the Sierra Nevada, California, *Science, 270,* 277-278.

376 Smith, J. A., R. C. Finkel, D. L. Farber, D. T. Rodbell, and G. O. Seltzer (2005), Moraine
377 preservation and boulder erosion in the tropical Andes: interpreting old surface exposure
378 ages in glaciated valleys, *J. Quaternary Sci.*, *20*(7-8), 735–758, doi:10.1002/jqs.981.

379 Stern, T. A., A. K. Baxter, and P. J. Barrett (2005), Isostatic rebound due to glacial erosion
380 within the Transantarctic Mountains, *Geology*, *33*(3), 221-224, doi:10.1130/G21068.1.

381 Turcotte, D. L., and G. Schubert (2002), *Geodynamics*, Cambridge University Press, 456 pp.

382 Willett, S. D. (1999), Orogeny and orography: The effects of erosion on the structure of
383 mountain belts, *Journal of Geophysical Research: Solid Earth (1978–2012)*, *104*(B12),
384 28957–28981.

385 Wise, J. M., and D. C. Noble (2003), Geomorphic evolution of the Cordillera Blanca,
386 Northern Peru, *Boletin de la sociedad Geologica del Peru*, *96*, 1–21.

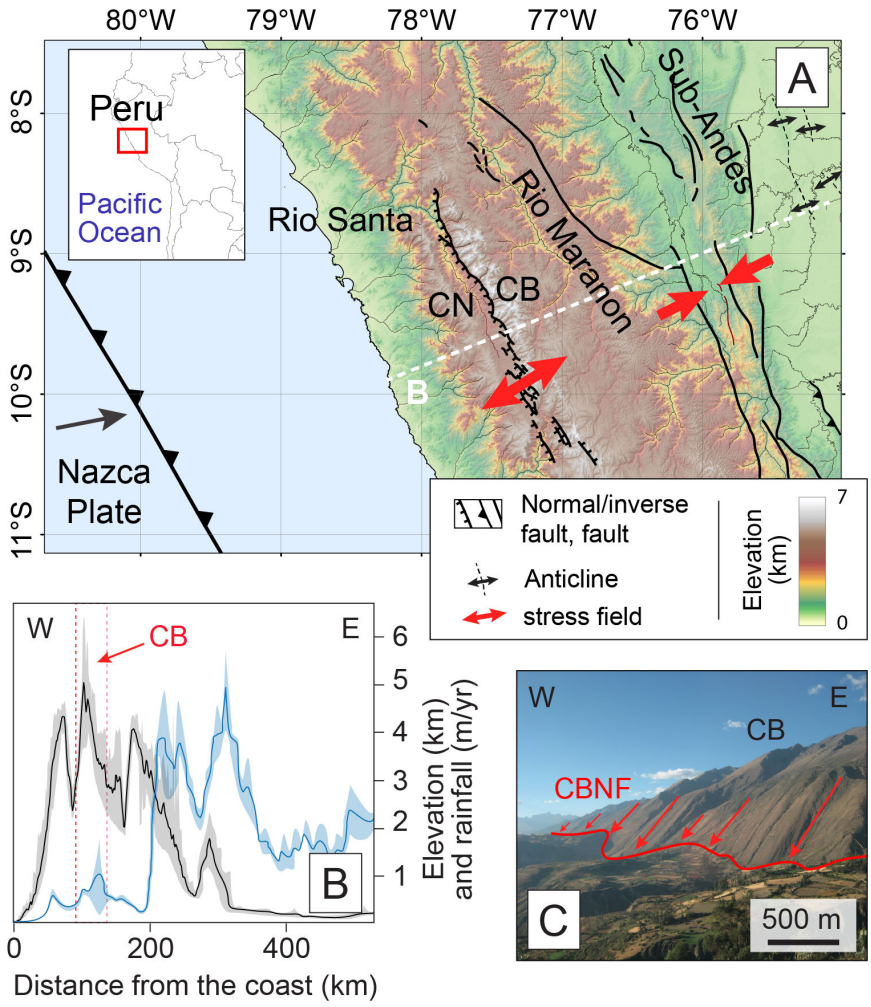

Figure 1: A) Topographic map of the northern Peru showing active tectonic features (Neotectonic Open Database), location of the Cordillera Blanca and of the Cordillera Negra. Inset shows map location within the South America. B) E-W cross-section of the Andes at the latitude of the Cordillera Blanca both the topography (black line) and the rainfall (blue line) are represented [*modified from Bookhagen and Strecker*, 2008]. C) Photograph of the CBNF showing the 1 km high triangular facets.

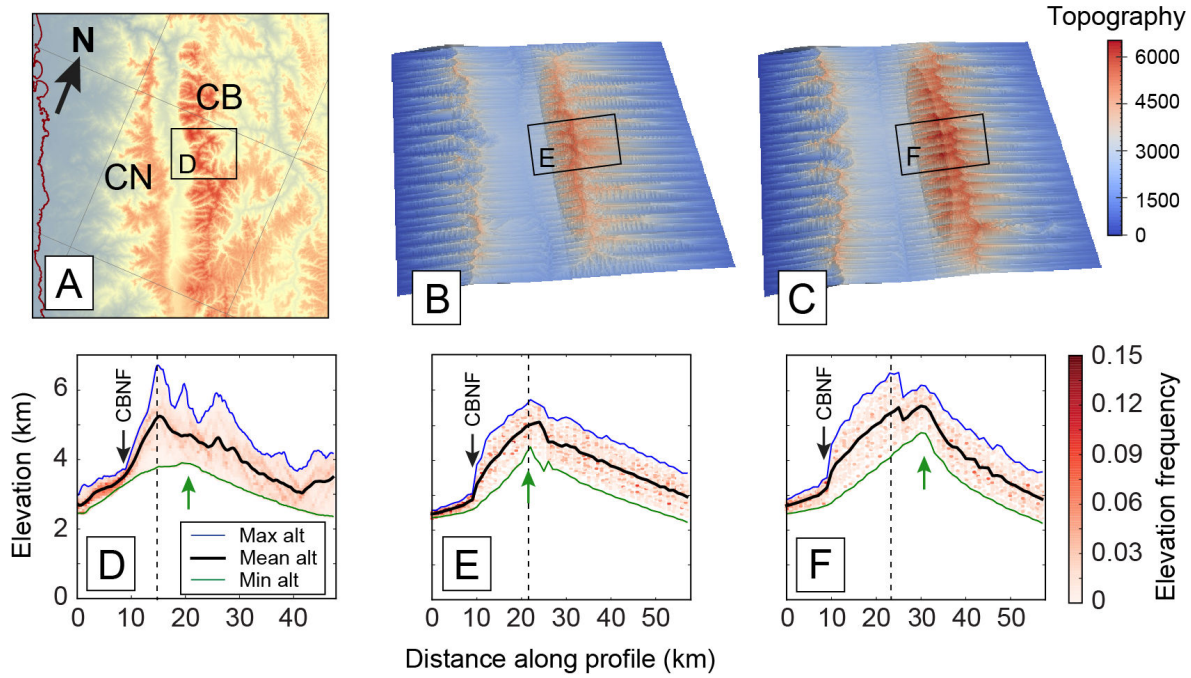

394

395 Figure 2: DEM and swath profiles through the Cordillera Blanca region and modeled
396 topography. A) DEM of the Cordillera Blanca region. B) DEM of the first model, which
397 involves a fault, a granitic batholith, a flexural rebound and a "proto" Cordillera Negra. C)
398 DEM of the second model similar to B) with the addition of a "proto" Cordillera Blanca. D-F)
399 Swath profiles through the Cordillera Blanca and from the two modeling showing elevation
400 (mean, maximum and minimum), the drainage divide position (green arrow), the CBNF
401 location (black arrow) and the maximum elevation (vertical dot line).

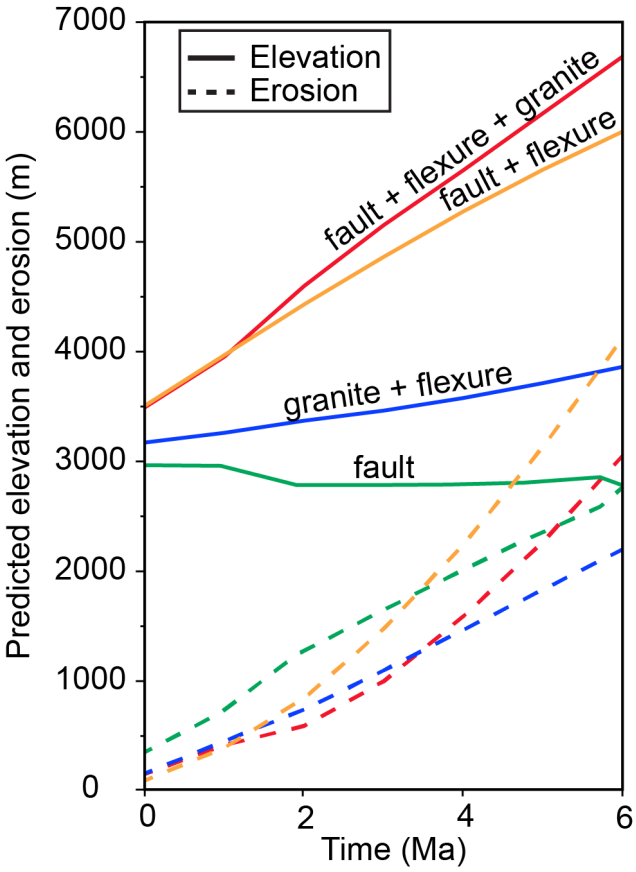

402

403 Figure 3: Graphic showing elevation (full lines) and uplift rate (dashed lines) evolution
404 through time with a fault (green), with a fault and flexural rebound (orange), with a fault,
405 flexural rebound and a dense intrusion (red) and without fault (blue).

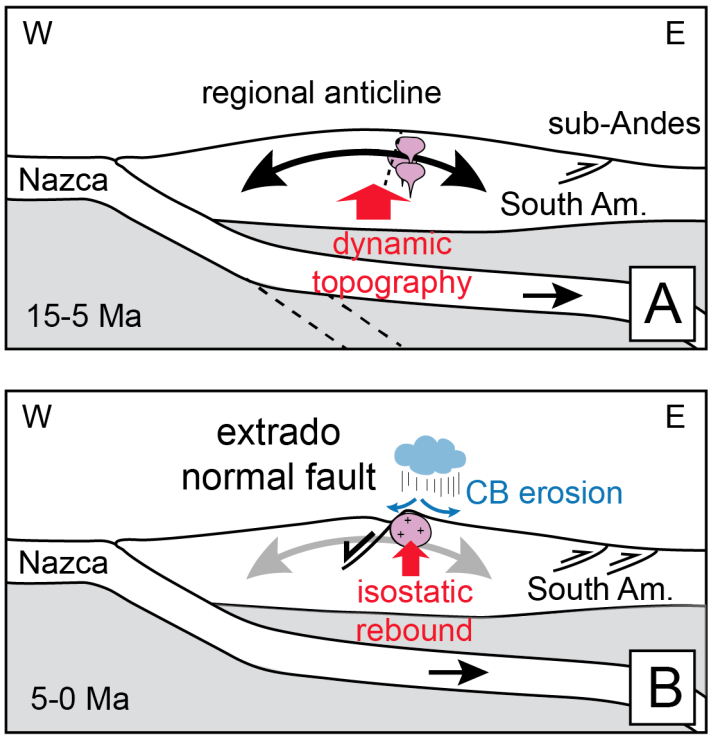

406

407 Figure 4: Model for the CBNF. A) 15-5 Ma: Dynamic topography after the slab flattening,
408 long wavelength antiform building above the Peruvian flat-slab and extrado normal faulting
409 (reactivation of an inherited structure). B) Then, between 5 and 0 Ma, the Cordillera Blanca
410 summits build an orographic barrier and erosion and flexural rebound contribute to surface
411 uplift in the Cordillera Blanca.

Conclusions et perspectives

7

Sommaire

Dans ce chapitre, je présente l'ensemble des interprétations et conclusions de mon travail de thèse. Les perspectives de mon travail seront détaillées dans la seconde partie.

This chapter presents the conclusions of my work and some outlooks.

7.1 Conclusions

Au cours de ma thèse j'ai été amenée à utiliser différentes techniques (thermochronologie basse température, géologie structurale, thermobarométrie et modélisation numérique) pour caractériser l'évolution de la Cordillère Blanche en lien avec le contexte géodynamique et la géologie régionale des Andes péruviennes. Dans les chapitres précédents, j'ai discuté mes résultats et leurs implications sur l'histoire du soulèvement et de l'exhumation des Andes du nord du Pérou, la paléogéographie de la Cordillère Occidentale et le régime de contraintes au dessus de la zone de subduction horizontale du nord Pérou. Ces nouvelles données font de cette région une des régions les mieux documentées du Pérou et des Andes. Mon travail a permis d'identifier différents processus qui participent au soulèvement et à la création du relief dans les Andes du nord du Pérou (Chapitres 3, 5 et 6). Je documente également les variations du régime de contraintes au dessus de la subduction plane péruvienne (Chapitre 4). Mon travail de thèse souligne l'impact de la géométrie de la subduction, notamment la présence d'une subduction horizontale, et du magmatisme sur le soulèvement et la création de relief dans la Cordillère Occidentale (Chapitre 3). Je mets également en évidence le rôle des glaciations dans l'exhumation récente de la Cordillère Blanche ainsi que l'importance de l'érosion et de la réponse flexurale associée dans le soulèvement et la création des hauts sommets de la Cordillère Blanche (Chapitres 5 et 6).

Les principaux résultats et conclusions de mon travail de thèse sont détaillés ci-dessous :

1. J'ai identifié, à partir de l'étude de la déformation fragile, une succession de différents épisodes tectoniques dans la région de la Cordillère Blanche depuis ~7 Ma (Chapitre 4). Ces changements de régimes de contraintes suggèrent que la présence d'une subduction horizontale n'entraine pas systématiquement une augmentation générale de la compression dans la plaque chevauchante comme précédemment suggéré (Ramos & Folguera 2009).
2. Mes nouvelles données de thermochronologie basse température (AFT et AHe) acquises dans la Cordillère Blanche et la Cordillère Noire ont permis de montrer puis de quantifier l'exhumation et le soulèvement régional de la Cordillère Occidentale au Nord du Pérou) à partir de 15 Ma (Chapitre 3). J'ai mis en évidence que le soulèvement régional enregistré par les données thermochronologiques peut être lié à l'aplatissement de la subduction et à la topographie dynamique induite par ce changement de pendage (Eakin et al. 2014).
3. A partir de l'étude de la déformation ductile (Chapitre 4), je suggère que le batholite de la Cordillère Blanche se met en place dans un régime décrochant dextre en accord avec les conclusions de Petford & Atherton (1992).
4. Les premières données de pression de mise en place du batholite de la Cordillère Blanche sont présentées dans ce manuscrit (Chapitre 5). Elles indiquent la mise en place du toit du batholite à faible profondeur dans la croûte (~3 km).

5. Sur la base des profondeurs de mise en place du batholite que j'ai obtenues et d'une compilation des âges de refroidissement (Chapitre 5), je propose la mise en place du batholite en une succession de sills, qui cristallisent de plus en plus profond, et/puis un basculement de la Cordillère Blanche vers l'est.

6. La modélisation des taux d'érosion basée sur l'ensemble des âges thermochronologiques disponibles dans la région de la Cordillère Blanche suggère une augmentation des taux d'érosion dans la Cordillère Blanche depuis 2 Ma (Chapitre 5). J'associe cette accélération de l'exhumation dans la Cordillère Blanche à l'érosion glaciaire. Finalement, le magmatisme ne semble alors pas contribuer de façon significative au soulèvement local de la Cordillère Blanche.

7. La modélisation de l'évolution du paysage avec FastScape met en évidence l'importance de l'érosion et du rebond flexural associé dans le soulèvement et la création du relief (Chapitre 6). Le climat et l'érosion semblent localement contribuer de façon importante à la morphologie de la Cordillère Occidentale, ce qui n'a jamais été démontré à ces latitudes.

8. Sur la base de tous ces résultats, je propose un nouveau modèle pour expliquer la présence de cette faille normale. Ce modèle implique un soulèvement régional de la Cordillère Occidentale, une faille normale d'extrado, une érosion importante de la Cordillère Blanche et un rebond flexural lié à l'érosion (Chapitre 6).

Mon travail contribue à la compréhension des processus qui contrôlent l'évolution du paysage dans les chaînes de montagnes. C'est la première étude qui traite des interactions entre processus de subduction (long terme), tectonique, climat et érosion glaciaire dans les Andes péruviennes. A l'échelle des Andes et de la construction de l'orogène (20 Ma), la géométrie de la subduction joue un rôle important dans le soulèvement. En revanche, le magmatisme ne semble pas induire de soulèvement en dépit de la génération de plutons dans la croûte supérieure et l'émission d'importants volumes de magmas. Cette absence de soulèvement pose la question de la contribution du magmatisme à l'épaississement crustal. Le climat et l'érosion semblent également contrôler l'évolution de la morphologie de la Cordillère Occidentale, au moins localement au cours du Quaternaire. L'importance du climat et de l'érosion sur la formation des hauts sommets andins est étonnante. En effet, la formation des hauts sommets dans d'autres chaînes de montagnes (e.g., Himalaya) est contrôlée principalement par la tectonique (e.g., Robert et al. 2009, Le Roux-Mallouf et al. 2015, Godard et al. 2014). Récemment, Vernant et al. (2013) ont proposé un contrôle de l'érosion sur le soulèvement des hauts sommets dans les chaînes de montagnes ou les taux de raccourcissement sont faibles (Pyrénées, Alpes Occidentales). Je pense qu'il serait également intéressant d'étudier l'influence du climat et de l'érosion sur le soulèvement dans d'autres chaînes de subduction (Colombie-Britannique, Alaska).

7.2 Perspectives

Grâce à mon travail de thèse, qui apporte de nouvelles données et contraint l'histoire de l'exhumation récente de la région de la Cordillère Blanche tout en intégrant le contexte géodynamique et la géologie régionale, cette région devient parmi les plus documentées des Andes Centrales en terme d'évolution du relief. J'ai répondu à certaines questions, mais néanmoins, mon travail ouvre des perspectives de recherche nouvelles et complémentaires :

1. Il serait intéressant de modéliser les âges déjà disponibles dans la Cordillère Occidentale au nord et au sud de la Cordillère Blanche (Eude 2014, Montario 2006) et d'acquérir d'autres données de thermochronologie basse-température, notamment de nouveaux profils âges-altitude pour (1) identifier une tendance dans l'initiation de l'exhumation du nord vers le sud qui confirmerait le rôle de la topographie dynamique proposé dans le chapitre 3, et (2) pour comparer le soulèvement de la Cordillère Noire au soulèvement d'une région soumise seulement à l'effet de l'aplatissement de la subduction.

2. Il faudrait également tester le modèle que j'ai proposé, pour expliquer la présence de la faille normale, en réalisant une modélisation thermo-cinématique de la région de la Cordillère Blanche, qui est maintenant bien documentée en terme de thermochronologie basse température, en prenant en compte mes modèles d'évolution du paysage.

3. L'exhumation totale sur la faille normale de la Cordillère blanche pourrait être contrainte sur l'ensemble du batholite en appliquant la thermobarométrie sur amphiboles à d'autres échantillons collectés le long de la faille.

4. Enfin, mon travail a concerné des échelles de temps allant d'une dizaine de million d'années au million d'années. L'échelle de temps plus court terme n'a pas été étudiée, ainsi que les liens entre ces différentes échelles temporelles. L'étude de la morphologie des rivières et la quantification des vitesses d'incision dans le Canyon del Pato et à l'amont du Rio Santa permettraient d'apporter une contrainte sur l'évolution du relief à une échelle de temps plus courte. Les vitesses d'incisions obtenues pourront être comparées aux taux d'exhumation de la Cordillère Blanche et si possible, le début de l'incision sera comparé avec l'augmentation de l'érosion à 2 Ma dans la Cordillère Blanche.

Bibliographie

Allmendinger, R. W. & Gubbels, T., 1996. Pure and simple shear plateau uplift, Altiplano-Puna, Argentina and Bolivia, *Tectonophysics*, **259**, 1–13. (Cité pages 20 et 44.)

Alpers, C. N. & Brimhall, G. H., 1988. Middle Miocene climatic change in the Atacama Desert, northern Chile: Evidence from supergene mineralization at La Escondida, *Geological Society of America Bulletin*, **100**(10), 1640–1656. (Cité page 18.)

Angelier, J., 1984. Tectonic analysis of fault slip data sets, *Journal of Geophysical Research: Solid Earth*, **89**(B7), 5835–5848. (Cité pages 38 et 55.)

Angelier, J. & Mechler, P., 1977. Sur une methode graphique de recherche des contraintes principales également utilisables en tectonique et en séismologie: la méthode des dièdres droits, *Bulletin de la Société Géologique de France*, **19**(6), 1309–1318. (Cité pages 37, 38 et 55.)

Atherton, M. P. & Petford, N., 1993. Generation of sodium-rich magmas from newly underplated basaltic crust, *Letters to Nature*, **362**, 144–146. (Cité pages 22 et 23.)

Avouac, J. P. & Burov, E. B., 1996. Erosion as a driving mechanism of intracontinental mountain growth, *Journal of Geophysical Research*, **101**(B8), 747–769. (Cité page 129.)

Bachmann, O. & Dungan, M. A., 2002. Temperature-induced Al-zoning in hornblendes of the Fish Canyon magma, Colorado, *American Mineralogist*. (Cité page 38.)

Barazangi, M. & Isacks, B. L., 1976. Spatial distribution of earthquakes and subduction of the Nazca plate beneath South America, *Geology*, **4**(11), 686–692. (Cité pages 13, 18, 22 et 43.)

Barke, R. & Lamb, S., 2006. Late Cenozoic uplift of the Eastern Cordillera, Bolivian Andes, *Earth and Planetary Science Letters*, **249**(3-4), 350–367. (Cité page 20.)

Barnes, J. B. & Ehlers, T. A., 2009. End member models for Andean Plateau uplift, *Earth Science Reviews*, **97**(1), 105–132. (Cité pages 20 et 89.)

Barnes, J. B. & Pelletier, J. D., 2006. Latitudinal variation of denudation in the evolution of the Bolivian Andes, *American Journal of Science*, **306**, 1–31. (Cité page 20.)

Beaumont, C., Fullsack, P., & Hamilton, J., 1992. Erosional control of active compressional orogens, in *Thrust tectonics*, pp. 1–18, ed. Springer, M., Springer Netherlands. (Cité page 129.)

Beckinsale, R. D., Sanchez-Fernandez, A. W., Brook, M., Cobbing, E. J., Taylor, W. P., & Moore, N. B., 1985. Rb-Sr whole rock isochron and K-Ar determination for the Coastal Batholith of Peru , in *Magmatism at a Plate Edge: The Peruvian Andes*, pp. 177–202, eds Pitcher, W. S., Atherton, M. P., Cobbing, E. J., & Beckinsale, R. D., Blackie Halstead press, Glasgow. (Cité pages 25 et 89.)

Boekhout, F., Spikings, R., Sempere, T., Chiaradia, M., Ulianov, A., & Schaltegger, U., 2012. Mesozoic arc magmatism along the southern Peruvian margin during Gondwana breakup and dispersal, *Lithos*, **146-147**(C), 48–64. (Cité page 89.)

Bonnot, D., 1984. Néotectonique et tectonique active de la Cordillère Blanche et du Callejon de Huaylas (Andes nord-péruviennes), *Thèse présentée pour obtenir le grade de docteur, Université de Paris-Sud, Centre d'Orsay*, pp. 1–202. (Cité pages 13, 21, 24 et 55.)

Bott, M., 1959. The mechanics of oblique slip faulting, *Geological Magazine*. (Cité page 37.)

Braun, J. & Willett, S. D., 2013. A very efficient O(n), implicit and parallel method to solve the stream power equation governing fluvial incision and landscape evolution, *Geomorphology*, **180-181**, 170–179. (Cité pages 40 et 129.)

Brenna, M., Price, R., Cronin, S. J., Smith, I. E. M., Sohn, Y. K., Kim, G. B., & Maas, R., 2014. Final Magma Storage Depth Modulation of Explosivity and Trachyte-Phonolite Genesis at an Intraplate Volcano: a Case Study from Ulleung Island, South Korea, *Journal of Petrology*, **55**(4), 709–747. (Cité page 39.)

Cederbom, C. E., Sinclair, H. D., & Schlunegger, F., 2004. Climate-induced rebound and exhumation of the European Alps, *Geology*, **32**(8), 709–712. (Cité page 129.)

Clapperton, C. M., 1983. The glaciation of the Andes, *Quaternary Science Reviews*, **2**, 83–155. (Cité page 23.)

Clapperton, C. M., 1993. Nature of environmental changes in South America at the Last Glacial Maximum, *Palaeogeography*, **101**, 189–208. (Cité page 90.)

Clift, P. D. & Ruiz, G. M. H., 2007. How does the Nazca Ridge subduction influence the modern Amazonian foreland basin ?: COMMENT and REPLY: COMMENT, *Geology*, **35**(1), e162–e162. (Cité pages 13 et 18.)

Clift, P. D., Pecher, I., Kukowski, N., & Hampel, A., 2003. Tectonic erosion of the Peruvian forearc, Lima Basin, by subduction and Nazca Ridge collision, *Tectonics*, **22**(3), n/a–n/a. (Cité pages 13 et 18.)

Cobbing, J., Pitcher, W., Baldock, J., Taylor, W., McCourt, W., & Snelling, N. J., 1981. Estudio geológico de la Cordillera Occidental del norte del Perú, *Instituto Geologico Minero y Metalurgico, Serie D. Estudios Especiales*, **10**(D), 1–252. (Cité pages 23, 25, 43 et 89.)

Coldwell, B., Clemens, J., & Petford, N., 2011. Deep crustal melting in the Peruvian Andes: Felsic magma generation during delamination and uplift, *Lithos*, **125**(1-2), 272–286. (Cité pages 23 et 24.)

Costa, F., Andreastuti, S., de Maisonneuve, C. B., & Pallister, J. S., 2013. Journal of Volcanology and Geothermal Research, *Journal of Volcanology and Geothermal Research*, **261**(C), 209–235. (Cité page 39.)

Dalmayrac, B. & Molnar, P., 1981. Parallel thrust and normal faulting in peru and constraints on the state of stress, *Earth and Planetary Sciences Letters*, **55**, 473–481. (Cité pages 13, 22, 23 et 89.)

Dávila, F. M., Lithgow-Bertelloni, C., & Giménez, M., 2010. Tectonic and dynamic controls on the topography and subsidence of the Argentine Pampas: The role of the flat slab, *Earth and Planetary Science Letters*, **295**(1-2), 187–194. (Cité page 13.)

De Angelis, S. H., Larsen, J., & Coombs, M., 2013. Pre-eruptive Magmatic Conditions at Augustine Volcano, Alaska, 2006: Evidence from Amphibole Geochemistry and Textures, *Journal of Petrology*, **54**(9), 1939–1961. (Cité pages 38 et 39.)

Delvaux, D., 2012. Release of program Win-Tensor 4.0 for tectonic stress inversion: statistical expression of stress parameters, in *EGU General Assembly Conference Abstracts*, Vienna. (Cité pages 37 et 55.)

Deverchère, J., Dorbath, C., & Dorbath, L., 1989. Extension related to a high topography: results from a microearthquake survey in the Andes of Peru and tectonic implications, *Geophysical Journal International*, **98**(2), 281–292. (Cité page 22.)

Doglioni, C., Harabaglia, P., Merlini, S., Mongelli, F., & Piromallo, C., 1999. Orogens and slabs vs. their direction of subduction, *Earth-Science Reviews*, **45**, 167–208. (Cité page 18.)

Donelick, R. A., 1993. Microscopic analysis of etch figure to determine fluorine chlorien and water rich apatite, *United States Patent*, **5267274**. (Cité page 31.)

Dunai, T. J., González López, G. A., & Juez-Larré, J., 2005. Oligocene–Miocene age of aridity in the Atacama Desert revealed by exposure dating of erosion-sensitive landforms, *Geology*, **33**(4), 321. (Cité page 18.)

Dunkl, I., 2002. TRACKKEY: a Windows program for calculation and graphical presentation of fission track data, *Computers & Geosciences*, **28**(1), 3–12. (Cité page 31.)

Eakin, C. M., Lithgow-Bertelloni, C., & Dávila, F. M., 2014. Influence of Peruvian flat-subduction dynamics on the evolution of western Amazonia, *Earth and Planetary Science Letters*, **404**(C), 250–260. (Cité pages 13, 18, 43, 44, 129 et 153.)

Ehlers, T. A. & Farley, K. A., 2003. Apatite (U–Th)/He thermochronometry: methods and applications to problems in tectonic and surface processes, *Earth and Planetary Science Letters*, **206**(1), 1–14. (Cité page 29.)

Erdmann, S., Martel, C., Pichavant, M., & Kushnir, A., 2014. Amphibole as an archivist of magmatic crystallization conditions: problems, potential, and implications for inferring magma storage prior to the paroxysmal 2010 eruption of Mount Merapi, Indonesia, *Contrib Mineral Petrol*. (Cité page 39.)

Espurt, N., Barbarand, J., Roddaz, M., Brusset, S., Baby, P., Saillard, M., & Hermoza, W., 2011. A scenario for late Neogene Andean shortening transfer in the Camisea Subandean zone (Peru, 12 S): Implications for growth of the northern Andean Plateau, *Geological Society of America Bulletin*, **123**(9-10), 2050–2068. (Cité page 20.)

Eude, A., 2014. *La croissance des Andes centrales du nord du Pérou (5-9 ° S): Propagation d'un prisme orogénique dans un contexte d'héritage tectonique et de subduction plane*, Ph.D. thesis, Université Toulouse III Paul Sabatier. (Cité page 155.)

Evans, N. J., Byrne, J. P., Keegan, J. T., & Dotter, L. E., 2005. Determination of uranium and thorium in zircon, apatite, and fluorite: Application to laser (U-Th)/He thermochronology, *Journal of Analytical Chemistry*, **60**(12), 1159–1165. (Cité page 33.)

Farber, D. L. & Hancock, G. S., submit. Tectonic and glacial forcing of motion along an active detachment fault in the Cordillera Blanca, central Peru, pp. 1–33. (Cité page 34.)

Farber, D. L., Hancock, G. S., Finkel, R. C., & Rodbell, D. T., 2005. The age and extent of tropical alpine glaciation in the Cordillera Blanca, Peru, *Journal of Quaternary Science*, **20**(7-8), 759–776. (Cité pages 23, 24 et 90.)

Farley, K. A., 2000. Helium diffusion from apatite: General behavior as illustrated by Durango fluorapatite, *Journal of Geophysical Research*, **105**(B2), 2903–2914. (Cité page 31.)

Farley, K. A., Wolf, R. A., & Silver, L. T., 1996. The effects of long alpha-stopping distances on (U-Th)/He ages, *Geochimica et Cosmochimica Acta*, **60**(21), 4223–4229. (Cité page 31.)

Farley, K. A., Reiners, P. W., & Nenow, V., 1999. An Apparatus for High-Precision Helium Diffusion Measurements from Minerals, *Analytical Chemistry*, **71**(10), 2059–2061. (Cité page 31.)

Farrar, E. & Noble, D. C., 1976. Timing of late Tertiary deformation in the Andes of Peru, *Geological Society of America Bulletin*, **87**(9), 1247–1250. (Cité pages 23 et 43.)

Feng, R. & Poulsen, C. J., 2014. Andean elevation control on tropical Pacific climate and ENSO, *Paleoceanography*, **29**(8), 795–809. (Cité page 43.)

Flowers, R. M., 2009. Exploiting radiation damage control on apatite (U–Th)/He dates in cratonic regions, *Earth and Planetary Science Letters*, **277**(1-2), 148–155. (Cité page 35.)

Fox, M., Herman, F., Willett, S. D., & May, D. A., 2014. A linear inversion method to infer exhumation rates in space and time from thermochronometric data, *Earth Surface Dynamics*, **2**(1), 47–65. (Cité pages 14, 35, 36, 89 et 90.)

Froidevaux, C. & Isacks, B. L., 1984. The mechanical state of the lithosphere in the Altiplano-Puna segment of the Andes, *Earth and Planetary Science Letters*, **71**(2), 305–314. (Cité page 56.)

Furlong, K. P. & Chapman, D. S., 1982. Thermal modeling of the geometry of subduction with implications for the tectonics of the overriding plate, *Journal of Geophysical Research*, **87**(B3), 1786–1802. (Cité page 18.)

Gallagher, K., 2012. Transdimensional inverse thermal history modeling for quantitative thermochronology, *Journal of Geophysical Research*, **117**(B2), B02408. (Cité page 35.)

Gallagher, K., Brown, R., & Johnson, C., 1998. Fission track analysis and its applications to geological problems, *Annu. Rev. Earth Planet. Sci.*, **26**(1), 519–572. (Cité page 14.)

Gallagher, K., Charvin, K., Nielsen, S., Sambridge, M., & Stephenson, J., 2009. Markov chain Monte Carlo (MCMC) sampling methods to determine optimal models, model resolution and model choice for Earth Science problems, *Marine and Petroleum Geology*, **26**(4), 525–535. (Cité page 35.)

Garzione, C. N., Molnar, P., Libarkin, J. C., & MacFadden, B. J., 2006. Rapid late Miocene rise of the Bolivian Altiplano: Evidence for removal of mantle lithosphere, *Earth and Planetary Science Letters*, **241**(3-4), 543–556. (Cité pages 20 et 44.)

Garzione, C. N., Hoke, G. D., Libarkin, J. C., Withers, S., MacFadden, B., Eiler, J., Ghosh, P., & Mulch, A., 2008. Rise of the Andes, *Science*, **320**(5881), 1304–1307. (Cité page 20.)

Gautheron, C. & Tassan-Got, L., 2010. A Monte Carlo approach to diffusion applied to noble gas/helium thermochronology, *Chemical Geology*, **273**(3-4), 212–224. (Cité pages 32 et 33.)

Gautheron, C., Tassan-Got, L., Barbarand, J., & Pagel, M., 2009. Effect of alpha-damage annealing on apatite (U–Th)/He thermochronology, *Chemical Geology*, **266**(3), 157–170. (Cité pages 14 et 35.)

Gautheron, C., Espurt, N., & Barbarand, J., 2012. Direct dating of thick– and thin– kin thrusts in the Peruvian Subandean zone through apatite (U–Th)/He and fission track thermochronometry, *Basin Reasearch*. (Cité page 20.)

Gautheron, C., Barbarand, J., Ketcham, R. A., Tassan-Got, L., van der Beek, P., Pagel, M., Pinna-Jamme, R., Couffignal, F., & Fialin, M., 2013. Chemical Geology, *Chemical Geology*, **351**(C), 257–267. (Cité page 35.)

Gephart, J. W., 1994. Topography and subduction geometry in the central Andes: Clues to the mechanics of a noncollisional orogen, *Journal of Geophysical Research: Solid Earth*, **99**(B6), 12279–12288. (Cité pages 20 et 44.)

Giambiagi, L. B., Tunik, M. A., & Ghiglione, M., 2001. Cenozoic tectonic evolution of the Alto Tunuyán foreland basin above the transition zone between the flat and normal subduction segment (33 °30'–34 °S), western Argentina, *Journal of South American Earth Sciences*, **14**(7), 707–724. (Cité page 13.)

Giletti, B. J. & Day, H. W., 1968. Potassium–Argon Ages of Igneous Intrusive Rocks in Peru, *Nature*, **220**(5167), 570–572. (Cité page 89.)

Giovanni, M. K., 2007. *Tectonic and Thermal Evolution of the Cordillera Blanca Detachment System, Peruvian Andes: Implication for Normal Faulting in a Contractionnal Orogen*, Ph.D. thesis, University of California, Los Angeles. (Cité pages 13, 21, 22, 24, 35, 43, 55, 89 et 90.)

Giovanni, M. K., Horton, B. K., Garzione, C. N., McNulty, B., & Grove, M., 2010. Extensional basin evolution in the Cordillera Blanca, Peru: Stratigraphic and isotopic records of detachment faulting and orogenic collapse in the Andean hinterland, *Tectonics*, **29**(6), TC6007. (Cité pages 23, 24, 26 et 43.)

Godard, V., Bourlès, D. L., Spinabella, F., Burbank, D. W., Bookhagen, B., Burch Fisher, G., Moulin, A., & Léanni, L., 2014. Dominance of tectonics over climate in Himalayan denudation, *Geology*, **42**(3), 243–246. (Cité page 154.)

Guillaume, B., Martinod, J., Husson, L., Roddaz, M., & Riquelme, R., 2009. Neogene uplift of central eastern Patagonia: Dynamic response to active spreading ridge subduction ?, *Tectonics*, **28**(2), TC2009. (Cité page 13.)

Gutscher, M. A., Malavieille, J., Lallemand, S., & Collot, J.-Y., 1999. Tectonic segmentation of the North Andean margin: impact of the Carnegie Ridge collision, *Earth and Planetary Science Letters*, **168**(3), 255–270. (Cité pages 14 et 43.)

Hagen, R. A. & Moberly, R., 1994. Tectonic effects of a subducting aseismic ridge: the subduction of the Nazca Ridge at the Peru Trench, *Marine geophysical researches*, **16**(2), 145–161. (Cité page 13.)

Herman, F. & Brandon, M. T., 2015. Mid-latitude glacial erosion hotspot related to equatorial shifts in southern Westerlies, *Geology*, **-**, 1–4. (Cité pages 35, 89 et 90.)

herman, F., Rhodes, E. J., Braun, J., & Heiniger, L., 2010. Uniform erosion rates and relief amplitude during glacial cycles in the Southern Alps of New Zealand, as revealed from OSL-thermochronology, *Earth and Planetary Science Letters*, **297**(1-2), 183–189. (Cité page 33.)

Hodson, K. R., 2012. Morphology, exhumation, and Holocene erosion rates from a tropical glaciated mountain range: the Cordillera Blanca, Peru, *McGill University Masters of science*, pp. 1–94. (Cité pages 35 et 90.)

Holland, T. & Blundy, J., 1994. Non-ideal interactions in calcic amphiboles and their bearing on amphibole-plagioclase thermometry, *Contributions to Mineralogy and Petrology*. (Cité page 38.)

Hoorn, C., Wesselingh, F. P., ter Steege, H., Bermudez, M. A., Mora, A., Sevink, J., Sanmartin, I., Sanchez-Meseguer, A., Anderson, C. L., Figueiredo, J. P., Jaramillo, C., Riff, D., Negri, F. R., Hooghiemstra, H., Lundberg, J., Stadler, T., Sarkinen, T., & Antonelli, A., 2010. Amazonia Through Time: Andean Uplift, Climate Change, Landscape Evolution, and Biodiversity, *Science*, **330**(6006), 927–931. (Cité page 43.)

Horton, B. K., 1999. Erosional control on the geometry and kinematics of thrust belt development in the central Andes, *Tectonics*, **18**(6), 1292–1304. (Cité pages 20, 44 et 130.)

Hurford, A. J. & Green, P. F., 1982. A users' guide to fission track dating calibration, *Earth and Planetary Science Letters*, **59**(2), 343–354. (Cité page 30.)

Husson, L., 2003. Thickening the Altiplano crust by gravity-driven crustal channel flow, *Geophysical Research Letters*, **30**(5), 1243. (Cité pages 20 et 44.)

Husson, L., Conrad, C. P., & Faccenna, C., 2010. Plate motions, Andean orogeny, and volcanism above the South Atlantic convection cell , *Earth and Planetary Science Letters*, **317-318**, 126–135. (Cité page 13.)

Isacks, B. L., 1988. Uplift of the central Andean plateau and bending of the Bolivian orocline, *Journal of Geophysical Research: Solid Earth (1978–2012)*, **93**(B4), 3211–3231. (Cité pages 20 et 44.)

James, D. E. & Sacks, I. S., 1999. Cenozoic formation of the Central Andes: a geophysical perspective, in *Geology and ore deposits of the Central Andes*, ed. skinner, B. J., Society of Economic Geologists. (Cité pages 20 et 89.)

Johnson, M. C. & Rutherford, M. J., 1989. Experimental calibration of the aluminum-in-hornblende geobarometer with application to Long Valley caldera (California) volcanic rocks, *Geology*. (Cité page 38.)

Jordan, T. E., Isacks, B. L., Allmendinger, R. W., Brewer, J. A., Ramos, V. A., & Ando, C. J., 1983. Andean tectonics related to geometry of subducted Nazca plate, *Geological Study of America Bulletin*, **94**, 341–361. (Cité pages 22 et 55.)

Ketcham, R. A., Carter, A., Donelick, R. A., Barbarand, J., & Hurford, A. J., 2007. Improved measurement of fission-track annealing in apatite using c-axis projection, *American Mineralogist*, **92**(5-6), 789–798. (Cité page 35.)

Ketcham, R. A., Gautheron, C., & Tassan-Got, L., 2011. Accounting for long alpha-particle stopping distances in (U-Th-Sm)/He geochronology: Refinement of the baseline case, *Geochimica et Cosmochimica Acta*, **75**(24), 7779–7791. (Cité page 33.)

Kiss, B., Harangi, S., Ntaflos, T., Mason, P. R. D., & Pál-Molnár, E., 2014. Amphibole perspective to unravel pre-eruptive processes and conditions in volcanic plumbing systems beneath intermediate arc volcanoes: a case study from Ciomadul volcano (SE Carpathians), *Contributions to Mineralogy and Petrology*, **167**(3), 1–27. (Cité page 39.)

Kley, J. & Monaldi, C. R., 1998. Tectonic shortening and crustal thickness in the Central Andes: How good is the correlation ?, *Geology*, **26**(8), 723–726. (Cité pages 20 et 44.)

Kono, M., Fukao, Y., & Yamamoto, A., 1989. Mountain building in the Central Andes, *Journal of Geophysical Research*, **94**(B4), 3891–3905. (Cité page 89.)

Kraml, M., Pik, R., Rahn, M., Selbekk, R., Carignan, J., & Keller, J., 2006. A New Multi,ÄêMineral Age Reference Material for 40Ar/39Ar,(U,ÄêTh)/He and Fission Track Dating Methods: The Limberg t3 Tuff, *Geostandards and Geoanalytical Research*, **30**(2), 73–86. (Cité page 33.)

Lallemand, S., Heuret, A., & Boutelier, D., 2005. On the relationships between slab dip, back-arc stress, upper plate absolute motion, and crustal nature in subduction zones, *Geochemistry Geophysics Geosystems*, **6**(9), 1–18. (Cité page 18.)

Lamb, S. & Davis, P., 2003. Cenozoic climate change as a possible cause for the rise of the Andes, *Nature*, **425**(6960), 792–797. (Cité pages 20 et 44.)

Lamb, S. & Hoke, L., 1997. Origin of the high plateau in the Central Andes, Bolivia, South America, *Tectonics*, **16**(4), 623–649. (Cité pages 20 et 44.)

Lanphere, M. A. & Baadsgaard, H., 2001. Precise K–Ar, 40 Ar/ 39 Ar, Rb–Sr and U/Pb mineral ages from the 27.5 Ma Fish Canyon Tuff reference standard, *Chemical Geology*, **175**(3), 653–671. (Cité page 30.)

Larson, R. L. & Ladd, J. W., 1973. Evidence for the opening of the South Atlantic in the Early Cretaceous, *Nature*, **246**, 209–212. (Cité page 19.)

Laslett, G. M., Galbraith, R. F., & Green, P. F., 1994. The analysis of projected fission track lengths, *Radiation measurements*, **23**(1), 103–123. (Cité page 31.)

Le Roux-Mallouf, R., Godard, V., Cattin, R., Ferry, M., Gyeltshen, J., Ritz, J. F., Drupka, D., Guillou, V., Arnold, M., Aumaitre, G., Bourlès, D. L., & Keddadouche, K., 2015. Evidence for a wide and gently dipping Main Himalayan Thrust in western Bhutan, *Geophysical Research Letters*, **42**. (Cité page 154.)

Luyendyk, B. P., 1970. Dips of downgoing lithospheric plates beneath island arcs, *Geological Society of America Bulletin*, **81**, 3411–3416. (Cité page 18.)

Mamani, M., Wörner, G., & Sempere, T., 2010. Geochemical variations in igneous rocks of the Central Andean orocline (13 S to 18 S): Tracing crustal thickening and magma generation through time and space, *Geological Society of America Bulletin*, **122**(1-2), 162–182. (Cité pages 20 et 89.)

Manea, V. C., Perez-Gussinye, M., & Manea, M., 2011. Chilean flat slab subduction controlled by overriding plate thickness and trench rollback, *Geology*, **40**(1), 35–38. (Cité page 13.)

Margirier, A., Robert, X., Audin, L., Gautheron, C., Bernet, M., Hall, S., & Simon-Labric, T., 2015. Slab flattening, magmatism and surface uplift in the Cordillera Occidental (northern Peru), *Geology*, pp. 1–4. (Cité pages 90 et 129.)

Martinod, J., Husson, L., Roperch, P., Guillaume, B., & Espurt, N., 2010. Horizontal subduction zones, convergence velocity and the building of the Andes, *Earth and Planetary Science Letters*, **299**(3-4), 299–309. (Cité pages 18 et 55.)

Masek, J. G., Isacks, B. L., & Gubbels, T. L., 1994. Erosion and tectonics at the margins of continental plateaus, *Journal of Geophysical Research*, **99**(B7), 13941–13956. (Cité pages 20, 44 et 130.)

McDowell, F. W., McIntosh, W. C., & Farley, K. A., 2004. A precise ^{40}Ar-^{39}Ar reference age for the Durango apatite (U-Th)/He and fission-track dating standard, *Chemical Geology*, **214**(3-4), 249–263. (Cité pages 30 et 33.)

McNulty, B. A. & Farber, D. L., 2002. Active detachment faulting above the Peruvian flat slab, *Geology*, **30**(6), 567–570. (Cité pages 13, 14, 22, 23, 55 et 89.)

McNulty, B. A., Farber, D. L., Wallace, G. S., Lopez, R., & Palacios, O., 1998. Role of plate kinematics and plate-slip-vector partitioning in continental magmatic arcs: Evidence from the Cordillera Blanca, Peru, *Geology*, **26**(9), 827–830. (Cité pages 22 et 23.)

McQuarrie, N., 2002. The kinematic history of the central Andean fold-thrust belt, Bolivia: Implications for building a high plateau, *Geological Society of America Bulletin*, **114**(8), 950–963. (Cité pages 20 et 44.)

McQuarrie, N., Horton, B. K., ZANDT, G., & BECK, S., 2005. Lithospheric evolution of the Andean fold–thrust belt, Bolivia, and the origin of the central Andean plateau, *Tectonophysics*. (Cité page 20.)

McQuarrie, N., Ehlers, T. A., Barnes, J. B., & Meade, B., 2008. Temporal variation in climate and tectonic coupling in the central Andes, *Geology*, **36**(12), 999. (Cité page 20.)

Mégard, F., 1984. The Andean orogenic period and its major structures in central and northern Peru, *Journal of the Geological Society*, **141**(5), 893–900. (Cité page 56.)

Mégard, F., Noble, D. C., McKEE, E. H., & Bellon, H., 1984. Multiple pulses of Neogene compressive deformation in the Ayacucho intermontane basin, Andes of central Peru, *Geological Society of America Bulletin*, **95**(9), 1108–1117. (Cité pages 20 et 21.)

Michalak, M., 2013. *Exhumation of the Peruvian Andes ; insight from mineral chronometers*, Ph.D. thesis, University of California Santa Cruz. (Cité pages 35 et 90.)

Mitchell, S. G. & Reiners, P. W., 2003. Influence of wildfires on apatite and zircon (U-Th)/He ages, *Geology*, **31**(12), 1025–1028. (Cité page 32.)

Molnar, P. & Atwater, T., 1978. Interarc spreading and Cordilleran tectonics as alternates related to the age of subducted oceanic lithosphere, *Earth and Planetary Science Letters*, **41**, 330–340. (Cité page 18.)

Montario, M. J., 2001. Exhumation of the Cordillera Blanca, NorthernPeru, based on apatite fission track analysis, *Departement of Geology, Unpublished Thesis, Union Colllege, Schenectady, New York*, pp. 1–12. (Cité pages 35 et 90.)

Montario, M. J., 2006. *Thermochronological evidence for Neogene incision of the Rio Pativilca Canyon, Northern Peru*, Ph.D. thesis, University at Albany, State University of New York. (Cité pages 35 et 155.)

Montgomery, D. R., 1994. Valley incision and the uplift of mountain peaks, *Journal of Geophysical Research: Solid Earth*, **99**(B7), 13913–13921. (Cité page 129.)

Montgomery, D. R. & Brandon, M. T., 2002. Topographic controls on erosion rates in tectonically active mountain ranges, *Earth and Planetary Science Letters*, **201**, 481–489. (Cité page 129.)

Montgomery, D. R., Balco, G., & Willett, S. D., 2001. Climate, tectonics, and the morphology of the Andes, *Geology*, **29**(7), 579–582. (Cité pages 13, 20, 44 et 130.)

Mortimer, C., 1980. Drainage evolution of the Atacama Desert of northernmost Chile, *Revista Geológica de Chile*, **11**, 3–28. (Cité page 18.)

Mukasa, S. B., 1984. *Comparative Pb isotope systematics and zircon U-Pb geochronology for the Coastal, San Nicolás and Cordillera Blanca Batholiths, Peru*, Ph.D. thesis, University of California, Santa Barbara. (Cité pages 13, 22, 43 et 89.)

Mukasa, S. B. & Tilton, G. R., 1984. Lead isotope systematics in batholithic rocks of the western and coastal cordilleras, Peru, in *Andean Magmatism*, pp. 180–189, Boston, Birkhäuser. (Cité page 25.)

Myers, J. S., 1976. Erosion surfaces and ignimbrite eruption, measures of Andean uplift in northern Peru, *Geological Journal*, **11**(1), 29–44. (Cité page 43.)

Nocquet, J.-M., Villegas-Lanza, J. C., Chlieh, M., Mothes, P. A., Rolandone, F., Jarrin, P., Cisneros, D., Alvarado, A., Audin, L., Bondoux, F., Martin, X., Font, Y., Régnier, M., Vallée, M., Tran, T., Beauval, C., Maguiña Mendoza, J. M., Martinez, W., Tavera, H., & Yepes, H., 2014. Motion of continental slivers and creeping subduction in the northern Andes, *Nature Geoscience*, **7**(4), 287–291. (Cité page 56.)

O'Driscoll, L. J., Richards, M. A., & Humphreys, E. D., 2012. Nazca-South America interactions and the late Eocene-late Oligocene flat-slab episode in the central Andes, *Tectonics*, **31**(2), n/a–n/a. (Cité page 18.)

Petford, N. & Atherton, M., 1996. Na-rich partial melts from newly underplated basaltic crust: the Cordillera Blanca Batholith, Peru, *Journal of Petrology*, **37**(6), 1491–1521. (Cité page 23.)

Petford, N. & Atherton, M. P., 1992. Granitoid emplacement and deformation along a major crustal lineament: the Cordillera Blanca, Peru, *Tectonophysics*, **205**(1), 171–185. (Cité pages 14, 22, 23, 55, 85 et 153.)

Putirka, K., 2014. Amphibole-liquid equilibria: Barometers and thermometers for volcanic systems, *2014 GSA Annual Meeting in Vancouver*. (Cité page 39.)

Ramos, V. A. & Folguera, A., 2009. Andean flat-slab subduction through time, *Geological Society, London, Special Publications*, **327**(1), 31–54. (Cité pages 18, 19, 22, 55 et 153.)

Ramos, V. A., Cristallini, E. O., & Pérez, D. J., 2002. The Pampean flat-slab of the Central Andes, *Journal of South American Earth Sciences*, **15**(1), 59–78. (Cité pages 13 et 22.)

Regard, V., Lagnous, R., Espurt, N., Darrozes, J., Baby, P., Roddaz, M., Calderon, Y., & Hermoza, W., 2009. Geomorphic evidence for recent uplift of the Fitzcarrald Arch (Peru): A response to the Nazca Ridge subduction, *Geomorphology*, **107**(3-4), 107–117. (Cité pages 13 et 18.)

Rhodes, E. J., Singarayer, J. S., Raynal, J. P., Westaway, K. E., & Sbihi-Alaoui, F. Z., 2006. New age estimates for the Palaeolithic assemblages and Pleistocene succession of Casablanca, Morocco, *Quaternary Science Reviews*, **25**(19-20), 2569–2585. (Cité page 34.)

Ridolfi, F. & Renzulli, A., 2012. Calcic amphiboles in calc-alkaline and alkaline magmas: thermobarometric and chemometric empirical equations valid up to 1,130 °C and 2.2 GPa, *Contributions to Mineralogy and Petrology*, **163**(5), 877–895. (Cité pages 9, 27, 38, 39 et 89.)

Ridolfi, F., Renzulli, A., & Puerini, M., 2010. Stability and chemical equilibrium of amphibole in calc-alkaline magmas: an overview, new thermobarometric formulations and application to subduction-related volcanoes, *Contributions to Mineralogy and Petrology*, **160**(1), 45–66. (Cité page 38.)

Ritz, J. F. & Taboada, A., 1993. Revolution stress ellipsoids in brittle tectonics resulting from an uncritical use of inverse methods, *Bulletin de la Société Géologique de France*, **164**(4), 519–531. (Cité page 37.)

Robert, X., Van Der Beek, P., Braun, J., Perry, C., Dubille, M., & Mugnier, J. L., 2009. Assessing Quaternary reactivation of the Main Central thrust zone (central Nepal Himalaya): New thermochronologic data and numerical modeling, *Geology*, **37**(8), 731–734. (Cité page 154.)

Rodbell, D. T., 1993. Subdivision of late Pleistocene moraines in the Cordillera Blanca, Peru, based on rock-weathering features, soils, and radiocarbon dates, *Quaternary Research*. (Cité pages 23 et 90.)

Rodbell, D. T., Smith, J. A., & Mark, B. G., 2009. Quaternary Science Reviews, *Quaternary Science Reviews*, **28**(21-22), 2165–2212. (Cité page 24.)

Rosenbaum, G., Giles, D., Saxon, M., Betts, P. G., Weinberg, R. F., & Duboz, C., 2005. Subduction of the Nazca Ridge and the Inca Plateau: Insights into the formation of ore deposits in Peru, *Earth and Planetary Science Letters*, **239**(1-2), 18–32. (Cité pages 14 et 43.)

Rutherford, M. J. & Devine, J. D., 2003. Magmatic conditions and magma ascent as indicated by hornblende phase equilibria and reactions in the 1995–2002 Soufriere Hills magma, *Journal of Petrology*. (Cité page 38.)

Rutherford, M. J. & Devine, J. D., 2008. Magmatic conditions and processes in the storage zone of the 2004-2006 Mount St. Helens dacite, *US Geological Survey professional*, **1750**. (Cité page 38.)

Schellart, W. P., 2005. Influence of the subducting plate velocity on the geometry of the slab and migration of the subduction hinge, *Earth and Planetary Science Letters*, **231**(3-4), 197–219. (Cité page 18.)

Schildgen, T. F., Hodges, K. V., Whipple, K. X., Reiners, P. W., & Pringle, M. S., 2007. Uplift of the western margin of the Andean plateau revealed from canyon incision history, southern Peru, *Geology*, **35**(6), 523. (Cité pages 20 et 44.)

Schmidt, M. W., 1992. Amphibole composition in tonalite as a function of pressure: an experimental calibration of the Al-in-hornblende barometer, *Contributions to Mineralogy and Petrology*. (Cité page 38.)

Sébrier, M., Mercier, J. l., Macharé, J., Bonnot, D., Cabrera, J., & Blanc, J. L., 1988. The state of stress in an overriding plate situated above a flat slab: The Andes of Central Peru, *Tectonics*, **7**(4), 895–928. (Cité page 13.)

Shane, P. & Smith, V. C., 2013. Using amphibole crystals to reconstruct magma storage temperatures and pressures for the post-caldera collapse volcanism at Okataina volcano, *Lithos*, **156-159**(C), 159–170. (Cité pages 38 et 39.)

Smith, J. A., Finkel, R. C., Farber, D. L., Rodbell, D. T., & Seltzer, G. O., 2005. Moraine preservation and boulder erosion in the tropical Andes: interpreting old surface exposure ages in glaciated valleys, *Journal of Quaternary Science*, **20**(7-8), 735–758. (Cité page 90.)

Somoza, R., 1998. Updated Nazca (Farallon)—South America relative motions during the last 40 My: implications for mountain building in the central Andean region, *Journal of South American Earth Sciences*, **11**(3), 211–215. (Cité page 56.)

Spiegel, C., Kohn, B., Belton, D., Berner, Z., & Gleadow, A., 2009. Apatite (U–Th–Sm)/He thermochronology of rapidly cooled samples: The effect of He implantation, *Earth and Planetary Science Letters*, pp. 1–10. (Cité page 31.)

Spikings, R. A., Dungan, M. A., Foeken, J., Carter, A., Page, L., & Stuart, F., 2008. Tectonic response of the central Chilean margin (35-38 S) to the collision and subduction of heterogeneous oceanic crust: a thermochronological study, *Journal of the Geological Society*, **165**(5), 941–953. (Cité pages 13 et 18.)

Stern, T. A., Baxter, A. K., & Barrett, P. J., 2005. Isostatic rebound due to glacial erosion within the Transantarctic Mountains, *Geology*, **33**(3), 221–224. (Cité page 129.)

Stewart, J. W., Evernden, J. F., & Snelling, N. J., 1974. Age determinations from Andean Peru: a reconnaissance survey, *Geological Society of America Bulletin*, **85**(7), 1107–1116. (Cité page 89.)

Strecker, M. R., Alonso, R., Bookhagen, B., Carrapa, B., Coutand, I., Hain, M. P., Hilley, G. E., Mortimer, E., Schoenbohm, L., & Sobel, E. R., 2009. Does the topographic distribution of the central Andean Puna Plateau result from climatic or geodynamic processes ?, *Geology*, **37**(7), 643–646. (Cité page 20.)

Thorpe, R. S., Francis, P. W., & Harmon, R. S., 1981. Andean andesites and crustal growth, *Royal Society of London Philosophical Transactions Series A*, **301**(1461), 305–320. (Cité page 20.)

Turner, S. J., Izbekov, P., & Langmuir, C., 2013. Journal of Volcanology and Geothermal Research, *Journal of Volcanology and Geothermal Research*, pp. 1–14. (Cité pages 38 et 39.)

Uyeda, S. & Kanamori, H., 1979. Back-arc opening and the mode of subduction, *J. geophys. Res*, **84**(B3), 1049–1061. (Cité page 18.)

van Hunen, J., Van Den BERG, A. P., & Vlaar, N. J., 2002. On the role of subducting oceanic plateaus in the development of shallow flat subduction, *Tectonophysics*, **352**(3), 317–333. (Cité page 19.)

Vernant, P., Hivert, F., Chery, J., Steer, P., Cattin, R., & Rigo, A., 2013. Erosion-induced isostatic rebound triggers extension in low convergent mountain ranges, *Geology*, **41**(4), 467–470. (Cité page 154.)

Vlaar, N. J. & Wortel, M., 1976. Lithospheric aging, instability and subduction, *Tectonophysics*, **32**, 331–351. (Cité page 18.)

Wallace, R. E., 1951. Geometry of shearing stress and relation to faulting, *The Journal of Geology*. (Cité page 37.)

Willett, S. D., 1999. Orogeny and orography: The effects of erosion on the structure of mountain belts, *Journal of Geophysical Research: Solid Earth (1978–2012)*, **104**(B12), 28957–28981. (Cité page 129.)

Wilson, P. A., 1975. *K-Ar age studies in Peru with special reference to the emplacement of the Coastal Batholith*, Ph.D. thesis, University of Liverpool, Liverpool. (Cité pages 25 et 89.)

Wipf, M., 2006. *Evolution of the Western Cordillera and Coastal Margin of Peru: Evidence from low-temperature Thermochronology and Geomorphology*, Ph.D. thesis, Swiss Federal Institute of Technology Zürich. (Cité pages 35 et 90.)

Wise, J. M. & Noble, D. C., 2003. Geomorphic evolution of the Cordillera Blanca, Northern Peru, *Boletin de la sociedad Geologica del Peru*, **96**, 1–21. (Cité page 23.)

Wolf, R. A., Farley, K. A., & Silver, L. T., 1996. Helium diffusion and low-temperature thermochronometry of apatite, *Geochimica et Cosmochimica Acta*, **60**(21), 4231–4240. (Cité page 31.)

Yücel, C., Arslan, M., Temizel, İ., & Abdioğlu, E., 2013. Volcanic facies and mineral chemistry of Tertiary volcanics in the northern part of the Eastern Pontides, northeast Turkey: implications for pre-eruptive crystallization conditions and magma chamber processes, *Mineralogy and Petrology*, **108**(3), 439–467. (Cité page 39.)

Zanon, V., Kueppers, U., Pacheco, J. M., & Cruz, I., 2013. Volcanism from fissure zones and the Caldeira central volcano of Faial Island, Azores archipelago: geochemical processes in multiple feeding systems, *Geological Magazine*, **150**(03), 536–555. (Cité page 39.)

ANNEXES

Annexes

8.1 Annexes du Chapitre 3

8.1.1 Methods and thermal histories modeling

Supplementary data

A- Methods

A.1- Sampling and mineral separation

Samples were collected in the Cordilleras Blanca and Negra in northern Peru (Fig. 1, Tab. 1 and 2). Apatite grains were separated at ISTerre (Grenoble, France) using heavy-liquid separation technique (LST and methylene iodide with densities of 2.8 and 3.3).

A.2- Apatite (U-Th-Sm)/He

We carried out apatite picking at ISTerre (Grenoble, France); and apatite grains were selected according to their morphology, size and purity (absence of visible inclusions; from 1 to 5 grains dated per sample, depending on sample apatite quality). We measured the selected crystals and placed them in platinum tubes for He extraction at Paris-Sud University (Orsay, France). We used a diode laser to heat the platinum tubes at 1050±50°C during 5 min to allow a total He degassing; a reheat under the same conditions allowed checking for the presence of He trapped in small retentive inclusions (e.g. zircon). We determined the ^{4}He content by comparison with a known amount of ^{3}He spike added during analysis. We placed platinum tubes into single-use polypropylene vials after He extraction and dissolved apatite grains for 1 h at 90 °C in a 50 µl HNO_3 solution containing a known concentration of ^{235}U, ^{230}Th and ^{149}Sm that we then filled with 1 ml of ultrapure MQ water. U, Th-Sm measurements followed a procedure similar to that of Evans *et al.* (2005). We measured U, Th and Sm concentrations in the solution using an inductively coupled quadrupole plasma mass spectrometry (ICP-QMS; series CCT Thermo-Electron at LSCE, Gif-sur-yvette, France). We calibrated the analysis using external age standards, including Limberg Tuff and Durango apatite, which provided mean AHe ages of 16.5 ± 1.6 Ma and 31.4 ± 2.3 Ma respectively. These values are in agreement with literature data, 16.8 ± 1.1 Ma for the Limberg Tuff (Kraml *et al.*, 2006) and 31.02 ± 0.22 Ma for Durango (McDowell *et al.*, 2005). We corrected single ages using the calculated ejection factor F_T, determined using the Monte Carlo simulation technique of Ketcham *et al.* (2011); we calculated the equivalent-sphere radius with the procedure of Gautheron and Tassan-Got (2010). AHe ages and He-U-Th-Sm content are reported on Table 1. The error on AHe age should be considered at 10%, reflecting the sum of errors in the ejection-factor correction and age dispersion of the standards.

A.3- FT dating methods

We performed AFT analysis at the Institut de Sciences de la Terre (ISTerre, Grenoble). We mounted the apatite grains in epoxy and polished their surfaces. We etched the mounts at 5.5M HNO_3 during 20 seconds at 21±1 °C to reveal spontaneous tracks. We obtained AFT ages with the external detector method (Hurford and Green, 1982) using a zeta calibration approach, with a zeta of 268±7 (A. Margirier) for the IRMM-540M dosimeter glass. Muscovite foils, as external detectors, covered apatite mounts. We carried out the irradiation of the samples at FRM II reactor in Garching (München, Germany) with a nominal fluence of 8×10^{15} neutrons/cm^2. After irradiation, we etched mica detectors for 18 minutes in 48% HF at 21±1°C to reveal induced tracks. We counted tracks and measured track length distribution using an Olympus optical microscope at a magnification of ×1250, according to the recommendations of Laslett *et al.* (1994). We carried out age calculation and statistics with Trackkey software (Dunkl, 2002). We report AFT ages as central age at ±1σ. Most of the samples do not yield enough confined track lengths to study track length distribution because of their low uranium content and young ages. To enhance the number of etchable confined tracks we irradiated 3 samples by a Cf source in the University of Melbourne (Australia). We used Dpar (mean fission-track etch pit diameter, parallel to the C axis of the crystal) measurement to characterize the chemical composition of the apatite crystals and estimate the kinetic behavior of single grains (Donelick, 1993). The results are presented in Table 2.

B- Thermal histories modeling

We determined the thermal history with the QTQt software that allows inverting AFT annealing and AHe diffusion parameters with the Markov chain Monte Carlo method (Gallagher *et al.*, 2009; Gallagher, 2012) for single samples and for complete vertical profiles. The inversion code incorporates kinetic models of He diffusion in apatite (Flowers *et al.*, 2009; Gautheron *et al.*, 2009) and AFT annealing multi-kinetic model (Ketcham *et al.*, 2007). The modeling procedure is detailed in Gallagher (2012). The input parameters used to model each profile are the central AFT ages, the track length distribution, the Dpar values and the single-grain AHe ages with grains sizes and chemical characteristics.

For the Cordillera Negra profiles the beginning of the model is fixed at t = 45±5 Ma and T = 300±50 °C based on Rb-Sr and U-Pb crystallization ages (48.7±0.5 Ma and 49.7±0 Ma; Beckinsale *et al.*, 1985; Mukasa and Tilton, 1985). For the Cordillera Blanca area, based on U-Pb ages the Cordillera Blanca pluton crystallization ages (12-5; Mukasa, 1984; McNulty *et al.*, 1998; Giovanni, 2007), the beginning of the model is fixed at t = 7±2 Ma and T = 800±50 °C. For all the areas at 0 Ma, the temperature is fixed at 0°C. Thermal history simulations are

the product of 100,000 iterations, which is here a sufficient amount to obtain stable and robust solutions (e.g. discussion in Gallagher, 2012). For all models, the grain chemical composition range can be taken into consideration following Gautheron *et al.* (2013). We performed simulations with the linear non-linear He damage model for all three profiles (Gautheron *et al.*, 2009 and Flowers *et al.*, 2009). The simulations with the two He damage models predict similar recent (20-0 Ma) thermal histories. These results are respectively reported in Fig. 3 and Fig. A. We choose to use the data generated by the simulation using the Gautheron *et al.* (2009) diffusion model in the Fig. 2 because our samples must have stayed a long time in the partial retention zone, so we have to into account the large amount of default in the apatite crystals to explain the AHe ages.

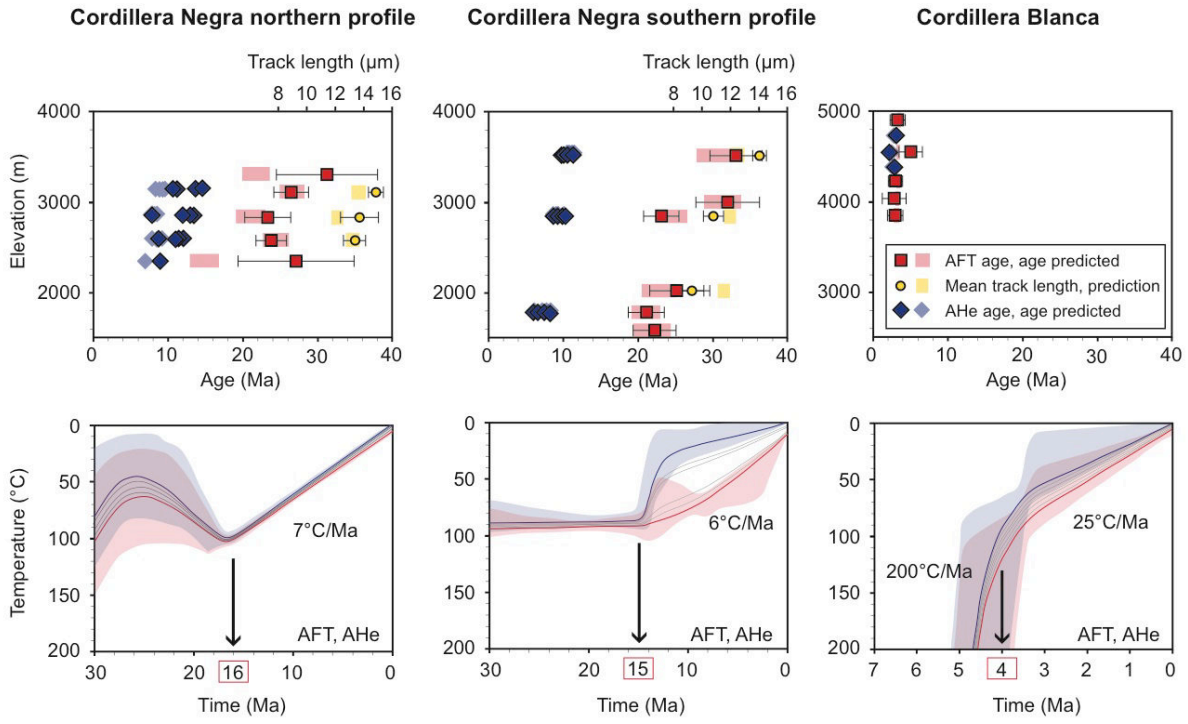

Fig. A: Age-elevation plots and Temperature-time (Tt) paths predicted for thermochronological ages using the Flowers *et al.* (2009) He diffusion model. A-C) Age-elevation plots showing AFT ages (red), mean track length (yellow) and AHe ages (blue), ages predicted by the thermal history are plotted in pastel colors. Northern Cordillera Negra profile (A), southern Cordillera Negra profile (B), and Cordillera Blanca profile (Quebrada Ulta) (C). D-F) Tt paths. Each line represents the Tt path of a sample; red line represents the

path of the lowest elevation sample whereas blue line represents the highest one, pastel shading represent uncertainties. Northern Cordillera Negra profile (D), southern Cordillera Negra (E), and Cordillera Blanca profile (F).

C- **Data**

C.1 – AHe

Table A1: AHe single-grain ages from the Cordillera Negra and the Cordillera Blanca samples.

Longitude and latitude coordinates are given in WGS 84 (degrees); *Rs* is the sphere equivalent radius of hexagonal crystal with the same surface/volume ratio; F_T is the geometric correction factor for age calculation; *eU* is the effective uranium concentration; *Corrected age* is the age corrected by the grain geometry and ejection factor F_T. (Gautheron and Tassan-Got, 2010; Ketcham *et al.*, 2011).

C.2 – AFT

Table A2: AFT data from the Cordillera Negra and the Cordillera Blanca samples.

Longitude and latitude coordinates are given in WGS 84 (degrees); ρs and ρi are the spontaneous and induced track densities (10^5 tracks/cm^2); *Ns* and *Ni* are the numbers of spontaneous and induced tracks counted, ρd is the dosimeter track density (10^5 tracks/cm^2); *Nd* the number of tracks counted on the dosimeter; *P* is the probability to obtain Chi-square value for n degree of freedom (n = No. of crystals – 1); *Dispersion* is 0 if all the data are identical, it increase when the data become more diverse; *MTL* is the mean track length; *SD* is

the standard deviation of track length distribution; *Dpar* is the average etch pit diameter of fission-track.

References

Beckinsale, R.D., Sanchez-Fernandez, A.W., Brook, M., Cobbing, E.J., Taylor, W.P. and Moore, N.D., 1985, Rb–Sr whole-rock isochron and K–Ar age determinations for the Coastal Batholith of Peru. In: Pitcher, W.S. & Atherton, M.P. (eds) Magmatism at a Plate Edge: The Peruvian Andes. Blackie, Glasgow, p. 177–202.

Donelick, R.A., 1993, Microscopic analysis of etch figure to determine fluorine chlorien and water rich apatite: U.S. Patent, no. 6, p. 267-274.

Dunkl, I., 2002, TRACKKEY: a Windows program for calculation and graphical presentation of fission track data: Computers & Geosciences, v. 28, no. 1, p. 3–12.

Evans, N.J., Byrne, J.P., Keegan, J.T., and Dotter, L.E., 2005, Determination of uranium and thorium in zircon, apatite, and fluorite: Application to laser (U-Th)/He thermochronology: Journal of Analytical Chemistry, v. 60, no. 12, p. 1159–1165.

Flowers, R.M., 2009, Exploiting radiation damage control on apatite (U–Th)/He dates in cratonic regions: Earth and Planetary Science Letters, v. 277, no. 1-2, p. 148–155, doi: 10.1016/j.epsl.2008.10.005.

Gallagher, K., 2012, Transdimensional inverse thermal history modeling for quantitative thermochronology: Journal of Geophysical Research, v. 117, no. B2, p. B02408, doi: 10.1029/2011JB008825.

Gallagher, K., Charvin, K., Nielsen, S., Sambridge, M., and Stephenson, J., 2009, Markov chain Monte Carlo (MCMC) sampling methods to determine optimal models, model resolution and model choice for Earth Science problems: Marine and Petroleum Geology, v. 26, no. 4, p. 525–535, doi: 10.1016/j.marpetgeo.20.

Gautheron, C., and Tassan-Got, L., 2010, A Monte Carlo approach to diffusion applied to noble gas/helium thermochronology: Chemical Geology, v. 273, no. 3-4, p. 212–224, doi: 10.1016/j.chemgeo.2010.02.023.

Gautheron, C., Barbarand, J., Ketcham, R.A., Tassan-Got, L., van der Beek, P., Pagel, M., Pinna-Jamme, R., Couffignal, F., and Fialin, M., 2013, Chemical Geology: Chemical Geology, v. 351, no. C, p. 257–267, doi: 10.1016/j.chemgeo.2013.05.027.

Gautheron, C., Tassan-Got, L., Barbarand, J., and Pagel, M., 2009, Effect of alpha-damage annealing on apatite (U–Th)/He thermochronology: Chemical Geology, v. 266, no. 3, p. 157–170, doi: 10.1016/j.chemgeo.2009.06.001.

Giovanni, M.K., 2007, Tectonic and Thermal Evolution of the Cordillera Blanca Detachment System, Peruvian Andes: Implication for Normal Faulting in a Contractionnal Orogen: Unpublished Thesis, University of California, Los Angeles, p. 1–255.

Hurford, A.J., and Green, P.F., 1982, A users' guide to fission track dating calibration: Earth

and Planetary Science Letters, v. 59, no. 2, p. 343–354.

Ketcham, R.A., Carter, A., Donelick, R.A., Barbarand, J., and Hurford, A.J., 2007, Improved measurement of fission-track annealing in apatite using c-axis projection: American Mineralogist, v. 92, no. 5-6, p. 789–798, doi: 10.2138/am.2007.2280.

Ketcham, R.A., Gautheron, C., and Tassan-Got, L., 2011, Accounting for long alpha-particle stopping distances in (U-Th-Sm)/He geochronology: Refinement of the baseline case: Geochimica et Cosmochimica Acta, v. 75, no. 24, p. 7779–7791, doi: 10.1016/j.gca.2011.10.011.

Kraml, M., Pik, R., Rahn, M., Selbekk, R., Carignan, J., and Keller, J., 2006, A New Multi-Mineral Age Reference Material for $^{40}Ar/^{39}Ar$, (U-Th)/He and Fission Track Dating Methods: The Limberg t3 Tuff: Geostandards and Geoanalytical Research, v. 30, no. 2, p. 73–86.

Laslett, G.M., Galbraith, R.F., and Green, P.F., 1994, The analysis of projected fission track lengths: Radiation measurements, v. 23, no. 1, p. 103–123.

McDowell, F., McIntosh, W., and Farley, K., 2005, A precise Ar-Ar reference age for the Durango apatite (U-Th)/He and fission-track dating standard: Chemical Geology, v. 214, no. 3-4, p. 249–263, doi: 10.1016/j.chemgeo.2004.10.002.

McNulty, B.A., Farber, D.L., Wallace, G.S., Lopez, R., and Palacios, O., 1998, Role of plate kinematics and plate-slip-vector partitioning in continental magmatic arcs: Evidence from the Cordillera Blanca, Peru: Geology, v. 26, no. 9, p. 827–830.

Mukasa S.B., 1984. Comparative Pb isotope systematics and zircon U-Pb geochronology for the Coastal San NicolAs and Cordillera Blanca batholiths, Peru. Unpublished Thesis, University of California, Santa Barbara.

Mukasa, S.B., and Tilton, G.R., 1984, Lead isotope systematics in batholithic rocks of the western and coastal cordilleras, Peru: Andean magmatism, p. 180-189.

8.1.2 Table A1: apatite (U-Th/He) ages

TABLE A1. APATITE (U-Th)/He SINGLE-GRAIN AGES FROM THE CORDILLERA BLANCA AND NEGRA SAMPLES

Sample	Rock	Location*		Elevation	Weight	Rs†	FT§	4He	U	Th	Sm	Th/U	eU	AHe age	Corrected	
		Latitude (°N)	Longitude (°W)	(m)	(mg)			(×10⁹ nmol/g)	(ppm)	(ppm)	(ppm)		(ppm)#	(Ma)	AHe age ± error (Ma)**	
Cordillera Blanca																
CB12-12-A	granite	-9.14225	-77.48451	4167	2.2	48.6	0.75	5300	40	37	39	0.9	49	2.0	2.7 ± 0.3	
CB12-12-B	granite	-9.14225	-77.48451	4167	1.8	47.5	0.74	4665	34	45	37	1.3	45	1.9	2.6 ± 0.3	
CB12-12-C	granite	-9.14225	-77.48451	4167	1.4	46.3	0.72	6580	53	57	41	1.1	67	1.8	2.6 ± 0.3	
CB12-12-D	granite	-9.14225	-77.48451	4167	1.7	46.1	0.70	5697	50	55	39	1.1	63	1.7	2.4 ± 0.2	
CB12-12-E	granite	-9.14225	-77.48451	4167	1.5	46.6	0.72	4746	46	52	42	1.1	59	1.5	2.1 ± 0.2	
CB12-14-A	granite	-9.14010	-77.51060	4734	3.7	53.0	0.79	5081	46	10	23	0.2	49	1.9	2.4 ± 0.2	
CB12-14-B	granite	-9.14010	-77.51060	4734	4.6	56.8	0.77	5024	35	8	26	0.2	37	2.5	3.3 ± 0.3	
CB12-14-C	granite	-9.14010	-77.51060	4734	2.2	49.3	0.71	4781	28	6	22	0.2	29	3.0	4.2 ± 0.4	
CB12-15-A	granite	-9.13552	-77.51144	4903	2.8	48.4	0.80	4422	13	26	43	2.0	20	4.2	5.2 ± 0.5	
CB12-15-B	granite	-9.13552	-77.51144	4903	4.1	54.1	0.81	3232	9	13	37	1.4	12	4.9	6.0 ± 0.6	
CB12-16-A	granite	-9.12742	-77.51728	4740	4.2	59.2	0.79	2758	13	19	20	1.5	17	3.0	3.7 ± 0.4	
CB12-17-A	granite	-9.12419	-77.52122	4555	2.9	49.7	0.79	1538	3	6	49	2.2	5	6.0	7.6 ± 0.8	
CB12-17-B	granite	-9.12419	-77.52122	4555	2.9	50.8	0.76	3432	7	12	86	1.7	11	6.2	8.1 ± 0.8	
CB12-17-C	granite	-9.12419	-77.52122	4555	1.8	48.5	0.70	2083	13	21	232	1.6	7	1.9	2.8 ± 0.3	e††
CB12-18-C	granite	-9.13195	-77.52807	4391	4.2	55.0	0.80	6490	15	18	63	1.3	20	6.2	7.7 ± 0.8	
CB12-18-D	granite	-9.13195	-77.52807	4391	6.0	57.5	0.80	2443	13	12	49	0.9	16	2.8	3.5 ± 0.4	e
CB12-18-E	granite	-9.13195	-77.52807	4391	3.2	53.0	0.75	12709	20	42	104	2.1	31	7.8	10.4 ± 1.0	
CB12-20-A	granite	-9.12600	-77.53145	4044	4.7	56.8	0.77	595	1	3	18	1.0	2	6.2	8.1 ± 0.8	
CB12-20-B	granite	-9.12600	-77.53145	4044	3.8	53.3	0.76	2762	9	7	31	0.9	11	4.8	6.3 ± 0.6	
CB12-22-A	granite	-9.19444	-77.59531	3567	2.8	43.8	0.70	1366	12	17	8	1.4	16	1.3	1.9 ± 0.2	e
CB12-22-B	granite	-9.19444	-77.59531	3567	2.8	46.6	0.73	3696	20	29	10	1.5	27	2.6	3.5 ± 0.4	e
CB12-22-C	granite	-9.19444	-77.59531	3567	3.2	49,0	0.74	4866	16	30	10	1.8	24	3.8	5.2 ± 0.5	
CB12-22-D	granite	-9.19444	-77.59531	3567	2.2	41.6	0.70	2396	17	31	11	1.8	25	1.8	2.5 ± 0.3	e
CB12-22-E	granite	-9.19444	-77.59531	3567	3.6	56.6	0.79	4372	16	32	12	2.0	24	3.4	4.3 ± 0.4	
CB12-26-A	granite	-9.70282	-77.31379	4026	6.2	64.8	0.80	7328	33	82	18	2.5	52	2.6	3.3 ± 0.3	
CB12-26-B	granite	-9.70282	-77.31379	4026	3.0	50.2	0.79	7488	32	89	21	2.7	54	2.6	3.3 ± 0.3	
CB12-26-C	granite	-9.70282	-77.31379	4026	4.7	58.5	0.75	7906	41	97	22	2.4	64	2.3	3.1 ± 0.3	
CB12-26-D	granite	-9.70282	-77.31379	4026	4.0	55.2	0.77	6325	33	68	15	2.0	50	2.4	3.1 ± 0.3	
CB12-26-E	granite	-9.70282	-77.31379	4026	6.1	61.3	0.81	4486	21	42	12	2.0	32	2.7	3.3 ± 0.3	
CB12-54-A	granite	-8.76495	-77.84775	2756	5.6	56.7	0.82	545	5	4	41	0.9	7	1.5	1.8 ± 0.2	
CB12-54-B	granite	-8.76495	-77.84775	2756	10.0	66.9	0.85	585	6	3	33	0.5	7	1.6	1.9 ± 0.2	
CB12-80-A	granite	-9.45959	-77.48723	4375	3.6	56.0	0.78	14107	93	18	33	0.2	97	2.7	3.4 ± 0.3	
CB12-85-C	quartzite	-9.88164	-77.19439	4557	2.6	97.8	0.74	1881	3	2	0	0.6	3	10.1	13.7 ± 1.4	
Cordillera Negra																
CB12 37-C	quartzite	-9.10905	-77.81791	2711	2.5	58.5	0.74	1014	2	7	1	4.0	4	5.4	7.3 ± 0.7	
CB12 37-F	quartzite	-9.10905	-77.81791	2711	0.4	58.1	0.53	77452	74	36	2	0.5	83	17.3	32.6 ± 3.3	e
CB12 38-B	quartzite	-9.11020	-77.82391	2896	1.3	45.1	0.66	174	1	6	0	5.4	3	1.2	1.9 ± 0.2	
CB12 39-A	quartzite	-9.10405	-77.83389	3096	5.8	71.4	0.79	143	0	1	0	3.3	1	5.0	6.3 ± 0.6	
CB12 39-B	quartzite	-9.10405	-77.83389	3096	2.7	58.1	0.75	284	1	5	0	3.6	2	2.1	2.9 ± 0.3	
CB12 39-C	quartzite	-9.10405	-77.83389	3096	2.4	55.0	0.73	297	1	2	0	2.8	1	3.8	5.2 ± 0.5	
CB12 47-A	granite	-9.09504	-77.96394	3309	1.4	39.2	0.69	6832	23	45	40	1.9	34	3.7	5.4 ± 0.5	
CB12 47-B	granite	-9.09504	-77.96394	3309	3.2	51.4	0.79	3324	2	20	21	8.7	7	8.7	11.1 ± 1.1	e
CB12 47-C	granite	-9.09504	-77.96394	3309	1.7	36.7	0.69	4944	14	32	47	2.3	22	4.2	6.1 ± 0.6	
CB12 48-A	granite	-9.08484	-77.97282	3114	3.8	59.1	0.76	68958	129	99	38	0.8	153	8.4	11.1 ± 1.1	
CB12 48-B	granite	-9.08484	-77.97282	3114	2.1	49.4	0.71	51025	95	82	33	0.9	115	8.2	11.5 ± 1.2	
CB12 48-C	granite	-9.08484	-77.97282	3114	4.2	55.8	0.78	95125	128	102	41	0.8	153	11.5	14.9 ± 1.5	
CB12 48-D	granite	-9.08484	-77.97282	3114	4.1	60.3	0.76	72083	106	85	35	0.8	127	10.6	13.9 ± 1.4	
CB12 49-A	granite	-9.07720	-77.98496	2834	3.1	51.9	0.74	42200	55	88	105	1.6	77	10.2	13.9 ± 1.4	
CB12 49-B	granite	-9.07720	-77.98496	2834	3.3	53.5	0.75	37888	50	73	95	1.5	68	10.3	13.8 ± 1.4	
CB12 49-C	granite	-9.07720	-77.98496	2834	3.6	53.4	0.75	31568	46	54	85	1.2	60	9.8	13.1 ± 1.3	
CB12 49-D	granite	-9.07720	-77.98496	2834	2.4	48.6	0.70	23947	139	120	100	0.9	168	2.6	3.8 ± 0.4	e
CB12 49-E	granite	-9.07720	-77.98496	2834	5.3	55.6	0.82	2086	4	8	4	2.1	6	6.7	8.1 ± 0.8	
CB12 50-A	granite	-9.08242	-77.99652	2579	2.7	52.8	0.73	36995	63	66	31	1.1	79	8.7	11.9 ± 1.2	
CB12 50-B	granite	-9.08242	-77.99652	2579	2.2	49.0	0.71	35422	66	58	34	0.9	80	8.2	11.6 ± 1.2	
CB12 50-C	granite	-9.08242	-77.99652	2579	3.4	57.3	0.75	46581	87	74	31	0.8	105	8.2	11.0 ± 1.1	
CB12 50-D	granite	-9.08242	-77.99652	2579	3.0	55.5	0.74	31893	54	41	31	0.8	64	9.2	12.4 ± 1.2	
CB12 50-E	granite	-9.08242	-77.99652	2579	5.6	65.2	0.81	25988	42	52	20	1.2	54	8.9	11.0 ± 1.1	
CB12 51-A	quartzite	-9.08907	-78.00752	2356	1.9	47.3	0.73	4457	6	15	43	2.6	10	8.5	11.7 ± 1.2	
CB12 71-A	granite	-9.54684	-77.81780	1790	3.1	51.6	0.78	35510	60	78	43	1.3	80	8.3	10.7 ± 1.1	
CB12 71-B	granite	-9.54684	-77.81780	1790	1.6	47.2	0.73	17983	36	83	52	2.3	56	6.0	8.2 ± 0.8	
CB12 71-C	granite	-9.54684	-77.81780	1790	2.3	43.9	0.68	27342	51	99	59	1.9	76	6.8	10.0 ± 1.0	
CB12 71-D	granite	-9.54684	-77.81780	1790	2.8	51.6	0.74	18386	32	59	41	1.9	46	7.4	10.1 ± 1.0	
CB12 71-E	granite	-9.54684	-77.81780	1790	2.0	48.1	0.75	9756	29	55	30	1.9	42	4.3	5.7 ± 0.6	
CB12 75-A	granite	-9.55195	-77.73795	2843	3.0	50.8	0.80	28579	40	53	37	1.3	53	10.1	12.6 ±1.3	
CB12 75-B	granite	-9.55195	-77.73795	2843	2.2	50.8	0.72	36657	58	84	48	1.5	79	8.7	12.1 ± 1.2	
CB12 75-C	granite	-9.55195	-77.73795	2843	2.6	47.7	0.74	19696	22	59	36	2.6	37	10.0	13.4 ± 1.3	
CB12 75-D	granite	-9.55195	-77.73795	2843	2.7	51.4	0.77	33114	40	86	48	2.2	61	10.1	13.1 ± 1.3	
CB12 75-E	granite	-9.55195	-77.73795	2843	1.6	42.5	0.67	51465	78	101	69	1.3	103	9.3	13.8 ± 1.4	
CB12 76-A	granite	-9.58094	-77.69408	3510	3.8	58.9	0.76	52062	74	77	35	1.0	93	10.4	13.7 ± 1.4	
CB12 76-B	granite	-9.58094	-77.69408	3510	2.4	50.2	0.72	54423	84	79	51	0.9	104	9.8	13.7 ± 1.4	
CB12 76-C	granite	-9.58094	-77.69408	3510	2.3	50.4	0.72	54906	75	77	53	1.0	94	10.9	15.2 ± 1.5	
CB12 76-D	granite	-9.58094	-77.69408	3510	4.0	58.4	0.79	36042	56	45	31	0.8	67	10.0	12.7 ±1.3	

Notes:

*Longitude and latitude coordinates are given in WGS 84 (degrees)

†Rs is the sphere equivalent radius of hexagonal crystal with the same surface/volume ratio

§FT is the geometric correction factor for age calculation

#eU is the effective uranium concentration

**Corrected age is the age corrected by the grain geometry and ejection factor FT. (Gautheron and Tassan-Got, 2010; Ketcham et al., 2011)

††e indicates that the age was rejected.

8.1.3 Table A2: apatite fission-track data

TABLE A2. APATITE FISSION-TRACK DATA FROM THE CORDILLERA BLANCA AND NEGRA SAMPLES

Sample	Rock	Location*		Elevation	Number	ρs†	Ns§	ρi†	Ni§	ρd#	Nd**	P††	Chi²††	Dispersion§§	Central age ± 1σ	Mean age ± 1σ	MTL##	SD***	Number	Dpar†††	U	Error
		Latitude (°N)	Longitude (°W)	(m)	of grains							(%)			(Ma)	(Ma)	(µm)	(µm)	of lenghts	(µm)	(ppm)	(%)
Cordillera Blanca																						
CB12-12	granite	-9.14225	-77.48451	4167	20	0.903	58	20.267	1302	13.04	7062	100	7	0.00	7.8 ± 1.1	8.4 ± 0.8	N.D.§§§	N.D.	N.D.	N.D.	5	42
CB12-13	granite	-9.13347	-77.49272	4406	29	1.259	114	33.019	2990	13.12	7695	89	19	0.00	6.7 ± 0.7	7.5 ± 1.3	N.D.	N.D.	N.D.	N.D.	16	101
CB12-14	granite	-9.14010	-77.51060	4734	20	0.729	60	37.335	3074	13.20	8264	100	5	0.00	3.5 ± 0.5	3.8 ± 0.3	N.D.	N.D.	N.D.	N.D.	14	35
CB12-15	granite	-9.13552	-77.51144	4903	33	0.206	52	10.285	2602	13.28	9070	92	22	0.13	3.6 ± 0.5	3.2 ± 0.5	N.D.	N.D.	N.D.	1.7	5	133
CB12-16	granite	-9.12742	-77.51728	4740	21	0.365	25	5.659	388	13.35	9612	10	29	0.45	14.0 ± 3.2	21.8 ± 4.6	N.D.	N.D.	N.D.	N.D.	3	87
CB12-17	granite	-9.12419	-77.52122	4555	34	0.210	40	7.392	1410	13.43	10203	99	17	0.00	5.1 ± 0.8	4.3 ± 0.8	N.D.	N.D.	N.D.	1.7	3	114
CB12-18	granite	-9.13195	-77.52807	4391	35	0.198	52	12.227	3214	13.51	10628	95	22	0.00	2.9 ± 0.4	2.9 ± 0.4	N.D.	N.D.	N.D.	1.8	8	50
CB12-19	granite	-9.13333	-77.53062	4235	30	0.233	44	14.241	2695	13.59	11080	88	20	0.00	3.0 ± 0.5	3.2 ± 0.5	N.D.	N.D.	N.D.	2.2	9	59
CB12-20	granite	-9.12600	-77.53145	4044	21	0.183	12	11.972	786	13.67	11317	1	39	0.00	2.8 ± 0.8	11.0 ± 8.5	N.D.	N.D.	N.D.	2.0	9	66
CB12-22	granite	-9.19444	-77.59531	3567	33	0.085	19	10.268	2284	13.75	11317	87	23	0.01	1.5 ± 0.4	1.6 ± 0.3	N.D.	N.D.	N.D.	1.9	8	27
CB12-26	granite	-9.70282	-77.31379	4026	20	0.381	50	24.287	3187	13.83	11317	57	17	0.02	2.9 ± 0.4	2.8 ± 0.4	N.D.	N.D.	N.D.	N.D.	20	26
CB12-52	granite	-8.76391	-77.84471	2956	23	0.109	13	12.065	1437	14.46	8116	81	16	0.04	1.8 ± 0.5	1.2 ± 0.4	N.D.	N.D.	N.D.	N.D.	14	77
CB12-54	granite	-8.76495	-77.84775	2756	25	0.290	43	12.001	1780	14.54	7062	0	53	0.86	4.2 ± 1.1	3.4 ± 0.9	N.D.	N.D.	N.D.	N.D.	17	156
CB12-56	granite	-8.77153	-77.84754	2550	28	0.138	22	16.684	2667	13.23	6610	77	21	0.17	1.5 ± 0.3	1.4 ± 0.3	N.D.	N.D.	N.D.	N.D.	15	41
CB12-77	granite	-9.44707	-77.48346	4841	24	0.290	27	21.500	2004	13.82	11562	87	16	0.00	2.5 ± 0.5	2.5 ± 0.5	N.D.	N.D.	N.D.	N.D.	15	41
CB12-82	granite	-9.46319	-77.48970	4164	24	0.451	38	39.038	3292	13.88	11562	95	13	0.00	2.1 ± 0.4	1.9 ± 0.3	N.D.	N.D.	N.D.	N.D.	35	85
CB12-84	quartzite	-9.88779	-77.21648	4557	7	0.236	6	9.725	247	13.95	11317	95	2	0.00	4.5 ± 1.9	3.5 ± 1.3	N.D.	N.D.	N.D.	N.D.	10	122
BR-06	granite	-9.71363	-77.30801	4143	30	0.666	104	25.159	3930	14.14	10000	91	20	0.00	5.0 ± 0.5	5.2 ± 0.5	N.D.	N.D.	N.D.	N.D.	25	38
BR-07	granite	-9.69493	-77.26539	4397	30	0.696	117	27.819	4678	14.21	9426	91	19	0.00	4.8 ± 0.5	4.7 ± 0.4	N.D.	N.D.	N.D.	N.D.	27	23
BR-08	granite	-9.68887	-77.25258	4601	30	0.761	115	29.542	4465	14.27	8734	98	15	0.00	4.9 ± 0.5	4.8 ± 0.5	N.D.	N.D.	N.D.	N.D.	32	14
Cordillera Negra																						
CB12-37	quartzite	-9.10905	-77.81791	2711	2	1.086	11	12.443	126	13.91	11080	75	0	0.00	16.3 ± 5.1	16.0 ± 0.0	N.D.	N.D.	N.D.	N.D.	13	46
CB12-47	granite	-9.09504	-77.96394	3309	24	1.869	101	11.271	609	14.07	10412	97	12	0.00	31.2 ± 3.5	34.1 ± 2.8	11.9	3.1	3	2.3	11	57
CB12-48	granite	-9.08484	-77.97282	3114	29	6.381	634	45.737	4544	14.15	9803	95	17	0.00	26.4 ± 1.3	26.6 ± 0.9	14.8	1.3	25	3.9	48	23
CB12-49	granite	-9.07720	-77.98496	2834	31	1.921	279	15.497	2251	14.23	9246	95	19	0.00	23.5 ± 1.6	23.3 ± 1.4	13.7	2.6	16	1.9	19	57
CB12-50	granite	-9.08242	-77.99652	2579	40	3.843	667	30.930	5368	14.30	8734	98	23	0.00	23.8 ± 1.2	23.5 ± 0.8	13.3	2.1	28	3.6	36	24
CB12-51	quartzite	-9.08907	-78.00752	2356	20	0.696	56	4.949	398	14.38	8116	99	7	0.00	27.1 ± 3.9	24.2 ± 3.4	N.D.	N.D.	N.D.	1.7	5	156
CB12-69	granite	-9.55566	-77.72498	2998	25	4.360	279	24.253	1552	13.30	7182	69	20	0.01	32.0 ± 2.3	32.5 ± 2,0	13.8	2.1	12	2.9	22	23
CB12-70	granite	-9.54947	-77.79244	2023	31	2.258	227	16.038	1612	13.36	7831	98	16	0.00	25.0 ± 2.0	27.2 ± 1.5	10.0 (Cf)	2.7	27	1.5	5	37
CB12-71	granite	-9.54684	-77.81780	1790	31	2.379	359	20.266	3058	13.43	8573	78	24	0.01	21.1 ± 1.3	21.8 ± 1.4	12.5	2.5	4	2,0	8	51
CB12-72	granite	-9.55091	-77.84055	1589	21	1.936	129	20.51	1367	13.49	9246	97	10	0.00	22.3 ± 1.5	22.5 ± 1.0	13.2	2.1	8	1.8	19	46
CB12-73	granite	-9.54838	-77.90289	1051	29	3.420	218	18.606	1186	13.56	9803	99	14	0.00	33.1 ± 2.7	34.9 ± 2.0	N.D.	N.D.	N.D.	N.D.	17	57
CB12-75	granite	-9.55195	-77.73795	3510	30	4.059	470	32.172	3725	13.69	10851	100	13	0.00	23.1 ± 1.3	24.5 ± 0.8	11.3 (Cf)	2.5	69	2.1	19	43
CB12-76	granite	-9.58094	-77.69408	3510	25	8.815	619	49.788	3496	13.75	11317	5	36	0.13	33.2 ± 1.9	35.0 ± 2.1	14.0 (Cf)	2.1	100	2.1	32	45

Note: Samples are stored in ISTerre fission-track laboratory (Grenoble, France).

*Longitude and latitude coordinates are given in WGS 84 (degrees).

†ρs and ρi are the spontaneous and induced track densities (10^5 tracks/cm^2).

§Ns and Ni are the numbers of spontaneous and induced tracks counted.

#ρd is the dosimeter track density (10^5 tracks/cm^2).

**Nd the number of tracks counted on the dosimeter.

††P is the probability to obtain Chi-square value for n degree of freedom (n = No. of crystals – 1).

§§Dispersion is 0 if all the data are identical, it increase when the data become more diverse.

##MTL is the mean track length.

***SD is the standard deviation of track length distribution.

†††Dpar is the average etch pit diameter of fission-track.

§§§N.D. is not determined.

8.2 Annexes du Chapitre 4

8.2.1 Table A1: sites locations and single site tensors

TABLE A1: SITES LOCATION AND SINGLE SITE STRESS TENSORS

										PBT axes				Right dieder			
Regional label		**Site**	**Longitude**	**Latitude**	**Altitude**	**Rock**	**Number of couples fault/striae**	**Tensor**	**Number of couples fault/striae**	**Sigma 1**	**Sigma 2**	**Sigma 3**	**Phi**	**Sigma 1**	**Sigma 2**	**Sigma 3**	**Phi**
Canyon del Pato	1	Pato1	77.87410	08.81169	1569	granite	28	T1	12	16/359	58/114	27/263	0.46	29/002	60/164	08/268	0.5
		-						T2	7	06/257	56/159	33/349	0.55	10/252	62/143	26/346	0.71
		-						T3	6	78/133	11/319	01/227	0.5	66/127	24/296	04/028	0.5
	2	Pato2	77.85102	08.81227	1561	granite	28	T1	16	71/102	13/332	14/239	0.49	53/106	32/320	17/220	0.56
	3	Pato3	77.83826	08.81637	1611	granite	29	T1	8	20/286	67/078	10/192	0.74	20/293	59/061	22/195	0.79
		-						T2	10	44/164	38/302	22/051	0.56	41/158	37/289	27/041	0.5
	4	Pato4	77.82299	08.85069	1746	granite	15	T1	12	80/038	04/148	09/238	0.62	49/146	41/331	03/239	0.79
	5	Pato5	77.83087	08.86431	1823	sediments and dykes	15	T1	9	72/199	08/314	16/047	0.28	77/236	06/355	11/087	0.55
	6	Caraz1	77.79971	09.03689	2560	Yungay tuff	34	T1	9	53/108	17/351	31/251	0.53	54/106	13/357	33/259	0.67
Caraz		-						T2	10	66/295	08/177	20/086	0.58	62/328	20/196	19/099	0.55
		-						T3	8	07/265	10/001	74/165	0.7	00/264	23/354	67/174	0.69
Pueblo Libre	7	PuebloL1	77.83820	09.10296	3148	quartzite	12	T1	12	-	-	-	-	61/197	29/012	02/103	0.62
Laguna Paron	8	QParon1	77.73323	09.03818	3331	granite	3	*									
	9	QParon2	77.72778	09.03160	3596	granite	3	*									
	10	QParon3	77.70361	09.01276	3929	granite	4	*									
	11	LParon1	77.68074	08.99658	4199	granite	34	T1	12	09/215	52/317	37/118	0.5	14/029	58/276	28/126	0.5
		-						T2	7	63/127	27/315	03/223	0.5	54/130	36/317	04/225	0.71
	12	LParon2	77.68198	08.99759	4195	granite	12	*									
	13	LParon3	77.68414	08.99857	4201	granite	18	T1	6	66/174	24/342	04/074	0.56	65/160	24/352	05/260	0.67
Quebrada Llanganuco	14	Llanga1	77.59944	09.04365	4478	granite	15	*									
	15	Llanga2	77.59113	09.05086	4704	granite	27	T1	6	78/340	10/146	01/056	0.52	72/325	18/148	01/058	0.58
		-						T2	7	55/093	07/356	33/269	0.66	52/080	09/181	37/278	0.58
	16	Llanga3	77.59706	09.04618	4473	granite	17	*									
	17	Llanga4	77.62769	09.05745	3851	granite	11	T1	6	50/039	10/142	38/240	0.52	50/039	08/139	39/236	0.67
	18	Llanga5	77.63135	09.06122	3865	granite	10	*									
Quebrada Ulta	19	Ulta1	77.59533	09.19451	3563	granite	22	T1	10	73/241	00/150	17/060	0.5	72/188	16/336	09/069	0.55
	20	Ulta2	77.52737	09.12840	4411	granite	33	T1	13	15/252	22/155	63/013	0.47	18/245	09/152	70/036	0.38
		-						T2	12	86/244	01/138	04/048	0.6	86/135	04/320	00/230	0.67
	21	Ulta3	77.51582	09.12794	4739	granite	13	T1	11	69/276	13/149	16/055	0.5	53/318	35/163	12/064	0.65
	22	Ulta4	77.63714	09.24201	2945	Tuff	14	*									
Q. Honda	23	Honda1	77.50579	09.33615	3506	granite	5	*									
	24	Honda2	77.49491	09.33510	3629	granite	17	T1	16	59/030	12/141	28/237	0.52	26/016	17/115	58/234	0.61
Q. Llaca	25	Llaca1	77.46375	09.46792	4130		15	*									
	26	Llaca2	77.44561	09.43367	4545		13	*									
Q. Rajucolta	27	Rajuco1	77.39893	09.55105	4096	granite	12	T1	11	62/311	28/137	03/046	0.74	54/302	35/136	07/041	0.82
	28	Rajuco2	77.35155	09.53100	4229		9	*									
Quebrada Queroccocha	29	Quero1	77.31303	09.71622	4162	granite	24	T1	8	23/342	67/177	05/074	0.73	13/339	76/176	04/069	0.75
		-						T2	9	30/091	57/242	13/353	0.66	24/088	63/238	12/352	0.7
		-						T3	7	26/263	06/355	64/097	0.61	32/257	01/166	58/074	0.5
	30	Quero2	77.23421	09.69098	4270		20	T1	7	44/304	45/138	08/041	0.63	38/314	52/127	04/221	0.29
		-						T2	9	55/067	28/206	19/307	0.21	51/058	35/209	14/310	0.39
	31	Quero3	77.25979	09.69182	4454		26	T1	7	48/098	25/219	31/325	0.25	53/101	19/219	31/321	0.29
		-						T2	11	70/299	10/179	17/086	0.76	71/217	12/347	14/080	0.68
Quebrada Pastoruri	32	Pasto1	77.23757	09.88668	4416	sediment	28	T1	17	47/153	43/341	04/247	0.57	38/156	51/350	07/252	0.62
		-						T2	7	05/312	12/043	77/200	0.64	11/314	01/044	79/140	0.79
	33	Pasto2	77.17747	09.87482	4750	Dacytic lava	13	T1	9	80/303	10/147	04/056	0.3	74/240	01/147	16/056	0.33
	34	Pasto3	77.17248	09.86922	4675		15	T1	6	15/201	70/340	13/108	0.4	29/201	54/342	19/100	0.5
		-						T2	6	76/042	02/141	13/231	0.5	61/332	25/119	14/216	0.67
	35	Pasto4	77.23010	09.88534	4483	sediment and lava	23	T1	14	48/188	34/319	27/065	0.57	54/193	15/305	31/045	0.5
		-						T2	8	39/262	48/106	10/003	0.5	33/256	53/108	15/356	0.38
	36	Pasto5	77.19167	09.88333	4370		10	*									
Q. Fortaleza	37	Forta1	77.53133	09.53037	3185	granite	12	T1	8	13/324	74/184	10/056	0.65	14/328	68/197	16/062	0.69
	38	Forta2	77.55593	10.20302	1271	granite	2	*									

* several tensors or not enought data for tensor analysis

8.2.2 Table A2: fault-striation measurements

TABLE A2: FAULT-STRIATION MEASUREMENTS FOR EACH SITE

Measurements were performed in July 2015 by **A. Margirier**, X. Robert, S. Schwartz and L. Audin

* Normal (N), inverse (I), senestral (S) and dextral (D) sense of slip.
** Confidence levels of the slip sense: certain (C), probable (P), supposed (S) and unknown (X).

Number of measurements	Fault plane		Slip line		Slip	Confidence
	Dip	Dip direction	Plunge	Azimut	Sense*	Level**
C. del Pato1						
1	69	135	19	217	IS	P
2	60	140	21	217	IS	P
3	43	60	43	60	NX	P
4	45	50	45	46	NS	P
5	73	40	73	47	ND	S
6	48	22	41	61	ND	P
7	30	356	14	61	ND	P
8	50	117	9	199	ND	S
9	52	132	13	212	IS	P
10	57	140	19	217	IS	P
11	52	144	16	221	IS	P
12	46	30	40	65	ND	S
13	56	120	4	33	IS	S
14	56	120	22	46	XX	X
15	64	142	27	218	IS	P
16	63	228	21	307	IS	S
17	64	232	27	308	IS	S
18	62	217	29	290	IS	S
19	51	147	50	160	ND	S
20	64	232	30	306	IS	S
21	61	201	10	285	IS	S
22	57	128	3	216	IS	S
23	76	120	70	168	IS	S
24	80	157	12	69	NS	S
25	76	200	48	274	ND	S
26	64	218	32	146	NS	S
27	64	218	16	300	ND	S
C. del Pato2						
1	56	230	56	230	NX	P
2	58	250	57	238	NS	P
3	88	250	88	250	NX	P
4	50	251	49	238	NS	P
5	62	60	62	60	XX	X
6	89	240	89	240	NX	P
7	47	240	42	208	NS	P
8	58	255	55	229	NS	P
9	52	260	50	239	NS	P
10	74	240	12	154	NS	P
11	78	270	73	223	NS	P
12	49	250	49	239	NS	P
13	75	259	73	233	NS	P
14	50	232	48	213	NS	P
15	65	25	65	25	XX	X
16	40	260	37	236	XX	X
17	45	260	39	224	NS	P
18	40	249	37	225	NS	P
19	46	244	45	230	NS	P
20	63	249	61	228	ID	P
21	52	258	48	227	NS	P
22	48	249	47	233	NS	P
23	65	224	65	224	NX	P
24	64	243	63	230	NS	P
25	55	259	54	245	NS	P
26	44	235	41	209	NS	P

27	70	234	12	149	NS	P
28	40	245	39	232	NS	P
C. del Pato3						
1	76	330	6	59	ND	P
2	85	328	2	58	ND	S
3	80	147	15	234	ND	P
4	65	174	59	213	ND	P
5	82	359	69	290	NS	P
6	89	349	65	261	NS	S
7	88	358	16	269	NS	P
8	80	180	76	225	ND	P
9	80	25	25	110	ND	P
10	90	2	20	272	NS	P
11	74	15	29	96	ND	P
1	84	10	84	10	NX	P
2	86	30	79	98	IS	P
3	75	37	57	103	ND	P
4	80	45	59	118	ND	P
5	72	36	41	109	ND	S
6	84	20	84	20	NX	P
7	85	150	6	61	ID	S
8	90	151	19	241	ND	P
9	88	179	71	263	ND	P
10	75	13	27	95	ND	P
11	84	40	74	109	ND	P
12	90	2	8	92	ND	P
C. del Pato4						
1	50	240	50	231	NS	P
2	70	135	21	217	IS	P
3	66	230	66	220	NS	P
4	70	52	70	60	ND	P
5	50	110	28	45	XX	X
6	64	55	64	50	NS	S
7	76	260	76	251	NS	S
8	87	250	50	164	NS	P
9	76	55	76	55	NX	P
10	55	228	55	238	ND	P
11	69	134	28	212	IS	P
12	61	237	61	245	ND	P
13	41	65	41	70	ND	P
14	63	55	61	34	NS	P
15	86	248	59	165	NS	P
C. del Pato5						
1	30	235	30	229	XX	X
2	30	235	30	229	XX	X
3	30	210	29	223	XX	X
4	30	196	28	219	ND	P
5	29	280	20	330	ND	S
6	50	190	34	245	ND	S
7	51	264	26	331	ND	S
8	84	55	36	141	ND	P
9	84	52	37	137	ND	S
10	28	232	27	249	XX	X
11	64	289	22	211	NS	S
12	61	288	27	214	NS	S
13	60	286	26	213	NS	S
14	29	211	29	220	ND	S
15	41	191	25	249	ND	S
Caraz						
1	80	265	68	201	NS	C
2	58	323	57	306	XX	X
3	79	273	61	204	ID	C
4	68	320	67	307	NS	P
5	30	315	15	253	NS	C
6	74	274	61	215	ID	C

7	80	175	76	220	ND	S
8	67	240	50	300	ND	S
9	30	225	25	261	IS	C
10	70	290	68	263	ID	P
11	15	275	15	274	NS	C
12	30	260	30	258	NS	C
13	73	250	67	206	NS	P
14	72	165	59	107	NS	S
15	85	110	55	27	NS	P
16	85	110	76	179	IS	P
17	85	254	66	332	ND	S
18	66	254	62	221	NS	C
19	90	180	18	270	XX	X
20	25	228	24	212	ID	P
21	82	272	59	196	NS	P
22	84	179	82	219	ND	P
23	80	162	74	215	ND	S
24	89	96	65	184	IS	S
25	69	332	64	295	ID	P
26	56	319	54	297	ID	P
27	67	260	51	201	NS	P
28	66	233	54	284	ND	P
29	26	254	26	248	NS	P
30	26	313	15	256	NS	P
31	90	293	76	203	ID	P
32	90	293	44	23	IS	P
33	87	152	82	219	ND	S
34	77	257	63	320	ND	S
35	70	65	69	48	ID	P
36	65	256	60	218	XX	X
37	71	270	57	211	NS	P
Pueblo Libre						
1	55	276	55	276	N	P
2	54	330			N	P
3	55	114			N	P
4	86	93			I	P
5	59	90			N	P
6	80	113			N	P
Q. Paron1						
1	51	250	51	242	NS	P
2	82	69	82	69	NX	P
3	49	247	49	250	ND	P
4	71	135	71	135	IX	S
5	65	132	65	132	IX	S
6	64	137	64	137	IX	S
7	80	270	80	280	ND	P
8	83	278	83	278	NX	P
9	83	271	83	271	NX	P
10	88	215	17	126	ID	P
Q. Paron2						
1	71	135	71	135	IX	S
2	65	132	65	132	IX	S
3	64	137	64	137	IX	S
L. Paron1						
1	74	230	47	158	NS	P
2	72	227	60	171	NS	P
3	50	270	27	205	ID	P
4	44	280	7	197	NS	S
5	59	230			NJ	P
6	40	280	14	207	ID	P
7	40	130	39	118	NS	P
8	85	68	10	157	ND	P
9	59	240	20	163	ID	P
10	40	250	36	219	NS	S
11	68	245	28	167	ID	P

12	76	245	40	167	ID	P
13	66	275	39	206	NS	S
14	66	134	32	208	ND	P
15	65	130	13	214	ND	P
16	65	221	65	221	NX	P
17	49	146	49	146	NX	P
18	39	272	23	214	ID	S
19	63	258	32	187	ID	P
20	36	259	29	218	NS	P
21	70	329	13	244	NS	P
22	64	328	13	51	IS	P
23	69	241	34	166	ID	P
24	46	317	18	245	NS	P
L. Paron2						
1	62	235	35	167	NS	P
2	54	230	54	222	NS	P
3	51	150	33	209	IS	P
4	65	210	63	187	ID	S
5	74	250	52	181	ID	P
6	72	230	47	160	ID	P
7	48	273	34	220	NS	P
8	54	189	2	101	NS	P
9	61	238	26	164	ID	P
10	70	249	70	249	NX	P
11	54	235	52	215	XX	X
L. Paron3						
1	84	325	28	238	ID	S
2	60	240	59	221	ID	P
3	78	315	24	231	NS	P
4	45	270	43	249	NS	P
5	48	149	44	180	IS	S
6	35	290	22	235	NS	P
7	32	265	31	250	NS	P
8	85	150	29	237	ND	P
9	86	319	17	230	ID	S
10	85	328	19	56	IS	P
11	46	282	28	222	NS	P
12	53	237	24	166	NS	S
13	68	211	67	190	NS	P
14	53	234	52	218	NS	P
15	30	311	18	7	ND	P
Q. Llanganuco1						
1	60	220	60	220	NX	P
2	46	200	46	193	NS	P
3	62	205	60	229	ND	P
Q. Llanganuco2						
1	78	264	71	316	ND	P
2	73	110	25	28	ID	P
3	62	205	46	261	ND	P
4	50	235	50	243	ND	P
5	85	295	42	209	NS	P
6	48	30	47	45	ND	P
7	70	230	67	198	NS	P
8	44	200	42	178	NS	P
9	84	120	67	45	NS	P
10	15	240	15	250	ND	P
11	65	110	42	45	NS	P
12	78	110	56	182	ND	P
13	68	335	53	278	ID	P
14	72	305	41	232	NS	P
15	90	235	80	145	NS	P
16	80	235	59	162	ID	P
17	70	50	42	339	NS	P
18	60	26	49	75	XX	X
19	75	212	38	290	IS	P

20	20	202	14	249	IS	P
21	68	275	53	332	ND	P
22	82	10	67	81	ND	P
23	8	210	8	200	NS	P
Q. Llanganuco3						
1	69	75	58	127	IS	S
2	89	0	84	279	ID	P
3	81	62	14	150	IS	P
4	49	262	35	210	NS	S
5	80	132	79	159	ND	P
6	39	247	34	213	NS	P
7	38	231	37	218	NS	P
8	40	140	32	98	NS	P
9	50	305	48	326	ND	P
10	25	315	2	41	ND	P
11	42	240	40	260	IS	P
12	30	200	28	223	ND	P
13	40	230	6	312	ND	P
Q. Llanganuco4						
1	70	240	5	152	ID	P
2	5	230	5	244	ND	P
3	5	235	5	235	NX	P
4	80	235	80	235	NX	P
5	90	240	78	330	ND	P
6	81	228	77	276	ND	P
7	88	235	80	314	ND	P
8	90	218	82	308	IS	P
9	84	213	67	288	ND	S
10	81	237	77	285	ND	S
Q. Llanganuco5						
1	80	72	76	27	NS	P
2	76	238	76	238	IX	P
3	74	90	12	177	ND	P
4	80	50	77	11	NS	P
5	55	257	50	291	ND	S
6	73	253	33	331	ND	P
7	87	235	80	308	ND	S
8	88	208	85	140	ID	P
9	79	237	63	305	ND	P
Q. Ulta1						
1	30	218	28	243	ND	P
2	86	45	76	332	NS	P
3	60	222	56	253	ND	P
4	68	75	57	24	ID	C
5	38	230	35	258	ND	S
6	70	310	43	240	NS	P
7	84	190	30	277	IS	P
8	30	240	30	241	ND	P
9	36	220	35	234	IS	P
10	90	45	73	135	ND	S
11	67	72	55	19	NS	P
12	34	232	33	244	ND	P
13	80	50	79	77	ND	S
14	72	241	72	241	NX	S
Q. Ulta2						
1	46	100	26	38	ID	C
2	32	120	18	61	ID	C
3	61	220	54	260	ND	C
4	48	110	19	38	ID	C
5	57	110	53	79	NS	P
6	54	225	39	279	ND	C
7	38	226	36	248	IS	S
8	66	216	20	297	ND	P
9	62	230	59	260	IS	C
10	44	246	18	176	NS	C

11	70	234	58	180	ID	C
12	64	235	64	235	IX	P
13	21	215	18	185	NS	P
14	50	300	20	13	ND	P
15	43	250	9	170	NS	P
16	30	222	27	248	ND	P
17	37	134	10	58	ID	P
18	42	213	31	261	ND	P
19	74	192	43	117	ID	S
20	75	189	50	260	ND	S
21	80	215	7	304	ND	S
22	75	223	38	145	ID	P
23	39	119	16	50	ID	P
24	64	237	39	303	IS	P
25	65	222	14	138	NS	P
26	60	249	60	245	ID	P
27	56	233	54	209	NS	P
28	56	229	45	181	NS	P
29	52	229	50	253	ND	P
30	52	120	30	56	ID	P
31	41	142	19	76	ID	P
32	59	277	20	354	ND	P
Q. Ulta3						
1	78	265	28	348	IS	P
2	74	245	68	291	ND	P
3	70	70	69	87	ND	P
4	62	85	61	102	ND	P
5	83	255	78	310	IS	P
6	78	64	73	110	ND	P
7	50	80	32	22	NS	P
8	82	62	82	62	NX	P
9	70	45	69	31	NS	P
10	86	170	76	243	IS	P
11	82	61	63	347	NS	P
12	34	115	2	28	NS	P
13	38	95	6	13	NS	P
Q. Ulta4						
1	30	250	29	264	ND	P
2	74	170	6	258	ND	P
3	51	200	9	282	ND	P
Q. Honda1						
1	41	254			NJ	P
2	36	248			NJ	P
3	26	230			NJ	P
4	29	260			NJ	P
5	40	255			NJ	P
Q. Honda2						
1	72	225	67	266	ND	C
2	76	220	73	256	ND	C
3	77	215	74	253	ND	S
4	78	220	62	286	ND	C
5	90	45	85	135	IS	P
6	76	225	42	302	ND	P
7	85	249	42	335	ND	S
8	86	221	86	221	NX	P
9	60	12	38	75	ND	P
Q. Llaca1						
1	60	225	56	256	IS	C
2	70	240	65	278	IS	C
3	17	170	9	227	ND	S
4	80	61	32	337	ID	S
5	87	346	24	75	IS	P
6	87	354	55	268	ID	S
Q. Llaca2						
1	37	225	37	230	ND	S

2	64	76			SJ	P
3	86	350	20	261	NS	P
4	90	80	47	350	NS	P
5	80	250	52	327	XX	X
6	48	134	35	185	ND	P
7	86	175	29	87	XX	X
8	78	165	66	227	IS	S
Q. Rajucolta1						
1	50	230	50	233	ND	S
2	42	240	42	243	ND	P
3	30	237	30	235	NS	S
4	30	265	23	223	NS	P
5	34	257	28	220	NS	P
6	90	65	15	335	NS	P
7	52	80	48	49	NS	P
8	58	90	11	7	NS	S
9	51	80	15	2	NS	P
10	80	72	18	345	NS	S
11	38	140	32	104	NS	S
12	66	75	4	347	NS	S
Q. Rajucolta2						
1	30	150	30	150	NX	P
2	78	10	23	95	ND	S
3	78	350	39	70	IS	P
4	88	230	87	275	IS	P
5	87	175	0	265	ND	P
6	83	250	15	162	NS	P
7	80	193	2	283	IS	C
8	52	250	8	334	IS	C
9	78	340	14	253	NS	P
Q. Queroccocha1						
1	78	205	77	186	ID	S
2	90	25	24	115	ND	P
3	56	225	44	176	NS	S
4	60	235	43	292	ND	C
5	74	310	73	289	ID	C
6	75	40	69	354	NS	C
7	78	205	61	273	ND	S
8	90	50	16	320	ID	C
9	90	80	22	170	ND	P
10	74	325	68	11	ND	P
11	74	235	68	281	ND	S
12	46	107	44	129	IS	S
13	52	245	26	312	IS	S
14	75	204	29	122	NS	P
15	67	294	64	323	ND	S
16	75	116	11	203	ND	S
17	88	213	27	124	ID	P
18	63	227	35	158	ID	P
19	59	237	56	264	ND	P
20	77	215	15	128	ID	P
21	88	22	47	110	ND	P
22	53	225	43	271	ND	P
23	53	225	8	309	ND	P
24	78	302	71	250	ID	P
Q. Queroccocha2						
1	58	325	54	357	ND	P
2	82	310	57	27	ND	P
3	88	75	67	350	NS	P
4	70	95	56	38	NS	S
5	86	358	53	273	ID	P
6	90	75	13	345	ID	P
7	90	75	64	345	ID	P
8	76	16	72	57	ND	P
9	77	340	76	1	ND	P

10	85	345	81	43	ND	P
11	42	165	31	117	NS	P
12	80	297	48	16	IS	P
13	87	223	70	305	ND	P
14	88	47	80	126	IS	P
15	46	321	36	7	ND	P
16	43	333	41	352	ND	P
17	81	183	80	207	ND	P
18	84	241	24	154	NS	S
19	88	258	60	345	ND	P
20	90	86	73	356	ID	P
Q. Queroccocha3						
1	90	110	50	20	ID	S
2	60	90	46	37	NS	P
3	54	345	31	49	ND	S
4	80	168	28	83	NS	P
5	82	116	80	79	NS	P
6	90	10	18	100	IS	S
7	75	105	71	66	NS	P
8	62	128	48	75	NS	P
9	80	130	79	108	ID	P
10	85	255	69	332	IS	P
11	80	330	47	49	ND	P
12	58	0	37	62	ND	P
13	75	340	69	26	ND	P
14	70	20	61	68	ND	P
15	72	140	36	216	IS	S
16	81	115	54	38	NS	P
17	89	0	38	89	ND	P
18	69	164	37	91	ID	P
19	44	125	27	66	NS	S
20	87	260	65	344	ND	S
21	56	95	43	145	ND	P
22	88	199	26	110	ID	S
23	87	342	38	70	IS	P
24	80	257	80	268	ND	P
25	65	325	45	263	NS	S
26	79	21	54	96	ND	P
Q. Pastoruri1						
1	42	315	0	225	NS	S
2	64	308	14	225	NS	P
3	44	230	43	246	ND	P
4	88	200	75	283	IS	P
5	60	322	51	278	ID	P
6	65	75	30	149	ND	S
7	63	22	0	292	ID	P
8	85	86	16	175	IS	C
9	50	15	43	337	ID	P
10	78	270	77	251	ID	S
11	78	270	29	187	NS	P
12	81	294	48	214	NS	P
13	49	267	42	228	NS	P
14	44	285	44	293	IS	P
15	43	272	41	251	NS	P
16	86	200	59	117	ID	P
17	61	43	14	125	ND	P
18	45	344	40	311	ID	P
19	65	64	26	141	IS	S
20	85	91	20	179	IS	P
21	34	356	21	301	NS	P
22	45	6	43	344	ID	P
23	83	279	32	193	NS	P
24	85	286	45	11	ND	P
25	80	271	70	211	NS	P
26	81	268	80	292	ND	P

27	35	267	28	225	NS	P
28	30	261	24	222	NS	P
Q. Pastoruri2						
1	56	34	51	67	XX	X
2	55	110	36	51	XX	X
3	49	62	47	43	NS	P
4	54	120	41	69	NS	S
5	45	95	36	51	NS	P
6	62	120	35	52	NS	P
7	55	65	50	33	ID	P
8	65	60	46	359	NS	C
9	55	88	50	120	ND	P
10	52	27	38	79	ND	P
11	34	145	27	186	ND	P
12	51	237	43	196	ID	P
13	42	175	40	194	ND	P
Q. Pastoruri3						
1	54	50	54	47	XX	X
2	82	60	8	149	ND	P
3	90	30	86	120	IS	P
4	80	35	54	111	ND	P
5	84	75	55	353	NS	P
6	84	75	12	346	ID	P
7	84	230	71	302	ND	P
8	84	230	10	319	ND	P
9	76	240	71	196	NS	P
10	55	31	45	76	ND	S
11	90	257	3	347	ND	S
Q. Pastoruri4						
1	90	205	10	115	NS	C
2	85	278	42	192	NS	S
3	84	143	80	90	ID	P
4	80	64	57	138	ND	P
5	76	303	49	16	ND	P
6	70	294	58	349	ND	P
7	80	62	76	17	NS	C
8	76	34	68	342	NS	C
9	73	30	60	332	NS	C
10	82	36	41	119	ND	P
11	72	150	31	229	ND	P
12	74	153	29	234	ND	P
13	65	100	50	44	XX	X
14	75	150	34	230	ND	P
15	83	0	54	80	ND	P
16	78	58	52	132	ND	P
17	82	60	49	141	IS	P
18	78	25	39	105	ND	S
19	86	168	74	92	ID	P
20	68	66	36	353	NS	P
21	82	135	61	60	ID	P
22	63	98	19	18	ID	P
23	63	98	9	183	ND	P
Q. Pastoruri5						
1	87	200			NJ	P
2	76	215			NJ	P
3	72	50	32	332	XX	X
4	67	175	15	91	ID	P
5	70	22	43	312	NS	P
6	37	170	0	80	NS	S
7	80	180	29	95	NS	P
8	75	215	6	303	IS	P
9	36	228	4	313	ND	P
10	80	180	4	91	ID	P
Fortaleza Valley1						
1	82	340	4	69	IS	P

2	90	10	0	100	ND	P
3	60	190	23	266	ND	S
4	84	185	24	272	ND	S
5	82	200	53	279	ND	P
6	80	210	43	130	ID	P
7	80	245	79	267	ND	P
8	85	205	20	117	ID	P
9	66	90	61	55	ID	P
10	82	207	23	120	ID	P
11	83	180	34	265	IS	P
12	90	65	64	335	NS	P
Fortaleza Valley2						
1	74	150	25	232	ND	P
2	76	70	64	11	ID	P

8.3 Annexes du Chapitre 5

8.3.1 Figure A1 : Map of the erosion rates over the past 10 Myr and chemistry of the amphiboles

Appendix 1

1. Map of the erosion rates over the past 10 Ma

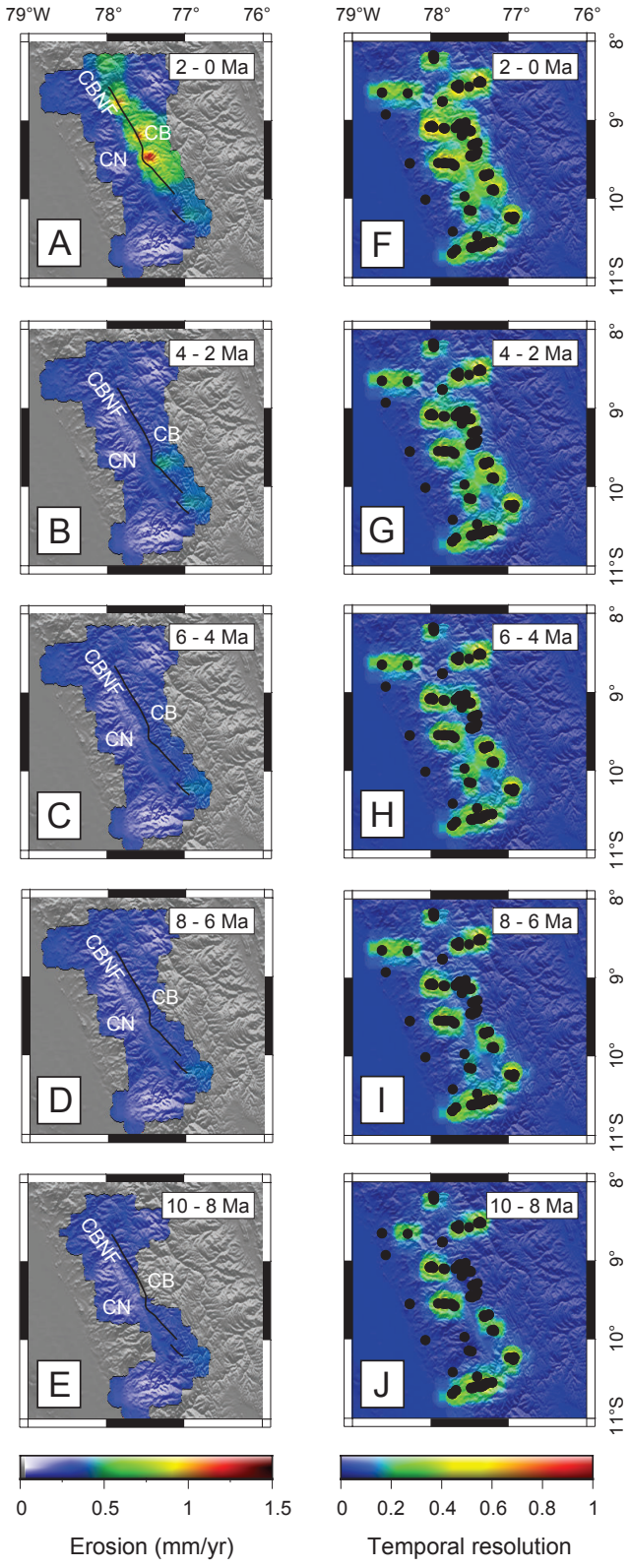

Fig. A: Erosion rate history and temporal resolution obtained from Glide inversions (Fox et al., 2014; Herman and Brandon, in press). A-E) Exhumation rates over the past 10 Myrs

inferred by analysis of 150 thermochronometric ages. E-J) Temporal resolution of the erosion rates estimation. Temporal resolution values of 1 imply perfect resolution in time, and are dimensionless. Important geologic units are indicated: Cordillera Blanca (CB), Cordillera Negra (CN). Gray regions have insufficient data to resolve exhumation rates. Model parameters include an *a priori* exhumation rate of 0.4 ± 0.2 km/Myr, an exponential correlation function with length scale of 20 km, and an initial geothermal gradient of 32°C/km.

2. Chemistry of the amphiboles

In situ major element abundances were measured on thin section with an electron microprobe JEOL JXA-8230 at ISTerre (Grenoble), operating condition were 15 kV and 12 nA. The amphiboles chemistry is reported in the excel table *Appendix2-chemistry-amphiboles.*

8.3.2 Table A1 : Samples location and amphibole compositions

Electronic appendix 2: Samples location and amphibole compositions

Sample	Latitude (°S)	Longitude (°W)	Elevation (m)
CB01	9.05021	77.59880	4247
CB08	9.03437	77.54872	3928
CB12	9.14225	77.48431	4167
CB24	9.46859	77.46396	4121
CB26	9.70282	77.31378	4026

Electron microprobe data
Data are separated by sample measured

Sample: CB01

SiO2	TiO2	Al2O3	Cr2O3	FeO	MnO	MgO	CaO	Na2O	K2O
Amphibole 1									
46.0193	0.9003	9.2075	0	20.0332	0.4221	9.3441	10.8111	1.0362	0.3591
47.5471	0.7017	6.7149	0	19.1598	0.3862	10.9059	10.0322	0.9474	0.2985
48.0230	0.7820	7.4894	0	18.7016	0.4257	10.9806	10.1817	0.8737	0.2440
47.8994	0.7777	7.5590	0	19.4476	0.4334	10.9537	10.3257	0.8104	0.2640
47.4056	0.8282	8.1385	0	18.1570	0.3250	10.6485	11.3757	0.9289	0.2634
46.9330	0.8826	7.9904	0	20.1625	0.4134	10.0838	10.1640	0.8514	0.2905
44.3707	0.6642	11.8913	0.0055	19.9586	0.3741	8.2298	11.2267	1.2982	0.4239
Amphibole 2									
46.6279	0.6613	8.7749	0.0039	19.6911	0.3876	9.8041	10.8071	1.0285	0.3154
46.7339	0.9621	8.6355	0.0185	18.6553	0.4128	10.3228	10.9427	1.0011	0.4096
Amphibole 3									
44.8449	0.6816	11.2478	0.0106	19.7012	0.3478	8.6379	11.2811	1.2191	0.4285
47.4597	0.9011	8.0602	0	18.7564	0.4195	10.8427	10.2976	0.9604	0.2325

Sample: CB08

SiO2	TiO2	Al2O3	Cr2O3	FeO	MnO	MgO	CaO	Na2O	K2O
Amphibole 1									
49.3204	0.8087	5.8166	0.0234	14.6566	0.7038	13.5554	11.8770	0.9976	0.5196
49.4603	0.7182	5.7419	0.0064	14.0914	0.6716	13.9911	11.8015	0.9202	0.5284
49.4836	0.7767	5.7716	0.0017	13.7781	0.6494	13.9004	11.9608	0.7876	0.4999
48.9840	0.7092	5.9588	0	14.5606	0.6570	13.7241	11.7192	1.2160	0.5860
47.1064	1.0766	7.3276	0.0072	15.3147	0.6363	12.5468	11.6703	1.4314	0.6894
47.4464	1.1023	7.2670	0.0040	15.4932	0.6103	12.6933	11.5667	1.4774	0.6610
47.1266	1.0567	7.4379	0.0029	15.2040	0.6231	12.6062	11.6413	1.3414	0.7208
45.0045	1.2938	8.8353	0.0212	16.4044	0.6316	11.3984	11.7175	1.5142	0.9623
48.2979	0.9411	6.6655	0	15.0154	0.6341	13.0731	11.8571	1.1394	0.6210
48.9747	0.7428	6.0544	0.0095	14.6475	0.7376	13.3846	12.0016	0.9399	0.5508
48.7315	0.7611	6.2655	0.0097	15.0925	0.7513	12.9713	11.7896	1.0699	0.5718
Amphibole 2									
48.3299	0.7751	6.1830	0	15.3488	0.6958	12.7907	11.8535	0.9453	0.5805
46.1675	1.1715	7.9123	0.0020	16.2283	0.6486	11.6671	11.5104	1.5063	0.7969
46.0388	1.1082	7.9979	0	16.4136	0.6808	11.5531	11.6370	1.4586	0.8189
46.5693	1.0288	7.5144	0.0267	16.5831	0.6394	11.7267	11.6873	1.3026	0.7611
47.0393	0.9611	7.1830	0.0236	16.2547	0.6930	11.9503	11.8283	1.1413	0.6848
48.0097	0.5600	6.5600	0	16.4554	0.6870	12.0602	11.9267	0.8723	0.6354
48.2292	0.8268	6.4498	0.0078	15.4714	0.7073	12.9552	11.7129	1.1861	0.6249
47.9325	0.8571	6.6155	0.0125	15.4959	0.7125	12.8385	11.6519	1.2886	0.6565
48.1353	0.8265	6.4929	0	15.1493	0.6141	12.8479	11.7945	1.1357	0.6328
47.5273	0.9357	6.7908	0	15.8011	0.6929	12.6090	11.7676	1.1542	0.6733
45.7633	1.1565	8.2512	0.0246	16.7669	0.6546	11.3790	11.7429	1.4477	0.8875
45.7543	1.1530	8.2940	0	16.7971	0.6584	11.4547	11.8374	1.3497	0.8859
48.1556	0.7815	6.6527	0.0139	15.7642	0.6180	12.4206	11.8869	1.0066	0.6363
48.1988	0.7749	6.5706	0.0134	15.8736	0.6122	12.5571	11.8123	1.0055	0.6081
Amphibole 3									
48.3457	0.6296	5.9102	0.0010	15.1123	0.6521	13.2268	11.7865	1.2227	0.5718
48.1964	0.7495	6.0692	0.0055	15.0868	0.7091	13.2748	11.5892	1.2975	0.5704
48.2972	0.7401	6.1190	0.0120	15.2694	0.6499	13.1298	11.7555	1.1289	0.6025
48.8302	0.6581	5.7963	0.0086	14.9662	0.6816	13.4388	11.8179	1.1847	0.5338
48.7341	0.6367	5.8476	0.0321	15.3689	0.6779	13.2364	11.8811	1.0989	0.5380
Amphibole 4									
47.0027	1.1982	7.3806	0	15.1376	0.5429	12.6488	11.6299	1.4084	0.7366
46.7582	1.2790	7.7259	0.0280	15.1254	0.5005	12.6747	11.6099	1.5638	0.6976
46.2641	1.2131	8.1679	0.0163	15.6712	0.5058	12.3039	11.7347	1.5521	0.8694
46.3934	1.1724	8.0414	0	15.4818	0.4900	12.3015	11.6888	1.5529	0.8446
45.9179	1.1600	8.2442	0	16.2494	0.6370	11.8859	11.6192	1.4904	0.8887
48.9179	0.6931	5.9003	0.0136	14.7319	0.6289	13.4767	11.7626	1.0617	0.5412
48.5772	0.7011	6.0592	0.0049	15.1487	0.6767	13.2875	11.6726	1.2164	0.5762
45.0727	1.3269	8.7712	0.0005	16.7072	0.6293	11.3077	11.6406	1.6083	0.9805
45.9040	1.2190	8.3866	0.0065	16.0108	0.5710	11.9465	11.6233	1.5321	0.8868
45.2266	1.3082	8.8549	0.0217	16.4918	0.5334	11.4745	11.6687	1.6284	0.9753
45.0926	1.2833	8.7347	0	16.5344	0.6163	11.5777	11.6115	1.5625	0.9796
45.1479	1.2884	9.1420	0.0089	16.7161	0.6043	11.2030	11.6015	1.5478	1.0099
46.1999	1.1663	8.1909	0.0150	16.0401	0.5456	11.8082	11.6022	1.5545	0.8525
45.9088	1.1873	8.3966	0	15.9484	0.5507	11.9496	11.5692	1.6022	0.8887
45.9807	1.1627	8.2271	0.0005	16.0731	0.5740	12.0728	11.6676	1.5756	0.8409
46.2694	1.1668	8.1769	0.0038	15.9079	0.5336	12.0876	11.6452	1.5460	0.8628
45.8258	1.2118	8.2529	0.0015	16.0333	0.5364	12.0211	11.6661	1.6247	0.8679
46.8412	1.0888	7.5711	0.0128	15.3291	0.5304	12.6552	11.7789	1.4153	0.7786
46.3116	1.1826	8.0521	0.0147	15.6597	0.5312	12.3015	11.6832	1.5074	0.8630
46.8545	1.1471	7.6638	0.0063	15.7252	0.6131	12.4789	11.6402	1.4952	0.7431

Sample: CB12

SiO2	TiO2	Al2O3	Cr2O3	FeO	MnO	MgO	CaO	Na2O	K2O
Amphibole 2									
45.5400	1.2303	9.3164	0.0602	19.2263	0.4512	9.3776	10.9566	1.0725	0.4344
45.3059	1.3012	9.3115	0.0334	19.4319	0.4516	9.4325	10.8204	0.9956	0.4921
48.2567	0.8853	6.7553	0.0039	18.5815	0.4681	11.2893	10.6316	0.7784	0.2949
47.9729	0.9229	7.0091	0	18.1431	0.4869	11.0223	11.0880	0.9458	0.3426
48.4795	0.8292	6.6892	0.0244	19.1784	0.4501	10.7132	10.7623	0.8217	0.3025
Amphibole 3									
48.8052	0.7092	6.8163	0.0189	19.1416	0.5692	11.2294	10.1773	0.6592	0.3015
48.4924	0.6673	6.9597	0.0230	19.1439	0.5647	11.1948	10.4847	0.6771	0.2712
49.0987	0.6021	6.4217	0.0030	18.614	0.6182	11.5392	10.4345	0.5484	0.2565
Amphibole 5									
48.8403	0.7107	6.7217	0	18.5623	0.4723	11.3492	10.5844	0.7751	0.2669
48.7734	0.7747	6.5722	0.0373	19.1456	0.4732	11.1966	10.5618	0.7510	0.2781
48.4926	0.7337	6.4385	0	19.3671	0.5626	11.2715	10.0232	0.7101	0.2988
49.0922	0.6631	6.2034	0.0129	17.8877	0.5548	11.6114	11.0225	0.7505	0.2425

Sample: CB24

SiO2	TiO2	Al2O3	Cr2O3	FeO	MnO	MgO	CaO	Na2O	K2O
Amphibole 1									
44.8471	0.7098	9.0721	0.0123	21.2436	0.5756	8.2775	11.5454	1.3036	1.0653
45.6440	0.7294	8.4789	0.025	20.7418	0.6408	8.4729	11.5693	1.2455	0.9363
45.5180	0.7380	8.3750	0	20.8612	0.6863	8.4982	11.5471	1.2207	0.9348
42.5966	0.8096	10.9696	0.0138	21.9077	0.6554	7.0165	11.5393	1.4544	1.3699
42.0313	0.7455	11.3885	0	22.1544	0.6151	7.0003	11.5407	1.4284	1.3600
42.0699	0.7145	11.3072	0.0177	22.1361	0.6100	7.0598	11.5586	1.4483	1.3538
42.2112	0.6801	11.4226	0.0163	21.8512	0.6398	7.0264	11.6416	1.3895	1.4016
42.2336	0.6611	11.3599	0	21.9982	0.6414	7.0631	11.5210	1.4070	1.3946
42.3238	0.6287	11.4391	0.0035	21.9701	0.7068	6.9454	11.5972	1.2906	1.4133
42.1096	0.6648	11.6260	0	22.0573	0.6278	6.7927	11.6171	1.3384	1.4406
42.4486	0.7200	11.1927	0.0208	21.6541	0.6485	7.1236	11.6120	1.2605	1.3392
43.8402	0.5958	10.2290	0	21.3165	0.6469	7.6279	11.6260	1.2056	1.1598
42.0511	0.7189	11.3472	0.0336	22.4019	0.6635	6.9078	11.4960	1.3562	1.3758
42.6033	0.6258	11.3502	0.0297	21.9732	0.6154	7.1021	11.6009	1.266	1.3495
42.7499	0.6383	10.8415	0.0118	22.0025	0.6403	7.3229	11.6567	1.3799	1.2636
42.3763	0.6474	11.1317	0	21.9614	0.6165	7.2567	11.5514	1.4065	1.3705
42.3038	0.6707	11.3416	0	21.8860	0.6665	7.1353	11.6186	1.4622	1.4441
41.9784	0.7181	11.4091	0.0202	21.7592	0.6442	7.0365	11.6687	1.3927	1.4328
42.2452	0.6380	11.2573	0.0010	21.9615	0.6649	7.1374	11.6434	1.3732	1.3660
42.3202	0.6712	11.4372	0	21.9435	0.6209	7.0698	11.6085	1.4185	1.3710
44.2122	0.5702	9.6453	0.0242	21.1072	0.6586	8.1164	11.7113	1.2638	1.0551
42.6916	0.6867	10.9943	0.0448	21.8945	0.5983	7.3152	11.5460	1.3720	1.2998
42.0235	0.7139	11.2730	0.0157	21.8615	0.6032	7.0960	11.6118	1.3643	1.4451
41.7585	0.7038	11.6401	0.0146	22.0759	0.6450	6.9705	11.4628	1.4743	1.4263
41.9627	0.6469	11.5003	0.0212	21.9754	0.6492	6.9918	11.5864	1.3795	1.4359
41.6182	0.6641	11.7858	0	22.2931	0.6023	6.8637	11.5865	1.4782	1.4575
41.3471	0.6258	11.8981	0	22.4650	0.6183	6.7435	11.6259	1.3998	1.5154
Amphibole 2									
41.4156	0.6089	11.8597	0	22.4119	0.6063	6.5120	11.5073	1.4013	1.5559
42.4399	0.6622	10.9292	0	22.1260	0.6017	7.0283	11.4824	1.4433	1.377
41.6156	0.6294	11.7717	0.0125	22.6745	0.6198	6.6048	11.4796	1.6158	1.5203
41.3533	0.6732	11.8704	0.0016	22.5001	0.6698	6.6033	11.4605	1.4849	1.5283
41.6054	0.6604	11.6788	0.0254	22.2982	0.5964	6.7308	11.473	1.5384	1.4621
41.7935	0.6388	11.4865	0.0148	22.2619	0.6566	6.7639	11.4781	1.5878	1.4553
41.5734	0.6552	11.7605	0	22.5745	0.6469	6.7091	11.5167	1.4607	1.4555
42.2391	0.6389	11.1931	0.0096	22.2760	0.6155	6.9843	11.4279	1.4272	1.3768
41.7339	0.6489	11.4905	0.0154	22.4245	0.6408	6.8624	11.5645	1.5103	1.4301
42.0195	0.6620	11.3128	0	22.2356	0.5732	6.8961	11.4981	1.4549	1.4068
42.0026	0.7034	11.4815	0.0048	22.2869	0.6284	6.9259	11.5866	1.4743	1.4111
41.7400	0.6916	11.5952	0.0274	21.9468	0.6701	6.7497	11.6245	1.4341	1.4590
42.2051	0.6838	11.2269	0	22.2558	0.6429	6.9721	11.6271	1.4592	1.3669
42.4664	0.3473	11.1627	0.0347	22.3938	0.5880	6.7242	11.5843	1.3964	1.2937
41.7343	0.7363	11.4726	0.0034	22.4206	0.6197	6.8257	11.5260	1.5001	1.4012
41.9535	0.7428	11.7205	0.0032	22.0105	0.6563	6.7206	11.4813	1.5376	1.4337
42.0581	0.6260	11.6469	0.0202	22.0234	0.6115	6.7545	11.5510	1.4112	1.5006
Amphibole 3									
42.4694	0.8709	11.2827	0.0400	22.0497	0.6768	6.9560	11.5238	1.5223	1.3086
42.9438	0.7662	10.5073	0.0366	21.6932	0.6569	7.4314	11.5381	1.4919	1.2381
43.1389	0.7262	10.3545	0.0456	21.8218	0.6496	7.4520	11.5335	1.4577	1.2121
42.9786	0.7633	10.4621	0.0128	21.7886	0.6777	7.4341	11.5936	1.4341	1.2232
43.2114	0.7843	10.4742	0.0250	21.8192	0.7134	7.4108	11.5935	1.3664	1.2251
42.9099	0.8860	10.8265	0.0071	21.7236	0.6701	7.2129	11.5197	1.4308	1.3246
42.9186	0.8077	10.7003	0.0337	21.8584	0.6365	7.2751	11.6212	1.3981	1.2905
43.1386	0.7788	10.4643	0.0566	21.7460	0.6155	7.4129	11.5686	1.4229	1.2014
42.8369	0.7755	10.4470	0.0220	21.6995	0.7042	7.4282	11.6928	1.4086	1.186
43.7418	0.7223	9.7372	0.0486	21.5844	0.7124	7.7550	11.6447	1.3462	1.1136
43.8088	0.6689	9.8767	0.0361	21.4331	0.6229	7.7698	11.5842	1.3228	1.106
43.8516	0.6671	9.8476	0.0100	21.2737	0.5962	7.8759	11.6722	1.2954	1.1298
46.6840	0.5525	7.5807	0.0218	20.3767	0.6644	9.0705	11.6964	1.0736	0.7958
46.1012	0.5454	8.0111	0.0313	20.6005	0.6829	8.8352	11.6005	1.1009	0.8299
44.3674	0.6819	9.5747	0.0297	21.4224	0.6607	7.8607	11.4603	1.3431	1.0670

Sample: CB26

SiO2	TiO2	Al2O3	Cr2O3	FeO	MnO	MgO	CaO	Na2O	K2O
Amphibole 1									
47.8035	0.9130	6.5248	0	16.4153	0.7532	12.0780	11.5685	1.2318	0.6740
48.1981	0.8718	6.2748	0.0184	16.2286	0.7645	12.3128	11.5963	1.2273	0.6028
48.4301	0.8570	6.2179	0	16.0614	0.7293	12.3274	11.6213	1.2313	0.6073
48.8333	0.8956	6.1589	0	16.0739	0.7777	12.4250	11.6753	1.1960	0.5874
48.2766	0.8946	6.3452	0	16.1801	0.7373	12.3394	11.5815	1.1669	0.6062
48.0751	0.9868	6.4833	0	16.2411	0.8166	12.0909	11.5808	1.2319	0.6383
49.0975	0.7837	5.8599	0.0096	15.8127	0.7961	12.5141	11.6857	1.1313	0.5158
47.8612	0.8844	6.6108	0.0101	16.5138	0.8038	12.0842	11.6290	1.1849	0.6591
48.4735	0.6438	6.3048	0.0092	16.0577	0.7584	12.4230	11.6499	1.0835	0.5744
48.8360	0.7151	6.0280	0.0110	16.1307	0.7654	12.7969	11.6072	1.1443	0.5739
48.5259	0.7975	6.0520	0	16.0676	0.7547	12.5763	11.5473	1.0772	0.5704
48.2849	0.9206	6.4920	0.0121	16.1561	0.7166	12.1770	11.6054	1.1861	0.6449
45.8531	1.3629	8.0804	0.0113	17.4901	0.7696	10.9430	11.5962	1.4357	0.8809
48.9613	0.9014	6.0195	0.0271	16.1171	0.7682	12.6134	11.7504	1.1186	0.5476
48.6810	0.8914	6.0788	0.0107	15.8110	0.6950	12.6649	11.5975	1.1519	0.5803
48.6858	0.9112	6.3080	0.0113	15.8646	0.6916	12.5013	11.6299	1.1221	0.5699
48.6872	0.8645	6.2290	0	16.0367	0.7671	12.5799	11.6939	1.0383	0.5699
48.9558	0.6995	6.0711	0.0099	16.0013	0.7799	12.4969	11.7346	1.0780	0.5543
48.5912	0.7755	6.1455	0.0071	16.4148	0.7607	12.3726	11.6853	1.0936	0.5927
48.6515	0.6125	6.2364	0.0169	16.4921	0.7287	12.0880	11.8755	1.0209	0.5671
Amphibole 2									
47.8780	0.7218	6.7908	0.0339	16.3904	0.7966	12.0167	11.7379	1.1037	0.6199
47.8862	0.7628	6.9547	0.0131	16.4773	0.6715	11.8838	11.7769	1.0763	0.6191
47.6969	0.7811	6.8256	0.0226	16.5626	0.7632	11.8808	11.8604	1.0913	0.6296
47.5689	0.8396	6.9951	0.0147	16.6472	0.7349	11.8671	11.7773	1.0785	0.655
48.2540	0.8123	6.3485	0.0311	16.3012	0.7052	12.3723	11.8055	1.0559	0.5759
48.6186	0.7800	6.3047	0.0282	16.0932	0.7698	12.3164	11.7832	0.9812	0.5673
48.5221	0.7982	6.2396	0.0196	16.1597	0.7389	12.3845	11.7386	1.1048	0.5700
48.7016	0.8153	6.1910	0.0232	16.1724	0.7335	12.4576	11.8600	0.9819	0.5439
49.1157	0.7523	5.7498	0.0042	15.9868	0.7893	12.7373	11.6778	1.0643	0.5505
48.9617	0.7690	5.9402	0.0010	15.8090	0.7617	12.5998	11.7113	1.0743	0.5479
48.9331	0.7696	5.8046	0.0179	15.8145	0.7442	12.7334	11.7928	1.0727	0.5324
48.4935	0.8437	6.3109	0.0014	16.1764	0.7502	12.5075	11.7238	1.1506	0.5923
48.8169	0.8181	6.1037	0.0289	15.9380	0.7257	12.5885	11.5799	1.1169	0.5677
48.6428	0.8058	6.2902	0.0213	16.0519	0.7471	12.5257	11.6962	1.1473	0.5917
46.6497	1.0333	7.6001	0.0133	17.1037	0.7524	11.4271	11.5632	1.3265	0.7709
48.2796	0.7721	6.2539	0.0023	16.3036	0.7358	12.3231	11.7824	1.1302	0.5614
Amphibole 3									
45.9211	1.2548	8.1816	0.0205	17.1531	0.6855	10.9097	11.5574	1.4032	0.9430
45.8822	1.4867	8.2937	0	17.2428	0.7151	11.0325	11.6266	1.3909	0.9225
45.4237	1.5186	8.5686	0.0126	17.2285	0.6666	10.8330	11.5758	1.4726	0.9809
44.8224	1.6262	8.9527	0.0169	17.2701	0.6589	10.5853	11.5987	1.5367	1.0127
44.6967	1.5877	8.9968	0.0056	17.4231	0.6548	10.7025	11.5526	1.5251	1.0313
45.0709	1.5678	9.0801	0.0108	17.2350	0.6666	10.6945	11.5231	1.5403	0.9922
45.9594	1.4270	8.3108	0	16.8535	0.6593	11.1509	11.4698	1.4827	0.9119
45.7076	1.4364	8.5282	0	17.2181	0.7076	10.9502	11.5950	1.5588	0.9379
45.6506	1.4054	8.5793	0	17.1282	0.6623	11.0711	11.5340	1.5426	0.9393
45.8317	1.4531	8.5345	0.0187	17.2299	0.6441	10.9631	11.4758	1.4905	0.9510
45.692	1.4324	8.4205	0.0020	17.2476	0.6794	10.9094	11.6404	1.5207	0.9488
45.7202	1.4596	8.3674	0.0044	17.2797	0.6973	11.0442	11.5555	1.5148	0.9459
46.351	1.4430	8.1194	0.0015	16.7691	0.6899	11.0618	11.6010	1.4870	0.8660
46.2624	1.3621	7.9747	0.0412	16.8530	0.7650	11.2900	11.5356	1.3875	0.8673
48.4276	0.8442	6.6800	0.0133	16.3493	0.7837	11.9676	11.6769	1.1943	0.6758
Amphibole 4									
46.3624	1.3027	7.8389	0.0110	17.2548	0.6802	11.2394	11.472	1.4712	0.8633
46.4325	1.2686	7.8600	0.0055	17.0623	0.6904	11.1914	11.5473	1.3786	0.8239
46.2907	1.3329	7.8973	0.0073	17.3037	0.6740	11.2232	11.5542	1.3978	0.8296
45.8969	1.3953	8.3933	0.0139	17.1997	0.7599	10.9135	11.5886	1.4480	0.8678
45.8594	1.4071	8.2581	0	17.1792	0.7321	10.8871	11.4768	1.5769	0.9115
46.5440	1.2554	7.5576	0.0027	17.1562	0.6785	11.4951	11.4516	1.3696	0.7636
45.9686	1.3875	8.2132	0.0193	17.2890	0.6923	10.9529	11.5101	1.5419	0.8611

45.7588	1.3799	8.2160	0	17.7599	0.7109	10.8657	11.5200	1.4073	0.8896
45.7899	1.3083	8.2151	0	17.0728	0.7319	11.0915	11.6007	1.4505	0.8810
45.8598	1.3273	8.2923	0.0386	17.2897	0.7016	10.9674	11.5348	1.5075	0.9077
45.7198	1.3709	8.3132	0.0109	17.4500	0.7242	10.9036	11.5918	1.4651	0.8649
45.7477	1.3633	8.2932	0.0116	17.4828	0.6943	10.9508	11.5469	1.4566	0.8879
45.9635	1.3304	8.0457	0.0074	17.2572	0.7058	11.0349	11.5049	1.4344	0.8594
46.0209	1.2444	8.0121	0.0100	17.0119	0.6718	11.2354	11.4797	1.4416	0.8460
45.9932	1.3209	8.1159	0.0338	17.2385	0.7305	10.9079	11.5782	1.4608	0.8232
46.1265	1.3289	8.1980	0.0285	17.3301	0.7207	10.9485	11.5223	1.5465	0.8635
46.2992	1.3354	8.0252	0.0192	17.0733	0.7021	11.2354	11.5414	1.4947	0.8542
46.2253	1.2899	7.9913	0.0217	17.0194	0.7393	11.1751	11.4617	1.4585	0.8459
46.4375	1.2906	7.9619	0	17.0742	0.6818	11.2756	11.5095	1.4535	0.8232
46.4557	1.2415	7.7862	0.0234	16.8854	0.7764	11.3375	11.6060	1.4415	0.7911
46.8370	1.2236	7.6391	0.0085	16.9863	0.7042	11.4893	11.5204	1.4063	0.7657
46.2597	1.2996	8.2190	0.0267	17.2254	0.6448	11.1515	11.4539	1.4654	0.8457
45.6308	1.3687	8.4770	0.0157	17.5093	0.7051	10.8466	11.5457	1.5133	0.9319
45.4067	1.3912	8.3872	0	17.4094	0.7634	10.7734	11.4893	1.5938	0.9269
45.5109	1.3597	8.4489	0.0021	17.4694	0.7225	10.8136	11.6324	1.5522	0.8912
45.3599	1.4457	8.6023	0.0301	17.3827	0.7341	10.7988	11.5264	1.4985	0.9093
45.8400	1.3619	8.1651	0	17.3192	0.6821	11.0876	11.5060	1.4845	0.8680
45.7846	1.3513	8.2609	0.0296	17.1646	0.7105	10.9898	11.5697	1.5645	0.8706

8.4 Annexes du Chapitre 6

8.4.1 Table A1: parameters of the modeling

TABLE A1: MAIN PARAMETERS OF THE MODELS

Symbole	Value	Meaning
Geometrical parameters		
nx	250	Number of grid points in the x direction
ny	250	Number of grid points in the y direction
xl	200000	x dimension of the rectangular domain (m)
yl	200000	y dimension of the rectangular domain (m)
Time stepping		
dt	1000.	Time step length (yr)
nstep	10000	Number of time step (yr)
nfreq	1000	Frequency of outputs (step number)
Boundary conditions (lower, right, top and left boundaries)		
-	1011	A boundary sets to 1 (0) is assumed to be at the base level (reflective)
Flexure		
thickflex	2000.	Elastic thickness (m)
ym	1×10^{11}	Young Modulus (Pa)
pratio	0.25	Poisson's ratio
rhocflex	2750.	Crustal density (kg/m^3)
rhoaflex	3300.	Asthenospheric density (kg/m^3)
Granite		
granite_x	120000	x coordinate of the center of the granite (m)
granite_y	100000	y coordinate of the center of the granite (m)
granite_rx	10000	x radius (m)
granite_ry	75000	y radius (m)
granite_top	500	Depth of the top of the granite (m)
granite_bottom		Depth of the bottom of the granite (m)
granite_drho	400	Density anomaly (kg/m^3)
granite_dk	0.6	Hardness, the fluvial incision parameter (kf) will be multiplied by granite_dk
Stream power law (assuming a linear slope dependence)		
m	0.4	Discharge exponent
kf	1×10^{-5}	K coefficient
sc	40.	Critical slope
Uplift parameters		
uplift	0.1	Regional uplift (mm/yr)
f	0.3; 0.5; 0.3	Uplift of the eastern block on a N-S fault at x = 100 000 (mm/yr)
Initial topography		
initial_topography	0-3500	Elevation range from 0 to 3500 m (See Appendices Fig. A1)
Precipitations		
precipitations	0-1.5	Rainfall range from 0 to 1 (m/yr) (See Appendices Fig. A2)

8.4.2 Figure A1 : Initial topography of the models

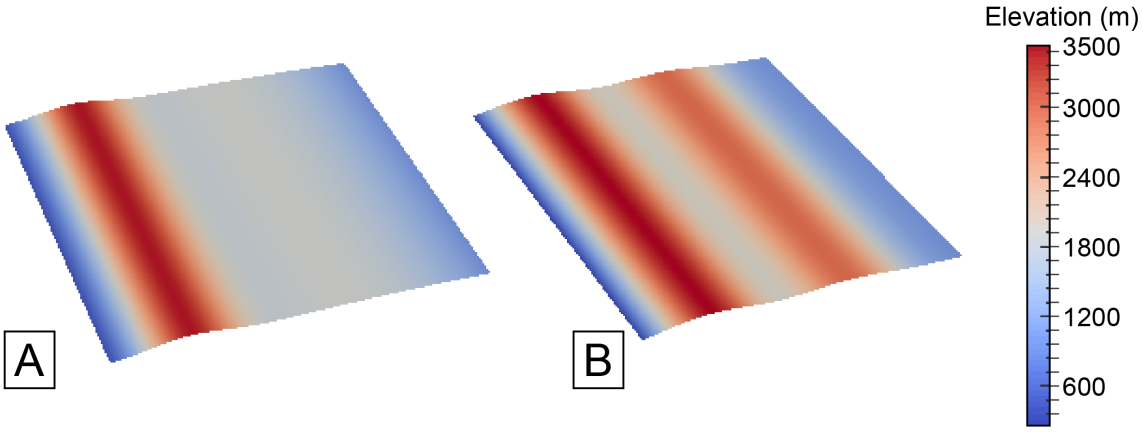

A) Initial topography without initial relief in the Cordillera blanca

B) Initial topography with relief in both the Cordillera Negra and Cordillera Blanca

8.4.3 Figure A2 : Rainfall spatial distribution

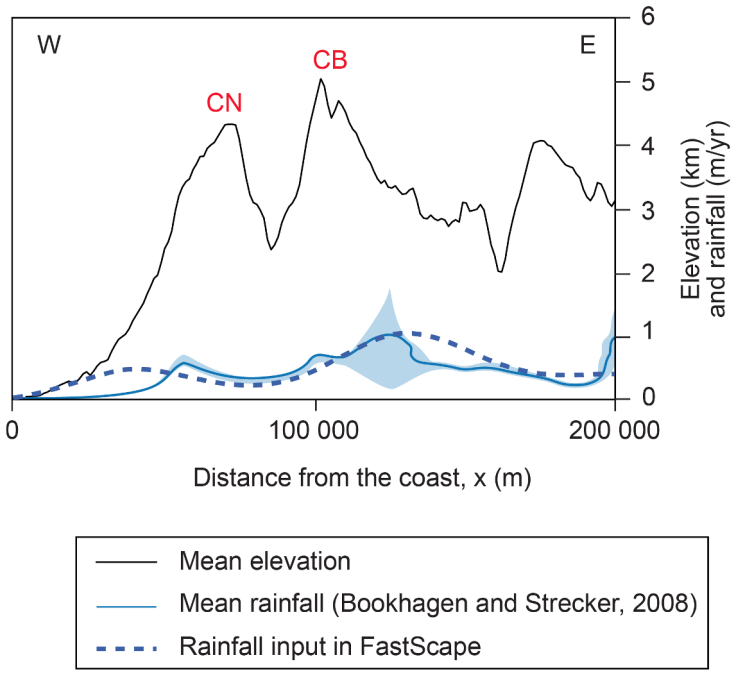

8.5 Article publié dans Earth Surface Dynamics : Tectonic and climatic controls on the Chuquibamba landslide (western Andes, southern Peru)

Dans cet article j'ai publié les données que j'ai obtenues au cours de mon stage de Master. Grâce à des datations ^{10}Be et l'analyse de la morphologie du glissement de terrain de Chuquibamba (sud du Pérou), je démontre le rôle de la tectonique et du climat sur la localisation et le déclenchement des glissements de terrain qui affectent la Cordillère Occidentale au sud du Pérou. Je propose également que les évènements humides identifiés sur l'Altiplano (i.e., Ouki, Michin) contrôlent l'érosion du flanc Pacifique des Andes.

Earth Surf. Dynam., 3, 281–289, 2015
www.earth-surf-dynam.net/3/281/2015/
doi:10.5194/esurf-3-281-2015

Earth Surface Dynamics
Open Access

Tectonic and climatic controls on the Chuquibamba landslide (western Andes, southern Peru)

A. Margirier[1], L. Audin[1,2], J. Carcaillet[1], S. Schwartz[1], and C. Benavente[3]

[1]Institut des Sciences de la Terre, Université Grenoble I, CNRS, 1381 rue de la Piscine, 38400 Grenoble CEDEX 09, France
[2]Institut de recherche pour le développement, Institut des Sciences de la Terre, 1381 rue de la Piscine, 38400 Grenoble CEDEX 09, France
[3]Instituto Geológico Minero y Metalúrgico, A. Canadà 1470, San Borja, Lima, Peru

Correspondence to: A. Margirier (audrey.margirier@ujf-grenoble.fr)

Received: 23 October 2014 – Published in Earth Surf. Dynam. Discuss.: 15 December 2014
Revised: 11 May 2015 – Accepted: 01 June 2015 – Published: 25 June 2015

Abstract. The contribution of landslides to the Quaternary evolution of relief is poorly documented in arid contexts. In southern Peru and northern Chile, several massive landslides disrupt the arid western Andean front. The Chuquibamba landslide, located in southern Peru, belongs to this set of large landslides. In this area, the Incapuquio fault system captures the intermittent drainage network and localizes rotational landslides. Seismic activity is significant in this region with recurrent M_w 9 subduction earthquakes; however, none of the latest seismic events have triggered a major landslide. New terrestrial cosmogenic dating of the Chuquibamba landslide provides evidence that the last major gravitational mobilization of these rotational landslide deposits occurred at $\sim$ 102 ka, during the Ouki wet climatic event identified on the Altiplano between 120 and 98 ka. Our results suggest that wet events in the arid and fractured context of the Andean forearc induced these giant debris flows. Finally, our study highlights the role of tectonics and climate on (i) the localization of large Andean landslides in the Western Cordillera and on (ii) the long-term mass transfer to the trench along the arid Andean front.

1 Introduction

In active mountain ranges, landslides are an important process in long-term erosion and thus contribute to the geomorphologic evolution of relief (Korup et al., 2007). Despite their importance in terms of hazards, landslide maps remain rare (Guzzetti et al., 2012) and information on the type, age or distribution of individual landslides is often lacking. Only a few publications deal with landslide triggering and/or evolution in arid contexts such as the western Andean flank, where several gigantic scarps disrupt the forearc piedmont (Audin and Bechir, 2006; Pinto et al., 2008; Strasser and Schlunegger, 2005; Wörner et al., 2002; Mather et al., 2014; Crosta et al., 2015). In contrast, because of the potential seismotectonic trigger (Keefer, 1984, 2002; McPhillips et al., 2014), landslide triggering along subduction active margins has been studied for a number of years, but most previous studies focused on humid climatic settings (Taiwan, New Zealand, Papua New Guinea, Japan; Meunier et al., 2008; Hovius et al., 2011). In southern Peru, the topographic gradient (average slope of 4 % between the coast and the Western Cordillera), the crustal seismotectonic activity and the aridity of the forearc region has been directly linked to Andean uplift and subduction of the Nazca Plate for the last 25 Myr at least (Devlin et al., 2012; Alpers and Brimhall, 1988; Dunai et al., 2005). However, Quaternary tectonic crustal activity and its role in the localization of landslides along the Western Andean Escarpment has never been explored in southern Peru and northern Chile. As a consequence, numerous questions remain concerning the importance of giant landslides in slope erosion relative to other nonseismic agents of erosion such as climatic forcing.

The "Chuquibamba landslide" is a large complex zone of imbricated landslides (about 80 km^2) affecting the western Andean Cordillera in southern Peru. It belongs to the Andean

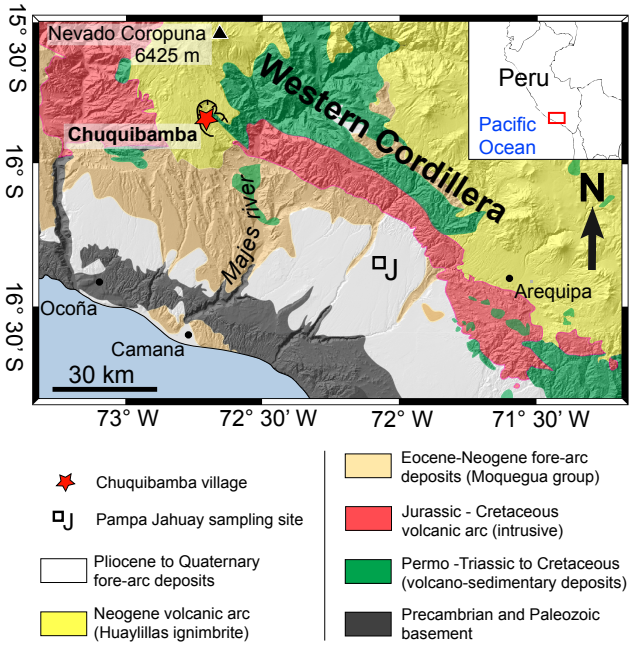

Figure 1. Simplified geological map of South Peru (modified from Roperch et al., 2006; INGEMMET, 2001), showing the village of Chuquibamba (red star), the destabilization zone and the Pampa Jahuay sampling site (J). Coordinates are given in WGS 84 longitude and latitude (degrees). Inset shows the study area location within Peru and a part of South America.

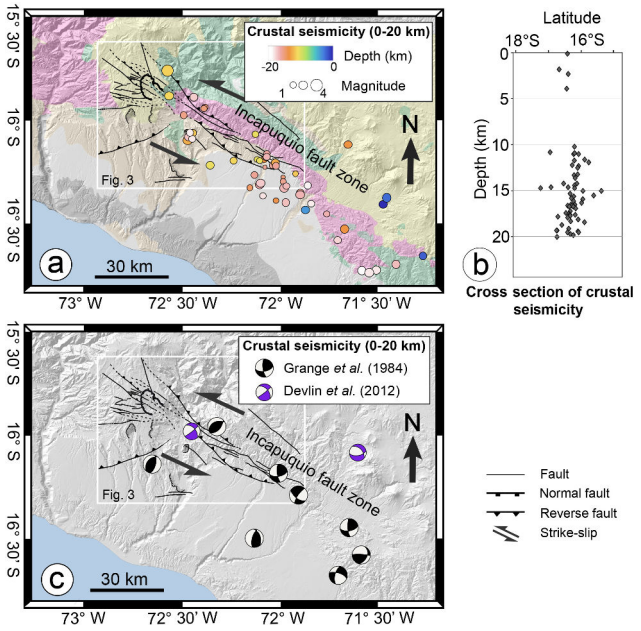

Figure 2. Regional crustal seismicity and focal mechanisms. **(a)** Crustal seismicity (depth < 20 km) and faults are represented on the geological map of South Peru (modified from Roperch et al., 2006; INGEMMET, 2001). **(b)** Cross section showing the vertical cluster of earthquakes. **(c)** Focal mechanisms from Grange et al. (1984) and Devlin et al. (2012); the kinematics of the Incapuquio fault system are indicated by black arrows.

arid piedmont, where geomorphic markers are minimally affected by erosion/transport processes (Hall et al., 2008). In this study, we aim to explore how seismotectonic activity and/or abrupt climate change may potentially have triggered the large Chuquibamba landslides. In this paper, we map out the area and characterize the tectonic and geomorphological settings, use terrestrial cosmogenic nuclides (TCN) to date pertinent markers of the last debris-flow event, and document the evolution of the landslide area.

2 Context

2.1 Geologic and climatic setting of Chuquibamba region

The Andean Pacific arid front comprises different morphological units: the Coastal Cordillera 0–1000 m above sea level (a.s.l.), the Pacific piedmont 1000–1500 m a.s.l. and the Western Cordillera 1500–6000 m a.s.l. In southern Peru, the Western Cordillera corresponds to a Jurassic to Cretaceous volcanic arc (Atherton et al., 1985) (Fig. 1). These magmatic and volcano-sedimentary rocks are emplaced within a Precambrian to Paleozoic basement. During the Eocene to Neogene, volcano-sedimentary deposits of the Moquegua group were overlain onto the Western Cordillera. This group is partly covered by the Huaylillas ignimbrite, produced during the Neogene volcanism and dated at 14.3–12.7 Ma ($^{40}Ar/^{39}Ar$; Thouret et al., 2007). The top of this ignimbrite forms a weathering surface. The Moquegua group and Huaylillas ignimbrite reach a maximum of 1500 m thick (Thouret et al., 2007; Gunnell et al., 2010). Some volcano-sedimentary rocks were deposited on the coastal plains during the late Neogene. Starting at ~ 9–10 Ma, these units were incised by 1–3 km deep canyons that strike perpendicular to NW–SE-striking range (Schildgen et al., 2007, 2009; Thouret et al., 2007; Gunnell et al., 2010).

The Western Cordillera and Pacific piedmont are affected by Quaternary tectonic deformation mainly expressed in the Western Cordillera by an active fault system striking parallel to the range (Sébrier et al., 1985; Hall et al., 2008, 2012) (Fig. 2). Along the Andes, the active subduction and induced crustal deformation largely control the geomorphologic evolution of the forearc (Keefer, 1994; Keefer and Moseley, 2004; Audin et al., 2006; Tavera et al., 2007; Perfettini et al., 2010). The piedmont region is exposed to extremely low denudation rates ranging from 0.1–1 mm kyr^{-1} in the coastal desert and Pacific piedmont to 1–46 mm kyr^{-1} in the Western Cordillera (values obtained for Quaternary timescale by TCN dating; Hall et al., 2008; Kober et al., 2007) due to the arid climatic conditions since at least the Neogene (Mortimer, 1980; Alpers and Brimhall, 1988; Dunai et al., 2005; Rech et al., 2006). Moreover, the Altiplano has been the target of

many paleoclimatic investigations (Thompson et al., 1998, 2000; Cross et al., 2001; Baker et al., 2001; Placzek et al., 2006, 2013) that highlighted climate fluctuations for the last 130 kyr. Steffen et al. (2009, 2010), Carretier et al. (2013) and Bekaddour et al. (2014) highlighted the contribution of these wet climatic events to mass transport in major canyons from the Altiplano to the Pacific coast. In contrast, McPhillips et al. (2014) observed that the landslide frequency appears to have not changed during the Quaternary and thus questioned the impact of the climatic fluctuations on landsliding and erosion rate.

2.2 Fault geometry and kinematics

In southern Peru, the Incapuquio fault zone has a strong geomorphic imprint on the Andean range (Huaman, 1985; Sébrier et al., 1985). Based on microtectonic studies, Sébrier et al. (1985, 1988) and Schildgen et al. (2009) identified different kinematic episodes. Sébrier et al. (1985, 1988) defined major Tertiary and early Quaternary compressional phases and a minor late Quaternary episode of normal faulting. Schildgen et al. (2009) proposed that a Tertiary episode of strike-slip and normal faulting occurred between 14 and 2.2 Ma. However, relocated microseismicity (Grange et al., 1984) and teleseismic data (Devlin et al., 2012) demonstrate present-day reverse and strike-slip components on the Lluta fault segment and more regionally for the Incapuquio fault system in the Arequipa region (Fig. 2). The Neogene surface and Quaternary drainage network are also affected by these fault segments (Fig. 3). Channel orientations and captures evidence a sinistral strike-slip component along an extrado graben (Fig. 3c). These Quaternary offsets and inferred kinematics are consistent with the vertical geometry of the fault plane imaged at depth (20 km) by the distribution of crustal earthquakes (Fig. 2b) and focal mechanisms (Fig. 2c) ($M_w < 5$; < 20 km, Grange et al., 1984; Devlin et al., 2012). Local reverse and normal apparent surface movements are known to occur along major strike-slip faults in the forearcs of northern Chile (Victor et al., 2004) and southern Peru (Hall et al., 2012). The present-day main sinistral strike-slip kinematics of the Incapuquio fault system demonstrated by the seismicity is compatible with normal apparent displacements as observed by Schildgen et al. (2009) and Sébrier et al. (1985, 1988).

2.3 Geomorphological setting

The Chuquibamba landslide is located in the Majes River catchment, along the western flank of the Central Andes, between 1000 and 4000 m a.s.l. (Fig. 1). The Chuquibamba landslide comprises an imbricated set of rotational landslides, a debris-flow deposit and, in the lower area, a megafan and alluvial terraces (Fig. 3a). Upstream, the rotational landslides remobilize the thick Huaylillas ignimbrite formation fractured by the activity along the Incapuquio fault system.

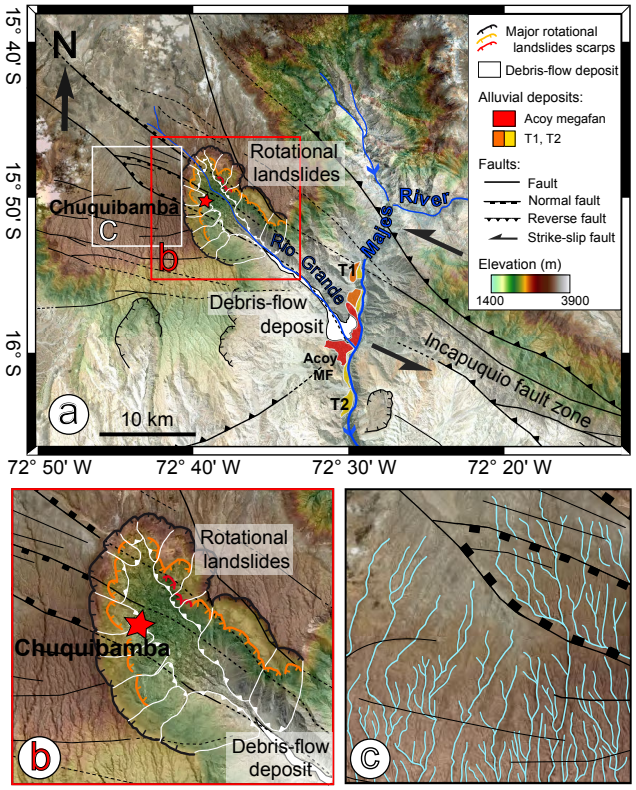

Figure 3. SRTM numerical elevation model overlay by Landsat image of the Chuquibamba destabilization zone. Coordinates are given in WGS 84 longitude and latitude (degrees). **(a)** Global view of the Chuquibamba area pointing major detachment scarps, debris-flow deposits, Acoy megafan, alluvial terraces and faults. **(b)** Close-up of the amphitheater-shaped scar of the rotational landslides showing the different head scarps. **(c)** Drainage network and faults.

We estimate the total volume mobilized for Chuquibamba landslide reaches ~40 km^3. These imbricated rotational landslides correspond to a succession of three head scarps (Fig. 3b). The scar of the rotational landslides, cutting the Huaylillas weathering surface, delimits the landslide area (Fig. 3b) and forms an elongated amphitheater trending in the NW–SE direction. This direction does not fit with the overall southwest-dipping topographic slope but rather corresponds to the structural trend of active faults (Fig. 3a). Moreover, several fault planes appear to control the shape of the polylobed rotational landslides (Fig. 3b).

The base of the cirque (2900 m a.s.l.) is formed by smooth, sub-horizontal surfaces (Fig. 3b). These surfaces likely correspond to former lateral landslide deposits re-incised by the river after the initiation of the Chuquibamba landslide.

The debris flow remobilizes the rotational landslide deposits. It consists of mixed angular clasts, breccias and numerous meter-size boulders embedded in a thin volcanic matrix (Fig. 4a), reworked from the Huaylillas ignimbrite. The debris-flow deposit displays a smooth and 100 m scale undulated surface (Fig. 4a). In its upper part, the debris flow

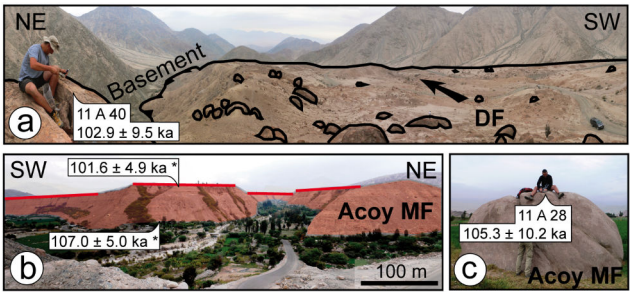

Figure 4. Field photographs showing the debris-flow deposit morphology and the Acoy megafan. **(a)** Characteristic block sampled on the debris-flow deposit. The arrow indicates flowing direction of the debris flow. **(b)** General view of the Acoy megafan (Acoy MF); red lines highlight the top of the terrace. The OSL ages obtained by Steffen et al. (2010) for the Acoy megafan are indicated with an asterisk. **(c)** Block sampled on the megafan.

rests directly on the basement (Fig. 4a), but 30 km downstream of the head scarp, in the vicinity of the Majes River (900 m a.s.l.), the debris flow overlays the Acoy megafan (Fig. 3a).

The megafan, located downstream of the Chuquibamba village at the outlet of the Rio Grande, is about 100 m thick and 8 km long (Fig. 3a). Its stratigraphy indicates both a response to multiple phases of sediment production and surface erosion in the Rio Grande and fluvial incision in the Majes Canyon (Steffen et al., 2010). Steffen et al. (2010) described an alternation of sheet flood units and debris-flow deposits, and a typical clast- to matrix-supported fabric. Optically stimulated luminescence (OSL) dating places the Acoy megafan formation between 107.0 ± 5.0 ka (base) and 101.6 ± 4.9 ka (top) (Steffen et al., 2010). Two levels of alluvial terraces (T1, T2) have been identified in the Majes canyon in the vicinity of the megafan. The Acoy megafan and alluvial-terrace development has been linked to wetter episodes, identified in paleoclimate proxies from Altiplano paleolake sediments (Placzek et al., 2006, 2013), driving the fluctuations in the Colca/Majes hydrologic regime (Steffen et al., 2010).

3 Sampling strategy and methods

The last debris-flow deposit is well preserved all along the Chuquibamba valley (Fig. 3a). Six meter-scale boulders of rhyolite entrapped in the Acoy megafan and debris-flow surfaces (Fig. 4a and c) have been sampled. The preserved surface of the boulders (evidenced by desert varnish) indicates minimal post-abandonment erosion; they are well anchored and sufficiently elevated on the debris-flow surface to minimize the possibility of post-depositional movement and potential covering by surficial material. In order to provide an additional constraint on the regional erosion rate and consequently improve the exposure age determination, we sampled a quartzite pebble from the preserved Pampa Jahuay surface in the pediplains 60 km southeast of Chuquibamba (Fig. 1, Table 1).

Sample preparation was conducted at the Institut des Sciences de la Terre (ISTerre, Grenoble). As the rhyolitic samples contained enough quartz, we extracted in situ produced beryllium-10 (^{10}Be) using the chemical procedures developed by Brown et al. (1991) and Merchel and Herpers (1999). The AMS ^{10}Be measurements were performed at the ASTER AMS French national facility (CEREGE, Aix en Provence). Analytical uncertainties include uncertainties associated with AMS counting statistics, AMS external error (1 %), standard reproducibility and chemical blank measurements (^{10}Be /^{9}Be blank $= 1.60 \pm 0.72 \times 10^{-15}$). External uncertainties include 6 % uncertainty in the production rate and 8 % uncertainty in the ^{10}Be decay constant. Exposure ages were calculated using the online CRONUS calculator (Balco et al., 2008). Results are computed using the time-dependent scaling scheme of Lal (1991) modified by Stone (2000).

4 TCN dating

In the debris-flow deposit and Acoy megafan samples, the ^{10}Be concentrations are relatively consistent and range from $6.67 \pm 0.28 \times 10^5$ to $1.38 \pm 0.08 \times 10^6$ atoms per gram of quartz (at g^{-1} qtz) (Table 1). The high ^{10}Be content of the sample ($1.33 \pm 0.02 \times 10^7$ at g^{-1} qtz, 11A28) collected from the Pampa Jahuay suggests an extremely low erosion rate lasting at least for the last 2 Myr in the southern Peruvian forearc (1.9 ± 0.3 Myr). The computed erosion rate (0.21 ± 0.05 mm kyr^{-1}) agrees with rates published by Hall et al. (2012) for the South Peru and by Kober et al. (2007) for Chile (Oxaya formation). These results support the hypothesis of an insignificant erosion of the sampled boulders of the debris-flow deposit. TCN exposure ages deduced from debris-flow boulders (with an erosion rate of 0.21 mm kyr^{-1}) range from 96.1 ± 8.9 to 108.5 ± 10.2 ^{10}Be-ka (Table 1, Fig. 5). Considering the uncertainties, exposure ages are consistent and suggest a single remobilization event with a weighted average age of 101.9 ± 5.5 ka. The age of the large boulder sampled on the Acoy megafan (Fig. 4) is 105.3 ± 10.2 ^{10}Be-ka (Table 1).

5 Discussion

5.1 Tectonic and climatic forcing on Chuquibamba landslide evolution

The weighted average age of debris-flow boulders indicates a last major debris flow at 101.9 ± 5.5 ka. The abandonment age of the megafan surface (105.3 ± 10.2 ^{10}Be-ka; Figs. 4 and 5) agrees with the OSL ages published by Steffen et al. (2010) (i.e., 107.0 ± 5.0 ka at the base of the megafan and 101.6 ± 4.9 ka near the top). The Ouki wet event has been

Table 1. TCN results of the Chuquibamba Valley and the Pampa Jahuay.

Sample	Latitude (° N)	Longitude (° W)	Elevation (m a.s.l.)	Production rate (atoms g^{-1} yr^{-1})		Geomorphic scaling factor[a]	Sample thickness factor[b]	Quartz (g)	^{9}Be (mg)	^{10}Be/^{9}Be[c]	Uncertainty ^{10}Be/^{9}Be (%)
				Spallation	Muons						
Blank											
BKGRE67	–	–	–	–	–	–	–	–	0.486	1.604×10^{-15}	44.74
Debris-flow deposit											
11A39	−15.9294	−72.5306	1315	7.15	0.27	0.99	0.98	9.54	0.291	3.998×10^{-13}	3.10
11A40	−15.5327	−72.9267	1356	7.43	0.28	0.99	0.99	6.02	0.254	3.257×10^{-13}	3.16
11A41	−15.5343	−72.9245	1391	7.39	0.28	0.98	0.97	5.10	0.290	2.566×10^{-13}	3.52
11A42	−15.9145	−72.5487	1543	8.40	0.29	0.99	0.98	10.98	0.292	5.468×10^{-13}	3.44
11A43	−15.8784	−72.5927	1899	10.54	0.33	0.98	0.98	10.44	0.291	6.981×10^{-13}	6.14
Acoy megafan											
11A28	−16.0091	−72.4892	817	5.13	0.24	1.00	0.99	9.77	0.294	3.196×10^{-13}	4.18
Pampa Jahuay											
11A62	−16.3408	−72.0840	1592	8.76	0.30	1.00	0.97	19.96	0.295	1.320×10^{-11}	1.71

Sample	^{10}Be concentration ($\times 10^3$ atoms g^{-1} qtz)	^{10}Be concentration uncertainty ($\times 10^3$ atoms g^{-1} qtz)	Erosion rate (m Myr^{-1})	Erosion rate external uncertainty (m Myr^{-1})	Age ^{10}Be (kyr) $e = 0$[d]	Age ^{10}Be internal uncertainty (kyr)[e]	Age ^{10}Be external uncertainty (kyr)[f]	Age ^{10}Be (ka) $e = 0.21$ m Myr^{-1}[d]	Age ^{10}Be internal uncertainty (kyr)[e]	Age ^{10}Be external uncertainty (kyr)[f]
Blank										
BKGRE67	31.374	14.036	–	–	–	–	–	–	–	–
Debris-flow deposit										
11A39	828.574	25.748	–	–	95.99	3.67	8.83	96.11	3.68	8.86
11A40	938.088	29.597	–	–	102.72	4.07	9.49	102.86	4.09	9.52
11A41	992.821	34.974	–	–	108.29	4.85	10.17	108.46	4.87	10.2
11A42	992.144	34.175	–	–	97.51	4.17	9.10	97.88	4.19	9.15
11A43	1375.656	84.507	–	–	106.7	8.30	11.42	106.87	8.34	11.46
Acoy megafan										
11A28	666.607	27.905	–	–	105.1	5.55	10.15	105.26	5.57	10.19
Pampa Jahuay										
11A62	13 318.936	227.531	0.21	0.05	1894.08	94.88	271.34	–	–	–

(a) The topographic scaling factor has been calculated following the method of Dunne et al. (1999). (b) The sample thickness correction has been calculated with a 2.7 density factor. (c) AMS (accelerator mass spectrometry) analyses were carried out at the French AMS facility ASTER. Calibration of ^{10}Be concentrations were done with NIST standard reference material 4325, using a ^{10}Be /^{9}Be ratio of 2.79×10^{-11} and a ^{10}Be half-life of $1.387 \pm 0.012 \times 10^{6}$ years (Chmeleff et al., 2010; Korschinek et al., 2010). Results have been corrected from the chemical blank (^{10}Be /^{9}Be blank $= 1.60 \pm 0.72 \times 10^{-15}$). Internal uncertainties consider the analytical uncertainties including counting statistics, the instrumental variability (1 %), the standard deviation and chemical blank. External uncertainties include 6 % uncertainty in the production rate and 8 % uncertainty in the ^{10}Be decay constant. (d) Ages have been computed with the CRONUS calculator (Balco et al., 2008) using the time-dependent production rate of Lal (1991) modified by Stone (2000). The production rate calibrate by Kelly et al. (2015) on recent timescale in Peruvian Andes is not relevant for this study. For our range of ages (100 kyr) geomagnetic variations have to be considered. Ages are presented with the internal (e) and the external uncertainties (f).

evidenced from sediments collected in the eponym paleolake located in the higher Bolivian Altiplano (Placzek et al., 2006, 2013). The chronological framework deduced from U–Th dating on carbonates indicates the Ouki deep lake cycle between 120 and 98 ka (Placzek et al., 2006, 2013).

Steffen et al. (2010) already suggested a correlation between wet time intervals on the Altiplano and sediment aggradation in the Majes Valley. According to Steffen et al. (2010), the Acoy megafan recorded two phases of Rio Grande catchment development characterized by landsliding during the Ouki wet climatic event. The data from Steffen et al. (2010) indicate that during the megafan emplacement, between 112.0 and 96.7 ka, the Rio Grande permits the sediment transport and aggradation in the Acoy megafan downstream. Similar to the Lluta catchment in Chile, landsliding might have been initiated by enhanced precipitation and reduced friction along a basal shear plane due to increasing hydrostatic pressure in the groundwater (Hoke et al., 2004; Strasser and Schlunegger, 2005). The weighted average age of the last debris-flow deposit (101.9 ± 5.5 ka) also correlates with the Ouki event (120–98 ka). In the western Andes, other landslides have been associated with wetter climatic conditions such as the older Lluta collapse (northern Chile, 18° S; Wörner et al., 2002), yielding a minimum age of 2.5 Ma (Strasser and Schlunegger, 2005), the Tomasiri landslide (southern Peru, 17°30′ S), dated at 400 ka (Blard et al., 2009) and younger landslides in Argentina, which have been associated with the Minchin wet event (40–25 ka; Trauth et al., 2003; Hermanns and Schellenberger, 2008).

We suggest that the Chuquibamba debris flow, which remobilized rotational landslide deposits, was triggered by an increase in pore-water pressure in the Huaylillas ignimbrite during the Ouki wet climatic event. After this event, none of the more recent wet climatic events identified on the Altiplano (e.g., Michin, 48–36 ka, and Tauca, 26–15 ka) triggered a large landslide or remobilized the Chuquibamba debris flow. Similarly, in Southern Peru, Keefer et al. (2003) identified only centimeter-scale debris flows for the last

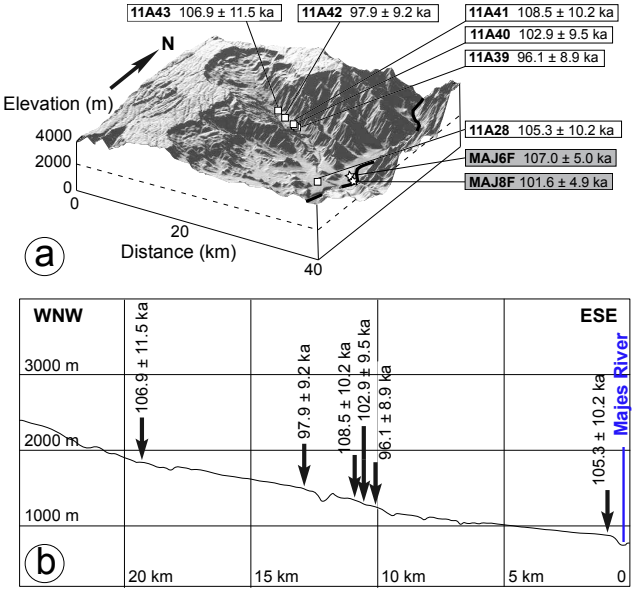

Figure 5. Samples location. **(a)** Digital elevation model (GeoMapApp, SRTM data, 90 m resolution) of the study area, showing samples location and TCN ages obtained for the debris-flow deposit and the Acoy megafan surface. OSL ages obtained by Steffen et al. (2010) for the Acoy megafan are noted in grey. **(b)** Elevation profile locating debris flow and the Acoy megafan ages.

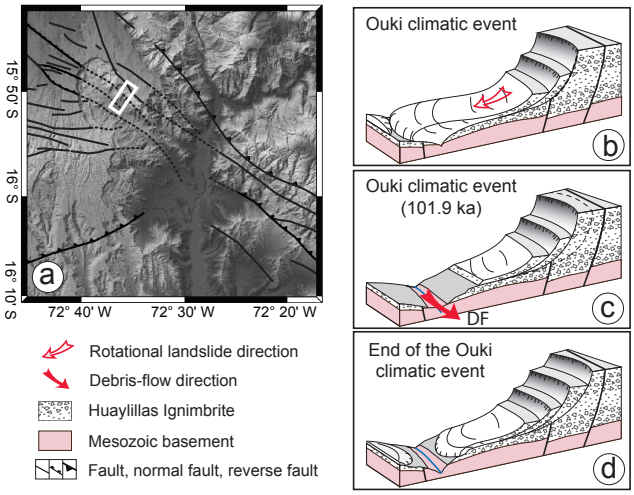

Figure 6. Map and block diagrams of the evolution of the Chuquibamba landslide. **(a)** SRTM numerical elevation model, the white rectangle localizes the block diagrams. **(b)** Block diagram showing rotational landslide initiation on the flank of the Chuquibamba Valley during the Ouki wet event. The landslide enlarges the valley and accumulates material at the bottom. **(c)** The accumulated materials are remobilized by debris flows during the wetter phases. **(d)** This remobilization allows new rotational landslides that enlarge the amphitheater-shaped valley.

38 kyr. These observations are consistent with the preservation of the Chuquibamba debris-flow morphology since its emplacement. We suggest that the Ouki event was the latest event whose duration and intensity was sufficient to trigger a large landslide in the arid western Andean flank (Wörner et al., 2002; Strasser and Schlunegger, 2005; Blard et al., 2009). Carretier et al. (2013) proposed that rare and strong erosive events contribute to more than 90 % of the long-term erosion of the arid western side of the Andean range. Accordingly, we suggest that climatic fluctuations that favor landsliding, such as the Ouki wet event, have a great impact on sediment transport and morphologic evolution of the western flank of the Andes.

The important role of the tectonic framework on the localization and flow direction of mega-landslides has already been suggested for the Andean forearc domain (Pinto et al., 2008; Antinao and Gosse, 2009; Mather et al., 2014). As the Chuquibamba landslide is elongated in a NW–SE trend guided by the Incapuquio fault system, we suggest that the localization and geometry of the landslide is mainly controlled by preferential fracture orientations (Fig. 3b). More broadly, in southern Peru and northern Chile, most of the large landslides are located in tectonically fractured regions (Audin and Bechir, 2006; Pinto et al., 2008; Strasser and Schlunegger, 2005; Wörner et al., 2002; Crosta et al., 2015). This preferential localization suggests that tectonic fracturing plays an important role in preconditioning the landscape for landsliding within this arid area.

No relationship between a M_w 8.0 subduction earthquake and a giant landslide has been previously documented in southern Peru (Lacroix et al., 2013). However, Keefer et al. (2003) point out that a close temporal succession of subduction earthquakes and El Niño events produces debris flows in the coastal region (southern Peru). In our study area, even if the Ouki wet phase would favor triggering, we cannot exclude a contemporaneous seismic triggering event (subduction or crustal earthquake) for the Chuquibamba debris flows. More generally, robust arguments indicating such a correlation for giant landslides are scarce along the South American margin; other triggering factors (increase in pore pressure, climate change, glacial debuttressing) are usually invoked in addition to a seismic triggering event (Keefer, 2002; Pinto et al., 2008).

5.2 Landscape evolution and tectono-climatic scenario

We propose a landscape evolution scenario based on geomorphic marker analysis and new TCN ages (Fig. 6). The initial drainage network flowed toward the coast (i.e., in a southerly direction) and incised the roof of the weathered Huaylillas ignimbrite (Fig. 6a). These parallel incisions are still preserved (Fig. 3b, c) and sometimes even abandoned. Afterwards, the development of a graben structured by the Incapuquio fault system captured the drainage network along a 110° N trending direction (Fig. 3c), creating a new tributary of the Majes River. Rotational landslides were initiated by slope instabil-

ity or pore pressure increase at the base of the Huaylillas ignimbrite during wet climatic events, as proposed by Hoke et al. (2004) and Strasser and Schlunegger (2005) for northern Chile (Fig. 6b). Sliding surfaces of rotational landslides are localized on fault planes and progressively enlarge the valley, as evidenced by the successive rotational landslide scarps (Fig. 3).

The rotational landslide deposits accumulated upstream in the valley (Fig. 6b) and were remobilized by debris flows during the Ouki event (120–98 ka; Fig. 6c). The accumulation of successive debris-flow and mudflow deposits at the outlet of the Rio Grande during the Ouki event formed the Acoy megafan (Steffen et al., 2010). Finally, at 101.9 ± 5.5 ka, the last major debris flow sealed the erosion/transport system (Fig. 6c). This pattern, with alternating upper slope destabilizations and sediment remobilization by debris flows, drove valley enlargement over time (Fig. 6d).

At the present time, the arid climate on the western flank of the Cordillera preserves geomorphologic features from erosion; the water yield comes only from rivers.

6 Conclusions

In this study we address how local tectonic activity and climatic fluctuations may control landslide occurrence at the arid western Andean front. Indeed, for the Chuquibamba landslide region, the sequence of debris flows (identified in the Acoy megafan stratigraphy and overlaying its roof) seems to have been favored by the occurrence of a wet climatic event (Ouki event), even if a contemporaneous seismic triggering event cannot be excluded. Our results suggest sediment accumulation in the valley during wet periods and incision during dry periods. Wet climatic events then appear to control the growth of the drainage network, participating in regressive erosion and in the creation of new tributaries on the western Andean front. Specifically, our results show that, during a wet event in a tectonically fractured region, hillslope processes, rather than fluvial erosion, dictate the evolution of the landscape at the channel head in the arid and high-relief area.

As rare and strong erosive events represent the most important contribution to the long-term erosion of the arid Western Cordillera (Carretier et al., 2013), we propose that events like the Chuquibamba landslide contribute significantly to the long-term erosion of the western escarpment of the Andes. We thus suggest a strong regional tectonic and climatic control of the long-term erosion of the arid western Andean front.

Acknowledgements. This project was supported by the Institut de Recherche pour le Développement (IRD). We acknowledge additional support from the Instituto Geologico Mineralogico y Metallurgico del Peru (INGEMMET, Peru). We thank all the staff from the ASTER AMS facility at CEREGE. We are grateful for detailed reviews from T. Schildgen and the anonymous reviewers, which helped to improve the manuscript. This work was carried out in the frame of the master's thesis of A. Margirier at ISTerre.

Edited by: V. Vanacker

References

Alpers, C. N. and Brimhall, G. H.: Middle Miocene climatic change in the Atacama Desert, northern Chile: Evidence from supergene mineralization at La Escondida, Geol. Soc. Am. Bull., 100, 1640–1656, 1988.

Antinao, J. L. and Gosse, J.: Large rockslides in the Southern Central Andes of Chile (32–34.5° S): tectonic control and significance for Quaternary landscape evolution, Geomorphology, 104, 117–133, 2009.

Atherton, M. P., Warden, V., and Sanderson, L. M.: The Mesozoic marginal basin of Central Peru: a geochemical study of within-plate-edge volcanism, in: Magmatism at a Plate Edge: the Peruvian Andes, edited by: Pitcher, M. P., Cobbing, E. J., and Beckinsale, R. D., Blackie Halsted Press, London, 47–58, 1985.

Audin, L. and Bechir, A.: Active Tectonics as Determinant Factor in Landslides Along the western Cordillera?, Congreso Peruano de Geologia, Lima, Peru, 17–20 October, 237–239, 2006.

Audin, L., David, C., Hall, S., Farber, D., and Hérail, G.: Geomorphic evidences of recent tectonic activity in the forearc, southern Peru, Special Volume on Neotectonics in South America, Revista de la Asociación Geológica Argentina, 61, 545–554, 2006.

Baker, P. A., Seltzer, G. O., Fritz, S. C., Dunbar, R. B., Grove, M. J., Tapia, P. M., Cross, S. L., Rowe, H. D., and Broda, J. P.: The history of South American tropical precipitation for the past 25,000 years, Science, 291, 640–643, 2001.

Balco, G., Stone, J. O., Lifton, N. A., and Dunai, T. J.: A complete and easily accessible means of calculating surface exposure ages or erosion rates from ^{10}Be and ^{26}Al measurements, Quat. Geochronol., 3, 174–195, 2008.

Bekaddour, T., Schlunegger, F., Vogel, H., Delunel, R., Norton, K. P., Akçar, N., and Kubik, P.: Paleo erosion rates and climate shifts recorded by Quaternary cut-and-fill sequences in the Pisco valley, central Peru, Earth Planet. Sc. Lett., 390, 103–115, 2014.

Blard, P. H., Lavé, J., Farley, K. A., Fornari, M., Jiménez, N., and Ramirez, V.: Late local glacial maximum in the Central Altiplano triggered by cold and locally-wet conditions during the paleolake Tauca episode (17–15 ka, Heinrich 1), Quaternary Sci. Rev., 28, 3414–3427, 2009.

Brown, E. T., Edmond, J. M., Raisbeck, G. M., Yiou, F., Kurz, M. D., and Brook, E. J.: Examination of surface exposure ages of Antartic moraines using in situ produced ^{10}Be and ^{26}Al, Geochim. Cosmochim. Ac., 55, 2269–2283, 1991.

Carretier, S., Regard, V., Vassallo, R., Aguilar, G., Martinod, J., Riquelme, R., Pepin, E., Charrier, R., Hérail, G., Farias, M., Guyot, J. L., Vargas, G., and Lagane, C.: Slope and climate variability control of erosion in the Andes of central Chile, Geology, 41, 195–198, 2013.

Chmeleff, J., von Blanckenburg, F., Kossert, K., and Jacob, D.: Determination of the 10Be half-life by multicollector ICP-MS and liquid scintillation counting, Nucl. Instrum. Methods, 268, 192–199, 2010.

Cross, S. L., Baker, P. A., Seltzer, G. O., Fritz, S. C., and Dunbar, R. B.: Late Quaternary Climate and Hydrology of Tropical South America Inferred from an Isotopic and Chemical Model of Lake Titicaca, Bolivia and Peru, Quat. Res., 56, 1–9, 2001.

Devlin, S., Isacks, B. L., Pritchard, M. E., Barnhart, W. D., and Lohman, R. B.: Depths and focal mechanisms of crustal earthquakes in the central Andes determined from teleseismic waveform analysis and InSAR, Tectonics, 31, TC2002, doi:10.1029/2011TC002914, 2012.

Crosta, G. B., Paolo, F., Elena, V., and Hermanns, R. L.: The Cerro Caquilluco–Cerrillos Negros Giant Rock Avalanches (Tacna, Peru), Engineering Geology for Society and Territory, 2, 921–924, doi:10.1007/978-3-319-09057-3_159, 2015.

Dunai, T. J., González López, G. A., and Juez-Larré, J.: Oligocene-Miocene age of aridity in the Atacama Desert revealed by exposure dating of erosion-sensitive landforms, Geology, 33, 321–324, 2005.

Grange, F., Hatzfeld, D., Cunningham, P., Molnar, P., Roecker, S. W., Suarez, G., Rodrigues, A., and Ocola, L.: Tectonic implications of the microearthquake seismicity and fault plane solutions in southern Peru, J. Geophys. Res., 89, 6139–6152, 1984.

Gunnell, Y., Thouret, J. C., Brichau, S., Carter, A., and Gallagher, K.: Low-temperature thermochronology in the Peruvian Central Andes: implications for long-term continental denudation, timing of plateau uplift, canyon incision and lithosphere dynamics, J. Geol. Soc. London, 167, 803–815, 2010.

Guzzetti, F., Mondini, A. C., Cardinali, M., Fiorucci, F., Santangelo, M., and Chang, K.-T.: Landslide inventory maps: new tools for an old problem, Earth-Sci. Rev., 112, 1–25, 2012.

Hall, S. R., Farber, D. L., Audin, L., Finkel, R. C., and Mériaux, A. S.: Geochronology of pediment surfaces in southern Peru: implications for Quaternary deformation of the Andean forearc, Tectonophysics, 459, 186–205, 2008.

Hall, S. R., Farber, D. L., Audin, L., and Finkel, R. C.: Recently active contractile deformation in the forearc of southern Peru, Earth Planet. Sc. Lett., 337–338, 85–92, 2012.

Hermanns, R. L. and Schellenberger, A.: Quaternary tephrochronology helps define conditioning factors and triggering mechanisms of rock avalanches in NW Argentina, Quatern. Int., 178, 261–275, 2008.

Hoke, G. D., Isacks, B. L., Jordan, T. E., and Yu, J. S.: Groundwater-sapping origin for the giant quebradas of northern Chile, Geology, 32, 605–608, 2004.

Hovius, N., Meunier, P., Ching-Weei, L., Hongey, C., Yue-Gau, C., Dadson, S., Ming-Jame, H., and Lines, M.: Prolonged seismically induced erosion and the mass balance of a large earthquake, Earth Planet. Sc. Lett., 304, 347–355, 2011.

Huaman, R.: Evolution tectonique Cenozoïque et néotectonique du piémont Pacifique dans la région d'Arequipa (Andes du Sud Pérou), PhD thesis, Université Paris Sud, Centre d'Orsay, 220 pp., 1985.

INGEMMET: Mapa Geológico del cuadrángulo de Caravelí, Ocoña, La Yesera, y Chuquibamba, scale 1 : 100 000, Lima, 2001.

Keefer, D. K.: Landslides caused by earthquakes, Geol. Soc. Am. Bull., 95, 406–421, 1984.

Keefer, D. K.: The importance of earthquake-induced landslides to long-term slope erosion and slope-failure hazards in seismically active regions, Geomorphology, 10, 265–284, 1994.

Keefer, D. K.: Investigating landslides caused by earthquakes – a historical review, Surv. Geophys., 23, 473–510, 2002.

Keefer, D. K. and Moseley, M. E.: Southern Peru desert shattered by the great 2001 earthquake: implications for paleoseismic and paleo-El Niño-Southern Oscillation records, P. Natl. Acad. Sci. USA, 101, 10878–10883, 2004.

Keefer, D. K., Moseley, M. E., and deFrance, S. D.: A 38 000 year record of floods and debris flows in the Ilo region of southern Peru and its relation to El Niño events and great earthquakes, Palaeogeogr. Palaeocl., 194, 41–77, 2003.

Kelly, M. A., Lowell, T. V., Applegate, P. J., Phillips, F. M., Schaefer, J. M., Smith, C. A., Kim, H., Leonard, K. C., and Hudson, A. M.: A locally calibrated, late glacial ^{10}Be production rate from a low-latitude, high-altitude site in the Peruvian Andes, Quat. Geochronol., 26, 70–85, 2015.

Kober, F., Ivy-Ochs, S., Schlunegger, F., Baur, H., Kubik, P. W., and Wieler, R.: Denudation rates and a topography-driven rainfall threshold in northern Chile: multiple cosmogenic nuclide data and sediment yield budgets, Geomorphology, 83, 97–120, 2007.

Korschinek, G., Bergmaier, A., Faestermann, T., Gerstmann, U. C., Knie, K., Rugel, G., Wallner, A., Dillmann, I., Dollinger, G., Gostomski von C. L., Kossert, K., Maiti, M., Poutivtsev, M., and Remmert, A.: A new value for the half-life of ^{10}Be by heavy-ion elastic recoil detection and liquid scintillation counting, Nuclear Instum. Methods, 268, 187–191, 2010.

Korup, O., Clague, J. J., Hermanns, R. L., Hewitt, K., Strom, A. L., and Weidinger, J. T.: Giant landslides, topography, and erosion, Earth Planet. Sc. Lett., 261, 578–589, 2007.

Lacroix, P., Zavala, B., Berthier, E., and Audin, L.: Supervised method of landslide inventory using panchromatic SPOT5 images and application to the earthquake-triggered landslides of Pisco (Peru, 2007, M_w8.0), Remote Sensing, 5, 2590–2616, 2013.

Lal, D.: Cosmic ray labeling of erosion surfaces: in situ nuclide production rates and erosion models, Earth Planet. Sc. Lett., 104, 24–439, 1991.

Mather, A. E., Hartley, A. J., and Griffiths, J. S.: The giant landslides of northern Chile: tectonic and climate interactions on a classic convergent plate margin, Earth Planet. Sc. Lett., 388, 249–256, 2014.

McPhillips, D., Bierman, P. R., and Rood, D. H.: Millennial-scale record of landslides in the Andes consistent with earthquake trigger, Nat. Geosci., 7, 925–930, 2014.

Meunier, P., Hovius, N., and Haines, J. A.: Topographic site effects on the location of earthquake induced landslides, Earth Planet. Sc. Lett., 275, 221–232, 2008.

Merchel, S. and Herpers, U.: An update on radiochemical separation techniques for the determination of long-lived radionuclides via accelerator mass spectrometry, Radiochim. Acta, 84, 215–219, 1999.

Mortimer, C.: Drainage evolution of the Atacama Desert of northernmost Chile, Rev. Geol. Chile, 11, 3–28, 1980.

Perfettini, H., Avouac, J.-P., Tavera, H., Kositsky, A., Nocquet, J.-M., Bondoux, F., Chlieh, M., Sladen, A., Audin, L., and Farber, D. L.: Seismic and aseismic slip on the central Peru megathrust, Nature, 465, 78–81, 2010.

Pinto, L., Hérail, G., Sepúlveda, S. A., and Krop, P.: A neogene giant landslide in Tarapacá, northern Chile: a signal of instability of the westernmost Altiplano and palaeoseismicity effects, Geomorphology, 102, 532–541, 2008.

Placzek, C., Quade, J., and Patchett, P. J.: Geochronology and stratigraphy of late Pleistocene lake cycles on the southern Bolivian Altiplano: implications for causes of tropical climate change, Geol. Soc. Am. Bull., 118, 515–532, 2006.

Placzek, C. J., Quade, J., and Patchett, P. J.: A 130 ka reconstruction of rainfall on the Bolivian Altiplano: implications for the causes of tropical climate change, Earth Planet. Sc. Lett., 363, 97–108, 2013.

Rech, J. A., Currie, B. S., Michalski, G., and Cowan, A. M.: Neogene climate change and uplift in the Atacama Desert, Chile, Geology, 34, 761–764, 2006.

Roperch, P., Sempere, T., Macedo, O., Arriagada, C., Fornari, M., Tapia, C., Garcia, M., and Laj, C.: Counterclockwise rotation of late Eocene–Oligocene fore-arc deposits in southern Peru and its significance for oroclinal bending in the central Andes, Tectonics, 25, TC3010, doi:10.1029/2005TC001882, 2006.

Schildgen, T. F., Hodges, K. V., Whipple, K. X., Reiners, P. W., and Pringle, M. S.: Uplift of the western margin of the Andean plateau revealed from canyon incision history, southern Peru, Geology, 35, 523–526, 2007.

Schildgen, T. F., Hodges, K. V., Whipple, K. X., Pringle, M. S., van Soest, M., and Cornell, K.: Late Cenozoic structural and tectonic development of the western margin of the central Andean Plateau in southwest Peru, Tectonics, 28, TC4007, doi:10.1029/2008TC002403, 2009.

Sébrier, M., Mercier, J. L., Mégard, F., Laubacher, G., and Carey-Gailhardis, E.: Quaternary normal and reverse faulting and the state of stress in the central Andes of south Peru, Tectonics, 4, 739–780, 1985.

Sébrier M., Lavenu, A., Fornari, M., and Soulas, J. P.: Tectonics and uplift in Central Andes (Peru, Bolivia and Northern Chile) from Eocene to present, Géodynamique, 3, 85–106, 1988.

Steffen, D., Schlunegger, F., and Preusser, F.: Drainage basin response to climate change in the Pisco valley, Peru, Geology, 37, 491–494, 2009.

Steffen, D., Schlunegger, F., and Preusser, F.: Late Pleistocene fans and terraces in the Majes valley (southern Peru) and their relation to climatic variations, Int. J. Earth Sci., 99, 1975–1989, 2010.

Stone, J. O.: Air pressure and cosmogenic isotope production, J. Geophys. Res., 105, 23753–23759, 2000.

Strasser, M. and Schlunegger, F.: Erosional processes, topographic length-scales and geomorphic evolution in arid climatic environments: the "Lluta collapse," northern Chile, Int. J. Earth Sci., 94, 433–446, 2005.

Tavera, H., Audin, L., and Bernal, I.: Source parameters of Sama (Tacna) earthquake (5.4 M_w) of 20 November 2006, Bol. Soc. geol. Perù, 102, 109–115, 2007.

Thompson, L. G., Davis, M. E., Mosley-Thompson, E., Sowers, T. A., Henderson, K. A., Zagorodnov, V. S., Lin P. N., Mikhalenko V. N., Campen R. K., and Bolzan J. F.: A 25,000-year tropical climate history from Bolivian ice cores, Science, 282, 1858–1864, 1998.

Thompson, L. G., Mosley-Thompson, E., and Henderson, K. A.: Ice-core palaeoclimate records in tropical South America since the Last Glacial Maximum, J. Quat. Sci., 15, 377–394, 2000.

Thouret, J. C., Wörner, G., Gunnell, Y., Singer, B., Zhang, X., and Souriot, T.: Geochronologic and stratigraphic constraints on canyon incision and Miocene uplift of the Central Andes in Peru, Earth Planet. Sc. Lett., 263, 151–166, 2007.

Trauth, M. H., Bookhagen, B., Marwan, N., and Strecker, M. R.: Multiple landslide clusters record Quaternary climate changes in the northwestern Argentine Andes, Palaeogeogr. Palaeocl., 194, 109–121, 2003.

Victor, P., Oncken, O., and Glodny, J.: Uplift of the western Altiplano plateau: evidence from the Precordillera between 20 and 21° S (northern Chile), Tectonics, 23, TC4004, doi:10.1029/2003TC001519, 2004.

Wörner, G., Uhlig, D., Kohler, I., and Seyfried, H.: Evolution of the West Andean Escarpment at 18° S (N. Chile) during the last 25 Ma: uplift, erosion and collapse through time, Tectonophysics, 345, 183–198, 2002.

8.6 Résumés des présentations faites à des conférences

Au cours de ma thèse j'ai eu l'occasion de participer à plusieurs conférences (EGU 2014, THERMO 2014, EGU 2015). Les résumés des présentations que j'ai faites sont présentés dans les pages suivantes.

8.6.1 Journée aléas gravitaire 2013 - Poster

Contrôle tectonique et climatique sur l'évolution de la zone instable de Chuquibamba (Sud Pérou)

Audrey Margirier[1], Laurence Audin[1, 2], Stéphane Schwartz[1] and Julien Carcaillet[1]

1-ISTerre, Université Grenoble I, CNRS, 1381 rue de la piscine, 38400 Grenoble Cedex 09, France

2-IRD, ISTerre, 1381 rue de la piscine, 38400 Grenoble Cedex 09, France

Correspondant :

Audrey Margirier, *audrey.margirier@ujf-grenoble.fr*, +33 4 76 51 40 70

Les glissements de terrains sont des phénomènes importants dans l'érosion et l'évolution géomorphologique des chaines de montagne. Paradoxalement, les phénomènes gravitaires ont peu été étudiés en contexte aride. Au Pérou, de gigantesques mouvements de terrain, mobilisant plusieurs centaines de million de m^3, sont observés le long du flanc ouest des Andes, pourtant sous l'influence d'un climat hyperaride depuis plus de 15 Ma. Notre étude se focalise sur la zone instable de Chuquibamba (~100 km^2) qui se situe entre 2000 et 4000 m d'altitude dans le piémont Andin, au sud du Pérou. La formation de cet objet exceptionnel par ses dimensions soulève plusieurs questions : (i) Dans quel contexte tectonique et climatique cette instabilité s'est mise en place ? (ii) Quelle est la cinématique associée ? L'étude géomorphologique de la région montre l'existence d'un faisceau actif de failles de direction N110° qui affecte en profondeur la surface structurale et participe à la capture du paléo-réseau de drainage. La zone instable de Chuquibamba s'aligne suivant le faisceau de faille, perpendiculairement au gradient topographique. Des datations ^{10}Be effectuées sur des blocs de rhyolites associés à une coulée de débris ont permis de mettre en évidence la remobilisation des dépôts de glissement rotationnels par une coulée de débris à 100 ± 10 ka durant la période climatique humide Ouki (120-98 ka), reconnue à l'échelle des Andes. A partir de l'analyse géomorphologique et des âges ^{10}Be, nous présentons un scénario où l'évolution de la zone instable de Chuquibamba est contrôlée par des fluctuations climatiques qui affectent des formations géologiques découpées par un système de failles préexistant.

Mots clefs : glissement de terrain, ^{10}Be, Andes, tectonique, fluctuations climatiques, érosion

8.6.2 EGU 2014 - Poster

Geophysical Research Abstracts
Vol. 16, EGU2014-7115-2, 2014
EGU General Assembly 2014

Recent (0-8 Ma) tectonics and exhumation processes in Cordilleras Blanca and Negra, Central Peru: Constraints from (U-Th)/He dating

Audrey Margirier (1,2), Xavier Robert (1,2,3), Cécile Gautheron (4), Laurence Audin (1,2,3)

(1) Univ. Grenoble Alpes, ISTerre, F-38041 Grenoble, France (audrey.margirier@gmail.com), (2) CNRS, ISTerre, F-38041 Grenoble, France, (3) IRD, ISTerre, F-38041 Grenoble, France, (4) UMR Interactions et Dynamique des Environnements de Surface, CNRS-UPS 8148, Université Paris Sud, 91405 Orsay, France

The Central Andes are a classical example of topography building in front of an oceanic subduction. However, many first order questions are still debated: How do subduction processes and observed tectonic uplift interact along the Andean margin? What is the impact of tectonic, magmatism and climate on exhumation?
The Cordilleras Blanca (6768 m) and Negra (5181 m), in north Central Peru, belong to the highest Andean reliefs. Both ranges trend parallel to the subduction zone and are separated by the NW-SE Rio Santa valley. The Cordillera Blanca pluton formed in an active subduction context at 8-5 Ma and renders an abnormal magmatic activity over a planar subduction. In contrast with the Cordillera Blanca, the Cordillera Negra is an older relief, which evolution and exhumation history has never been studied. A remarkable $\sim$200 km-long normal fault system showing $\sim$4500 m of vertical displacement since 5 Ma edges the western flank of the Cordillera Blanca. This region is a perfect target to study the impact of magmatism and subduction processes on exhumation. We perform a morphotectonic study on both cordilleras coupled with low-temperature thermochronology apatite (U-Th)/He dating to quantify these processes.
Geomorphic parameters and altitude contrasts between these two ranges indicate a differential uplift. The Cordillera Negra displays a smooth and asymmetric relief from the West to the East whereas the Cordillera Blanca shows higher and sharper relief with North/South and East/West contrasts. We obtain apatite (U-Th)/He ages for twenty samples located along vertical and horizontal profiles at different latitudes of the Cordilleras Blanca and Negra. The (U-Th)/He ages range from 13.4 $\pm$ 1.3 to 5.6 $\pm$ 0.6 Ma in the Cordillera Negra and range from 11.8 $\pm$ 1.2 to 2.0 $\pm$ 0.2 Ma in the Cordillera Blanca. We use them as inputs in QTQt tools for time-temperature reconstructions and thus to constrain the exhumation history.
Whole ages evidence a more regional exhumation than previously proposed, in both Cordilleras Blanca and Negra. Exhumation history inferred from low-temperature thermochronology ages coupled with geomorphologic characteristics suggests a regional uplift above the Peruvian flat-slab. However, ages from the Cordillera Blanca indicate higher exhumation rates than in the Cordillera Negra. We propose that the Cordillera Blanca exhumation is in addition facilitated by structural inheritance and controlled by plutonism. These processes occur as a response to the flattening of the Peruvian slab and confirm the role of the subducting plate geometry in topography building in Central Andes.

8.6.3 THERMO 2014 - Poster

Recent (< 8 Ma) tectonics and exhumation processes in Cordilleras Blanca and Negra, Central Peru:

Constraints from apatite (U-Th)/He and Fission-Track dating

Audrey Margirier[1,2], Xavier Robert[1,2,3], Cécile Gautheron[4], Laurence Audin[1,2,3]

1 Univ. Grenoble Alpes, ISTerre, F-38041 Grenoble, France

2 CNRS, ISTerre, F-38041 Grenoble, France

3 IRD, ISTerre, F-38041 Grenoble, France

4 UMR GEOPS, CNRS 8148, Université Paris Sud, 91405 Orsay, France

The Central Andes are a classical example of topography building in front of an oceanic subduction. However, many first order questions are still debated: How do subduction processes and observed tectonic uplift interact along the Andean margin? What is the impact of tectonic, magmatism and climate on exhumation?

Here we focus on one of the highest Andean relief, the Cordilleras Blanca (6768 m) and Negra (5181 m), located above the Peruvian flat-slab in north Central Peru, to investigate the link between slab flattening and uplift and to identify the impact of magmatism on crustal thickening. Both ranges trend parallel to the subduction zone and are separated by the NW-SE Rio Santa valley (Fig. 1). The Cordillera Blanca pluton formed in an active subduction crustal context at 8-5 Ma[1,2] and renders an abnormal magmatic activity over a planar subduction. In contrast with the Cordillera Blanca, the Cordillera Negra is an older relief[3], which evolution and exhumation history has never been studied. The Cordillera Blanca composed the footwall of a ~200 km-long normal fault (Fig. 1). This fault located on the western flank of the CB shows ~4500 m of vertical displacement since 5 Ma[4]. We perform a morphotectonic study on both Cordilleras coupled with low-temperature thermochronology apatite (U-Th)/He and fission-track dating to quantify the impact of magmatism and subduction processes on exhumation.

Geomorphic parameters and altitude contrasts between these two ranges indicate a differential uplift. The Cordillera Negra displays a smooth and asymmetric relief from the West to the East whereas the Cordillera Blanca shows higher and sharper relief with North/South and East/West contrasts. We obtain 35 new apatite fission-tracks ages and 20 (U-Th)/He ages for samples located along vertical and horizontal profiles at different latitudes of the Cordilleras Blanca and Negra (Fig. 1). The (U-Th)/He ages range from 5.6 ± 0.6 to 13.4 ± 1.3 Ma in the Cordillera Negra and range from 2.0 ± 0.2 to 11.8 ± 1.2 Ma in the Cordillera Blanca. The fission-track ages range from 23.6 ± 2.5 to 30 ± 3.0 Ma in the Cordillera Negra and range from 2.8 ± 2.2 to 8 ± 2.5 Ma in the Cordillera Blanca. We use these thermochronological data as inputs for QTQt tools for time-temperature reconstruction and thus to constrain the exhumation history.

Whole ages evidence a regional exhumation in both Cordilleras Blanca and Negra. Exhumation history inferred from low-temperature thermochronology ages coupled with geomorphologic characteristics suggests a regional component of uplift above the Peruvian flat-slab. Time-temperature reconstruction indicates a recent exhumation initiated ~4 Ma ago in the Cordillera Negra. Moreover, ages from the Cordillera Blanca indicate higher exhumation rates than in the neighbouring Cordillera Negra. Our set of thermochronological data brings new constraint on both Cordilleras thermal histories suggesting that the flattening of the Peruvian slab controls the regional exhumation as locally proposed for the Cordillera Blanca exhumation[5]. The Cordillera Blanca records additional exhumation controlled by plutonism and facilitated by structural inheritance. These processes occur as a response to the flattening of the Peruvian slab and confirm the role of the subducting plate geometry in topography building in Central Andes.

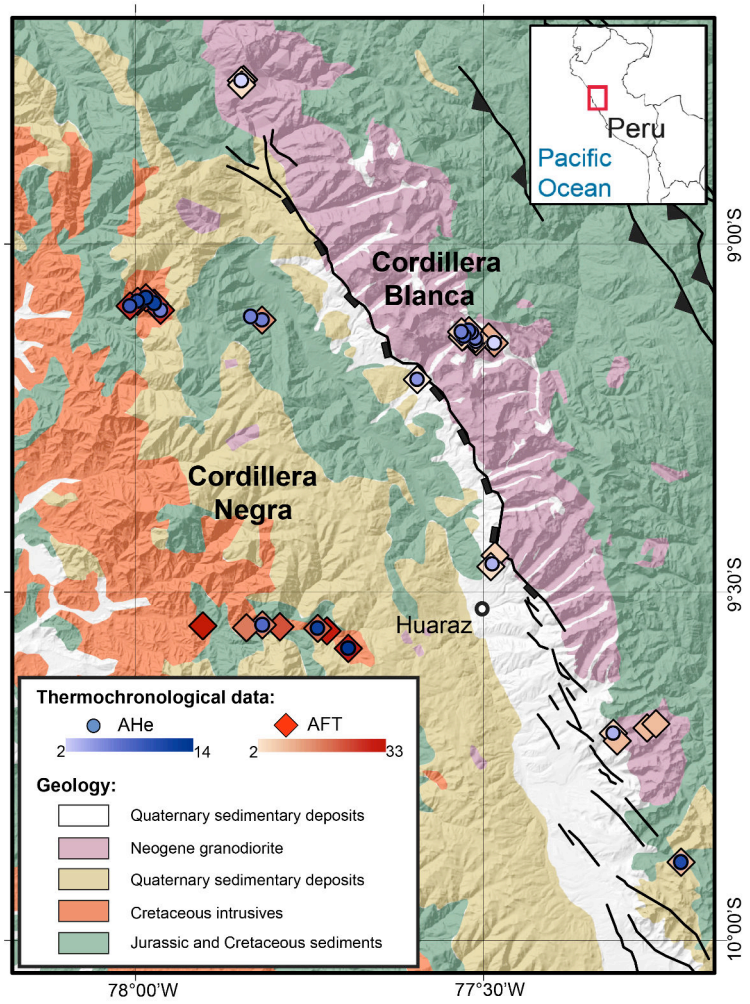

Figure 1. *Geological map (modified from INGEMMET, 2012) draped on a digital elevation model (GDEM data, 30 m resolution) showing location of the Cordillera Blanca and the Cordillera Negra. The apatite (U-Th)/He ages and apatite fission-track ages are localized respectively by blue circles and red squares. Coordinates are given in WGS 84 longitude and latitude (degrees).*

References

1. McNulty, B. A., Farber, D. L., Wallace, G. S., Lopez, R., & Palacios, O. Role of plate kinematics and plate-slip-vector partitioning in continental magmatic arcs: Evidence from the Cordillera Blanca, Peru. *Geology*, **26**, 827-830 (1998).
2. Giovanni, M. K. Tectonic and thermal evolution of the Cordillera Blanca Fault Zone, Peruvian Andes: Implications for normal faulting in contractional orogen. *Ph.D. Dissertation, Department of Earth Sciences, University of California, Los Angeles* (2007).
3. Noble, D. C., McKee, E. H., Mourier, T., & Mégard, F. Cenozoic stratigraphy, magmatic activity, compressive deformation, and uplift in northern Peru. *Geological Society of America Bulletin*, **102**, 1105-1113 (1990).
4. Bonnot, D. Néotectonique et tectonique active de la Cordillère Blanche et du Calllejon de Huaylas (Andes nord-péruviennes). *Thèse de l'université de Paris sud, Centre d'Orsay* (1984).
5. McNulty, B. A., & Farber, D. L. Active detachment faulting above the Peruvian flat slab. *Geology*, **30**, 567-570 (2002).
6. INGEMMET, 2012. Mapa geológica del Departemento de Ancash (Escala 1:500,000). Instituto Geológico Minero y Metalúrgico, Lima.

8.6.4 EGU 2015 - Oral

Geophysical Research Abstracts
Vol. 17, EGU2015-10797, 2015
EGU General Assembly 2015

Slab flattening driving regional uplift in the Cordilleras Blanca and Negra, Western Andes

Audrey Margirier (1,2), Laurence Audin (1,2,3), Xavier Robert (1,2,3), Matthias Bernet (1,2), and Cécile Gautheron (4)

(1) Univ. Grenoble Alpes, ISTerre, F-38041 Grenoble, France (audrey.margirier@gmail.com), (2) CNRS, ISTerre, F-38041 Grenoble, France, (3) IRD, ISTerre, F-38041 Grenoble, France, (4) Université Paris Sud, UMR GEOPS (Geosciences Paris Sud), CNRS-UPS 8145, F-91405 Orsay, France

The Andean range topographic evolution is known to have had a strong impact on regional climate by building an orographic barrier that preserved its western flank from the south Atlantic moisture. Even if largely invoked, the impact of subduction processes on the uplift and relief building is not yet well understood in the Andes. The northern Peru is characterized by a present day flat subduction zone (3-15°S), where both the geometry and temporal evolution of the flat-slab are well constrained. The subduction of two buoyant anomalies, the Nazca ridge and the lost Inca plateau controlled the slab flattening. The highest Peruvian peaks in the Cordillera Blanca (6768 m), and the Cordillera Negra (5187 m) are located just above the flat-slab segment. Both ranges trend parallel to the subduction zone and are separated by the NW-SE Rio Santa valley. The Cordillera Blanca batholith emplaced at 8-5 Ma and renders of an abnormal magmatic activity over a planar subduction. This area is a perfect target to explore the impact of slab flattening on the topography and uplift in the Occidental Cordillera of the Andes. We present new AHe and AFT data from three vertical profiles located in both the Cordilleras Blanca and Negra. We compare time-temperature paths obtained from inverse modeling of the thermochronological data with the timing of the slab flattening, the arrival of the Nazca ridge and magmatism. Our thermochronological data evidences a regional exhumation in the Occidental Cordillera from $\sim$10 Ma. We propose that the Nazca ridge subduction below the Occidental Cordillera (11 Ma) and slab flattening (8 Ma) drive the Occidental Cordillera uplift and thus exhumation. We evidence the important contribution of the magmatism in the Cordillera Blanca exhumation and high relief building in the Occidental Cordillera. Our new thermochronological data highlight the control of both the subduction processes and magmatism on the paleogeography and uplift in the Andes. Finally, the high topography of the Occidental Cordillera in northern Peruvian Andes was not built during compressive phases but is mainly controlled by subduction processes (ridge subduction, slab flattening and magmatism).

8.6.5 EGU 2015 - Poster

Geophysical Research Abstracts
Vol. 17, EGU2015-11516, 2015
EGU General Assembly 2015

The Cordillera Blanca normal fault and its contribution to the Andean topographic evolution (northern Peru)

Audrey Margirier (1,2), Xavier Robert (1,2,3), Stéphane Schwartz (1,2), Laurence Audin (1,2,3)

(1) Univ. Grenoble Alpes, ISTerre, F-38041 Grenoble, France (audrey.margirier@gmail.com), (2) CNRS, ISTerre, F-38041 Grenoble, France, (3) IRD, ISTerre, F-38041 Grenoble, France

Nature and localization of Quaternary tectonics remains largely unconstrained in Peruvian Andes as well as the mechanism driving rock uplift. The Cordillera Blanca normal fault accommodates extension in a convergent context. The fault system trends parallel to the subduction zone, just above the Peruvian flat-slab, and separate the Cordilleras Blanca and Negra. The Cordillera Blanca batholith (8-5 Ma) is an elongated pluton, emplaced at ∼6 km depth in the Jurassic sedimentary country rocks. The Cordillera Blanca range (6768 m) that comprises the highest Peruvian peak built the footwall of the fault. The ∼200 km-long fault has showed ∼4500 m of vertical displacement since 5 Ma. This normal fault is described as active despite the lack of historical seismicity and constitutes a striking singularity within the prevailing compressional setting of the Andean orogeny. This region is a perfect target to explore the contribution of large normal fault in relief building. Our goals are to determine if the fault was pre-existing before the Cordillera Blanca batholith emplacement, when it has been reactivated and how does it interact with the batholith exhumation. For that purpose, we focus on brittle deformation analysis from a regional scale (faults trends) to outcrop scale (fault planes, striaes and kinematics). We present here new structural data and focal mechanisms indicating a senestral transtensive component on the Cordillera Blanca normal fault and a regional extensional regime in the Cordillera Negra area. We compare the paleotensors obtained from the inversion of the microstructural data and focal mechanisms with the exhumation history deduced from the thermochronological data to constrain the role of the normal fault in relation with relief building. We propose that the Cordillera Blanca normal fault is an inherited tectonic feature reactivated in transtension after the slab flattening at ∼8 Ma. The differential exhumation of the Cordillera Blanca with respect to the Cordillera Negra can be explained by contemporaneous strike-slip deformation and magmatic emplacement before the plutonism cessation at ∼5 Ma. Finally, the regional exhumation inferred from our tectonic and thermochronological data comes in contradiction with models previously proposed for the Cordillera Blanca normal fault, which involved mainly extensional collapse.